NASA-CR-166,269

NASA CONTRACTOR REPORT 166269

NASA-CR-166269
19840020698

Study of Aerodynamic Technology for
Single-Cruise-Engine V/STOL Fighter/Attack Aircraft

FOR REFERENCE

NOT TO BE TAKEN FROM THIS ROOM

Phase I Final Report

J. R. Hess
R. L. Bear
McDonnell Aircraft Company

CONTRACT NAS2– 11001
February 1982

NASA

NF02333

Study of Aerodynamic Technology for
Single-Cruise-Engine V/STOL Fighter/Attack Aircraft

Phase I Final Report

J. R. Hess
R. L. Bear
McDonnell Aircraft Company
McDonnell Douglas Corporation
St. Louis, Missouri

NASA

N82-75515#

FOREWORD

This report was prepared by McDonnell Aircraft Company (MCAIR), St. Louis, Missouri, a division of the McDonnell Douglas Corporation, for the National Aeronautics and Space Administration (NASA). This study was performed under NASA Ames Research Center contract NAS2-11001, "Study of Aerodynamic Technology for Single-Cruise-Engine V/STOL Fighter/Attack Aircraft," from June 1981 through January 1982. The program was jointly sponsored by NASA and the Navy (DTNSRDC and NAVAIR). Program direction was provided by Mr. W. P. Nelms, Program Manager, and Mr. D. A. Durston, Program Engineer, of NASA Ames Research Center. The Navy points of contact were Mr. J. H. Nichols at DTNSRDC and Mr. M. W. Brown at NAVAIR. The program was managed at MCAIR by Mr. R. E. Martens, Program Manager, and Mr. J. R. Hess, Technical Manager.

The authors of this report wish to acknowledge the technical assistance provided by R. B. Jenny, W. E. Simon, M. L. Jones, D. R. Watson, and L. W. Gross (Aerodynamics), T. A. Kaemming (Propulsion), R. K. Konsewicz (Guidance and Control), D. W. Sweeney (Design), G. R. Parkan (Weights) and L. L. Pagel (Thermodynamics).

For the sake of clarity, U. S. Customary Units have been used throughout in lieu of S. I. (Metric) Units. A conversion table is provided in Appendix A.

i

SUMMARY

The overall objective of this two phase NASA and Navy sponsored program is to develop aerodynamic technology for post-1990 time period single-cruise-engine V/STOL fighter/attack aircraft. The major accomplishments of this Phase I study were:

o A supersonic, high performance V/STOL fighter/attack aircraft conceptual design in the 30,000 pound VTOGW class was defined.
o Its aerodynamic characteristics were estimated and performance evaluated.
o Aerodynamic and aerodynamic-propulsion uncertainties requiring additional investigation were identified.
o A research program to resolve these uncertainties and validate the aerodynamic prediction methods was defined.

The aircraft concept defined is a four nozzle, thrust vectoring, canard-wing configuration with an advanced Pratt and Whitney separated flow turbofan engine with fan stream augmentation. This configuration, the MCAIR Model 279-3, has leading and trailing edge flaps for maneuver enhancement and a leading edge decamber flap for improved supersonic performance. Ailerons provide roll control and a rudder provides directional control. Aircraft design relating to the propulsion system, structures, control system and subsystems was investigated in sufficient depth to ensure the credibility of the concept.

The configuration was sized to prescribed NASA weight and performance guidelines. These guidelines were:

o VTOL gross weight from 15,000 to 30,000 pounds,
o Sustained Mach number capability of at least 1.6,
o Sustained load factor of 6.2 at 0.60 Mach, 10,000 foot altitude,
o 1.0 g specific excess power capability of 900 feet per second at 0.90 Mach, 10,000 foot altitude, and
o STO sea-based gross weight = VTOGW + 8,000 to 10,000 pounds.

The Model 279-3 has a VTOGW of 29,840 pounds. Performance relative to the NASA guidelines is:

o A sustained Mach number capability of 2.0 (limited by inlet design),
o Sustained load factor of 6.2 at 0.60 Mach, 10,000 feet,
o 1.0 g specific excess power of 995 feet per second at 0.90 Mach, 10,000 feet, and
o STOGW = 41,800 pounds with a flat deck run of 400 feet (0 kts WOD).

All NASA performance guidelines were met or exceeded. Mission performance estimates also showed that the study configuration has good air-to-air and air-to-ground mission performance.

Longitudinal and lateral-directional aerodynamic characteristics, including control effectiveness characteristics, were estimated using current technology analytical and empirical prediction techniques and wind tunnel data from similar canard configurations. Characteristics were estimated up to 30 degrees angle of attack subsonically and 15 degrees supersonically.

Significant aerodynamic and aerodynamic-propulsion interaction uncertainties were identified in the design of the study configuration and in estimating its aerodynamic characteristics. Their effect on aircraft sizing and performance was assessed. Most of the uncertainties identified were associated with:

- o The close-coupled horizontal canard,
- o The leading and trailing edge flaps,
- o The large inlets for the high bypass ratio engine, and
- o The forward location of the vectored thrust propulsion system (more forward maximum cross sectional area plus exhaust plume interaction with fuselage flow field and lifting surfaces).

The uncertainties involved both subsonic and supersonic minimum drag, induced drag, and longitudinal and lateral-directional stability and control.

Existing analytical/empirical methods were found to be inadequate to accurately predict in many areas the effect of horizontal canards. Supersonically, existing linear theory methods tend to overestimate by 55 to 75% the destabilizing effect of horizontal canards and canard control effectiveness capability by as much as 60%. Subsonic, high angle of attack flap effects and canard-flap interactions also cannot be accurately predicted. Comparison of wind tunnel data for several different canard configurations showed that canard effects on lateral-directional stability were very configuration dependent, with wind tunnel testing being the only way to accurately predict them. Another prediction uncertainty identified is the power dependent effects of variable inlet mass flow on canard-wing characteristics.

Wind tunnel testing is required to thoroughly assess the uncertainties identified in Phase I. A Phase II wind tunnel test plan, utilizing an aerodynamic flow through model concept was defined. This test plan is designed to provide a high quality aerodynamic data base for assessing the identified uncertainties as well as evaluating the aerodynamic prediction methods used in Phase I. Most of the uncertainties can be assessed with an aerodynamic flow through model, but a powered model is required to assess all of them. An aerodynamic flow through model concept was defined for the Phase II test program. One of its features is that it can be converted at low cost to a jet effects model for follow on testing.

TABLE OF CONTENTS

LIST OF PAGES

LIST OF FIGURES

LIST OF FIGURES

LIST OF SYMBOLS AND ABBREVIATIONS

Symbol	Definition	Units
a	Acceleration	ft/sec^2
a/g	Longitudinal Acceleration Ratio	—
A_{exit}	Exit Area	ft^2
A_{max}	Maximum Fuselage Cross Sectional Area Immediately Forward of the Exhaust Nozzles	ft^2
Ao/Ac	Capture Area Ratio	—
ALT	Altitude	ft
AMAD	Airframe Mounted Accessory Drive	—
AND, ND	Aircraft Nose Down	—
ANL	Aircraft Nose Left	—
ANU, NU	Aircraft Nose Up	—
ANR	Aircraft Nose Right	—
AR	Aspect Ratio	—
b	Wing Span	ft
b/2	Wing Semispan	ft
$\bar{c}$, MAC	Mean Aerodynamic Chord	in
c_R	Root Chord	in
c_T	Tip Chord	in
C_D	Drag Coefficient	—
$C_{D_{AB}}$	Afterbody Drag	—
C_{Di}	Induced Drag Coefficient	—
$C_{D_{MIN}}$	Minimum Drag Coefficient	—
C_{D_0}	Drag Coefficient for Zero Lift	—
C_f	Roughness Factor	—
C_{fi}	Incompressible Skin Friction Coefficient	—

Symbol	Definition	Units
$C_{l_{\delta_A}}$	Rolling Moment Derivative Due to Aileron Deflection	1/Deg
C_{l_β}	Rolling Moment Stability Derivative due to Sideslip	1/Deg
$C_{l_{\delta_R}}$	Rolling Moment Derivative due to Rudder Deflection	1/Deg
$C_{l_{\beta_{INLET}}}$	Rolling Moment Sideslip Stability Derivative Increment due to Inlet Momentum	1/Deg
C_L	Lift Coefficient	–
$C_{L_{BUFFET}}$	Buffet Lift Coefficient	–
$C_{L_{MAX}}$	Maximum Lift Coefficient	–
C_{L_α}	Lift Curve Slope	1/Deg
$C_{L_{\delta_C}}$	Lift Coefficient due to Canard Deflection	1/Deg
$C_{L_{\delta_F}}$	Lift Coefficient due to T.E. Flap Deflection	1/Deg
C_m	Pitching Moment Coefficient	–
$C_{m_{INLET}}$	Inlet Momentum Pitching Moment Coefficient	–
C_{m_o}	Pitching Moment at Zero Lift	–
$C_{m_{\delta_C}}$	Pitching Moment Coefficient due to Canard Deflection	1/Deg
$C_{m_{\delta_F}}$	Lift Coefficient due to T.E. Flap Deflection	1/Deg
$C_{n_{\beta_{DYNAMIC}}}$	Sideslip Stability Derivative	1/Deg
$C_{n_{\beta_{STAB}}}$	Yawing Moment Stability Derivative	1/Deg
$C_{n_{\beta_{INLET}}}$	Side Force Stability Derivative Due to Inlet Momentum	1/Deg
$C_{n_{\delta_A}}$	Yawing Moment Derivative Due to Aileron Deflection	1/Deg
$C_{n_{\delta_R}}$	Yawing Moment Derivative Due to Rudder Deflection	1/Deg
C_V	Nozzle Velocity Coefficient	–
C_{Y_β}	Side Force Stability Derivative	1/Deg
$C_{Y_{\delta_A}}$	Side Force Derivative Due to Aileron Deflection	1/Deg
$C_{Y_{\beta_{INLET}}}$	Side Force Sideslip Stability Derivative Increment Due to Inlet Momentum	1/Deg

Symbol	Definition	Units
$C_{Y_{\delta_R}}$	Side Force Derivative Due to Rudder Deflection	1/Deg
CAP	Combat Air Patrol Mission	-
C.G.	Center of Gravity	$\% \ \bar{c}$
CTOL	Conventional Takeoff and Landing	-
D/T	Drag to Thrust Ratio	-
D_{lip}	Inlet Cowl Lip Drag	lb
DLI	Deck Launched Intercept	-
ECS	Environmental Control System	-
FOD	Foreign Object Damage	-
FS	Fuselage Station	in
FSB	Fan Stream Burning	-
g	Acceleration due to Gravity	ft/sec^2
GW	Gross Weight	lb
$h_{c/\bar{c}}$	Height of Canard's Aerodynamic Center Above the Wing Chord Plane Divided by the Mean Aerodynamic Chord of the Wing	-
h/D_e	Ratio of the Aircraft Height Above Ground to an Equivalent Diameter of the Total Exit Area of all the Nozzles	-
I_Y	Pitch Moment of Inertia	$slug\text{-}ft^2$
I_Z	Yaw Moment of Inertia	$slug\text{-}ft^2$
L/D	Lift to Drag Ratio	-
Δ L/T	Lift Loss to Gross Thrust Ratio	-
L/T	Lift to Thrust Ratio	-
LCIU	Longitudinal Control Integration Unit	-
LIDS	Lift Improvement Devices	-
LVDT	Linear Variable Differential Transformers	-
LWD	Left Wing Down	-

Symbol	Definition	Units
LWU	Left Wing Up	-
M	Mach Number	-
MCAIR	McDonnell Aircraft Corporation	-
MFCF	Mass Flow Calibration Facility	-
N.P.	Neutral Point	$\% \bar{c}$
NPR	Nozzle Total Pressure Ratio	-
P	Pressure	lb/ft^2
P_s	Specific Excess Power	ft/sec
P_{exit}	Exit Pressure	lb/ft^2
P_∞	Ambient Pressure	lb/ft^2
P_{exit}/P_{T_o}	Nozzle Exit Pressure Ratio	-
PCB	Plenum Chamber Burning	-
PSTF	Propulsion Subsystem Test Facility	-
P_{exit}/P_o	Exit Static Pressure Ratio	-
PWT	Pressure Wind Tunnel	-
q	Dynamic Pressure	lb/ft^2
Rn, Re	Reynolds Number	-
RCS	Reaction Control System	-
RLS	Reservoir Level Sensing Valve	-
S_C	Exposed Canard Area	ft^2
S_{VT}	Vertical Tail Area	ft^2
S_c/S_w	Exposed Canard Area to Wing Area Ratio	-
S_w	Wing Area	ft^2

Symbol	Definition	Units
SAS	Stability Augmentation System	–
SCM	Signal Conversion Mechanism	–
SFC	Specific Fuel Consumption	–
SSWT	Supersonic Wind Tunnel	–
STO	Short Take Off	–
t/c	Thickness to Chord Ratio	–
T	Temperature	$°F$, $°R$
T_{amb}	Ambient Temperature	$°F$
TS	Tunnel Station	in
T/W	Thrust to Weight Ratio	–
TVC	Thrust Vectoring Control	–
TUWT	Transonic Unitary Wind Tunnel	–
TWT	Transonic Wind Tunnel	–
V_e	Equivalent Velocity Ratio = ratio of aircraft Forward Velocity to Engine Nozzle Exit Velocity	–
VSCF	Variable Speed Constant Frequency	–
V/STOL	Vertical or Short Take Off and Landing	–
VTOGW	Vertical Take Off Gross Weight	lb
W/S	Wing Loading	lb/ft^2
$W\sqrt{T_T}/P_T$	Normalized Mass Flow	–
WL	Waterline	in
x/c	Chordwise Station	–
2y/b	Spanwise Station	–
Y/T	Ratio of Side Force to Gross Thrust	–

Symbol	Definition	Units
Zc/c	Camber Distribution	–
$X\ \alpha$	Angle of Attack	Deg
α_{O_L}	Angle of Attack at Zero Lift	Deg
β	Sideslip Angle	Deg
δ_A	Aileron Deflection (positive trailing edge down TED)	Deg
δ_{A_L}	Left Aileron Deflection (positive TED)	Deg
δ_{A_R}	Right Aileron Deflection (positive TED)	Deg
δ_C	Canard Deflection (positive TED)	Deg
δ_F	T.E. Flap Deflection (positive TED)	Deg
δ_H	Horizontal Stabilator Deflection (positive TED)	Deg
δ_R	Rudder Deflection (positive TED)	Deg
θ	Pitch Attitude	Deg
λ	Taper Ratio ($\lambda = c_T/c_R$)	–
Λ_{LE}	Leading Edge Sweep	Deg

1. INTRODUCTION

V/STOL capability can significantly increase the utility of an advanced supersonic fighter/attack aircraft, but it also imposes challenges on the aircraft designer. Chief among these are the efficient integration of the thrust vectoring V/STOL propulsion system and aerodynamic control-lifting surfaces into the airframe to achieve the desired performance.

Designing the "best" aircraft configuration in terms of either VTOGW or life cycle cost for a given set of requirements requires accurate prediction of the aerodynamic and propulsion characteristics. The propulsion system characteristics can generally be predicted with confidence after the engine has been developed, but there are some significant uncertainties in the aerodynamic and aerodynamic-propulsion interaction characteristics. Inaccurate predictions and imprecise assessments of these uncertainties can lead to the selection of the wrong airframe propulsion concept, i.e., one with inadequate performance or excessive life cycle costs.

NASA and the Navy have a number of ongoing research programs related to the development of the aerodynamic and aerodynamic-propulsion interaction technologies required for V/STOL fighter/attack aircraft. Currently NASA and the Navy (DTNSRDC and NAVAIR) are jointly sponsoring a two phase research program to address the development of these technologies as required for development of single engine supersonic V/STOL fighter/attack aircraft. The Phase I objectives were to define the aircraft concept, estimate the aerodynamic characteristics, assess the aerodynamic uncertainties requiring additional research, and define the wind tunnel program and model concept.

The MCAIR aircraft concept for this program is the Model 279-3, Figure 1-1, which uses a four nozzle, thrust vectoring, Pegasus type propulsion system with fan stream burning. This concept evolved from previous IRAD and Navy funded studies, and incorporates lessons learned in aerodynamics, propulsion, controls, materials and operability on numerous previous CTOL and V/STOL aircraft studies.

We have drawn heavily on the practical V/STOL aircraft experience gained in our work with the AV-8A and development of the AV-8B, Figure 1-2. These single-cruise-engine attack aircraft, also use the four nozzle, thrust vectoring Pegasus engine, and engine-bleed reaction control system. This experience represents over 95% of the free world's V/STOL expertise. This expertise has been coupled with the latest design and operational considerations drawn from the F-15 and F-18 fighter programs.

In developing the Model 279-3 configuration, we have identified several specific aerodynamic and aerodynamic-propulsion interaction uncertainties for detailed study, Table 1-1. These uncertainties are associated with the close-coupled canard, the large inlet (high bypass ratio engine, BPR = 1.2), and the forward location of the thrust vectoring propulsion system (more forward maximum cross sectional area plus exhaust plume interactions with the fuselage flowfield and lifting surface circulation). The parametric model concept planned for the Phase II assessment of these uncertainties is shown schematically in Figure 1-3.
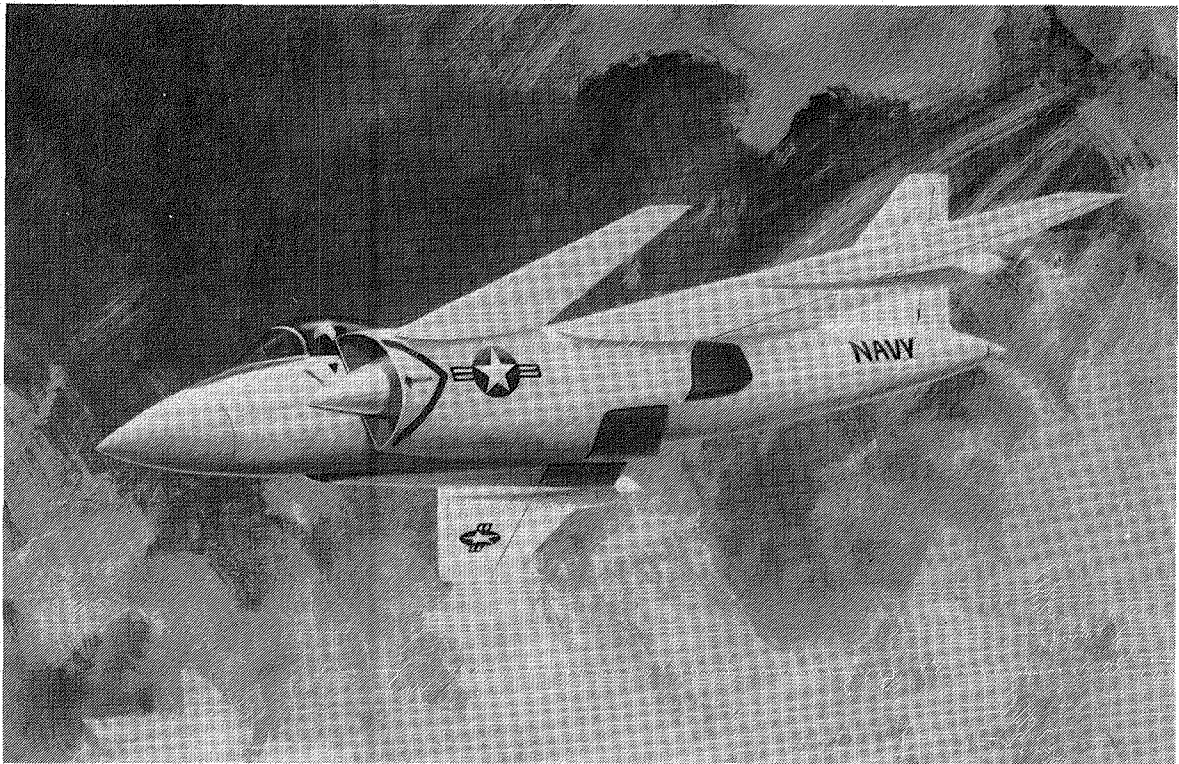
GP13-0983-254

FIGURE 1-1
MODEL 279-3
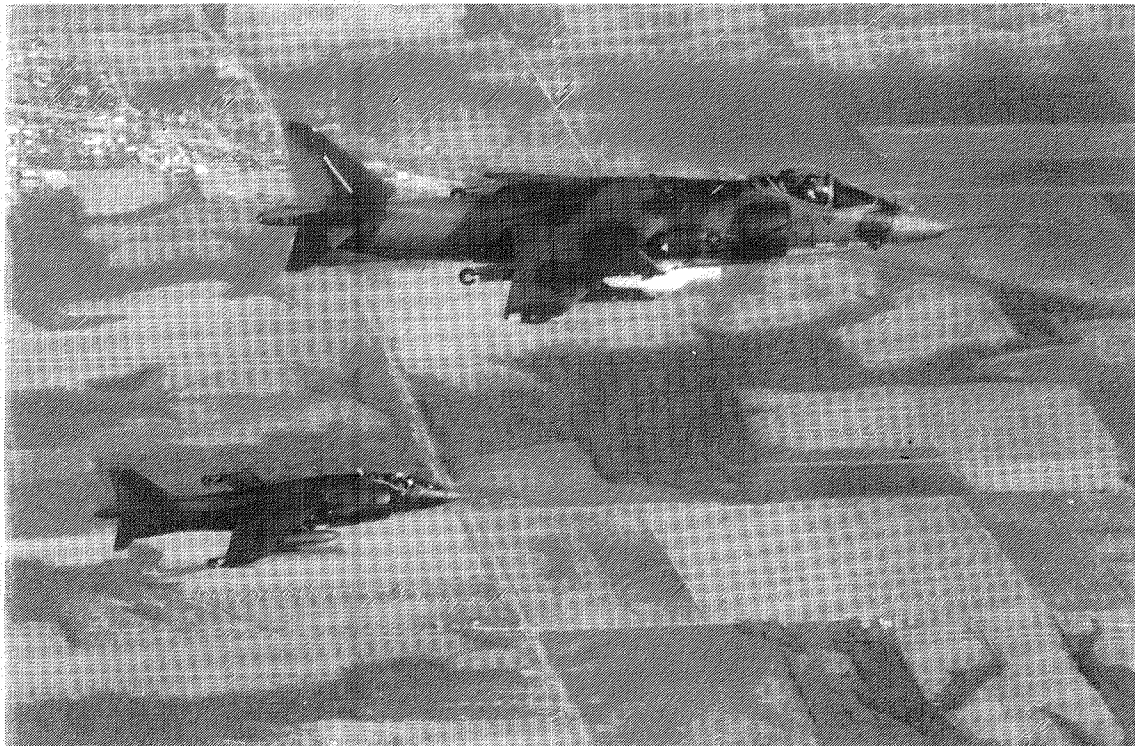
GP13-0983-232

FIGURE 1-2
AV-8A AND AV-8B

TABLE 1-1
AERODYNAMIC UNCERTAINTIES IDENTIFIED DURING STUDY

UNCERTAINTY	SOURCES			
	WING AND CLOSE-COUPLED CANARD	L E AND T E FLAPS	LARGE INLET	FORWARD LOCATION OF PROPULSION SYSTEM
$C_{D_{MIN}}$	✓	✓	✓	✓
DRAG DUE TO LIFT	✓	✓		✓
TRIM DRAG	✓	✓		
C_L BUFFET ONSET	✓	✓		✓
C_L MAXIMUM	✓	✓		
LONGITUDINAL STABILITY	✓	✓		✓
LONGITUDINAL CONTROL	✓	✓		
LATERAL-DIRECTIONAL STABILITY	✓		✓	
LATERAL CONTROL	✓	✓		

GP13-0983-144

CANARD
● ON/OFF
● DEFLECTION

WING
● LOCATION
● DECAMBER FLAP
● AILERON
● FLAP
● ON/OFF

VERTICAL TAIL
● RUDDER DEFLECTION
● ON/OFF

INLET
● HALF AXISYMMETRIC

NOZZLES
● MASS FLOW CHOKES

HORIZONTAL TAIL
● ON/OFF
● DEFLECTION

GP13-0983-13

FIGURE 1-3
MODEL REQUIRED TO RESOLVE UNCERTAINTIES

The Phase I results for the high performance Model 279-3 aircraft are presented in the following sections. The Phase II program objectives are to design and fabricate a flow through model of this concept and participate in a wind tunnel test program. These tests will resolve the areas of aerodynamic and interaction uncertainties identified in Phase I and provide an adequate data base, with related improvements in prediction techniques.

2. AIRCRAFT DESIGN

One of the objectives of this study was to define a V/STOL fighter design which satisfied the Reference (1) NASA study guidelines. The MCAIR Model 279-3 aircraft, Figure 2-1, designed to the NASA study guidelines, is in the 30,000 lb. vertical take off gross weight class and is compatible with a wide range of air capable surface ships. The following section describes the Model 279-3 design philosophy, the aircraft sizing, and presents a comparison with the NASA design guidelines.

2.1 DESIGN PHILOSOPHY

The innovative design features incorporated in the Model 279-3 result directly from the thrust vectoring propulsion system. The major characteristics of this system are:

a) Vectoring nozzles located forward and aft of the aircraft c.g.,
b) Modulated fan stream burning (called plenum chamber burning by Rolls Royce),
c) Swivel nozzle design,
d) Thrust vectoring capability up to 150 degrees,
e) In-flight thrust vectoring,
f) Integrated flight propulsion control system.
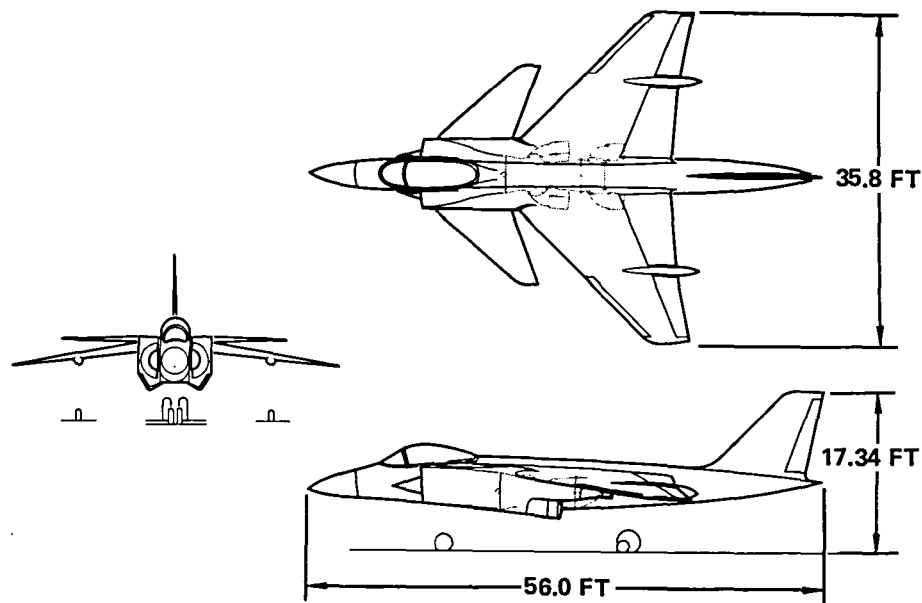
GP13-0983-199

FIGURE 2-1
MODEL 279-3
GENERAL ARRANGEMENT

Modulation of the fan stream burning and engine speed provides the unique capability of trimming wide ranges in c.g. travel associated with fuel burnoff and large variations in potential store loadings and store release effects. It also provides part of the large control moments required for safe V/STOL operation with high inertia store loading conditions. Fan stream augmentation can be modulated in the high control requirement regime, over and above trim, to provide a portion of the pitch maneuvering control or for use as a backup system.

The ability to modulate fan flow burning and engine speed also offers the advantage, over some other propulsion systems, in minimizing the impact on VTOL environment. For example, during VTOL operation from an unimproved site our aircraft would be off-loaded and operated at lower thrust and hence lower exhaust temperatures.

The swivel nozzle design incorporates a 90 degree elbow, which provides excellent IR suppression by shielding the hot engine parts from all aspects. Recent USAF/MCAIR studies have indicated that such suppression will significantly improve aircraft survivability.

At a typical combat condition thrust vectoring increases the Model 279-3 instantaneous load factor by 2.0 g. Large thrust deflections provide a deceleration that can be used to position the aircraft with the capability for rapid reacceleration since a high engine rpm is maintained. The aircraft can also be pitched rapidly, providing an effective attack and evasive capability. Thrust vectoring is also useful in air-to-ground missions for speed control during the attack and rapid egress from the target area.

In-flight thrust vectoring, coupled with the location of the aft nozzles, near the slotted flap and wing trailing edge offers the potential for enhanced circulation. This translates into increased maneuverability and STOL performance.

The potential of this concept to produce a V/STOL fighter with proven V/STOL characteristics and uncompromised – actually enhanced – combat characteristics clearly justifies a thorough aerodynamic analysis substantiated by wind tunnel tests. The single engine thrust vectoring concept is elegantly simple and hence the most successful V/STOL concept to date. The close coupled canard with active controls is the technological fore front of the high performance fighter.

The wing planform is a compromise between subsonic and supersonic performance. Subsonic emphasis is placed on high sustained maneuverability requiring low drag due to lift. Supersonic emphasis is directed toward lower lift maneuverability conditions where C_{D_0} is equally important.

To reduce the subsonic drag due to lift, the wing is cambered and twisted. The camber and twist were determined by analytic techniques and verified in wind tunnel tests, Reference (2). Half span trailing edge flaps are included to increase the subsonic maneuverability. These trailing edge flaps plus drooped ailerons provide high lift in V/STOL and STOVL operations. In addition, lift during STOL is increased by placing the aft nozzles near the flap and the forward nozzles farther under the wing. Partial span leading edge flaps are included to increase the STOL lift and subsonic L/D at high angles of attack. These leading edge flaps also act as decamber flaps to reduce the

supersonic camber drag. The effect of the decamber flap on supersonic drag has also been verified in the wind tunnel, Reference (2).

A close-coupled canard provides longitudinal control power. Differential ailerons provide roll control and the rudder provides directional control.

The close-coupled canard also provides vortex interaction with the wing. This increases lift and L/D of the basic wing in the high angle of attack region. The canard also increases maneuvering flap and aileron control effectiveness.

A three axis reaction control system (RCS), operating on engine bleed air, provides control moments independent of dynamic pressure. During VTOL operation and into transition the maneuvering control is provided by the RCS. A pitch thruster in the forward fuselage blows downward, a second pitch thruster in the aft fuselage blows up or down. Roll reaction jets are located in the wing tips and blow up or down. The yaw control thruster is located in the aft tip of the fuselage and blows laterally in each direction.

In VTOL operation the aircraft is balanced in the pitch axis when the resultant of the VTOL thrust from the forward nozzles and from the rear nozzles coincides with the aircraft center of gravity (c.g.). The position of this resultant, or thrust center, can be moved fore and aft by changing the percentage of thrust furnished by the forward and aft nozzles. The percentage contributed by the front nozzles can be decreased by a decrease in FSB thrust level. The constant total thrust is maintained by increasing engine fan speed. The thrust added by the increase in fan speed is through the rear nozzles, moving the thrust center aft. This ability to move the center of thrust can be used to trim the aircraft in the pitch axis in VTOL flight as the aircraft c.g. changes with fuel usage or with different stores loadings. Otherwise, the pitch trim would be accomplished using engine bleed air through the RCS. This demand on the RCS would reduce jetborne performance and decrease the RCS availability for maneuvering and for trim in the roll and yaw axes.

Thrust vectoring provides unique low speed air combat attack and defensive capabilities. Rotating the nozzles down increases the instantaneous turn rate and load factor and provides a deceleration which is a function of the nozzle angle. The maximum turn rate may be improved 20%. The maximum load factor change may be 0.9 g in the lift direction and -1.2 g in the drag direction at 1.2 Mach number and 30,000 ft. This deceleration is much higher than for conventional aircraft with speed brakes; for example, under the same conditions the F-4 decelerates at 0.2 g using speed brakes.

There is the potential for direct force modes to enhance air combat and ground attack. The thrust vectoring in combination with deflection of the canard and flap would provide the longitudinal mode. The lateral-directional direct force modes are provided by differential deflection of the canards and rudder deflection.

The operational weight empty (OWE) of the Model 279-3 is 19,808 lb and 9,950 lb of fuel can be carried internally. VTO performance requirements sized the engine to provide a total installed sea level static thrust of 34,316 lb on a 90°F day. With this level of thrust, the short take-off gross weight (STOGW) is 41,800 lb when 400 feet of deck is available under no-wind

conditions, or 200 ft is available with 20 knots of wind over the deck (WOD). For vertical take-off operation, a thrust-to-weight ratio of 1.15 is maintained. Thus, the vertical take-off gross weight (VTOGW) is 29,840 lb.

2.2 AIRCRAFT SIZING

The Model 279-3 was sized to the Reference (1) NASA guidelines and a STOVL Deck Launch Intercept (DLI) mission requirement using the MCAIR Computerized Aircraft Design and Evaluation (CADE) program. The DLI mission, Figure 2-2, was selected since it requires sustained high supersonic speed and is compatible with future requirements of the Navy. A DLI mission radius of 150nm was selected as the design mission radius. This is considered adequate for a STOVL interceptor operating from forward dispersed ships.

2.2.1 NASA DESIGN GUIDELINES - These guidelines, which are listed below, were selected to ensure that high performance supersonic V/STOL fighter/attack designs would be defined for this study. The NASA guidelines were:

o   VTOL gross weight from 15,000 to 30,000 pounds
o   Sustained Mach number capability of at least 1.6
o   Sustained load factor capability of 6.2 at 0.6 Mach, 10,000 foot altitude (88% VTOGW)
o   1.0 g specific excess power capability of 900 feet per second at 0.90 Mach, 10,000 foot altitude (88% VTOGW)
o   STO sea-based gross weight = VTOGW + 8,000 to 10,000 pounds.

The MCAIR Model 279-3 met or exceeded all NASA guidelines.

2.2.2 DESCRIPTION OF SIZING PROGRAM - CADE, Figure 2-3, is an interdisciplinary program (aerodynamics, weights, propulsion) which utilizes a similar aircraft for component scaling. Each major component of the aircraft is input to the program in terms of geometry, weight, aerodynamic lift and drag plus size and shape scaling rules. The unity size engine and scaling rules are also inputs. Based on the mission and maneuvering requirements, CADE converges on a vehicle design. CADE also is an excellent program for conducting trade studies required in advanced design.

2.2.3 RESULTS OF SIZING STUDIES - The engine was sized for a VTOGW capability of 29,900 lb. This VTOGW changed later to 29,840 lb because of updated propulsion data received from Pratt and Whitney. The engine was sized for VTO based on the estimated ground effects discussed in Section 6.3.1. The $(T/W)_{VTO}$, as estimated is 1.15.

A carpet plot of $(T/W)_{VTO}$ and W/S is presented in Figure 2-4 with the NASA performance guidelines superimposed. This figure shows that the wing was sized by the 6.2 sustained load factor requirement at 0.6 Mach number, 10,000 ft altitude resulting in a $(W/S)_{VTO}$ of 69.8 lb/ft^2. For the design VTOGW of 29,900 lbs, this resulted in wing reference area of 428.4 ft^2 for the Model 279-3. Internal fuel capacity required for the design DLI mission (150nm radius) was determined to be 9,950 lbs. Take off gross weight with full internal fuel for the design STOVL DLI mission is 31,224 lb. Internal fuel is off-loaded for VTO operation. A comparison of the predicted Model 279-3 performance relative to the NASA guidelines is presented in Table 2-1.
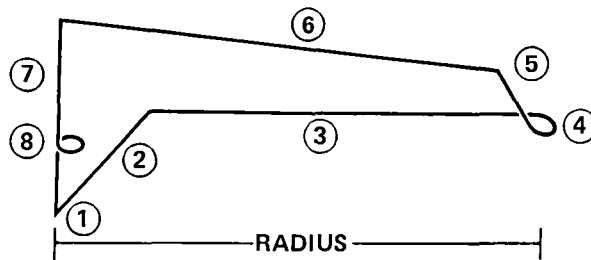
STORE LOADING: (2) SRM + (2) AMRAAM	
① WARM-UP, STO, ACCELERATION	2 MIN, IRT; 0.5 MIN MAXIMUM POWER
② CLIMB	TO DASH CONDITION: MAXIMUM POWER
③ DASH	MACH 1.6 @ 40,000 FT
④ COMBAT	2 MIN, MAXIMUM POWER AT DASH CONDITION
⑤ DECELERATE-CLIMB	TO BCAV
⑥ CRUISE	BCAV
⑦ DESCENT	TO SEA LEVEL NO FUEL OR DISTANCE CREDIT

⑧ LANDING ALLOWANCE
    LOITER
    LANDING
	
	10 MIN, AT SEA LEVEL, MINIMUM FUEL
	45 SEC AT LANDING POWER

RESERVE	5% TOTAL FUEL

Service tolerance
5% fuel flow

GP13-0983-237

FIGURE 2-2
STOVL SUPERSONIC DLI MISSION

2.2.4 <u>CANARD SIZING</u> - A review of the rapidly growing body of information pertaining to the design of canard-wing combinations, e.g., References (3) through (12), has established several "rules-of-thumb" applicable to the canard sizing. Since the canard functions as a highly loaded wing in the up-wash field of the main wing, similar planform design constraints apply to both surfaces. The canard should have a similar critical Mach number to that of the wing, which establishes the canard leading edge sweep angle. Strength and weight considerations tend to drive the aspect ratio to low values. However, since the canard functions as a control surface, it should develop a high maximum lift. This, and a requirement for aerodynamic efficiency (high L/D values), moderates the extremes of the range of leading edge sweep and aspect ratio that can be considered. In general, the canard planform is similar to that of the wing.
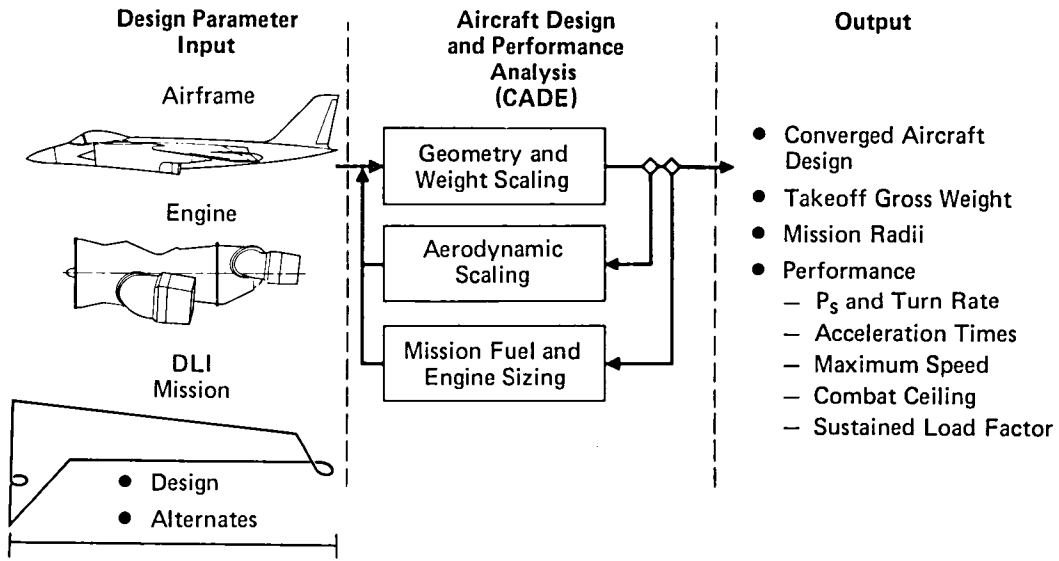
GP13-0983-14

FIGURE 2-3
COMPUTERIZED AIRCRAFT DESIGN
EVALUATION (CADE) PROCEDURE
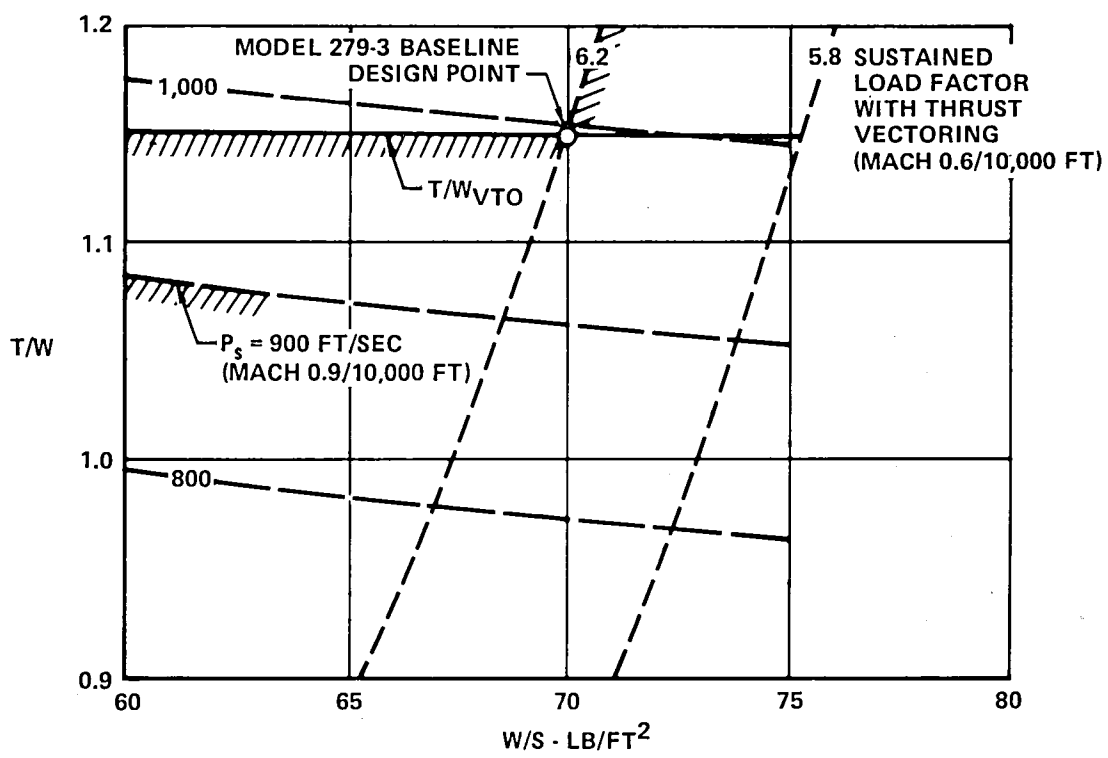
GP13-0983-125

FIGURE 2-4
MODEL 279-3 BASELINE PERFORMANCE

The sources referenced also indicate that the most favorable canard effect will result whenever the canard is at or above the chord line of the wing and ahead of the wing. The majority of the aerodynamic improvement due to the canard is realized when the canard is raised above the wing by at least 10 percent of the wing mean aerodynamic chord, and the aerodynamic centers of the canard and wing (both defined at one-quarter of their respective mean aerodynamic chords) are separated by $\sim$ 80 percent of the wing MAC. The Model 279-3 canard height ($h_c/\bar{c}$) is 0.1 and the longitudinal moment arm ($l_c/\bar{c}$) is 0.8.

TABLE 2-1
COMPARISON WITH NASA GUIDELINES

ITEM	NASA GUIDELINES	Model 279-3
VTOGW	15,000 to 30,000 lb	29,840 lb
Sustained Load Factor (0.6M, 10,000 ft, 88% VTOGW)	6.2	6.2
Sustained Mach Number	1.6	2.0
Specific excess power (0.9M, 10,000 ft, 88% VTOGW, 1 g)	900 fps	995 fps
STO sea based gross weight	VTOGW + 8,000 to 10,000 lb	41,800* lb

*Flat deck run of 400 ft (0 Kts WOD) or 200 ft (20 Kts WOD)

In order to establish the relative size of the canard with respect to that of the wing, it is necessary to consider both the effect of the canard on the wing and its ability to function as a control surface. A close-coupled canard exerts a favorable vortex interference on the wing. This enables the combination to continue to develop lift up to higher angles of attack than would the wing alone. An exposed canard area to wing area ratio of 0.2 was selected for the Model 279-3. This size canard provides a significant level of favorable vortex interaction with the wing, Figure 2-5, and also the level of static longitudinal stability required for optimum performance.

This canard size, 20 percent of the wing area also is sufficient to provide sufficient maneuvering control capability. The MCAIR guideline for minimum nose-down control margin, Reference (13), is the generation of a 5 degree/per second nose down pitch rate within 1 second when the aircraft is trimmed at $C_{L_{max}}$ at the 1.0 g stall speed. This has been checked utilizing
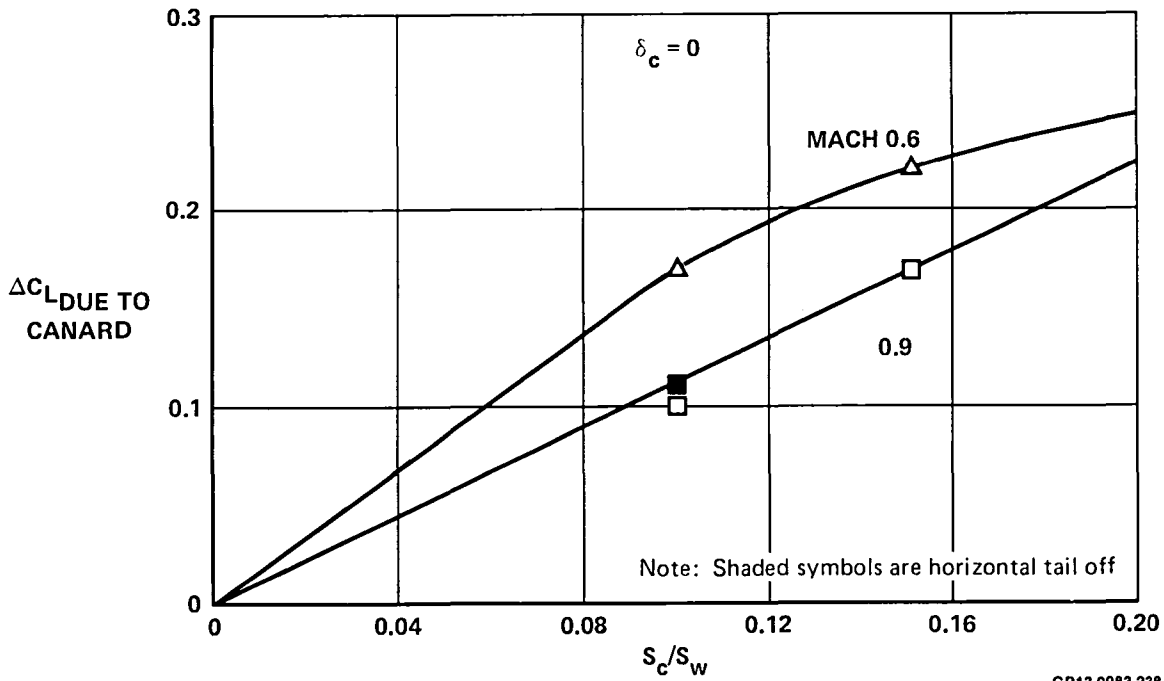
FIGURE 2-5
EFFECT OF HORIZONTAL CANARD ON LIFT AT $\alpha = 24°$
3-Surface F-15
$h_c/c \simeq 0.1$

the mass properties of the Model 279-3 aircraft from Section 3.4 and the estimated aerodynamic characteristics from Section 4.1. This pitch rate can be established, for example, by an incremental nose-down pitching moment of -0.028 at 0.5 Mach, 30,000 ft altitude. This is achievable with the $\delta_c = -20°$ canard deflection shown in Section 4.1. Testing of canard deflections as great as $\delta_c = -30°$ is proposed in Section 8.2. This size canard can also trim the aircraft up to the design load factor at supersonic speeds above 40,000 ft. It is readily seen that the canard size chosen is sufficient.

2.2.5 <u>VERTICAL TAIL SIZING</u> - The approach to vertical tail sizing was also based on the MCAIR guidelines of Reference (13). The general guideline is that lateral-directional stability be sufficient to maintain static aerodynamic stability up to the maximum angle of attack for trimmed flight. It is further recommended that the aircraft is sufficiently stable in sideslip that any lateral weight asymmetries would not cause departure.

In order to size the vertical tail, its directional stability contribution was first established by means of the Vortex Lattice Aerodynamic Analysis Program, Reference (14). Using a fuselage shape representative of the Model 279-3 configuration, vertical tails of varying size were studied. The predicted tail contributions are compared in Figure 2-6 to that predicted for a representative tail by DATCOM, Reference (15).

2-8
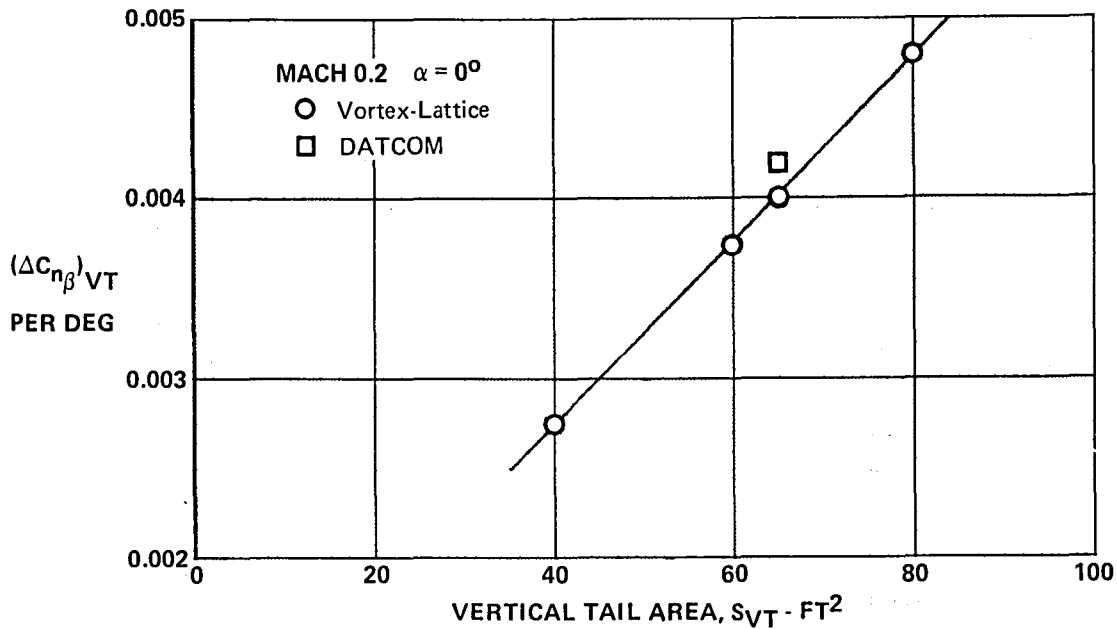
FIGURE 2-6
VERTICAL TAIL CONTRIBUTION TO DIRECTIONAL STABILITY

Once the vertical tail contribution had been established, the lateral-directional characteristics of the aircraft could be established, Section 4.2. It was determined that a vertical tail of 65 ft^2 would maintain positive stability throughout the angle of attack range studied. Figure 2-7 illustrates this in terms of $C_{n\beta}$ in stability axes. $C_{n\beta_{DYNAMIC}}$, which is a measure of departure susceptibility was also determined, Figure 2-8. In order to determine the minimum desired level, it was noted that the F-15 maintained a minimum $C_{n\beta_{DYNAMIC}}$ = 0.004 per degree. Since the F-15 is known to have good post-stall characteristics, it was felt that the Model 279-3 would have comparable post-stall characteristics if the minimum yawing accelerations due to sideslip of the two aircraft were comparable. The mass characteristics of the two aircraft are such that $C_{n\beta_{DYNAMIC}}$ = 0.0031 is the equivalent level for the Model 279-3. It can be seen from Figure 2-7 that this minimum level is exceeded by the Model 279-3 at high angle of attack.

2.2.6 <u>AILERON SIZING</u> - The ailerons were sized to meet the MIL-F-8785, Level 1 requirement that the aircraft be able to roll from 0° to 90° within 1 second. This requirement was checked at two flight conditions; 0.9 Mach at 30,000 feet altitude and 0.6 Mach at 10,000 ft. altitude. A modified three-dimensional analysis was used with roll-damping characteristics determined by the Vortex Lattice method. Aileron actuators similar to those used in the AV-8B were assumed. These actuators are rate limited to ± 80 degrees/second. With the aircraft mass characteristics of Section 3.4 and the estimated aileron power given in Section 4.2, the time to roll was calculated. It was determined that a 90 degree roll required 0.79 second at 0.9 Mach, 30,000 ft and 0.5 second at 0.6 Mach, 10,000 ft. No allowances were made for wing-aileron flexibility.
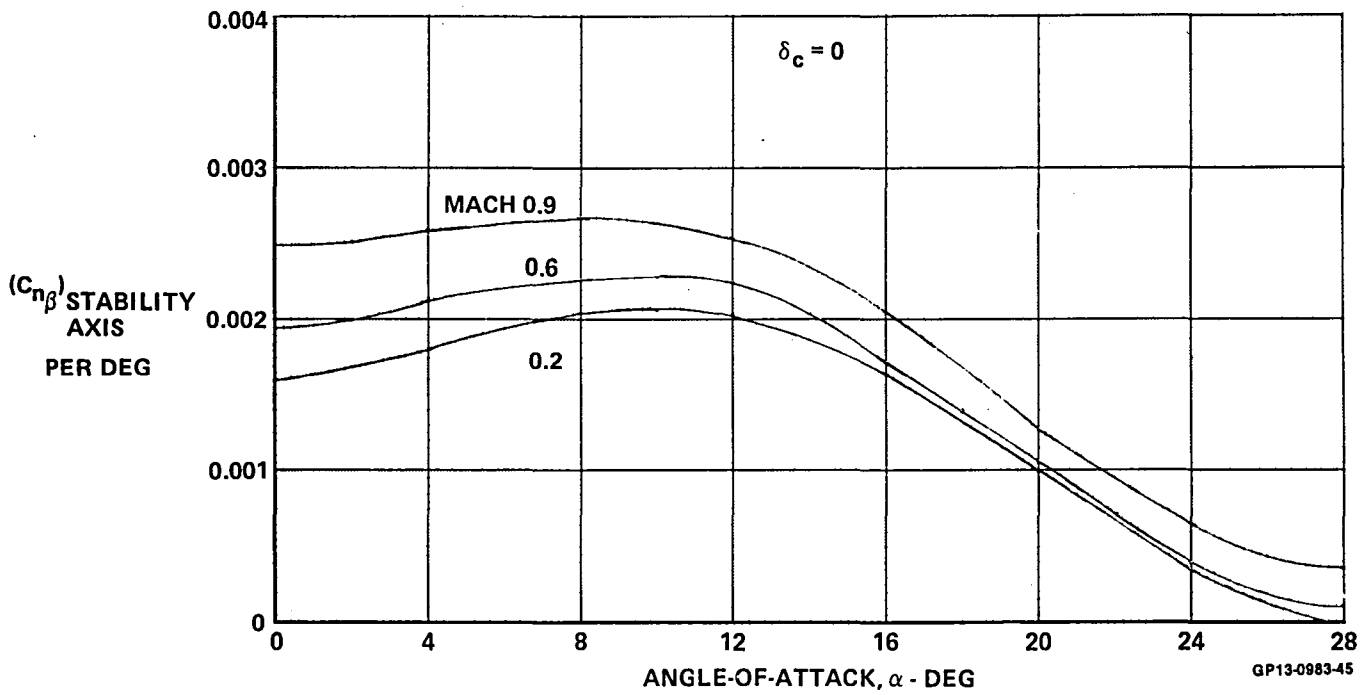
FIGURE 2-7
DIRECTIONAL STABILITY IN STABILITY AXES
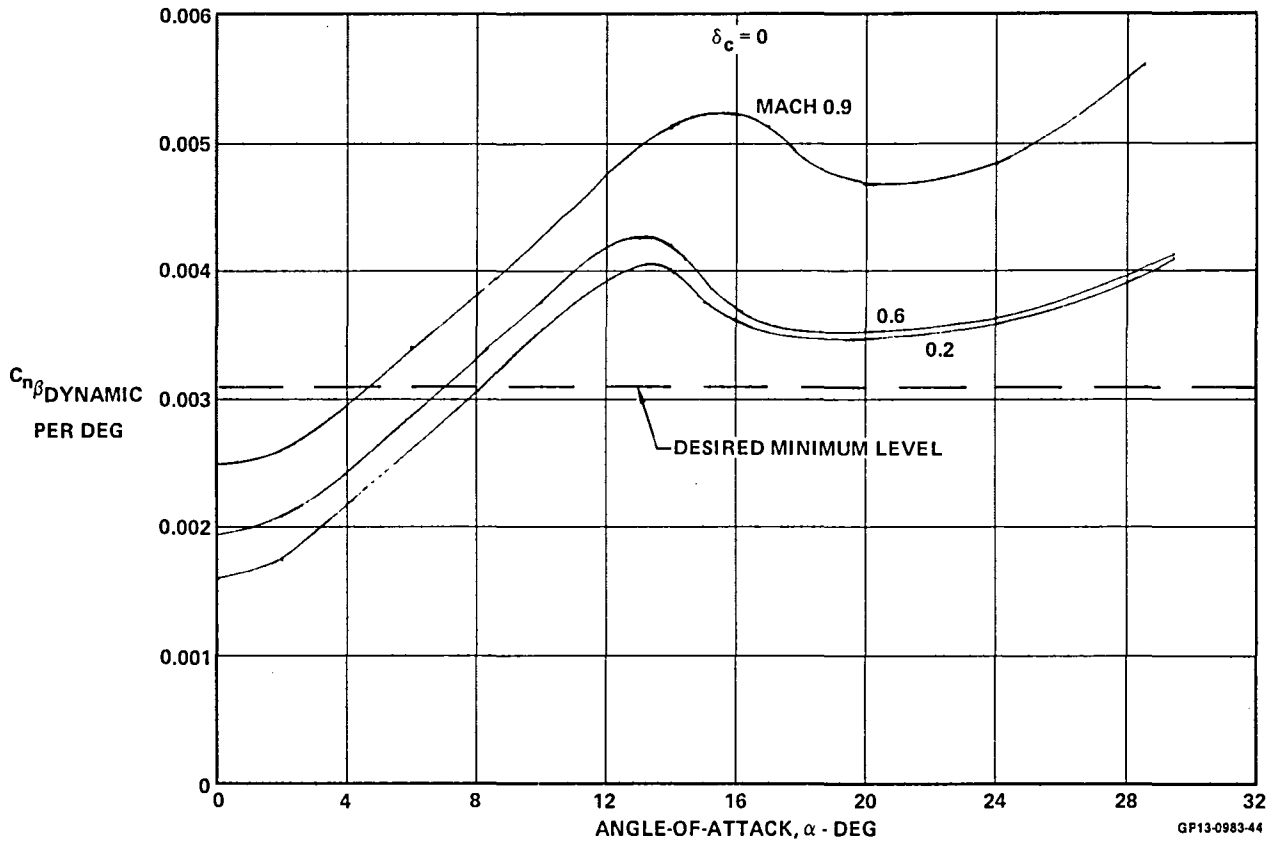
FIGURE 2-8
SUBSONIC SIDESLIP STABILITY

2.2.7 <u>STATIC MARGIN</u> – Due to the upwash of the wing and positive trimmed angles of attack, the minimum drag position of the canard is at some nose-down deflection. If the deflection of the canard can be held near this position, then its trimming load and associated induced drag is small and the trim drag increment is small. This occurs when the aircraft is balanced to have an unstable static margin. With a stable static margin, positive canard deflections are required for trim and the induced drag of the canard becomes large.

When a canard-wing aircraft is compared to a conventional wing-horizontal tail configuration, the canard configuration is found to have similar drag at low angles of attack. However, at maneuvering angles of attack the favorable interference between the canard and the wing keeps the separation drag low. Therefore, above some given lift coefficient the drag of the canard-wing configuration is less than that of the wing-horizontal tail configuration. Balancing the canard-wing aircraft with an unstable static margin reduces the lift coefficient at which the canard-wing combination has the lower drag and, in general, the aircraft with the greater unstable static margin has less drag at maneuvering lift coefficients. However, when an aircraft has an unstable static margin, the available control power for nose-down recovery is reduced. In addition, the sacrifice of natural stability requires the control surfaces to be used as an active stability system. The Model 279-3 design static margin was $-8.0\%\bar{c}$ at 0.8 Mach number. The discussion in Section 2.2.4 showed that the Model 279-3 has sufficient control power at maximum trimmed lift coefficient to initiate a sufficient nose-down recovery pitch rate.

3. AIRCRAFT DESCRIPTION

The Model 279-3 physical characteristics are summarized, including the structural design and aircraft weight-breakdown. The flight control system and subsystem applicability to the V/STOL fighter/attack mission role are also summarized.

3.1 GENERAL ARRANGEMENT

The single engine, single seat Model 279-3, shown in Figure 3-1, utilizes a four nozzle, vectored thrust, advanced P&WA study engine arranged to place the thrust center approximately on the airplane center of gravity at VTO. The engine air induction system consists of two fixed geometry half-axisymmetric supersonic inlets. Bifurcated ducts channel the inlet airflow into the advanced turbofan P&WA STF561-C2 engine. Fan stream burning is provided for the forward nozzles.

Aerodynamic surfaces include a cambered and twisted 428 ft^2 wing, an 85.6 ft^2 canard, and a 65 ft^2 vertical tail. Aerodynamic controls consist of ailerons, leading and trailing edge wing flaps, all movable canards, and a rudder. In hover, control about all three axes is provided by reaction control jets located at the wing tips, tail cone and nose of the airplane.

The airplane internal and structural arrangements, shown in Figures 3-2 and 3-3, have been developed in preliminary form. These ensure structural realism as well as accurate configuration weight and balance assessments.

QP13-0983-216
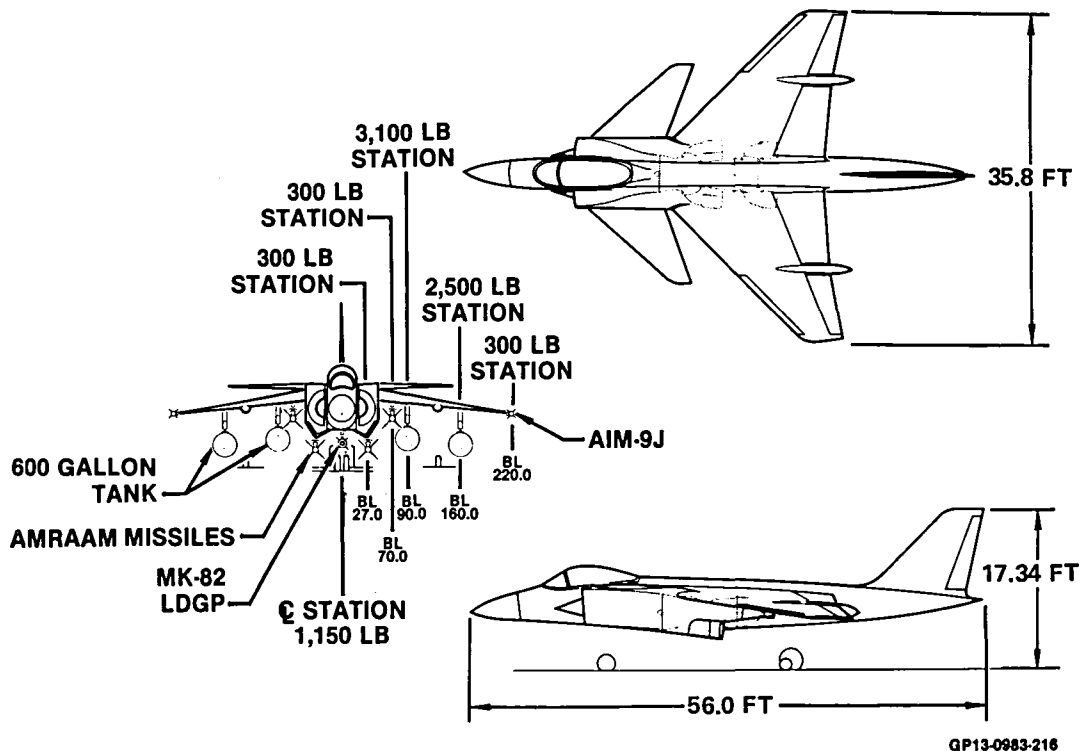
FIGURE 2-1
MODEL 279-3 THREE VIEW

3-1
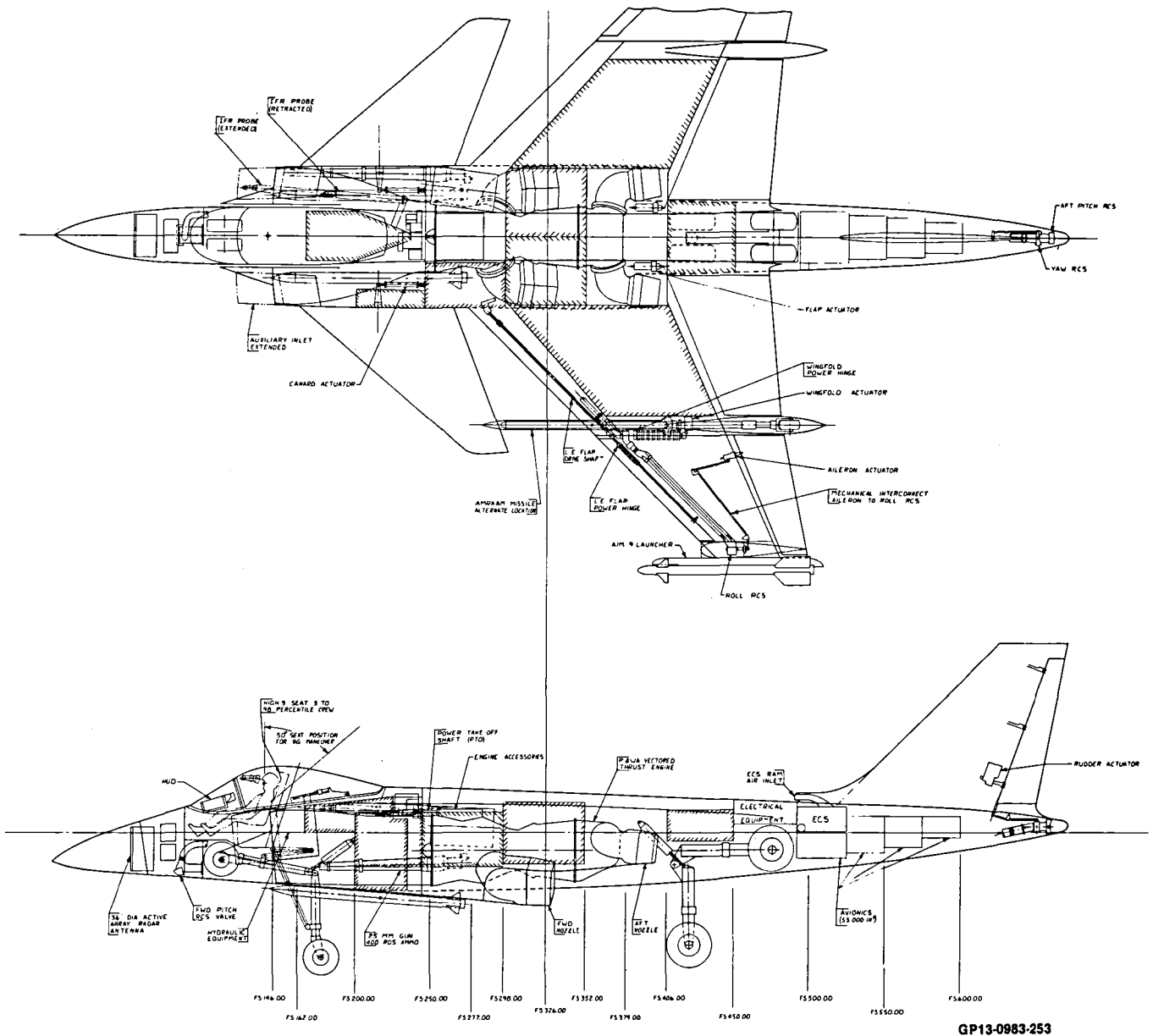
FIGURE 3-2
INTERNAL ARRANGEMENT

A dual tandem bicycle type main landing gear, similar to the AV-8 landing gear, is used. A tire pressure of 120 PSI and CBR of 5 to 6 is used to provide good soft field capability. Outriggers, also used by the AV-8 airplane, are located on the wing. The outrigger track will allow use of the airplane from existing single lane roadways.

CANARD SPINDLE

- BL 790
- BL 90.0 STORES STATION
- BL 124.0
- BL 160.0 STORES STATION
- WING FOLD

---·— Denotes secondary structure
——— Denotes primary structure
✕ Denotes non-structural doors
✕ Denotes structural doors/access panels

FS 000
FS 100.0
FS 200.0
FS 242.0
FS 300.0
FS 355.0
FS 403.0
FS 450.0
FS 500.0
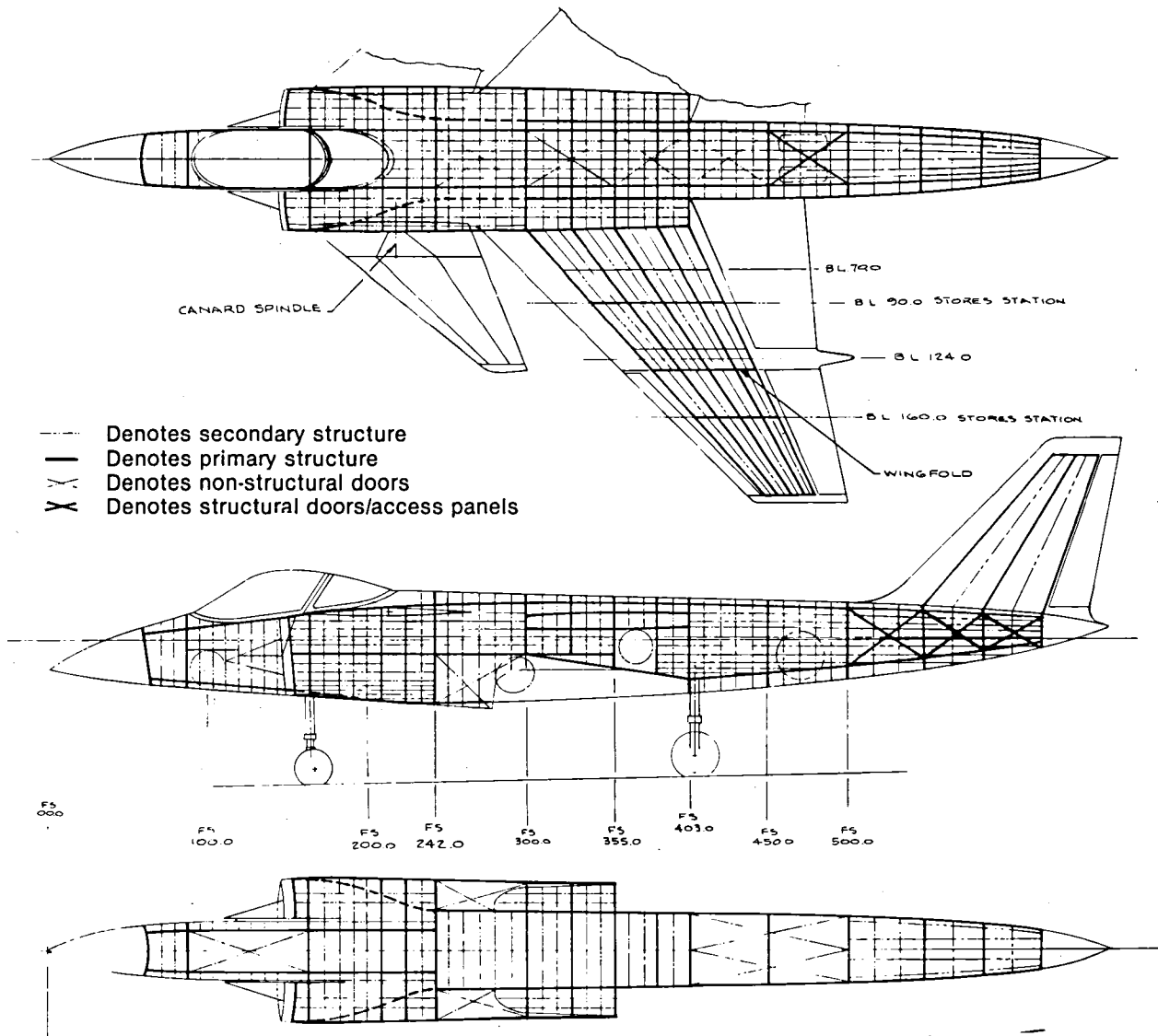
GP13-0983-252

**FIGURE 3-3
STRUCTURAL ARRANGEMENT**

Carrier suitability has been a prime consideration in the development of this airplane. Wing fold, 15 ft/sec sink speeds, maintenance concepts, etc. have been tailored around shipboard V/STOL use from flat decks and ski jumps. The V/STOL concept precludes the need for high sink rate requirements, catapult or arrestment provisions, and some wing high lift devices.

Fighter/attack armament carrying capability includes tip mounted Sidewinders, advanced AMRAAM missiles, conventional and smart weapons, and includes the capability of carrying four 300 or 600 gallon external fuel tanks. The armament stations are summarized in Figure 3-1.

Table 3-1 presents a summary of the geometry, propulsion, and weight characteristics for the Model 279-3. Figure 3-4 presents the cross sectional area distribution.

TABLE 3-1
MODEL 279-3
GEOMETRIC, WEIGHT AND PROPULSION CHARACTERISTICS

DIMENSIONAL DATA				
PARAMETER	UNITS	WING (THEORETICAL)	CANARD (EXPOSED)	VERTICAL TAIL (EXPOSED)
REFERENCE AREA(S)	FT^2	428.4	85.6	65.0
ASPECT RATIO (AR)	—	3.0	3.0	1.2
TAPER RATIO (λ)	—	0.25	0.25	0.35
SPAN (b)	FT	35.84	16.02	8.83
SEMISPAN (b/2)	IN.	215.04	96.14	105.98
ROOT CHORD (C$_R$)	IN.	229.44	102.59	130.84
TIP CHORD (C$_T$)	IN.	57.36	25.64	45.80
MEAN AERO, CHORD ($\bar{c}$)	IN.	160.52	71.81	95.14
LE SWEEP (Λ_{LE})	DEG	45	50	45
INCIDENCE	DEG	0 @ FUSE	0	0
DIHEDRAL	DEG	−9	0	—
TWIST	DEG	−4 @ TIP	0	—
AIRFOIL SECTION ROOT	—	64AX06.2MOD	64A005	64A005
TIP	—	64AX04MOD	64A003	64A003
VOLUME ($\bar{c}_{w/4}$ TO $\bar{c}/4$)	—	—	0.1600	0.0826

PROPULSION
ENGINE: P&WA STF-561-C2
F$_N$ TOTAL: 34,316 LB$_{INST}$ (F$_N$ VTO @ 90°F, T/W = 1.15)
THRUST SPLIT: FWD 61%, AFT 39%
INLET: FIXED HALF CONICAL SPIKE, 16.5° CONE
A$_C$ = 12.2 FT^2
BPR = 1.16, FPR = 3.50, OPR = 25.0

	WEIGHTS (LB)
STRUCTURE	9,592
PROPULSION	4,415
FIXED EQUIPMENT	4,820
WEIGHT EMPTY	18,827
OPERATING WEIGHT EMPTY	19,808
PAYLOAD*	1,466
VTO USABLE FUEL	8,566
STO USABLE FUEL	9,950
FUSELAGE	7,132
WING	2,818
VTO GROSS WEIGHT*	29,840
STO GROSS WEIGHT*	31,224

*Includes (2) AMRAAM and (2) AIM-9 missiles and 25 mm gun with 400 rounds of ammo

GP13-0983-214

3-4

WETTED AREAS (FT^2)	
FUSELAGE, INLETS, BLD	799.7
CANARD	171.2
EXPOSED WING	664.0
VERTICAL TAIL	130.0
TOTAL	1,764.9

SUMMARY		
PARAMETERS	UNITS	VOLUME
VTOGW/MAX STOGW (1,000 FT GROUND ROLL)	LB	29,840/52,150
W/S AT VTOGW	LB/FT^2	69.8
T/W AT VTOGW, SLSU	—	1.27
FUEL FRACTION, VTOGW (MAX FUEL)	—	0.29 (0.32)
STRUCTURAL FRACTION	—	0.32
COMPOSITE MATERIAL FRACTION	—	0.13
LIMIT LOAD FACTOR	g	− 3, 7.5, (9.0 WITH THRUST VECTORING)
DESIGN RATE OF SINK	FT/SEC	15
AIRCRAFT DIMENSION		
LENGTH	FT	56.0
SPAN, BASIC/FOLDED	FT	35.8/21.8
HEIGHT	FT	17.34
NUMBER WEAPON STATIONS	—	11
TOTAL WETTED AREA	FT^2	1,764.9
MAXIMUM CROSS SECTION AREA W/O Ac	FT^2	31.33

GP13-0983-215

3.2 STRUCTURAL DESIGN

Figure 3-3 shows a side and plan view of the basic structural arrangement. The major structural characteristics are as follows: composite multispar wing and vertical tail structure utilizing intergral hat-stiffened composite skins; composite control surfaces with metal attachment fittings; composite fuselage moldline skins with integral stringers and hat stiffeners, and metal frames where concentrated loads are introducted to the fuselage; and integral fuel tanks in both wing and fuselage structure.

The baseline airplane design limit load factors are -3.0 to +7.5 for symmetrical maneuvers and 0 to +6.0 for asymmetrical maneuvers at all speeds and weights not exceeding the basic flight design weight. The structure is designed to withstand limit load without permanent deformation and ultimate load (1.5 times limit load) without failure. Full advantage of postbuckling

strength for composite panels has been used in the design. The structure is designed to last through a 6000 flight hour service life. In order to provide a high probability of that length of survival, fatigue strength allowables based on a 12,000 hour life are used in the analysis. The factor of 2 between these lives is commonly called a scatter factor and is applied to both the maneuvering spectrum and number of landings included in the 6000 hour life. Fatigue allowable stresses are also corrected to account for the reductions inherent to operation at and lengthy exposure to elevated temperature. The scatter factor mentioned above is used to account for the "scatter" found in fatigue test data and will provide a probability of success in excess of 90%.
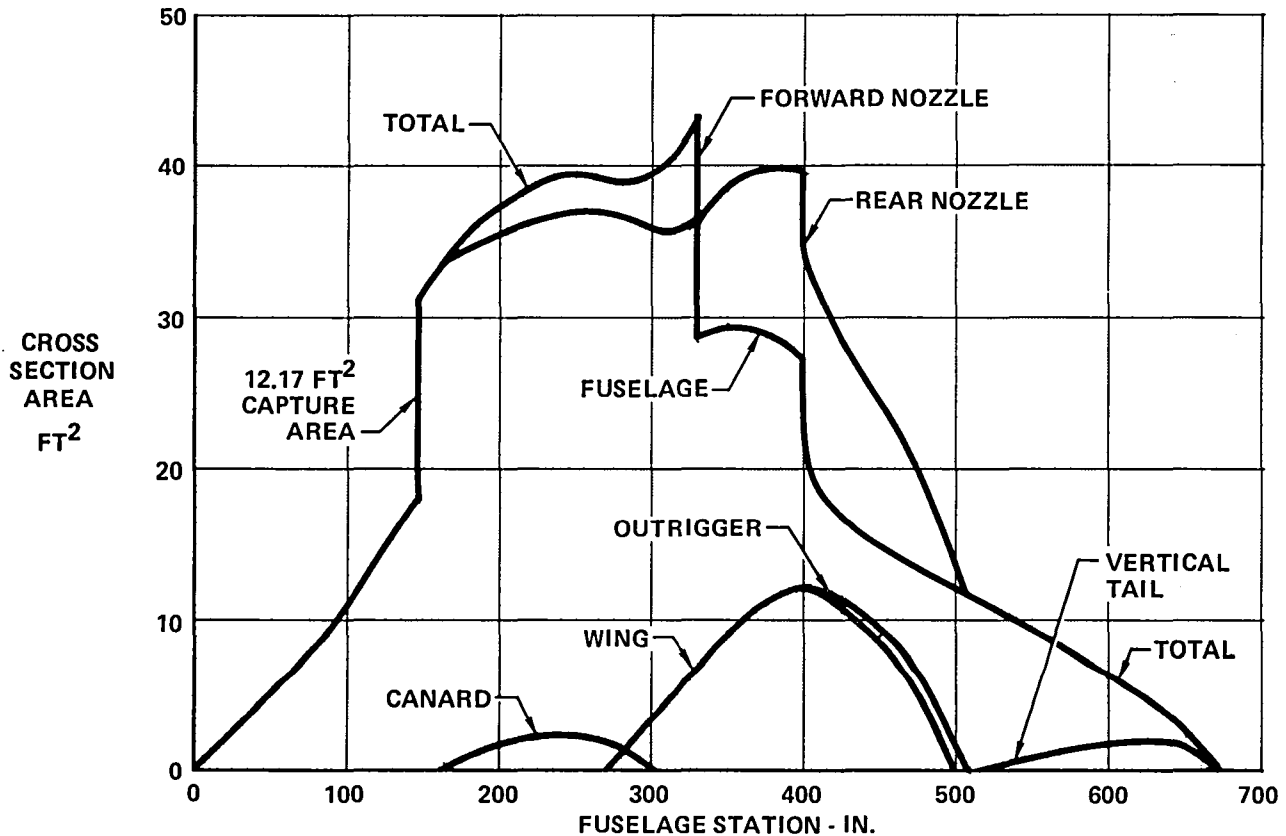
GP13-0983-213

FIGURE 3-4
CROSS-SECTIONAL AREA DISTRIBUTION

Maximum aircraft temperatures resulting from aerodynamic heating effects are presented in Figure 3-5. As indicated, aircraft skin temperatures are less than 250°F throughout the flight envelope. Stagnation regions and internal walls of the air induction system exceed 250°F for a portion of the flight envelope, reaching a maximum temperature of about 280°F at the Mach 2 and 30,000 ft altitude flight condition. Localized areas of the fuselage exposed to exhaust heating effects will experience significantly higher temperatures. These areas will require special consideration, such as thermal shielding, to limit structural temperatures to acceptable levels.

The fuselage sidewalls and lower surfaces are subjected to high engine noise levels. The highest overall sound pressure levels occur during periods of maximum thrust in the VTOL mode and during supersonic dash. The high sound pressure levels on the lower surface are primarily due to VTOL noise levels
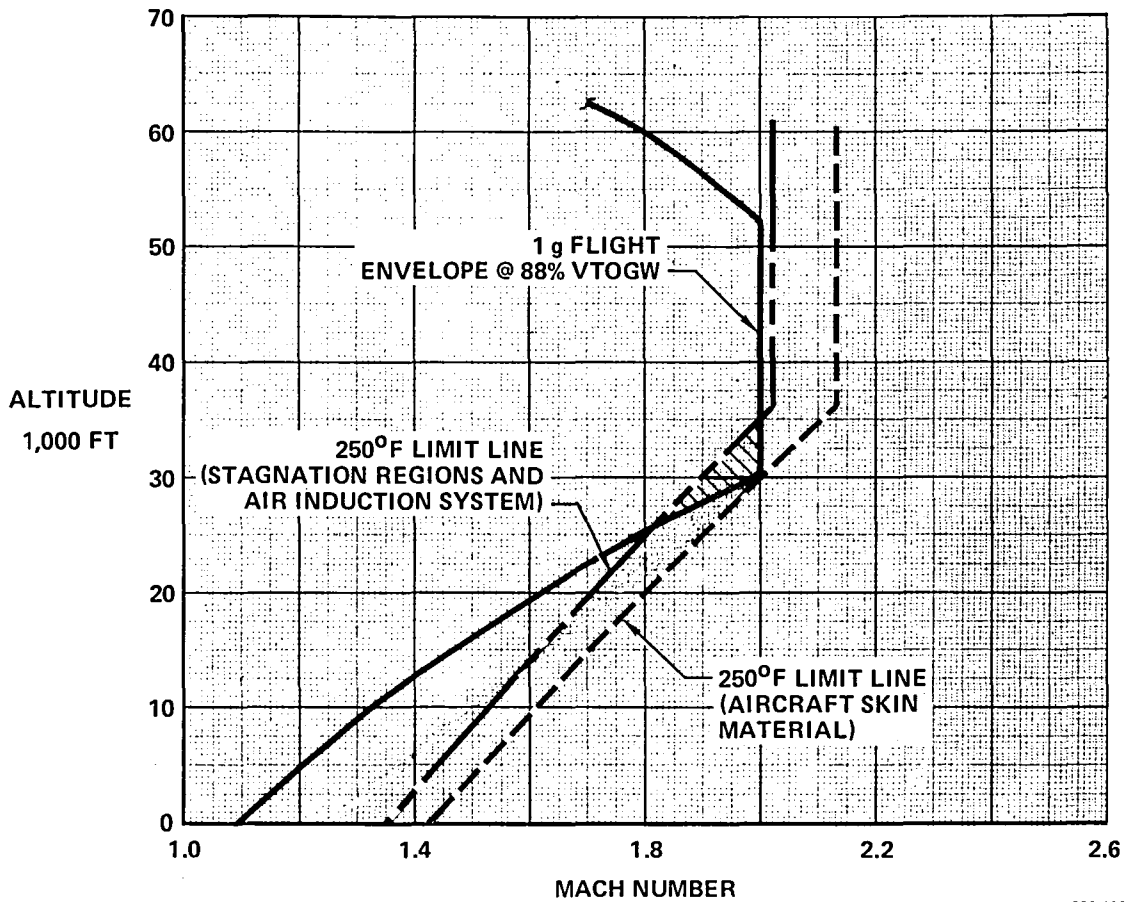
FIGURE 3-5
DESIGN TEMPERATURES

coupled with ground reflection. Maximum fuselage sidewall sound pressure levels occur during flight as a result of exhaust flow from the forward FSB nozzles.

3.3 MATERIALS

Extensive use of composite structure is used in the wing, control surfaces and fuselage moldline skins. Except for localized areas, which are heated by exhaust from the engines, external skin temperatures are below the allowable for graphite epoxy and graphite bismaleimide systems. Composite materials which can be used include: AS/3501-6 and T300/5208 graphite epoxy for temperatures up to 250°F and 350°F, respectively; graphite bismaleimide for regions with temperatures up to 450°F. Currently, considerable effort is being expended on the development of new, high temperature matrices for graphite composite materials. By the 1995 time period it can be anticipated that operating composite structure at elevated temperatures will result in little or no weight penalty.

Maximum use of advanced metals is made for all metal structure. Aluminum- lithium is considered a prime weight saving alloy as its strength is comparable to that of 7075-T73, its stiffness is greater, and its density is less. Superplastic formed and diffusion bonded titanium is used in areas requiring high strength metals at elevated temperatures.

In the proximity of the rear nozzles, super alloy metals such as Rene' 41 can be used for heat shield materials. Carbon-carbon, a newly emerging material, offers the potential for lightweight shielding at elevated operating temperatures. This material would be used in the small areas affected by the forward FSB nozzles.

3.4 MASS PROPERTIES

The prediction technique used to estimate the Model 279-3 weight resulted from an extensive effort to develop a method providing a high degree of accuracy and versatility. In developing the prediction technique, three approaches were considered for estimating weights and establishing weight relationships:

o Statistical Analyses - Theoretical relationships were developed, describing the weight effects of the important design criteria and configuration characteristics.

o Detailed Analyses - Weights are calculated from detailed drawings with the aid of strength and environmental analyses.

o Empirical Analyses - Weights are related to specific parameters without determining theoretical relationships.

Inspection of each of the three approaches indicated that no one method was suitable for estimating all weights due to the following constraints:

o Statistical analyses, although highly accurate when applied with sufficient technical data, do not allow weight appraisals of unique or special features.

o Detailed analyses provide the ability to analyze any type of structural component or system, but require extreme detail in design and strength analyses. This approach was deemed impractical for initial development and optimization studies due to the time required for appraisals, plus the uncertainty of non-optimum factors.

o Empirical analyses are useful on small components, but are much too inaccurate for total aircraft weight estimation.

The best approach to weight prediction was found to be a method which applies each of the above three techniques where it is best suited. Basically, this is the MCAIR method; a statistical approach with appropriate analytical techniques to account for special features, and analytically derived correction factors to allow for application of new materials and construction techniques.

The total structural groups were combined and analyzed for accuracy by the probability-tolerance-interval method for a 95 percent confidence level as shown in Figure 3-6. The methods described above were applied in estimating the weights of 13 MCAIR and 17 additional aircraft to determine the accuracy. The resulting tolerance interval is -7.33 to +5.11 percent.
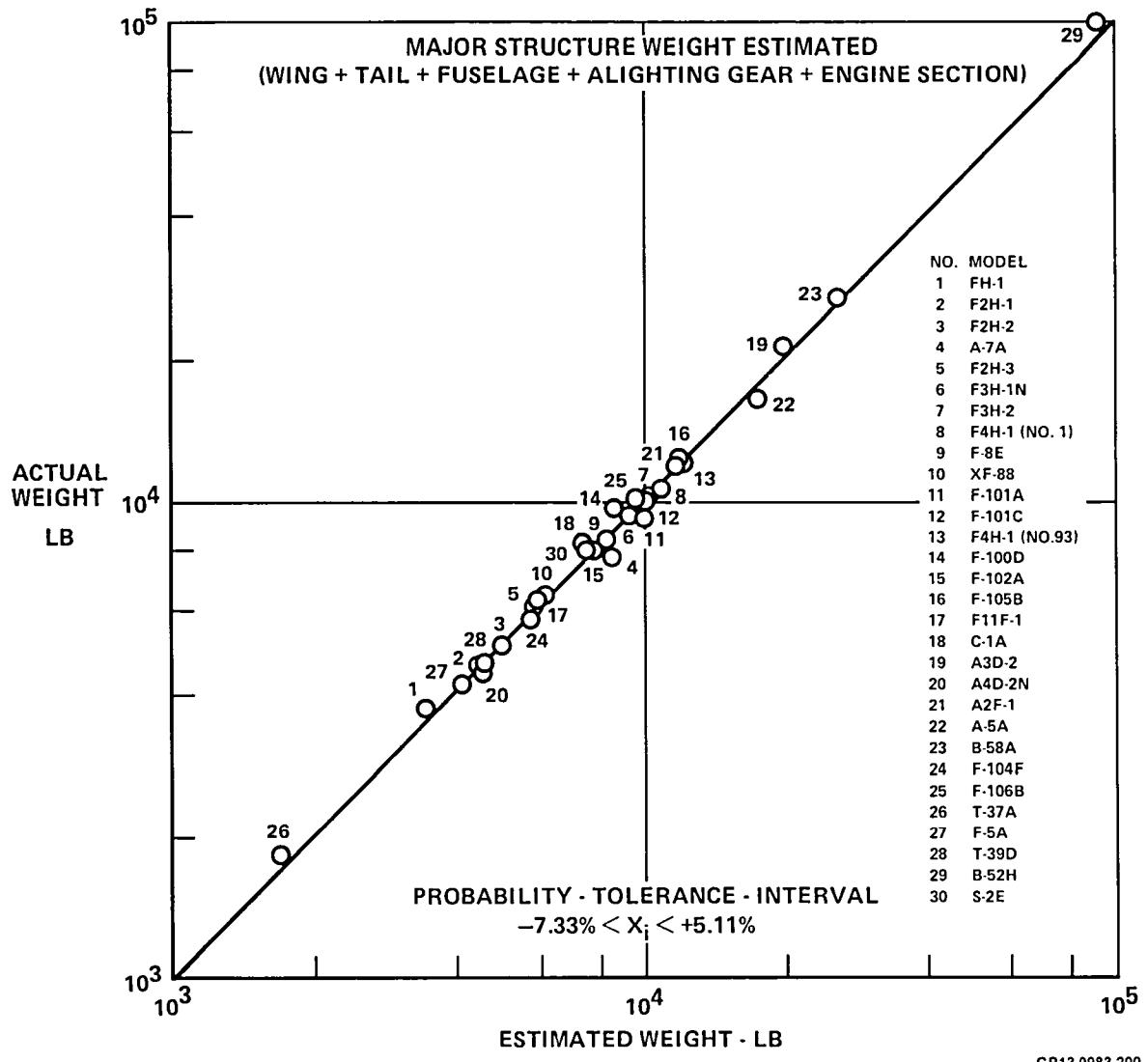
FIGURE 3-6
MCAIR STRUCTURAL WEIGHT ESTIMATION METHOD
Probability-Tolerance-Interval

The group weight statement for Model 279-3 is incorporated in MIL-STD-1374 Part I, shown as Table 3-2. Page 1 of MIL-STD-1374 is a breakdown of the airframe structural components; page 2 lists the propulsion group and the systems and equipment group. The totals from pages 1 and 2 are the weight empty of the airplane. Page 3 is an itemized list of the mission useful load components for the DLI and interdiction missions. The moment of inertia characteristics for the DLI loadings are summarized in Table 3-3.

TABLE 3-2
GROUP WEIGHT STATEMENT
WEIGHT EMPTY

MIL-STD-1374 PART I - TAB
NAME
DATE

1	WING GROUP						3016
2	BASIC STRUCTURE-CENTER SECTION						
3	-INTERMEDIATE PANEL						
4	-OUTER PANEL						
5	-GLOVE						
6	SECONDARY STRUCTURE-INCL.WING FOLD WEIGHT						
7	AILERONS - INCL. BALANCE WEIGHT						
8	FLAPS - TRAILING EDGE						
9	- LEADING EDGE						
10	SLATS						
11	SPOILERS						
12							
13							
14	ROTOR GROUP						
15	BLADE ASSEMBLY						
16	HUB & HINGE - INCL. BLADE FOLD WEIGHT						
17							
18	CANARD GROUP						696
19	TAIL GROUP						208
20	STRUCT. - STABILIZER						
21	- FIN-INCL.DORSAL						
22	VENTRAL						
23	ELEVATOR - INCL.BALANCE WEIGHT						
24	RUDDERS - INCL.BALANCE WEIGHT						
25	TAIL ROTOR - BLADES						
26	- HUB & HINGE						
27							
28	BODY GROUP						3282
29	BASIC STRUCTURE - FUSELAGE OR HULL						
30	- BOOMS						
31	SECONDARY STRUCTURE - FUSELAGE OR HULL						
32	- BOOMS						
33	- SPEEDBRAKERS						
34	- DOORS, RAMPS, PANELS & MISC.						
35							
36							
37	ALIGHTING GEAR GROUP - TYPE **						1571
38	LOCATION	RUNNING	*STRUCT.	CONTROLS			
39	MAIN						
40	NOSE/TAIL						
41	ARRESTING GEAR						
42	CATAPULTING GEAR						
43							
44							
45	ENGINE SECTION OR NACELLE GROUP						92
46	BODY - INTERNAL						
47	- EXTERNAL						
48	WING - INBOARD						
49	- OUTBOARD						
50							
51	AIR INDUCTION GROUP						727
52	- DUCTS						
53	- RAMPS, PLUGS, SPIKES						
54	- DOORS, PANELS & MISC.						
55							
56							
57	TOTAL STRUCTURE						9592

* CHANGE TO FLOATS AND STRUTS FOR WATER TYPE GEAR.
**LANDING GEAR "TYPE": INSERT "TRICYCLE", "TAIL WHEEL", "BICYCLE", "QUADRICYCLE", OR SIMILAR
DESCRIPTIVE NOMENCLATURE.

GP13-0983-220

TABLE 3-2 (Continued)
GROUP WEIGHT STATEMENT
WEIGHT EMPTY

MIL-STD-1374 PART I - TAB
NAME
DATE

			X	AUXILIARY	XX	MAIN	X 4415
58	PROPULSION GROUP						
59	ENGINE INSTALLATION						
60							
61							
62	ACCESSORY GEAR BOXES & DRIVE						
63	EXHAUST SYSTEM						
64	ENGINE COOLING						
65	WATER INJECTION						
66	ENGINE CONTROL						
67	STARTING SYSTEM						
68	PROPELLER INSTALLATION						
69°	SMOKE ABATEMENT						
70	LUBRICATING SYSTEM						
71	FUEL SYSTEM						
72	TANKS - PROTECTED						
73	- UNPROTECTED						
74	PLUMBING, ETC.						
75							
76	DRIVE SYSTEM						
77	GEAR BOXES, LUB SY & ROTOR BRK						
78	TRANSMISSION DRIVE						
79	ROTOR SHAFTS						
80							
81	FLIGHT CONTROLS GROUP						1085
82	COCKPIT CTLS.					148	
83	SYSTEMS CONTROLS - REACTION					337	
84	CONVENT.					600	
85							
86	AUXILIARY POWER PLANT GROUP						206
87	INSTRUMENTS GROUP						155
88	HYDRAULIC & PNEUMATIC GROUP						250
89							
90	ELECTRICAL GROUP						435
91							
92	AVIONICS GROUP						1069
93	EQUIPMENT						
94	INSTALLATION						
95							
96	ARMAMENT GROUP						629
97	FURNISHINGS & EQUIPMENT GROUP						407
98	ACCOMMODATION FOR PERSONNEL						
99	MISCELLANEOUS EQUIPMENT						
100	FURNISHINGS						
101	EMERGENCY EQUIPMENT						
102							
103	AIR CONDITIONING GROUP						300
104	ANTI-ICING GROUP						
105							
106	PHOTOGRAPHIC GROUP						
107	LOAD & HANDLING GROUP						7
108	AIRCRAFT HANDLING						
109	LOADING HANDLING						
110	BALLAST						
111	CONTINGENCY						277
112	TOTAL CONTRACTOR CONTROLLED						
113	TOTAL GFAE						
114	TOTAL WEIGHT EMPTY - PG 2-3						18827

GP13-0983-221

TABLE 3-2 (Concluded)
GROUP WEIGHT STATEMENT
USEFUL LOAD AND GROSS WEIGHT

MIL-STD-1374 PART I – TAB
NAME
DATE

	LOAD CONDITION	GALS.	DLI MISSION	INTER-DICTION
115	LOAD CONDITION		DLI	INTER-
116			MISSION	DICTION
117	CREW (NO. 1)		180	180
118	PASSENGERS (NO. 0)			
119	FUEL LOCATION TYPE	GALS.		
120	UNUSABLE JP-5	16.3	111	111
121	INTERNAL JP-5	1259.7	8566	9950
122				
123				
124				
125	EXTERNAL (TOTAL) JP-5			7940
126				
127				
128	OIL			
129	TRAPPED			
130	ENGINE		59	59
131				
132	FUEL TANKS			640
133	WATER INJECTION FLUID			
134				
135	BAGGAGE			
136	CARGO			
137				
138	GUN INSTALLATIONS		300	300
139	GUNS LOCAT.FIX.OR FLEX.QUANTITY CALIBER			
140	FUS. 1	25 mm		
141				
142	AMMO.		440	440
143				
144				
145	SUPP'TS *			
146	WEAPONS INSTALL. **			
147	MRM's (2)		600	
148	SRM's (2)		400	400
149				
150	MK-82 SNAKEYES (14)			7700
151	EJECTORS (2)		102	
152	LAUNCHERS (2)		200	200
153	VER (2)			175
154	MER (2)			440
155	PYLONS			
156	INTERMEDIATE			580
157	OUTBOARD			580
158	CENTERLINE			150
159				
160				
161				
162	SURVIVAL KITS		29	29
163	LIFE RAFTS			
164	OXYGEN			
165	MISC.			
166	CHAFF		26	26
167				
168				
169	TOTAL USEFUL LOAD		11013	29900
170	WEIGHT EMPTY		18827	18827
171	GROSS WEIGHT		29840	48727

* IF REMOVABLE AND SPECIFIED AS USEFUL LOAD.
**LIST STORES, MISSILES, SONOBUOYS, ETC. FOLLOWED BY RACKS, LAUNCHERS, CHUTES, ETC. THAT ARE NOT
  PART OF WEIGHT EMPTY. LIST IDENTIFICATION, LOCATION, AND QUANTITY FOR ALL ITEMS SHOWN
  INCLUDING INSTALLATION.

GP13-0983-222

TABLE 3-3
MOMENT OF INERTIA SUMMARY

VTOL
DLI MISSION (2) MEDIUM RANGE MISSILES (2) SHORT RANGE MISSILES 400 ROUNDS AMMO

TAKEOFF (GEAR DOWN)	
WEIGHT — LB	29,840
CENTER OF GRAVITY	
FUSELAGE STATION	323.7
WATERLINE	93.4
INERTIA — SLUG FT^2	
ROLL	19,612
PITCH	72,178
YAW	86,325
COMBAT (GEAR UP)	
WEIGHT — LB	26,260
CENTER OF GRAVITY	
FUSELAGE STATION	327.3
WATERLINE	95.0
INERTIA — SLUG FT^2	
ROLL	15,727
PITCH	69,254
YAW	81,784
⚠1 **LANDING (GEAR DOWN)**	
WEIGHT — LB	22,424
CENTER OF GRAVITY	
FUSELAGE STATION	320.6
WATERLINE	90.9
INERTIA — SLUG FT^2	
ROLL	15,371
PITCH	62,878
YAW	73,469

⚠1 Landing condition
DLI Mission (all stores retained approx 1,150
pounds of fuel)

GP13-0983-230

    The equipment in the Model 279-3 has been positioned in the aircraft to attain the optimum location of the center of gravity. External store stations have been located on the wing and fuselage such that expenditure of stores, in conjunction with fuel consumption, maintains the desired negative stability margin between the airplane neutral point and the center of gravity. Figure 3-7 is a center of gravity trace for the DLI mission showing a typical c.g. excursion during flight. The c.g. plot shows the effect of internal fuel consumption as well as the effect of firing missiles and ammunition at combat gross weight. The c.g. excursion is shown in terms of percent Mean Aerodynamic Chord (MAC), where the chord is 160.52 inches. The leading edge of the MAC is at Fuselage Station 313.16. The effect of landing gear retraction and extension is shown at both Takeoff Gross Weight and zero fuel condition.
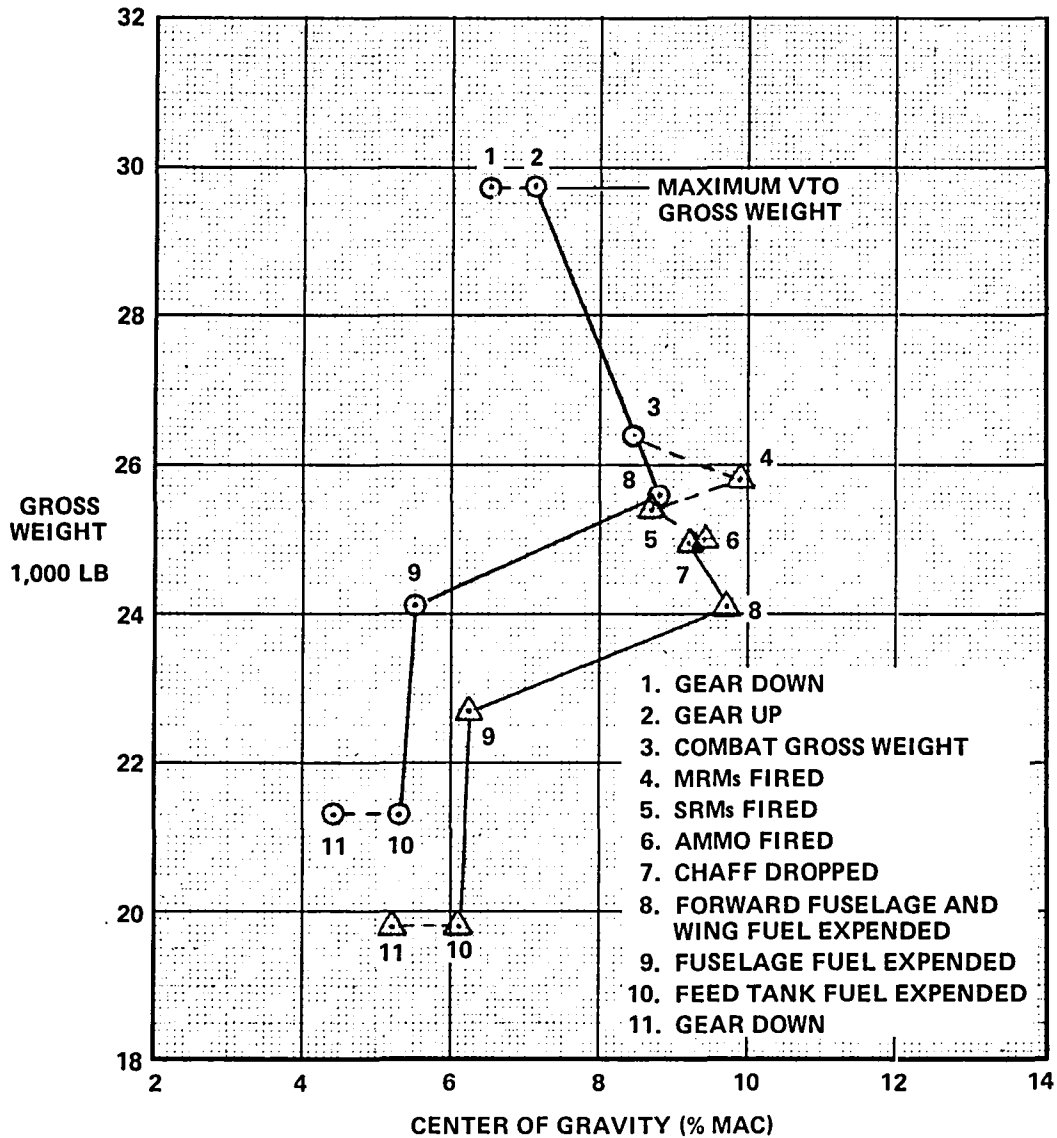
FIGURE 3-7
CENTER OF GRAVITY TRACE
DLI Mission   (2) MRMs, (2) SRMs, Ammo, Chaff

3.5 FLIGHT CONTROL

Control of the V/STOL and STOVL aircraft in the powered lift portion of the flight envelope is provided by an airspeed and nozzle deflection dependent blend of the aerodynamic control surfaces and the reaction control system. During transition from hover to conventional aerodynamic flight, the reaction jets are phased out as the effectiveness of the aerodynamic surfaces increases.

3.5.1 AIRCRAFT CONTROL - The aerodynamic control surfaces consist of canards, trailing edge flaps, ailerons, and rudder. These surfaces are powered by hydraulic actuators, and remain operational throughout the flight envelope, even though their effectiveness becomes insignificant in VTOL. To generate control forces at low airspeeds, some engine compressor air is diverted to the reaction control system with thrust jets located in the nose, tail, and wings of the aircraft. The reaction control system is turned on at low airspeeds or when the engine nozzles are deflected.

Height control in VTOL is synonymous with engine thrust control, and it is accomplished by modulation of engine power. Automatic control is added to provide vertical rate damping. This improves height control precision and reduces the effects of external disturbances on the aircraft. The automatic control also compensates for any lift changes resulting from the use of engine bleed air for attitude control.

In addition to the RCS attitude control and engine power modulating height control, the vectored thrust engine with Fan Stream Burning (FSB) provides two additional means of augmenting V/STOL control: (1) core fuel flow vs. FSB fuel flow modulation; and (2) independent vectoring of forward and aft nozzles in transition. The ability to vary core and FSB fuel flow rates in a quasi-independent manner permits limited control of the thrust split between the forward and aft engine nozzles which, in turn, produces aircraft pitching moments. These moments are used to trim the aircraft, which allows greater reserves of reaction control capability for pitch, roll, and yaw attitude control. Integration of this longitudinal control and trim system is shown functionally in Figure 3-8. Additional information on this pitch/trim control concept is included in Section 6.3.
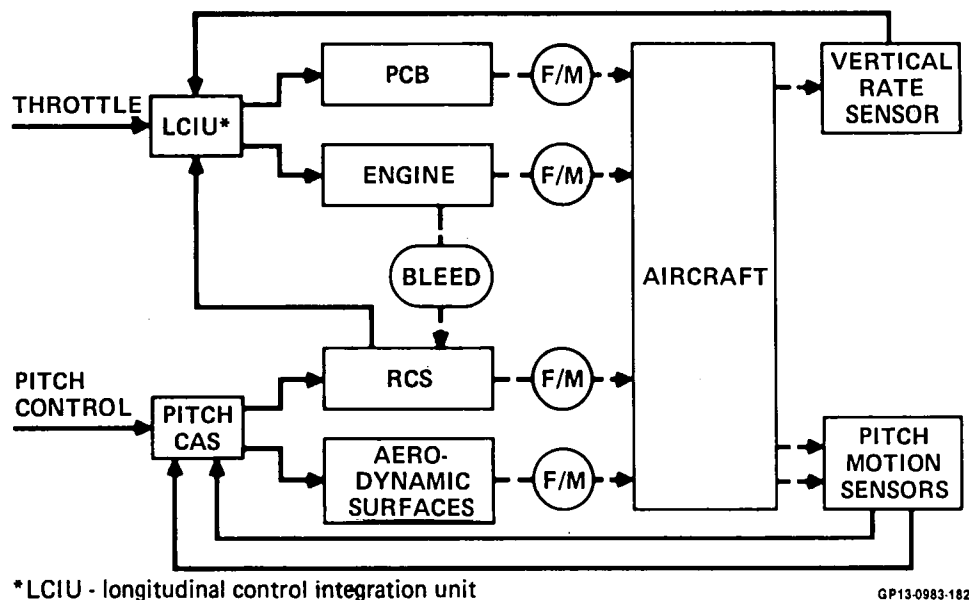
*LCIU - longitudinal control integration unit   GP13-0983-182

FIGURE 3-8
LONGITUDINAL CONTROL FUNCTIONAL DIAGRAM

3.5.2 FLIGHT CONTROL SYSTEM – The flight control system is a digital control-by-wire system using dedicated flight control computers. The digital computers incorporate several primary flight modes, autopilot modes, and automatic landing modes. The computers, pilot input sensors, aircraft motion sensors and Signal Conversion Mechanisms (SCMs) provide a triple redundant system. This system is illustrated in concept in Figure 3-9.

GP13-0983-191
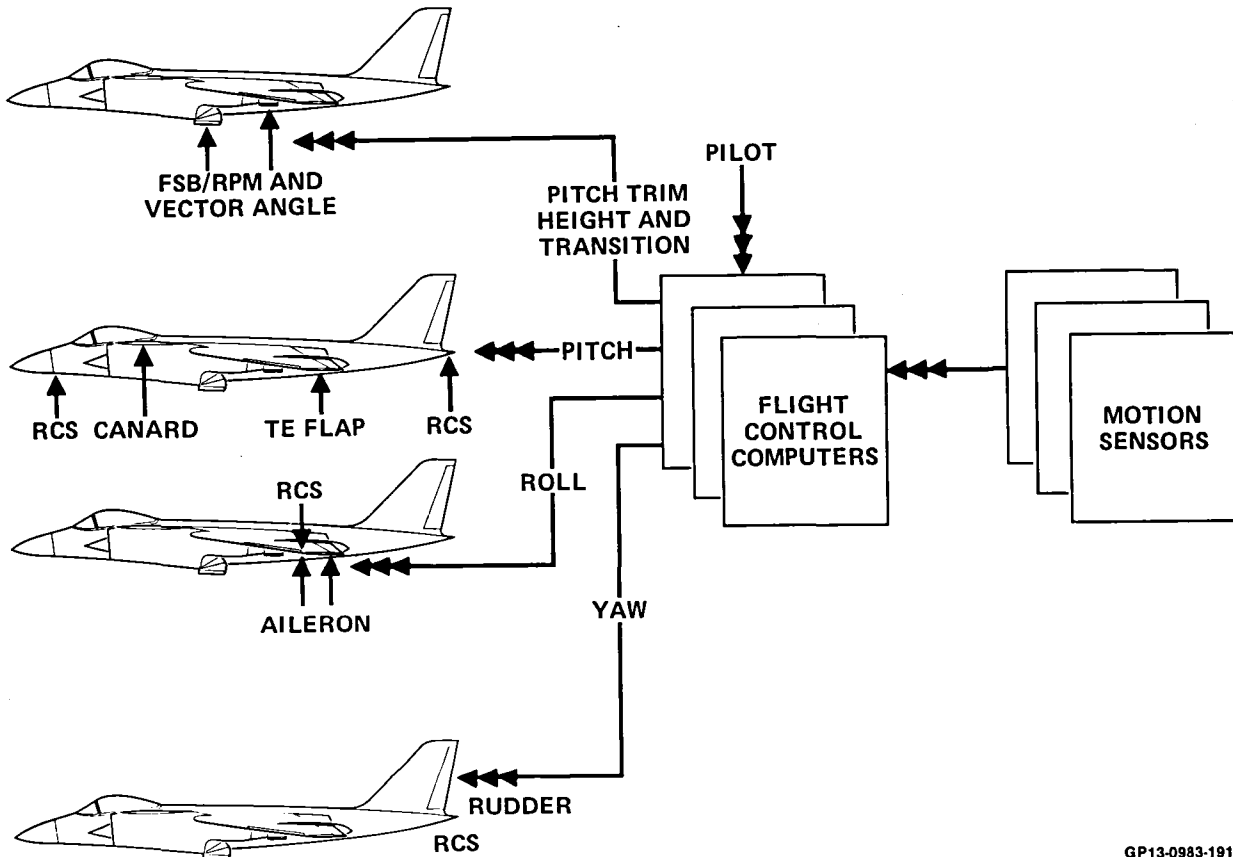
FIGURE 3-9
FLIGHT CONTROL SYSTEM

The sensors are comparison and in-line monitored in the computers using data exchange between computers. Failure of two like sensors will cause digital reversion modes to be used. Thus, the system can survive failure of two like sensors and a safe landing can be made.

Dual tandem hydraulic actuators with triplex SCMs are used on all flight-critical control actuation functions. The triplex SCMs are in-line monitored in the digital computers. Sensors detect position and hydraulic pressure differential at each SCM channel to enable accurate detection of an SCM failure.

The primary crew station controls consist of control stick, rudder pedals, master power lever and a thrust vector or transition lever. The master power lever contains a thrust vector trim switch to permit the pilot limited thrust vector angle corrections without moving his hand from the power lever control. Conventional rudder pedals are provided in the crew station; however, the control stick is a side-arm controller located on the high "g" seat right hand arm rest. No direct mechanical linkage exists between the pilot controls and the primary control system. The rudder, aileron, trailing edge flaps, and canards are operated by dual hydraulic power actuators. The power control actuators are tandem and one cylinder in each tandem actuator is connected to hydraulic system No. 1, and the other to hydraulic system No. 2.

The RCS installation is similar to that on the AV-8B. Engine bleed air is piped via specially designed ducting to isolate and insulate the ducting from the aircraft structure. RCS bleed air is piped to reaction control valves mounted in the nose and tail of the aircraft to provide pitch control during hover and V/STOL. The nose mounted valve is down blowing while the tail mounted valve provides both up and down blowing. The forward and aft reaction control valves are each operated by a separate actuator. Yaw control is provided via an additional set of jet ports blowing right and left with the control valve operated by a rudder linkage. Roll control is attained through wing tip RCS valves which are operated by linkages from the aileron. The wing tip RCS valves control engine bleed air which is routed through the wing leading edge. Due to the thin airfoil of the supersonic wing, the RCS duct in the wing leading edge is divided into multiple smaller diameter ducts through the outer wing, and terminated in a plenum at the RCS valve. Pitch, roll and yaw control systems are provided with artificial feel systems and electrically operated trimming devices. The artificial feel is provided by double acting spring cartridges.

Pilot inputs are converted to electrical signals by Triplex linear variable differential transformers (LVDT), and fed to the flight control computers. There the input signals are shaped as a command signal and fed to the appropriate SCMs. The Triplex SCMs convert the electrical signals to mechanical displacement of the power actuator. Force summing is used among the three independent SCM segments.

The thrust is vectored by lift/cruise nozzles which are controlled from the cockpit by the transition lever. A parallel servo is installed to position the lever in response to commands from the power lever-mounted thumb switch or from the automatic landing system.

3.6 SUBSYSTEMS

Subsystem design has been addressed to the degree that it determines the configuration viability, including weight, volume and location to ensure feasible integration into the weapon system. Figure 3-2 shows the subsystems arrangement.

3.6.1 ENGINE INSTALLATION - Engine installation and removal is accomplished through the lower fuselage moldline via easily reached and quickly attached engine mounts. The aircraft is elevated for engine removal clearances by extending the landing gear to the maximum strut extension. After the rear nozzles are disconnected, the engine is lowered onto a modified 4000A "airlog trailer" and rolled laterally out the left side of the aircraft. The "airframe mounted accessory drive" (AMAD) is located forward of the engine compartment. All fuel, control and hydraulic lines not directly connected to the engine are routed outside of the compartment to facilitate engine access and simplify engine change procedures. This also reduces the fire hazard.

3.6.2 ELECTRICAL SYSTEM - The electrical system consists of a primary ac system powered by a single 30/40 KVA variable speed, constant frequency (VSCF) generator, a secondary dc system composed of a 200 amp dc TR (transformer rectifier for conversion of ac to dc) and a single NiCad battery with a temperature controlled charger. A power distribution (bus) system, a gas turbine starter auxiliary power unit (APU) and an external power receptacle are included. The VSCF generator is located on the AMAD and the APU is located near the engine face. The remainder of the system is located in the aft fuselage equipment bay.

Power distribution wiring for the aircraft is flat bus, with solid state electronic power controllers that serve as circuit breakers and relays. Fibre optics are employed in the electrical power control and in the low level sensor electronic circuitry for electromagnetic interface protection from external radiation, lightning and nuclear impulse.

3.6.3 HYDRAULIC SYSTEM - The hydraulic system is a lightweight, high pressure (8,000 psi) system powered by two hydraulic pumps, driven by the AMAD, to preclude a single pump malfunction from disabling the system. The pump outputs are routed through a MCAIR designed reservoir level sensing (RLS) valve which divides the system flow into two protected branches. Thus, fluid loss from one branch will cause that branch to shut-off while the remaining branch functions normally. RLS also reduces repair maintenance by negating the need for a pump replacement because the pump has been "run dry".

The hydraulic system includes fatigue and corrosion resistant titanium tubing, permanently swaged connectors, and coiled titanium tubes at actuators (in place of flex hoses) to improve reliability. The system uses the less flammable MIL-H-83282 fluid. Design features, such as use of an appendage type make-up reservoir, quick response pumps and system relief valves, and pump ripple-transient supression devices, preclude the use of system accumulators, with the resulting R&M improvement. With the exception of the 8,000 PSI concept (under development and test at NADC), these features are state-of-the-art on operational F-15 and F-18 aircraft.

3.6.4 FUEL SYSTEM - Internal fuel storage provides 9,950 lb of JP-5 fuel, distributed in five fuselage and two wing tanks. The fuel center of gravity closely approximates the aircraft center of gravity to maintain balance while the fuel is being depleted. Five percent (5%) fuel expansion space is provided. The two feed tanks (on the aircraft c.g.) are self sealing bladder tanks with a 3,117 lb capacity, amounting to 31% of the total capacity. This

provides 30 minutes of cruise power at 10,000 ft altitude as required by MIL-F-17847. A low level warning alerts the pilot when all of the tanks but the feed tanks are empty. The two wing tanks and remaining three fuselage tanks are integral with the aircraft structure. This is anticipated to be largely of a graphite epoxy type of construction currently being developed under contract for the U.S. Navy.

Fuel transfer and feed is by electrically operated pumps. The fuel transfer sequence provides for first transfer from the wing tanks into the feed tank, on demand, by sensing low levels of feed fuel. Transfer of the fuselage tanks to the feed tanks follows a sequence designed to minimize C.G. shift. Fuel jettison is for 98% of all fuel, at a minimum rate of 300 G.P.M., per MIL-F-17874. Dump time will not exceed 5 minutes and the dumps will be located well away from ignition sources and other parts of the airplane. Provisions are made for four wet wing pylon stations, allowing carriage of 300 gal or 600 gal droppable fuel tanks. Transfer from these tanks will be powered by air pressure provided by engine bleed. The external tanks are the survivable type developed for use on the F-18; i.e., crash and 2000°F fire survivable.

An inflight refueling probe, similar to the F-18 installation, is provided on the right side of the aircraft immediately aft of the cockpit. The probe is extended on command from the pilot's control panel and is positioned within the visibility range of the pilot, per specification.

3.6.5 ENVIRONMENTAL CONTROL SYSTEM (ECS) – The major portion of the ECS is installed in the aft fuselage to aid aircraft balance. The ECS will incorporate 1) closed cabin air cycle, 2) liquid cooled avionics and 3) fuel heat sink; technological developments feasible within the aircraft developmental time frame.

3.6.6 LANDING GEAR AND BRAKES – The tandem landing gear arrangement is patterned after the AV-8A/B, using outriggers immediately inboard of the wing-fold to provide lateral stability. The nose and main landing gears have dual tires and provide a California Bearing Ratio (CBR) of 5 to 6. This allows off runway operation. Brakes are on the main gear only and consist of multi-piston type plates attached to each main wheel, similar to the AV-8B. Nose wheel steering is provided by rudder pedal travel when selected via cockpit controls.

3.6.7 INTERNAL GUN INSTALLATION – A 25 mm Gatling type gun is installed in the outboard structure of the right hand nacelle. The firing barrel of the gun requires a small moldline protrusion. Four hundred (400) rounds of ammunition are provided in a drum type recirculating ammunition container. The gun and ammunition have been located to provide minimum impact on aircraft weight and balance.

3.6.8 AVIONICS – The avionics system provides a versatile complement adaptable to changes in tactics and techniques. It includes 1995 state-of-the-art sensor and data processing technology to ensure detection, classification and location of targets. Displays and controls permit rapid and accurate

assessment of processed sensor data and assist in rapid tactical decisions. Redundancy is included for navigation, sensors, communications and data processing functions to ensure mission success.

The active module, non-gimballed array radar sensor provides medium range multiple target detection and track. Radar operates in look-up and look-down modes, and provides the capability for tail acquisition of enemy aircraft. Multiple launch of medium range AMRAAM missiles is possible, and synthetic aperture radar provides adverse weather acquisition and attack of a broad spectrum of ground targets. An advanced, focal plane array, forward looking infra-red (FLIR) pod adds clear day/night identification and recognition. Data processing equipment supplies track maintenance and weapon assignment data, target intercept information, and correlation of active and passive sensor information.

The control/display group allows multiple sensor selection and display of target and weapon tracks. A projected moving map for simplified ground navigation display is added for attack modes. Communication/Radio Navigation subsystem ensures jam resistant voice/data communication and high accuracy global navigation with secure satelite transmission.

3.6.9 <u>CREW STATION</u> - The single crew station is patterned after the USN F-18, with canopy and ejection clearances for a high "g" type ($\geqslant$9.0g) ejection seat. Pilot displays are multi-purpose (CRT) type in consonance with 1995 technology. Pilot visibility is a key factor in V/STOL aircraft crew station design, and 17° over-the-nose and 62° over-the-side visibility has been provided. This geometry is assessed as satisfactory based upon comparisons with AV-8B visibility.

4. AERODYNAMIC CHARACTERISTICS

The aerodynamic estimates for the Model 279-3 were made using MCAIR analytical and empirical techniques. Comparison of the results of these techniques with wind tunnel data on configurations similar to the Model 279-3 gave correction factors that were applied to the estimates. In areas where analytical or empirical techniques were not applicable, estimates were made for the Model 279-3 using wind tunnel data for similar configurations. Table 4-1 lists the aerodynamic analysis methods that were used and defines the regions of applicability.

The MCAIR Statistical Method is a set of empirical equations for calculating the lift, drag-due-to-lift, zero lift pitching moment, low lift neutral point, the lift coefficient for neutral point break, and the neutral point above this break for wing-body configurations. The coefficients in these equations were obtained by applying regression techniques to a large amount of wing-body wind tunnel data. The MCAIR Statistical Method is included in DATCOM. This method was used primarily to estimate wing-body drag-due-to-lift. The MCAIR Semi-Empirical Method is a set of correlations based on wind tunnel data and involving various configuration parameters. This method was used to estimate wing-body buffet onset lift coefficient as well as drag-due-to-lift.

For the Vortex-Lattice method, used only at subsonic Mach numbers, portions of the planform of a configuration are projected onto a maximum of four flat surfaces. The surfaces may all be in one plane, but are usually at the respective mean heights of the wing and control surfaces. On each surface, the planforms are subdivided into quadrilateral panels. Each of these panels contains a single horseshoe vortex and a control point where the boundary condition for the panel (the local slope of the camber surface) is satisfied. Summing the effect of all of the vortices at each control point gives a set of n equations for n unknowns, where n is the number of panels. This gives a solution to the linear flow equations in the subsonic region. The method is applicable to symmetric or asymmetric configurations, including canard-wing or 3-surface configurations. Control surface deflections or wing leading edge and trailing edge flap effects can be included by properly specifying the boundary conditions on each panel. However, the method does not determine the effect of the camber surface on the pressure drag at zero degrees angle of attack.

The Middleton-Carlson method is similar to the Vortex-Lattice technique in that the configuration also is reduced to a flat surface. However, the method is restricted to a coplanar surface which is subdivided into quadrilateral panels. The supersonic solution to the linearized flow equations is used to obtain aerodynamic data in the supersonic region. Canard and symmetric control deflection effects are included.

The Woodward method uses an approach to the solution of the linearized flow equations that is similar to the Vortex-Lattice method. However, this method arranges the quadrilateral panels making up the planform along the mean camber surface. Constant strength distributed doublets (ring vortices) are arranged on the panels. The boundary condition is the slope of the camber

TABLE 4-1
AERODYNAMIC ANALYSIS METHODS

AERODYNAMIC CHARACTERISTICS	PREDICTION TECHNIQUE (REFERENCE)
A. MINIMUM DRAG	
1. SUBSONIC	
SKIN FRICTION	KARMAN-SCHOENHERR, TURBULENT (16)
COMPRESSIBILITY	SOMMER - SHORT T PRIME (17)
THICKNESS CORRECTIONS	HOERNER (18)
NACELLE/FUSELAGE INTEGRATION	WALCK (19)
EXPERIMENTAL DATA	WIND TUNNEL DATA FROM SIMILAR CONFIGURATIONS
2. SUPERSONIC	
SKIN FRICTION	KARMAN-SCHOENHERR, TURBULENT (16)
COMPRESSIBILITY	SOMMER - SHORT T PRIME (17)
WAVE DRAG	NASA LANGLEY WAVE DRAG PROGRAM (20)
	VON KARMAN SIMILARITY PARAMETERS (21)
EXPERIMENTAL DATA	WIND TUNNEL DATA FROM SIMILAR CONFIGURATIONS
3. TRANSONIC DRAG RISE	DATCOM (15)
4. ROUGHNESS DRAG	DEFINED BY EXPERIENCE
5. EXHAUST PLUME SCRUBBING	MODIFICATION TO SKIN FRICTION
6. EXHAUST PLUME INTERFERENCE (SUPERSONIC)	NASA LANGLEY WAVE DRAG PROGRAM (20)
B. DRAG DUE TO LIFT	
1. SUBSONIC	
WING-BODY	MCAIR SEMI-EMPIRICAL (22)
	MCAIR STATISTICAL (22)
CANARD	VORTEX LATTICE (14)
	WOODWARD (24)
EXPERIMENTAL DATA	WIND TUNNEL DATA FROM SIMILAR CONFIGURATIONS
2. SUPERSONIC	
WING-BODY	MCAIR SEMI EMPIRICAL (22)
	MCAIR STATISTICAL (22)
CANARD	MIDDLETON CARLSON (23)
	WOODWARD (24)
EXPERIMENTAL DATA	WIND TUNNEL DATA FROM SIMILAR CONFIGURATIONS
C. LIFT AND PITCHING MOMENT	
1. SUBSONIC	
WING-BODY	MCAIR STATISTICAL (22), VORTEX-LATTICE (14),
	WOODWARD (24), DATCOM (15)
CANARD	VORTEX-LATTICE (14)
	WOODWARD (24)
EXPERIMENTAL DATA	WIND TUNNEL DATA FROM SIMILAR CONFIGURATIONS
2. SUPERSONIC	
WING-BODY	MCAIR STATISTICAL (22), WOODWARD (24),
	MIDDLETON-CARLSON (23), DATCOM (15)
CANARD	MIDDLETON CARLSON (23)
	WOODWARD (24)
EXPERIMENTAL DATA	WIND TUNNEL DATA FROM SIMILAR CONFIGURATIONS
3. FLAP DEFLECTIONS	VORTEX-LATTICE (14)
EXPERIMENTAL DATA	WIND TUNNEL DATA FROM SIMILAR CONFIGURATIONS
D. TRIM DRAG	COMPUTED FROM LIFT, DRAG, AND PITCHING MOMENT DATA
E. MAXIMUM LIFT COEFFICIENT	DATCOM (15), WIND TUNNEL DATA FROM SIMILAR CONFIGURATIONS
F. BUFFET LIFT COEFFICIENT	MCAIR SEMI-EMPIRICAL (22)
G. LATERAL-DIRECTIONAL	DATCOM (15)
	PANAIR (25)
	VORTEX-LATTICE (14)
	WIND TUNNEL DATA FROM SIMILAR CONFIGURATIONS

surface at the position of the specified control point. Thickness effects can be included by arranging linearly variable sources on the panels. When this is done 2m + 1 boundary conditions are required for each column of panels, and they are specified as the slopes of the upper and lower surfaces, plus a closure condition at the wing or control surface trailing edge. The fuselage is simulated by a cylinder of panels upon which are arranged sources and sinks. Both subsonic and supersonic solutions to the linearized equations are possible.

The PANAIR method also arranges constant strength distributed doublets and linearly varying sources on quadrilateral panels. However, for this method the panels are arranged on the surface of the wing or fuselage. This panel arrangement gives the most accurate representation of the aircraft when the aircraft is properly paneled. Paneling is difficult in regions such as the wingtips and wing fuselage junctures, but improved paneling techniques are being developed. When an aircraft is properly paneled, the method calculates forces and moments very accurately. Its principal drawbacks are its cost and the difficulty of setting up a given case for calculation. Subsonic and supersonic solutions also are available.

DATCOM, the U. S. Air Force Stability and Control Handbook, is a collection of correlations based on wind tunnel data and simple theoretical analysis. Aerodynamic estimates are produced by component build up. Leading edge and trailing edge flap and aileron effects can be obtained from these correlations. However, DATCOM does not address itself directly to canard configurations.

Propulsion induced effects are based on MCAIR advanced design techniques. The VTOL lift effects are obtained from correlations of numerous configurations tested in the MCAIR Advanced Design Wind Tunnel. The STOL jet effects on forces and moments are assumed to be the same as for the YAV-8B due to the similarity in configuration. The STOL inlet momentum effects are based on predicted ram drag.

During the last ten years MCAIR has conducted comprehensive wind tunnel test programs on several close-coupled horizontal canard configurations. Data for four of these configurations were used in the estimation of the Model 279-3 aerodynamic characteristics. All four of these wind tunnel model configurations had the same wing planform as the Model 279-3. Figure 4-1 illustrates the four wind tunnel configurations.

Six different constant area wings were tested on the 6% scale Model 263(ANF) in the MCAIR Polysonic Wind Tunnel (PSWT Test No. 339). These wings had a leading edge sweep of 45° and an aspect ratio of 3.0, each with a different camber surface. A variety of control surfaces also were tested, including a leading edge flap used as a supersonic decamber flap. Four canards were tested, with exposed canard area-to-wing area ratios of .04, .09, and .138, with leading edge sweep angles of 51° or 55°. The canards were tested in two locations; one directly in front of the wing and the other above the wing. A single vertical tail with rudder was used.
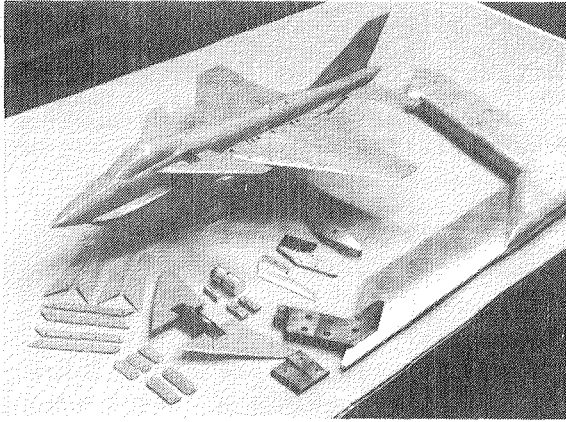
MODEL 279-1
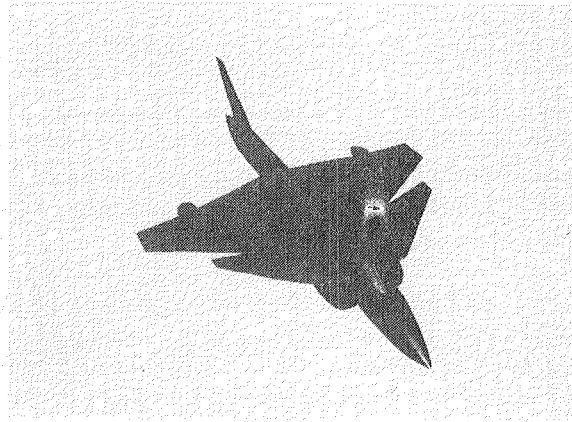
PARAMETRIC MODEL
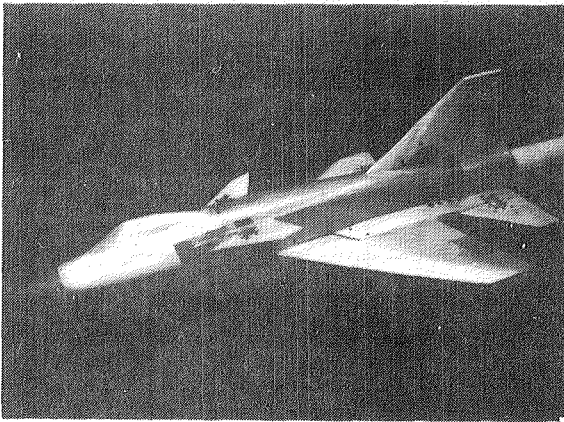
MODEL 263 (ANF)
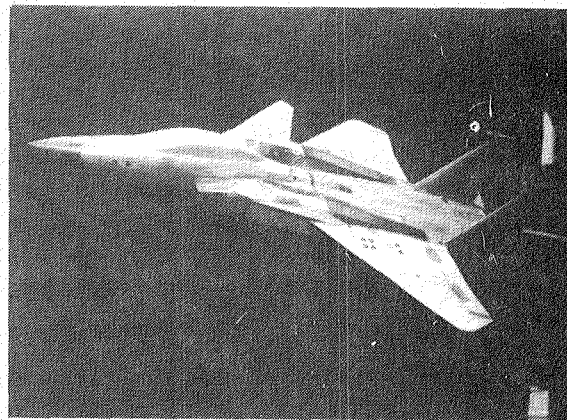
3-SURFACE F-15

GP13-0983-95

FIGURE 4-1
HORIZONTAL CANARD WIND TUNNEL DATA BASE
FOR SINGLE ENGINE SUPERSONIC
TECHNOLOGY

The 3-Surface F-15, tested in the MCAIR Low Speed Wind Tunnel (LSWT) and Polysonic Wind Tunnel is representative of an F-15 with a close-coupled horizontal canard. The canard height, $h_c/\bar{c}$, was approximately 0.1. A variety of canard planforms ($S_c/S_w \sim 0.1$) were tested at dihedral angles of 0°, 10° and 20°. A larger canard ($S_c/S_w = 0.15$) was also tested. These data, References (6), (7), (8), (11), and (26) were extensively used in this study due to their availability on the MCAIR Wind Tunnel Data System (WTDS), Reference (27).

The Model 279-1 is a supersonic V/STOL lift-cruise vectored thrust configuration with a single two dimensional chin inlet. This 4.5 percent wind tunnel model, tested in MCAIR Advanced Design Wind Tunnel (ADWT), Reference (9), had the inlet faired over. The wing had the same planform as the Model 279-3, but was not cambered. This model was tested as a two surface and a three surface configuration. Leading and trailing edge flaps and ailerons were tested. Two canards of aspect ratio 3.0 were tested; one with a leading

edge sweep of 50° and the other with a cranked leading edge with a sweep of 45°/50°. The exposed canard area-to-wing area ratio for both canards was 0.2. The canard height above wing chord plane for both canards was 0.149 for zero canard dihedral.

The parametric model, representative of a side-mounted inlet supersonic V/STOL lift-cruise vectored thrust configuration, was also tested in the MCAIR ADWT, Reference (10). This model utilized many of the Model 279-1 model parts including the wing and was tested as a two surface and a three surface configuration.

4.1 LONGITUDINAL CHARACTERISTICS

The longitudinal aerodynamic characteristics of the Model 279-3 are presented in this section. Included are a discussion of the wing selection for the Model 279-3, untrimmed lift, drag and pitching moment, longitudinal control effectiveness, trimmed lift and drag, lift coefficient for buffet onset, and maximum trimmable lift coefficient. Data are presented for the Mach numbers of 0.2, 0.6, 0.9, 1.2 and 1.6 with zero trailing edge flap deflection. In addition, aerodynamic data with trailing edge flap deflections are presented at the subsonic Mach numbers.

4.1.1 WING SELECTION – As part of the ongoing Independent Research and Development (IRAD) studies, McDonnell-Douglas has investigated minimum drag wings for fighter/attack aircraft. The design criteria for these wings involved various span loadings, design lift coefficients, and drag rise Mach numbers.

One set of design criteria for these wings was:

(1) elliptic span loading,
(2) low cruise trim drag and,
(3) drag rise Mach number, M_{DD} = 0.92.

These criteria, applied to an existing low drag, high speed wing, resulted in the camber and twist distributions shown in Figures 4-2 and 4-3.

To verify the drag reduction, this wing was tested with the existing F-15 fuselage in the MCAIR Polysonic Wind Tunnel. The results of this wind tunnel test are reported in Reference (2). Comparison of these results and test data from previous wings showed large reductions in untrimmed drag in the subsonic and low transonic region, and small drag reductions in the high transonic and supersonic regions. With a leading edge decamber flap, data showed a further drag reduction in the high transonic and supersonic region.

Due to this favorable drag reduction across the Mach number range, the camber and twist of this wing, Figures 4-2 and 4-3, were selected for the Model 279-3 and used in a study to define the Model 279-3 wing planform. Using the advanced design prediction techniques of Table 4-1 and the CADE aircraft sizing program, Figure 2-3, a parametric variation was made for wing sweep, aspect ratio, taper ratio and thickness ratio. The mission performance goals were consistent with fleet air defense, attack capability, high maneuverability and low acceleration times. The resulting wing planform parameters selected were: Λ_{LE} = 45°, AR = 3.0, λ = 0.25 and t/c = 6/4% (fuselage moldline/wing tip). Another reason for selecting this planform was the availability of a partial test data base.
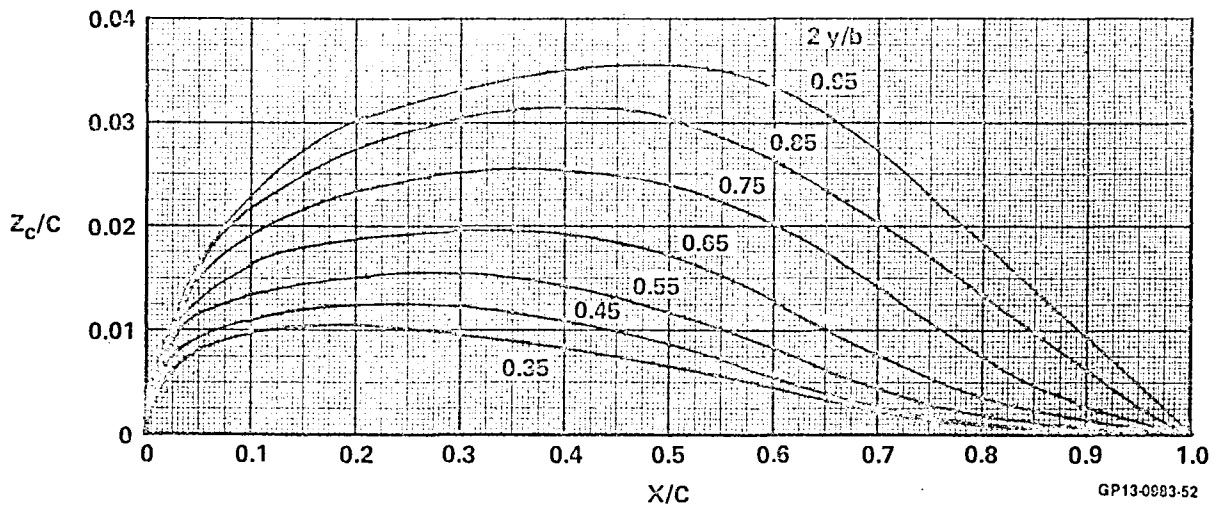
FIGURE 4-2
CAMBER DISTRIBUTION
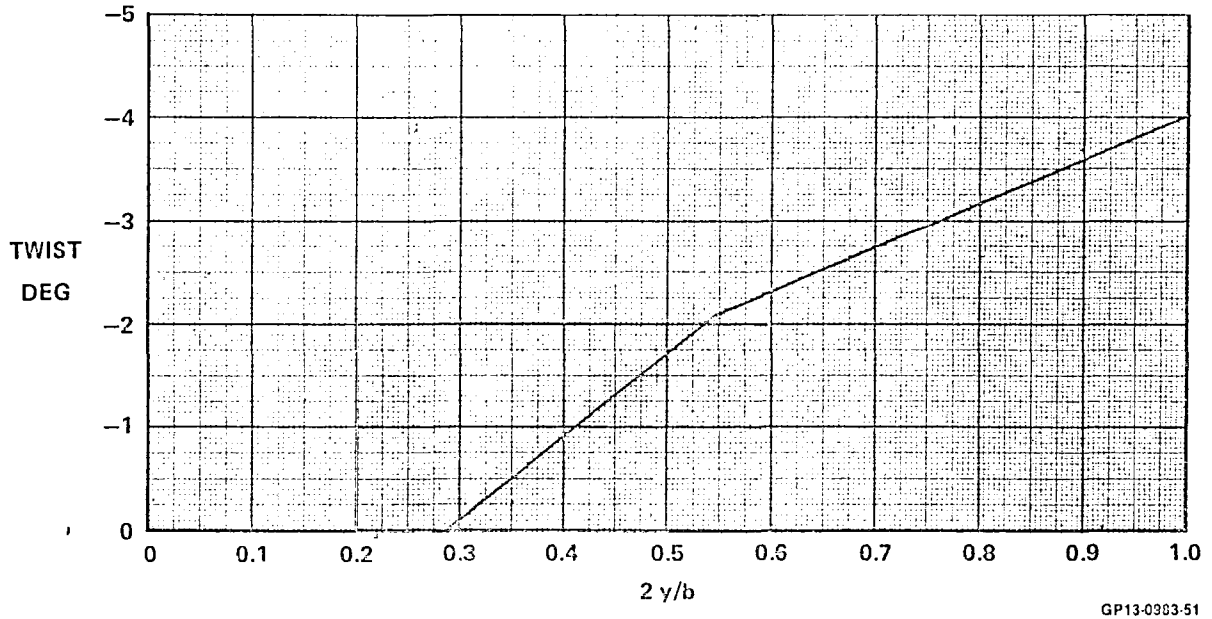
FIGURE 4-3
TWIST DISTRIBUTION

4.1.2 <u>LINEAR LIFT AND PITCHING MOMENT CHARACTERISTICS</u> - Lift curve slope $(C_{L\alpha})$, angle of attack at zero lift (α_{O_L}), pitching moment at zero lift (C_{m_O}) and static stick-fixed neutral point are presented as functions of Mach number in Figures 4-4 through 4-6 for both canard off and on. The Vortex-Lattice, Woodward and Middleton-Carlson linear theory methods were used to calculate these parameters. The accuracy of these methods was evaluated by comparing their results for other horizontal canards with wind tunnel data for these configurations. These comparisons determined the empirical adjustments, if any, necessary for the Model 279-3.

Figure 4-4 shows that the added lifting surface of the horizontal canard significantly increases the lift curve slope at all Mach numbers. Lift curve slope is increased by as much as 18% at 1.6 Mach number. This characteristic agrees with other horizontal canard configurations. Lift curve slope estimates, both canard off and on, from the three linear theory methods, agreed very well with each other. Comparison of the lift curve slope estimates for other horizontal canard configurations with wind tunnel data showed these methods were quite accurate.

Angle of attack at zero lift (α_{O_L}) and pitching moment at zero lift (C_{m_O}) for both canard off and on are presented in Figures 4-5 and 4-6. Estimates were made using the Vortex-Lattice, Woodward and Middleton-Carlson methods. Woodward results were used for subsonic Mach numbers (M<0.90) and Middleton-Carlson results for supersonic (M>1.20). Supersonic Woodward and Middleton Carlson estimates, especially for C_{m_O}, were not in close agreement. Middleton-Carlson results reflected a more realistic level of wing-body C_{m_O} at these higher speeds based on wind tunnel data for a similar wing, Reference (2). These wind tunnel data also were used to determine the transonic Mach number (0.90<M<1.20) fairing of wing-body C_{m_O}.

The effect of the horizontal canard on C_{m_O} was empirically adjusted in the transonic Mach regime. Both the Woodward and Middleton-Carlson methods appear to predict too large an effect, based on results from wind tunnel data for other horizontal canard configurations.
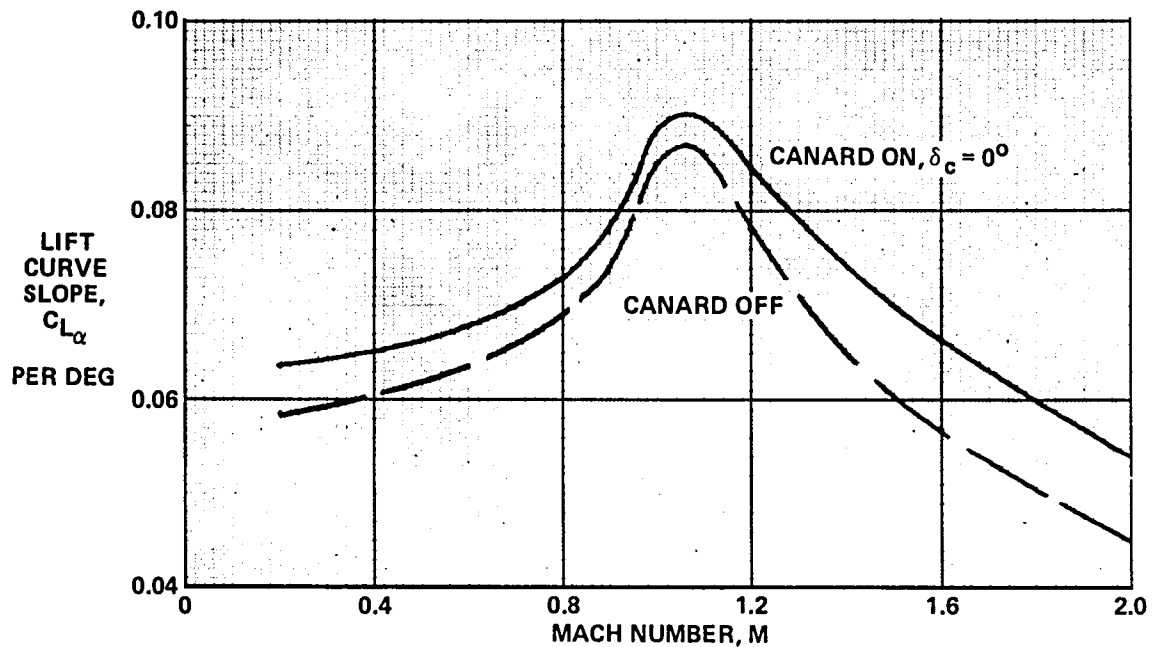
GP13-0983-27

FIGURE 4-4
LIFT CURVE SLOPE
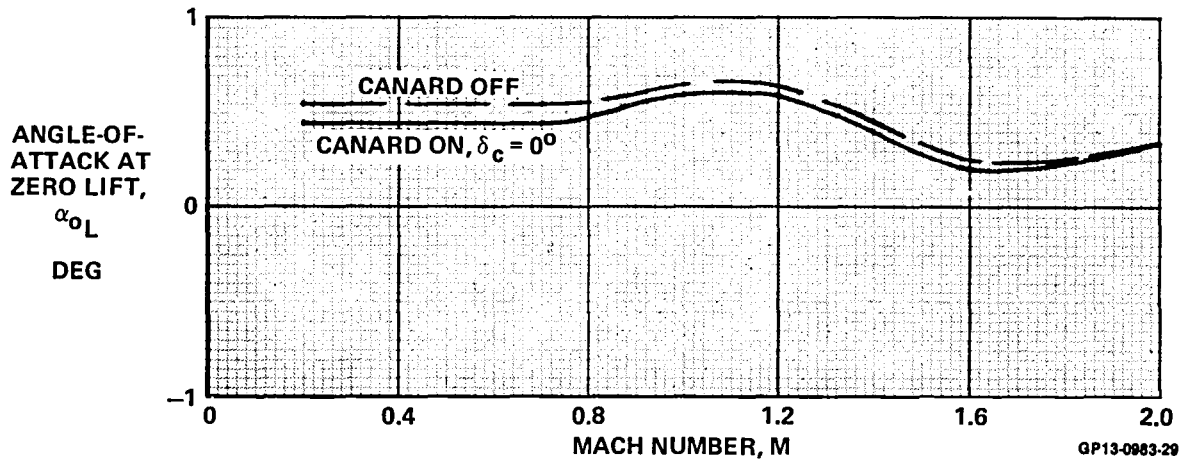
FIGURE 4-5
ANGLE-OF-ATTACK AT ZERO LIFT
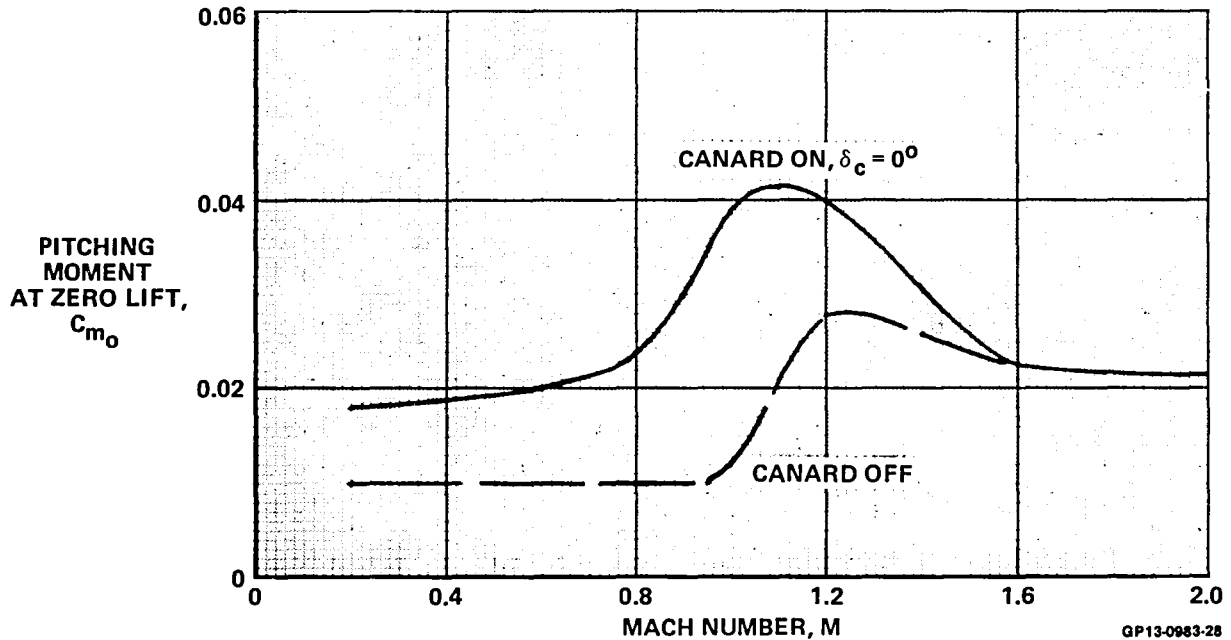
FIGURE 4-6
PITCHING MOMENT AT ZERO LIFT

Predicted values of subsonic α_{o_L} and C_{m_o} canard off and on, using the Vortex-Lattice methods were found to be unrealistic. This was confirmed by comparing Vortex-Lattice results for the 3-Surface F-15 configuration with wind tunnel data.

The static longitudinal stability of the Model 279-3 in terms of stick-fixed neutral point is presented in Figure 4-7. The Model 279-3 was
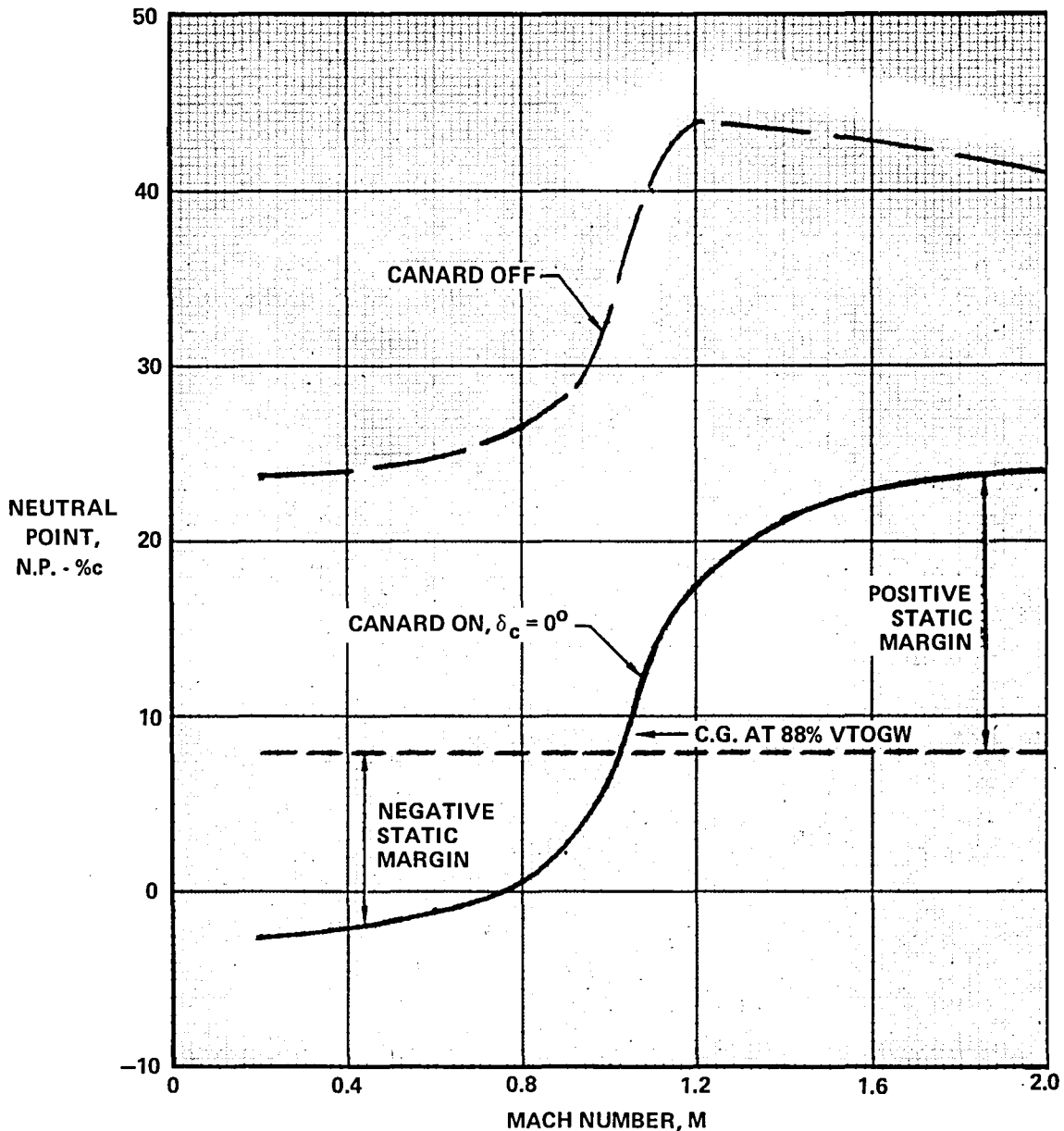
FIGURE 4-7
STICK FIXED NEUTRAL POINT

designed to be longitudinally unstable at subsonic Mach numbers to achieve the performance benefits associated with relaxed static stability. The degree of relaxed static stability, negative static margin, was carefully chosen to achieve the desired performance benefits while considering the capabilities of the control surfaces and control system. The neutral point must be accurately determined to achieve the desired negative static margin.

The Vortex-Lattice, Woodward and Middleton-Carlson methods were used in predicting the neutral point location with Mach number, and to estimate the destabilizing effect of the horizontal canard. Estimates were made using these methods for other horizontal canard configurations for which wind tunnel data was available to determine their accuracy.

It was found subsonically both the Woodward and Vortex-Lattice techniques accurately predict wing-body neutral point location and the effect of horizontal canards. Supersonically, however, the Woodward and Middleton-Carlson methods overestimate the destabilizing effect of canards, especially the Woodward method, and also tend to predict a too stable level of wing-body stability. The Middleton-Carlson method, however, accurately predicts the supersonic canard-on neutral point. A more detailed discussion of the uncertainty in the prediction of the neutral point can be found in Section 7.2.

The supersonic canard-on neutral point for the Model 279-3, Figure 4-7, was based on Middleton-Carlson results; the subsonic neutral point was based on both Vortex-Lattice and Woodward results. Supersonic wing-body neutral point location was empirically adjusted to a more forward location based on the comparison of analytical results and wind tunnel data.

With a center of gravity location of 8.4% $\bar{c}$, the center of gravity at 88% of the VTOGW, for the Supersonic DLI mission, the Model 279-3 exhibits a negative static margin of -7.9% at 0.8 Mach number which is very close to the design goal of -8.0% $\bar{c}$. Supersonically, the Model 279-3 has a stable positive static margin of only 14.6% $\bar{c}$, much less than a conventional stable wing-horizontal tail configuration, resulting in improved supersonic maneuvering performance.

4.1.3 <u>ZERO LIFT DRAG</u> - Subsonic zero lift drag is composed of skin friction, roughness, nacelle fuselage integration, outrigger and camber drag.

Skin friction drag was estimated by applying flat plate turbulent skin friction coefficients to the components of the configuration, i.e., fuselage, wing, canard, and vertical tail. The flat plate incompressible skin friction coefficients of Karman-Shoenhoerr were used for this purpose. These coefficients are given by:

$$\frac{0.242}{C_{fi}} = \log_{10} (R_e \cdot C_{fi})$$

where C_{fi} is the incompressible skin friction coefficient and R_e is the Reynolds number.

The incompressible skin friction coefficient is calculated for each component based on its characteristic length and hence Reynolds number. These data were corrected for compressibility using the T-prime method of Sommer and Short. Corrections were also made for the thickness of surfaces and the fineness ratio of bodies using factors from Hoerner.

The roughness drag includes additional friction drag caused by surface imperfections and surface gaps. MCAIR experience has indicated an "average" roughness factor for fighter aircraft is C_f = .00038. This factor is applied to the total wetted area of the configuration and added to the computed skin friction drag described previously.

Drag increments accounting for nacelle fuselage integration are presented in Reference (19). These data were obtained from wind tunnel results for a wing-body, with and without the nacelle attached in which the total wetted

area remained constant. Drag increments were obtained for a variety of nacelle shapes, lengths, and locations. These data were used to calculate the subsonic drag increment for nacelle fuselage integration.

Subsonic outrigger drag was estimated using a technique in Hoerner for wing fairings. The camber drag estimate was based on wind tunnel data for the wing planform and camber distribution presented in Section 4.1.1. Camber drag is computed with the leading edge decamber flap deflected upward.

Supersonic Drag - Supersonic zero lift drag consists of skin friction, roughness and camber, drag and body surface, outrigger and boundary layer diverter wave drag. The supersonic skin friction drag was estimated using the Karman-Schoenhoerr incompressible turbulent skin friction coefficients with corrections for compressibility using the T-prime method. The thickness and fineness ratio corrections are not applied in the supersonic region. MCAIR's experience indicates that supersonic roughness is about 50% higher than the subsonic roughness, or $C_f = 0.00056$. Supersonic camber drag was estimated in the same way as subsonic camber drag.

The NASA Langley wave drag program, using the cross sectional area distribution of Figure 3-4, was used to estimate the wave drag of the body and the interference drag between the body and wing. To evaluate interference drag, the wing was transferred into an equivalent body of revolution whose area was added to the fuselage area. The area distribution of the transferred wing is the average of the area distributions obtained by intersecting the wing with a set of Mach planes at specified radial angles.

The wave drag of the wing, canard and vertical tail was computed based on transonic similarity rules of Reference (21). Outrigger and boundary layer diverter wave drag were estimated using MCAIR advanced design techniques. Table 4-2 presents the minimum profile drag buildup.

Transonic Drag Rise - There is no accurate method of predicting the transonic $0.7 < M < 1.1$ minimum drag rise, due to the mixed subsonic-supersonic flow in this region. DATCOM presents a method for estimating the drag rise for wing-body-horizontal tail configurations. A drag divergence Mach number (M_{DD}) was obtained by using this method and wind tunnel data for a similar wing. At the drag divergence Mach number (M_{DD}) the following values are applied:

$$(C_D)_{M_{DD}} = (C_D)_{M = 0.7} + 0.002$$

$$\left(\frac{\partial C_D}{\partial M}\right)_{M_{DD}} = 0.1$$

With the above data, a curve is faired between $(C_D)_{M = 0.7}$ and $(C_D)_{M = 1.1}$, passing through the point M_{DD} and $(C_D)_{M_{DD}}$ with a slope of 0.1.

Zero Lift Drag Summary - Table 4-2 presents the zero lift drag as a function of Mach number. The analytically predicted subsonic skin friction drag decreases with Mach number due to the increase in Reynolds number. Based on wind tunnel experience MCAIR has found that subsonic skin friction drag is nearly constant with Mach number, therefore, the value of skin friction drag obtained at Mach number M = .6 has been used for all subsonic Mach numbers per Figure 4-8, in calculating Model 279-3 performance.

TABLE 4-2
ZERO LIFT DRAG BUILDUP

MACH	SKIN FRICTION	NACELLE INTERFER	CAMBER	BLD	OUTRIGGERS	SURFACE WAVE	BODY WAVE	TOTAL
0.2	0.0140	0.0011	0.0011	0	0.0005	0	0	0.0167
0.4	0.0126		0.0011					0.0153
0.6	0.0117		0.0011					0.0144
0.8	0.0111		0.0011					0.0138
0.9	0.0108	0.0011	0.0011	0	0.0005	0	0	0.0135
1.0	0.0099	0	0.0012	0.0008	0.0009	0.0098	0.0092	0.0318
1.05	0.0105		0.0013	0.0010		0.0098	0.0092	0.0327
1.1	0.0104		0.0014	0.0010		0.0107	0.0092	0.0336
1.2	0.0102		0.0017	0.0012		0.0118	0.0092	0.0350
1.4	0.0097		0.0026	0.0014		0.0126	0.0090	0.0362
1.6	0.0093		0.0028	0.0014		0.0129	0.0090	0.0363
1.8	0.0089		0.0030	0.0014		0.0130	0.0089	0.0361
2.0	0.0086	0	0.0032	0.0012	0.0009	0.0130	0.0086	0.0355

GP13-0983-239

CLEAN CONFIGURATION
$S_W = 428$ FT^2

● SUBSONIC C_{D_o} BASED ON
0.6 MACH NUMBER ANALYTICAL PREDICTION

C_{D_o}
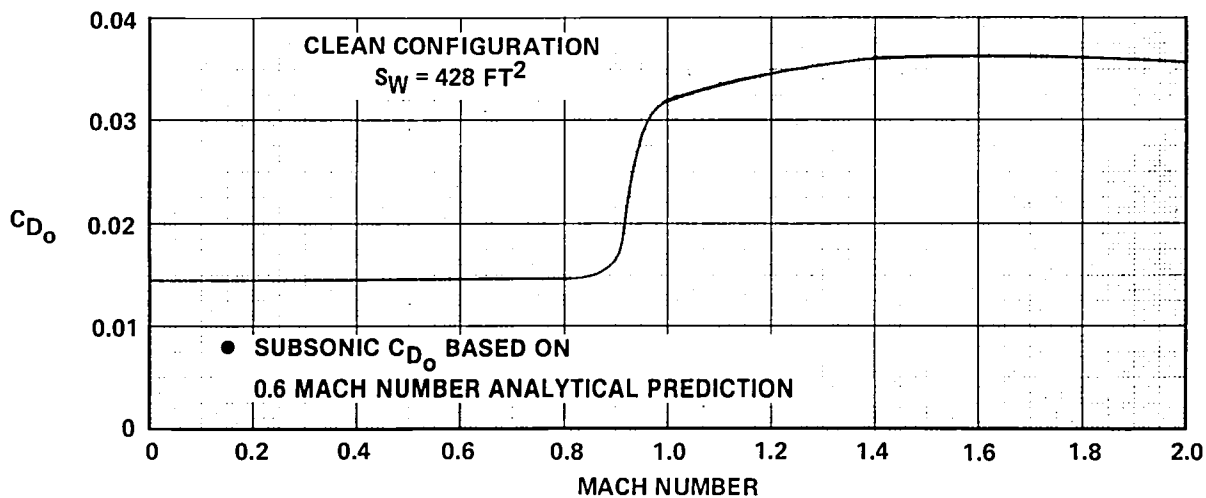
MACH NUMBER

GP13-0983-240

FIGURE 4-8
ZERO LIFT DRAG vs MACH NUMBER

4.1.4 <u>CONTROL EFFECTIVENESS</u> - Primary longitudinal pitch control for the Model 279-3 is provided by the close-coupled horizontal canard. It is sized to provide adequate nose-up and nose-down pitching moment capability at all Mach numbers. The wing trailing edge flap also can be used, if necessary, to provide nose-down pitching moment capability at critical flight conditions.

The large chord Model 279-3 wing trailing edge flap in up and away flight is used for lift enhancement during subsonic and transonic maneuvering to improve lift/drag at high angles of attack. Flap effectiveness data are presented only at 0.2, 0.6 and 0.9 Mach number. No data were available with which to estimate supersonic flap effectiveness. The flap is not anticipated to be used supersonically because of the large hinge moments that would be incurred and the expected reduced lift/drag ratio. Supersonic flap effectiveness data, however, will be acquired in Phase II as shown in Section 8.2.

The Vortex-Lattice, Woodward and Middleton-Carlson linear theory programs were used to predict the linear lift and pitching moment effectiveness of the horizontal canard. By comparing results from these methods for other canard configurations with wind tunnel data, it was found that the Middleton-Carlson and Woodward methods overestimate supersonic canard pitching moment effectiveness. However, subsonic canard pitching moment effectiveness is accurately predicted by the Woodward and Vortex-Lattice methods. More discussion on the uncertainty in predicting canard pitching moment effectiveness with these methods is found in Section 7.2.

Figure 4-9 presents the estimated Model 279-3 canard lift and pitching moment effectiveness. Supersonic pitching moment effectiveness has been empirically adjusted based on comparisons between analytical predictions and wind tunnel data for other canard configurations. Canard lift effectiveness was estimated for this study to be constant with Mach number, based on canard lift effectiveness observed for other canard configurations. These linear predictions of canard lift and pitching moment effectiveness were used as the initial building block in estimating canard effectiveness for all canard deflections and angles of attack.

Wing trailing edge flap lift and pitching moment effectiveness at 0.2, 0.6 and 0.9 Mach number are presented in Figure 4-10. These control effectiveness derivatives are based on scaled wind tunnel data from other canard configurations. Analytical estimates of flap lift and pitching moment effectiveness using the Vortex-Lattice method tended to overestimate flap effectiveness based on comparison of analytical results and wind tunnel data for other canard configurations. These linear methods also cannot estimate angle of attack effects on flap effectiveness, or the effect of a close-coupled horizontal canard on flap effectiveness at angle of attack. The beneficial effect of a close-coupled horizontal canard on flap effectiveness is shown for two canard configurations in Section 7.2.4, Figures 7-16 and 7-17.

4.1.5 <u>LIFT, DRAG AND PITCHING MOMENT</u> - The lift, drag and pitching moment characteristics of the Model 279-3 are presented in this section at 0.2, 0.6, 0.9, 1.2 and 1.6 Mach number. Subsonic characteristics are presented up to 30 degrees angle of attack and supersonic characteristics up to 15 degrees angle of attack for canard deflections of 0, +10 and +20 degrees and zero trailing edge flap deflection. Lift, pitching moment and drag characteristics with trailing edge flaps deflected 10 and 20 degrees are also presented at 0.2, 0.6 and 0.9 Mach number for zero canard deflection.
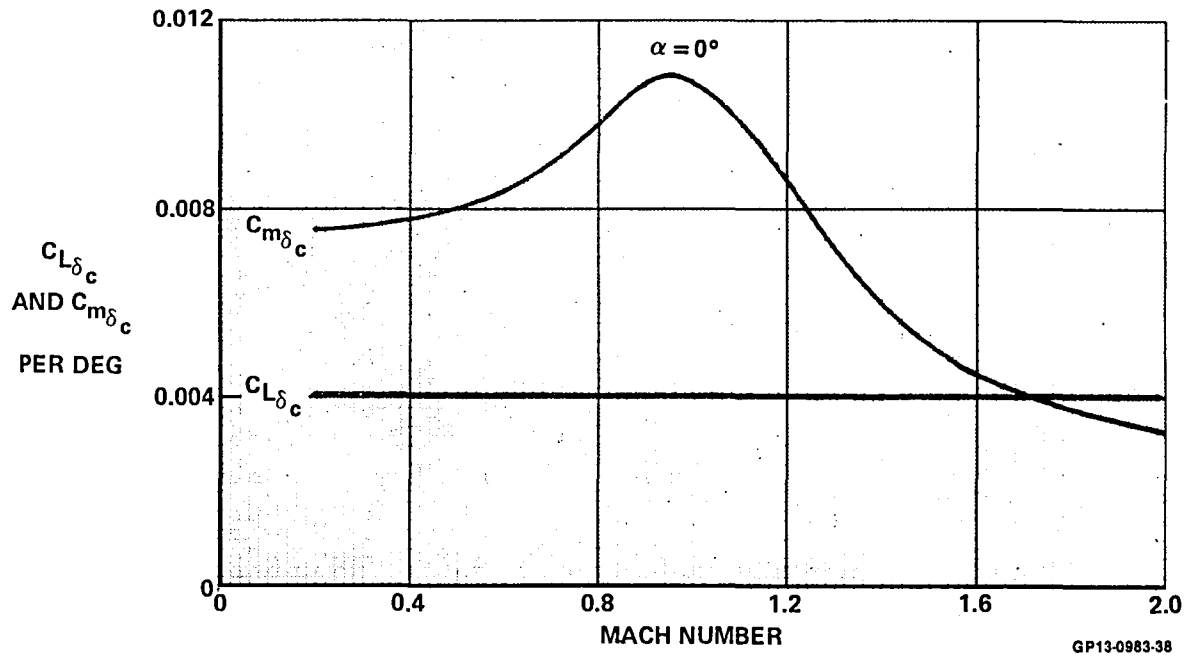
FIGURE 4-9
HORIZONTAL CANARD LIFT AND
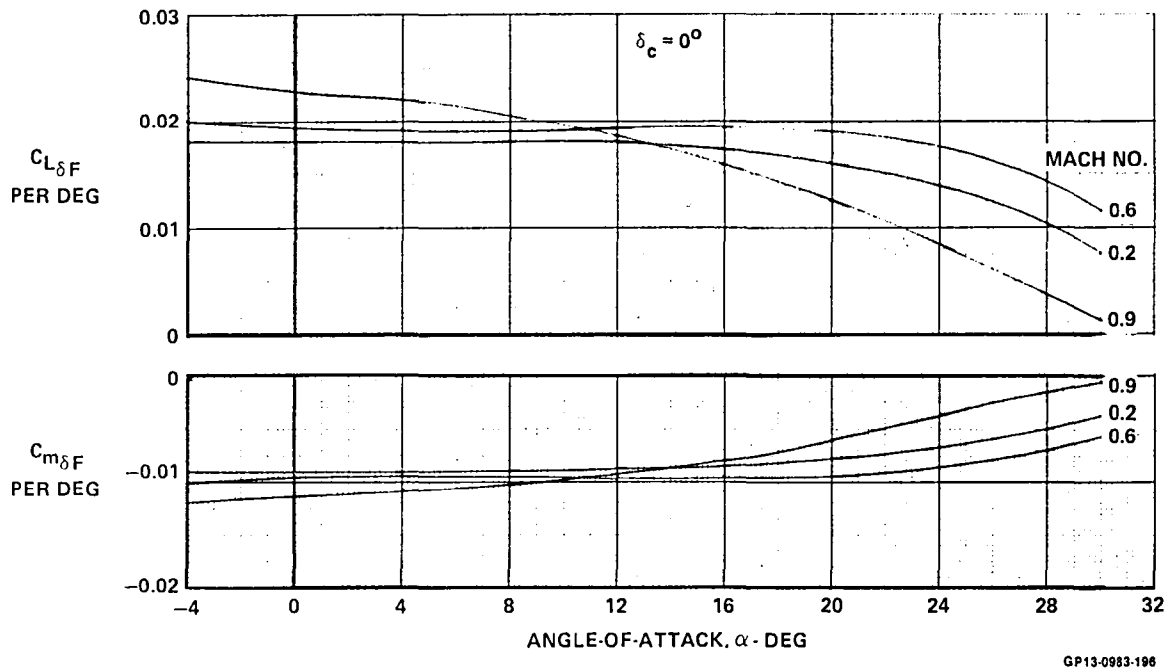**PITCHING MOMENT EFFECTIVENESS**

FIGURE 4-10
MANEUVERING TRAILING EDGE FLAP EFFECTIVENESS

The low angle of attack wing-body and canard zero deflection lift and pitching moment characteristics are based on the linear theory estimates of Section 4.1.2. High angle of attack wing-body characteristics are based on F-15 wind tunnel data. The F-15 and Model 279-3 wing planforms are identical. The effect of the undeflected canard at high angle of attack is based on scaled 3-Surface F-15 canard lift and pitching moment increments. These data were scaled to represent the Model 279-3 canard based on trends shown from available canard size parametric wind tunnel data. It was found subsonically that at high angle of attack, lift and pitching moment due to the horizontal canard did not necessarily scale linearly as canard size increased.

The effect of canard deflection on lift and pitching moment at low angle of attack is based on the canard effectiveness derivatives presented in Section 4.1.4. The 3-Surface F-15 canard data were scaled to match the estimated linear derivatives in the -10 to +10 degree canard deflection range to provide canard lift and pitching moment effectiveness characteristics at angle of attack and for larger canard deflections, -20 and +20 degrees.

Wing-body induced drag for the Model 279-3 is based on estimates made with the MCAIR Statistical Method supplemented at high lift coefficients with F-15 wing-body induced drag. The effect of the horizontal canard ($\delta_c = 0°$) and the effect of horizontal canard deflection on induced drag is based on 3-Surface F-15 wind tunnel data scaled to the Model 279-3 canard to wing area ratio ($S_c/S_w = 0.2$).

Lift characteristics showing the effect of the horizontal canard and canard deflection are presented in Figures 4-11 through 4-15. The horizontal canard provides a significant increase in lift subsonically at high angle of attack due to vortex interaction with the wing. This favorable interaction is reduced for positive canard deflections.

Pitching moment characteristics showing the effects of the horizontal canard and canard deflection are presented in Figures 4-16 through 4-20. Subsonically, the horizontal canard provides a destabilizing moment which results in an unstable configuration which is desired for optimum performance in the subsonic Mach regime. The horizontal canard provides adequate maneuvering and sufficient nose-down control capability at high angle of attack to prevent undesired pitch excursions. A desirable nose-down stable break provides a large restoring moment at high angle of attack that will minimize the possibility of pitch departure.

Supersonically, the canard provides a large destabilizing effect, although the aircraft is still longitudinally stable. Twenty degrees of canard deflection provides sufficient maneuvering capability.
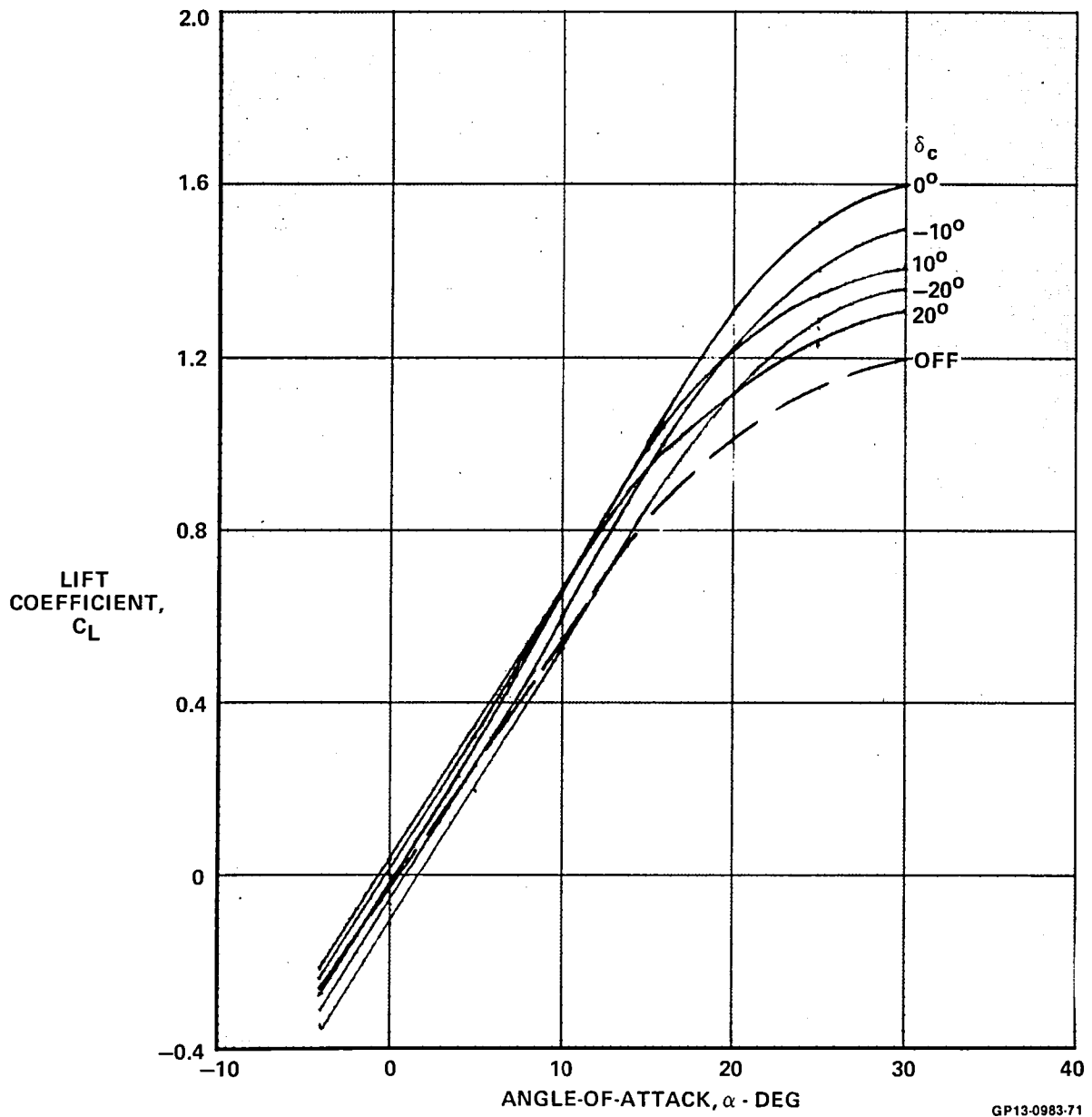
FIGURE 4-11
LIFT CHARACTERISTICS AT MACH 0.2

GP13-0983-71

FIGURE 4-12
LIFT CHARACTERISTICS AT MACH 0.6
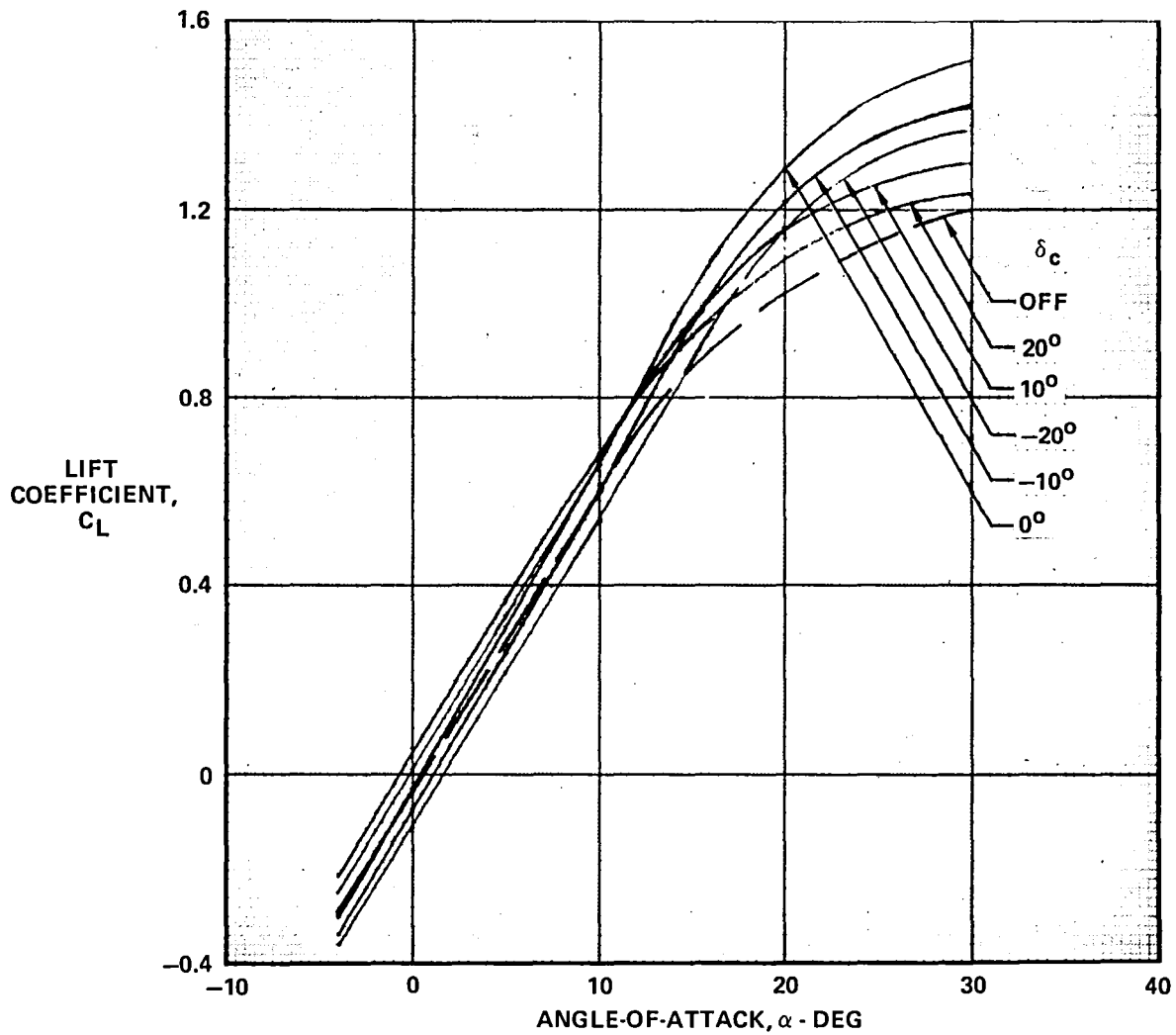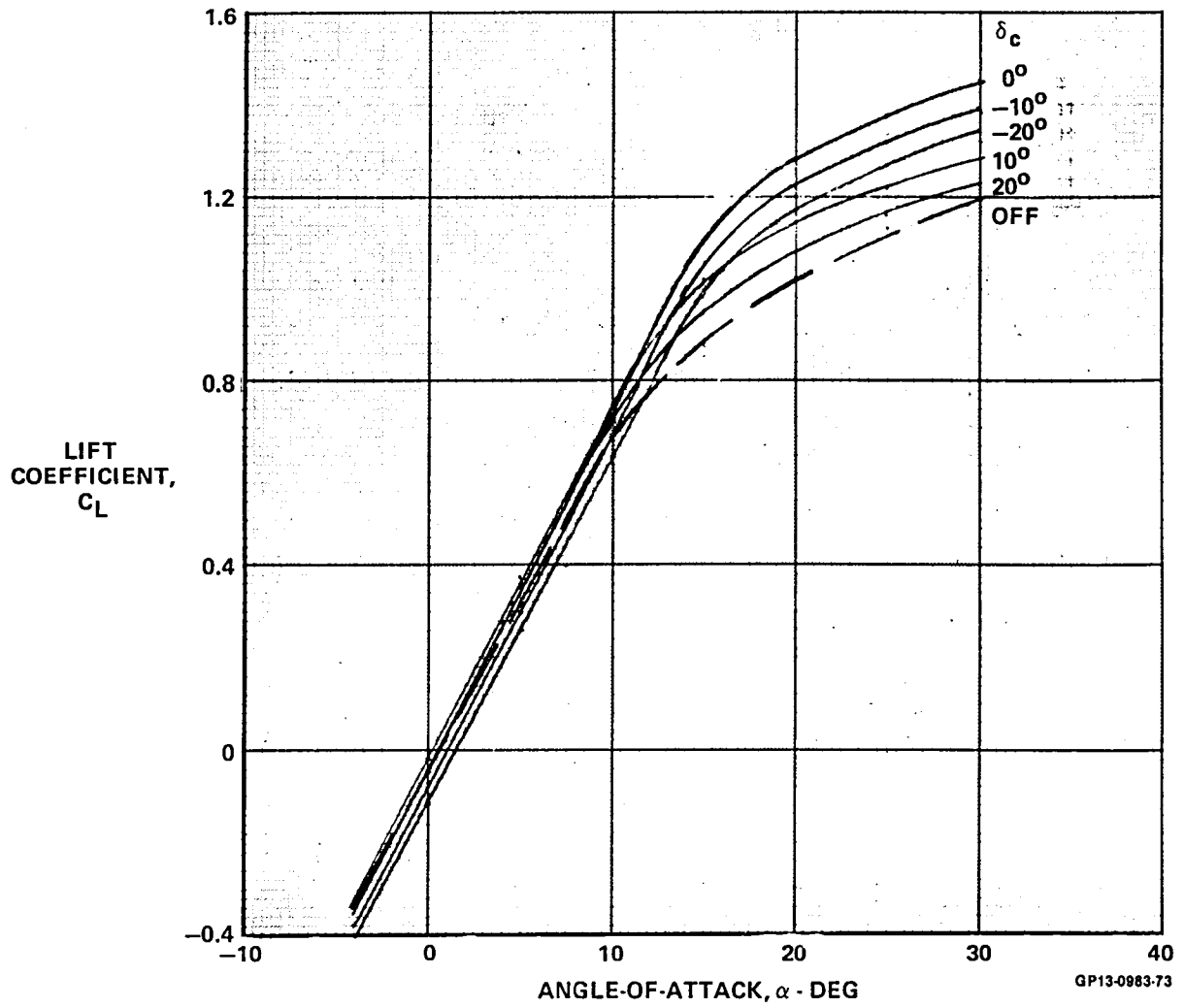
GP13-0983-72

FIGURE 4-13
LIFT CHARACTERISTICS AT MACH 0.9

FIGURE 4-14
LIFT CHARACTERISTICS AT MACH 1.2
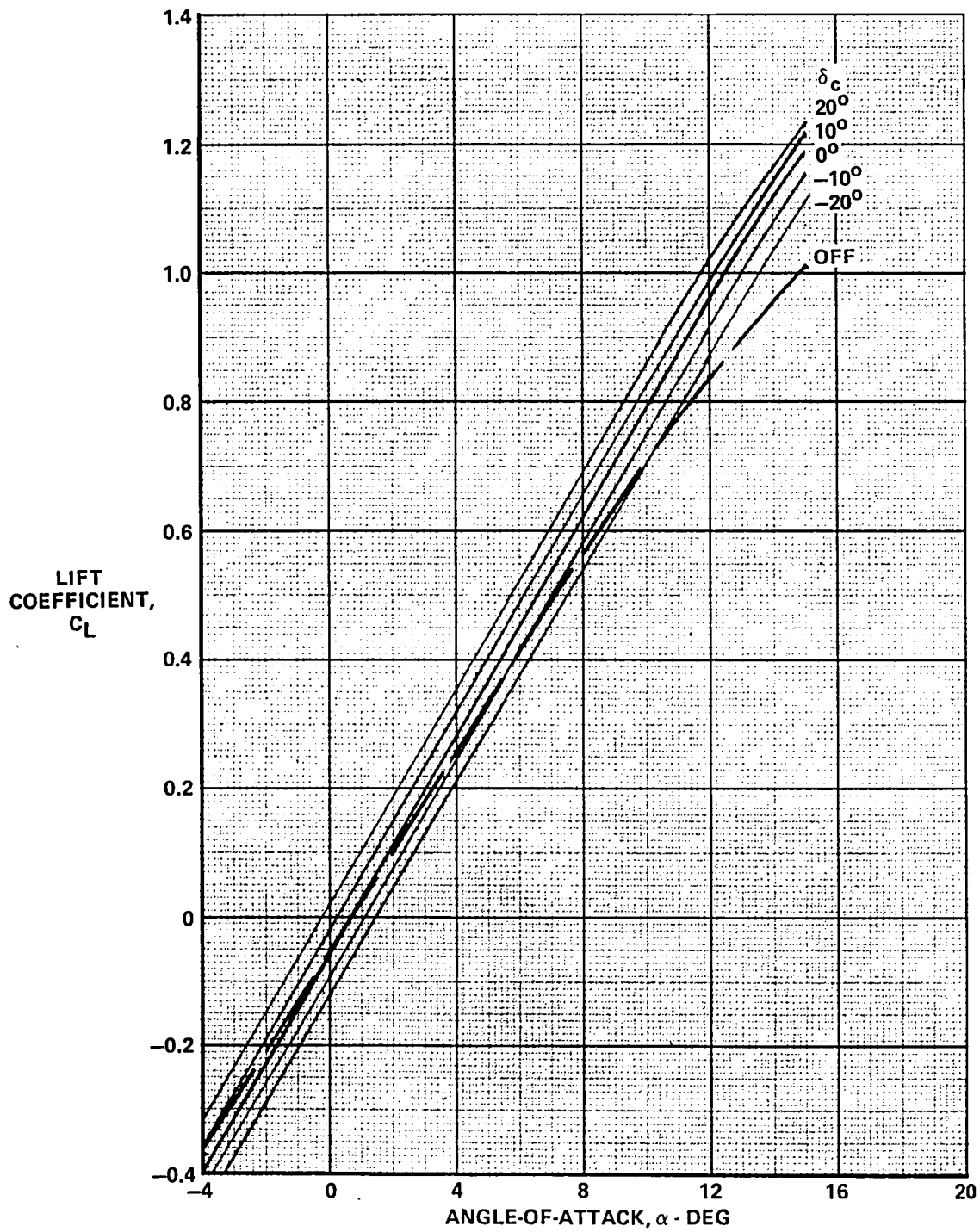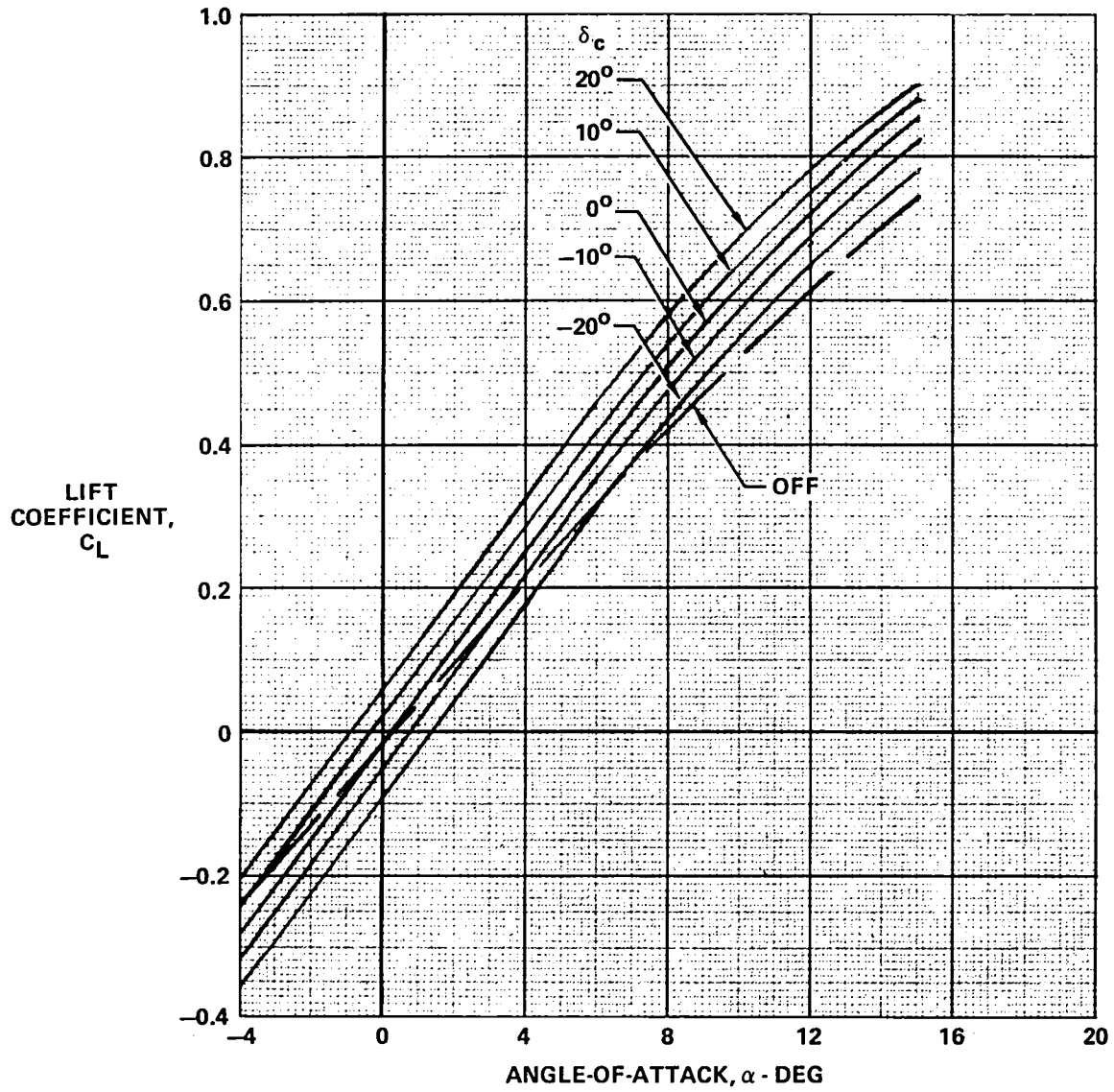
GP13-0983-74

FIGURE 4-15
LIFT CHARACTERISTICS AT MACH 1.6
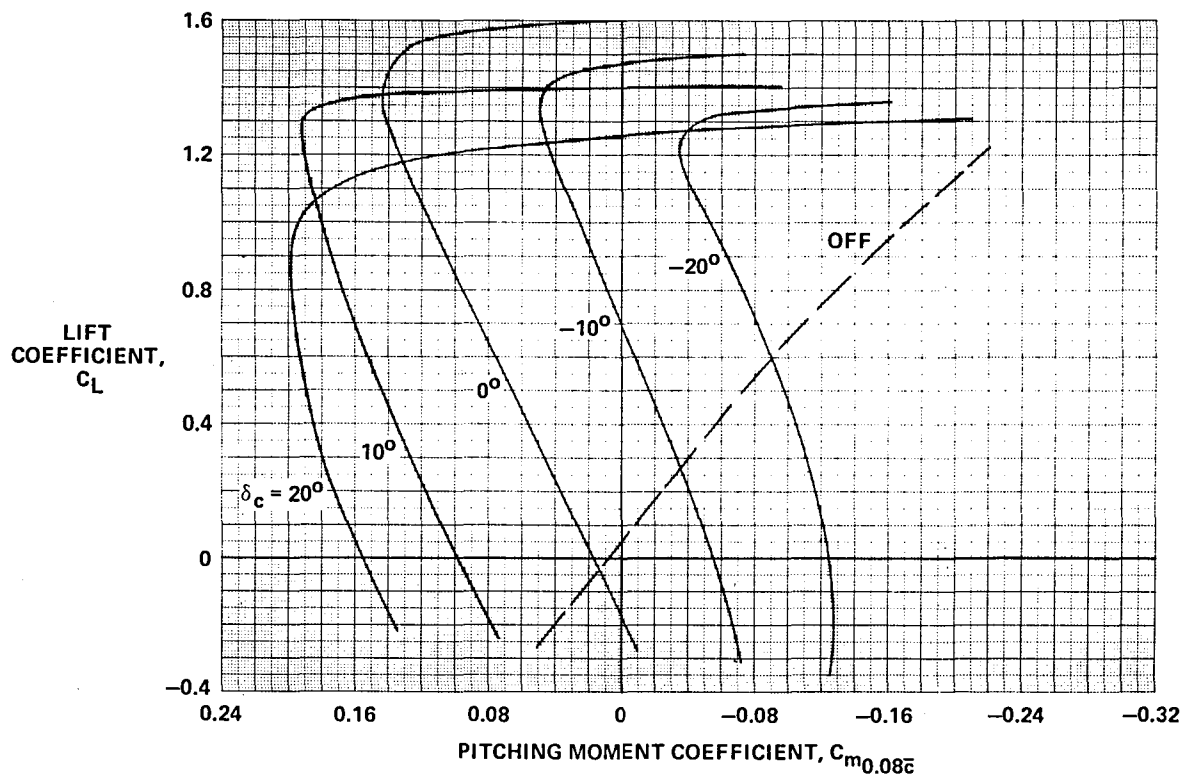
GP13-0983-75

FIGURE 4-16
PITCHING MOMENT CHARACTERISTICS AT MACH 0.2

GP13-0983-78
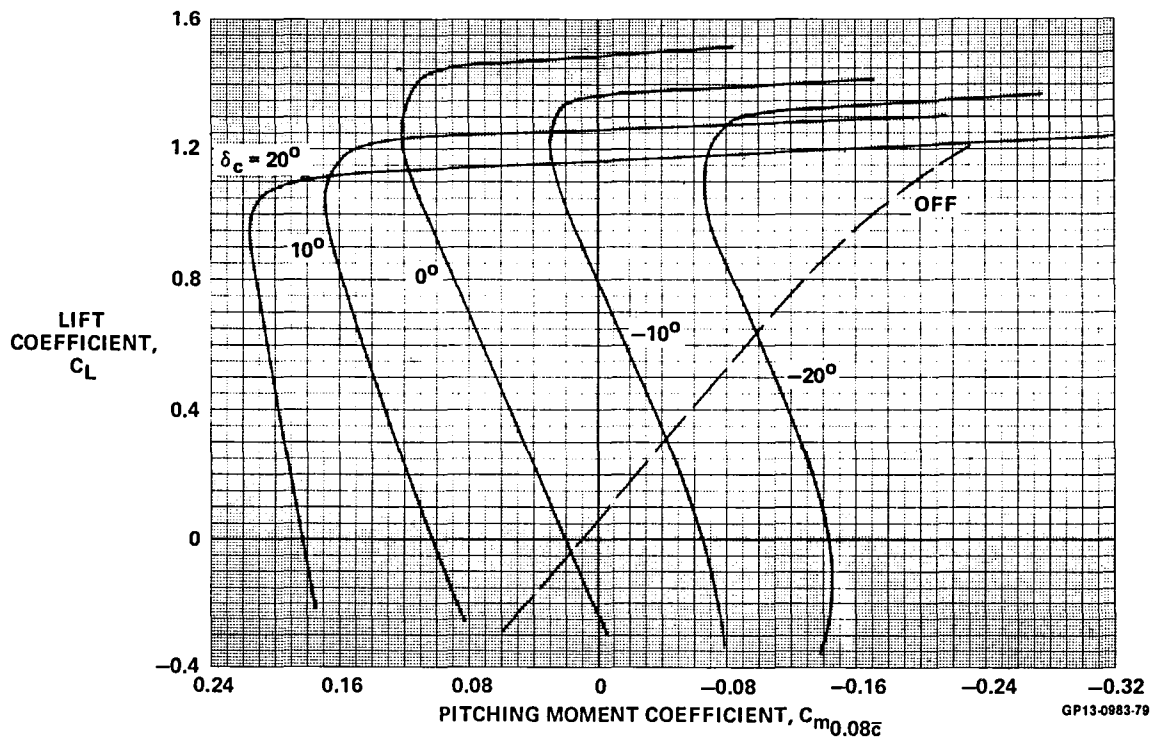
FIGURE 4-17
PITCHING MOMENT CHARACTERISTICS AT MACH 0.6

GP13-0983-79
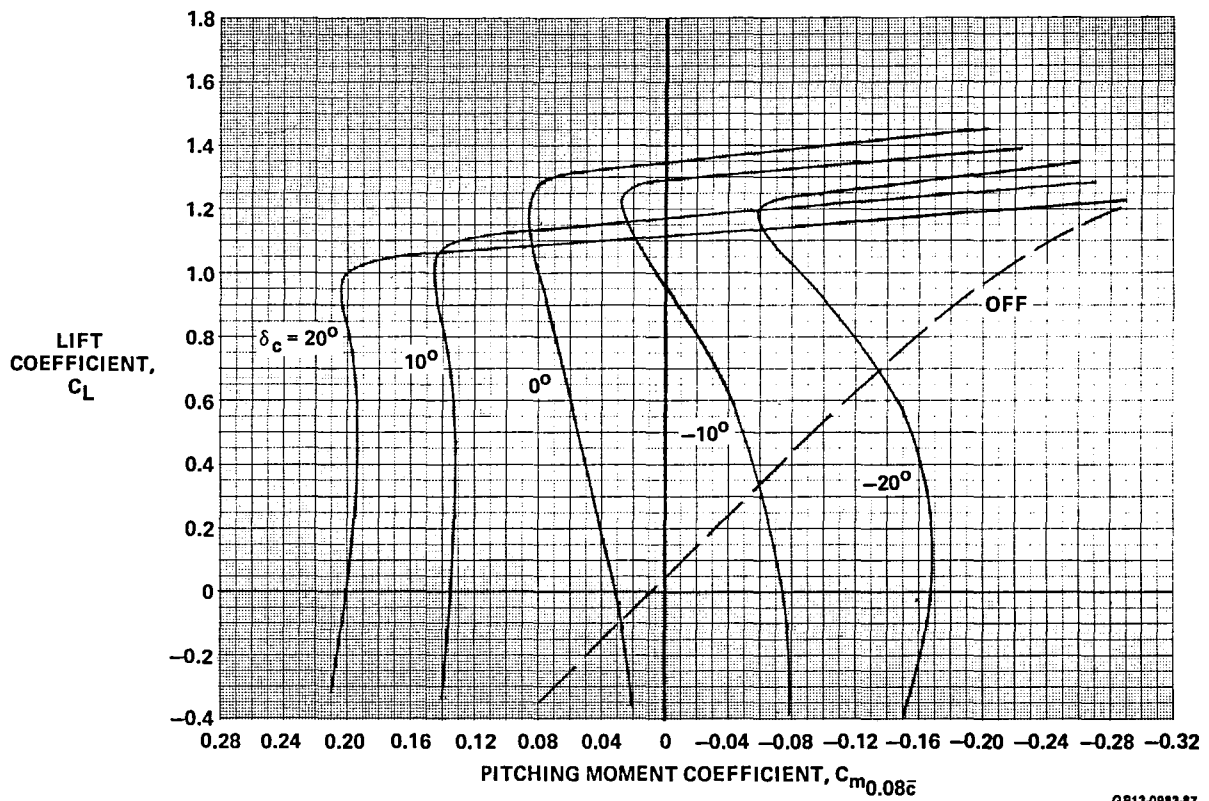
FIGURE 4-18
PITCHING MOMENT CHARACTERISTICS AT MACH 0.9
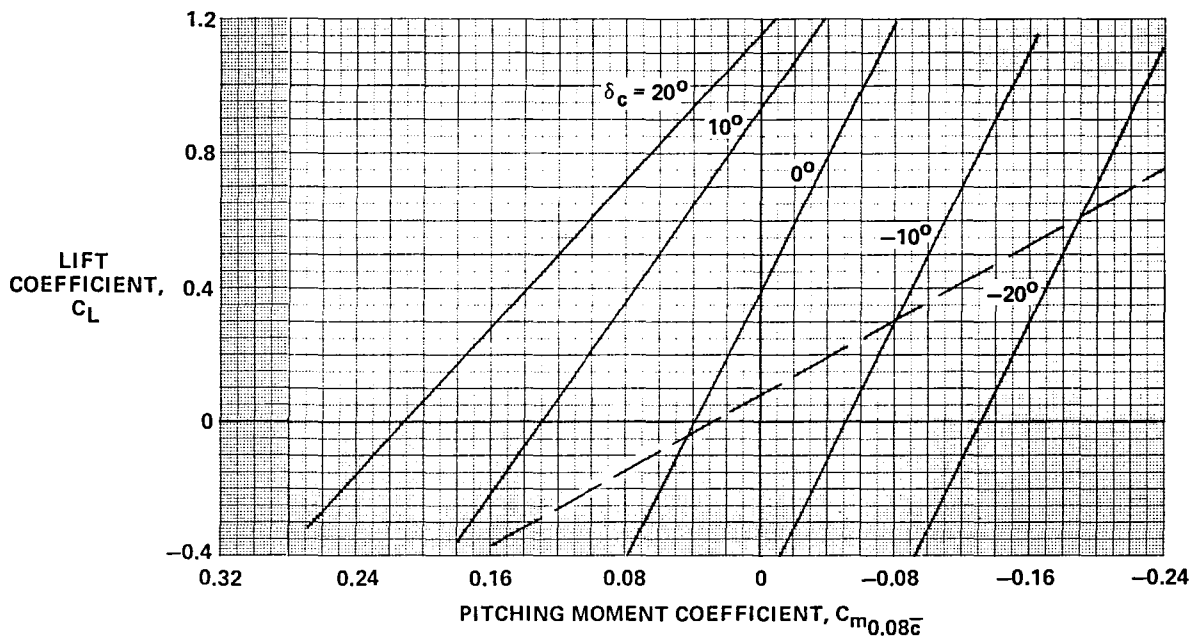
FIGURE 4-19
PITCHING MOMENT CHARACTERISTICS AT MACH 1.2
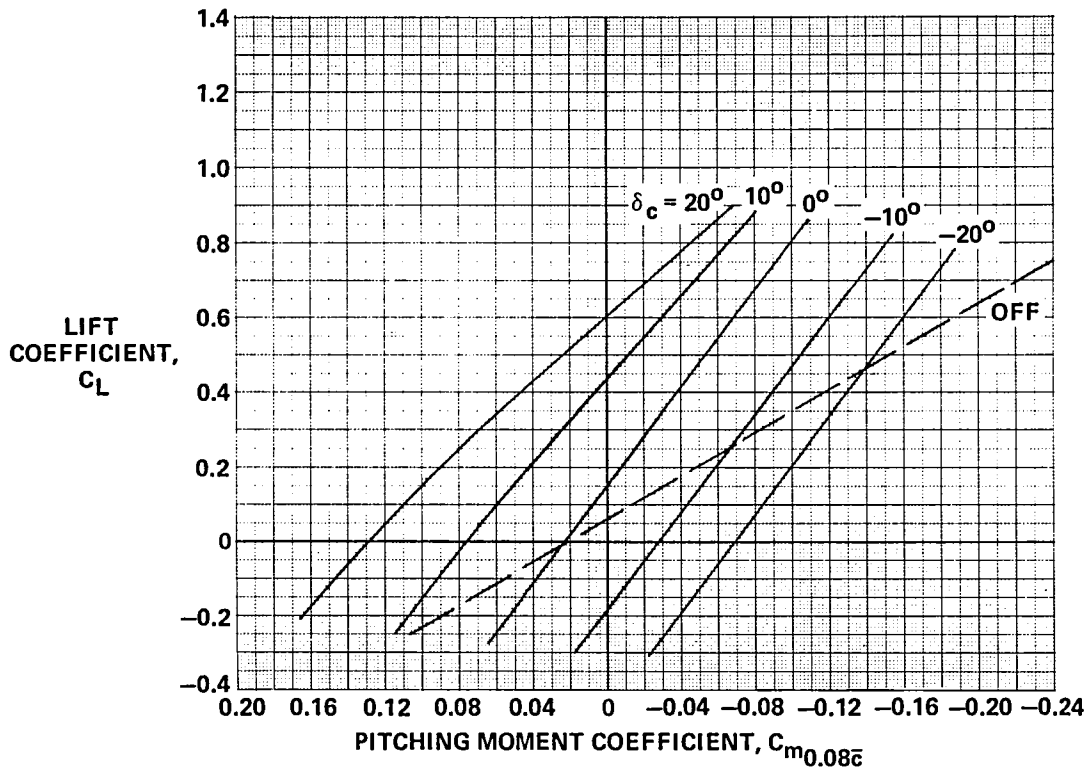
FIGURE 4-20
PITCHING MOMENT CHARACTERISTICS AT MACH 1.6

The untrimmed drag characteristics of the Model 279-3 are presented in Figures 4-21 through 4-25. These drag characteristics include aerodynamic drag only. Propulsion drag effects are presented in Section 5.0. The horizontal canard, except at large positive deflections, greatly reduces induced drag at high lift coefficient, resulting in increased lift/drag. Larger negative canard deflection increases lift/drag ratio with increasing lift coefficient.

Untrimmed lift to drag ratio, aerodynamic only, as a function of lift coefficient for zero canard deflection is presented in Figure 4-26.

The effect of wing trailing edge flap deflection on lift and pitching moment at 0.2, 0.6, and 0.9 Mach number is presented in Figures 4-27 through 4-29. These data are for zero canard deflection. The Model 279-3 trailing edge flaps result in significantly increased lift capability, but also generate a large nose-down pitching moment. The horizontal canard can balance this pitching moment, resulting in excellent flap effectiveness at high angle of attack.

Trailing edge flap effect on drag is presented in Figures 4-30 through 4-32; the effects on lift/drag ratio is presented in Figures 4-33 through 4-35. The flaps do not increase untrimmed lift/drag at cruise lift coefficient (C_L _ 0.4), but result in decreased induced drag, increased lift/drag, at high lift coefficient.
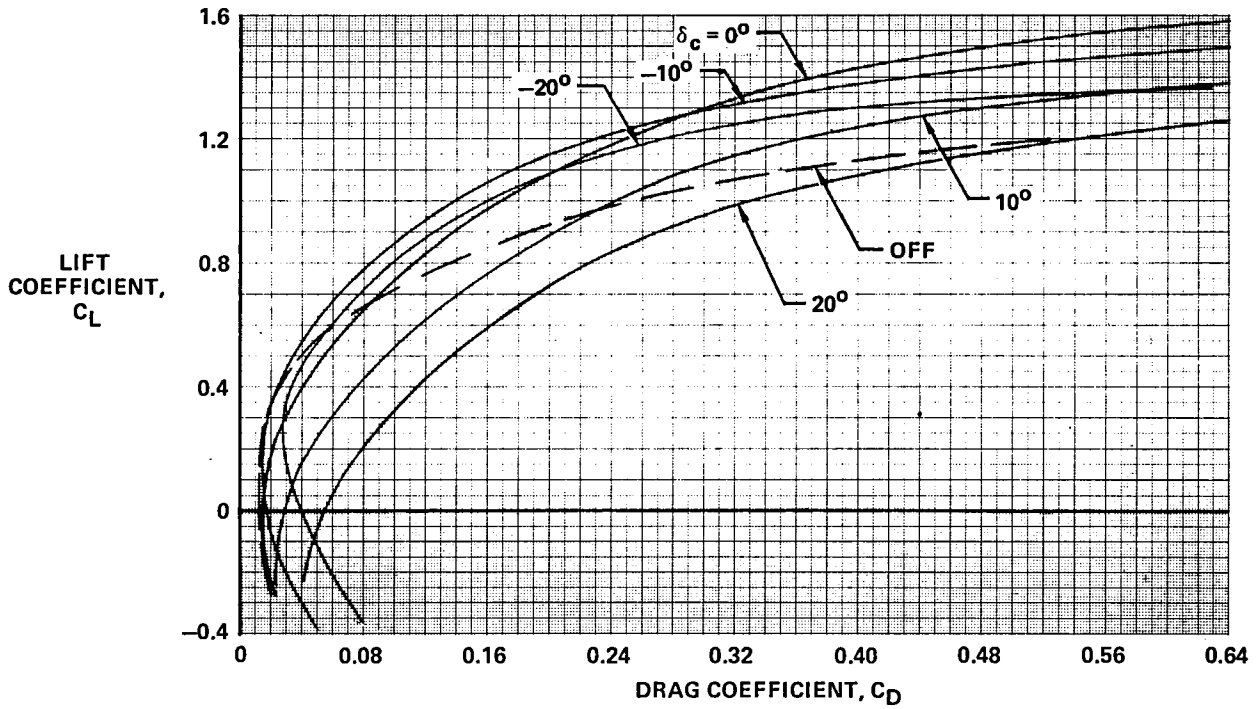
GP83-0983-82

FIGURE 4-21
DRAG CHARACTERISTICS AT MACH 0.2
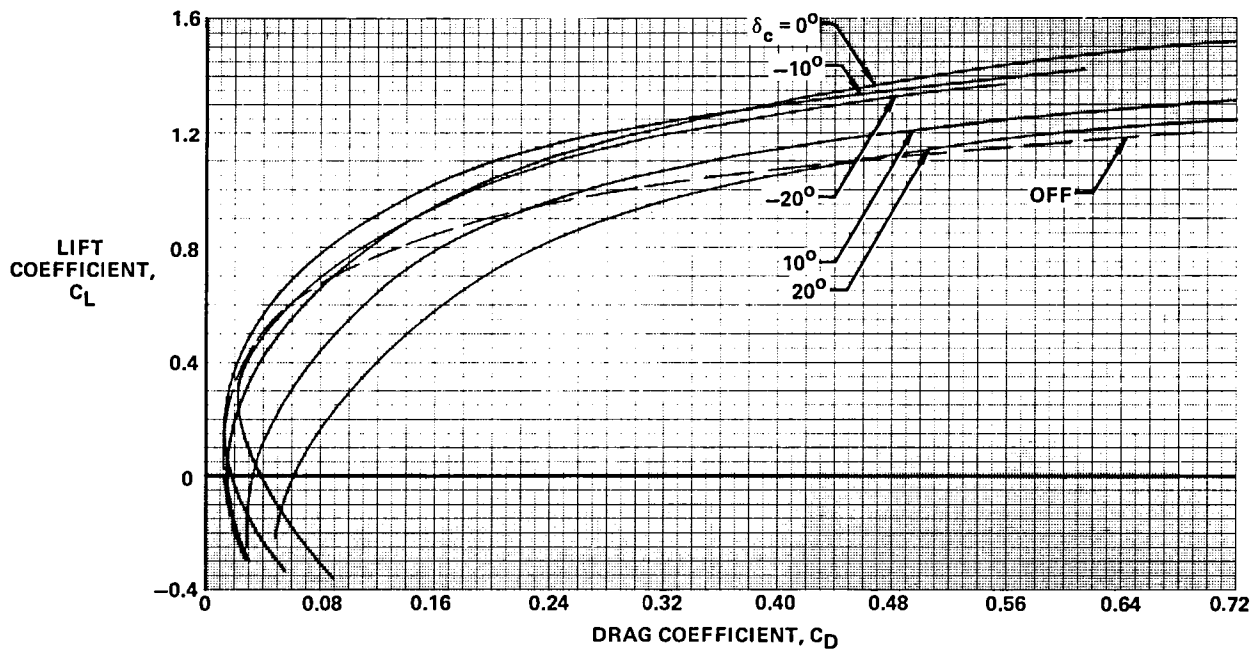
GP13-0983-83

FIGURE 4-22
DRAG CHARACTERISTICS AT MACH 0.6
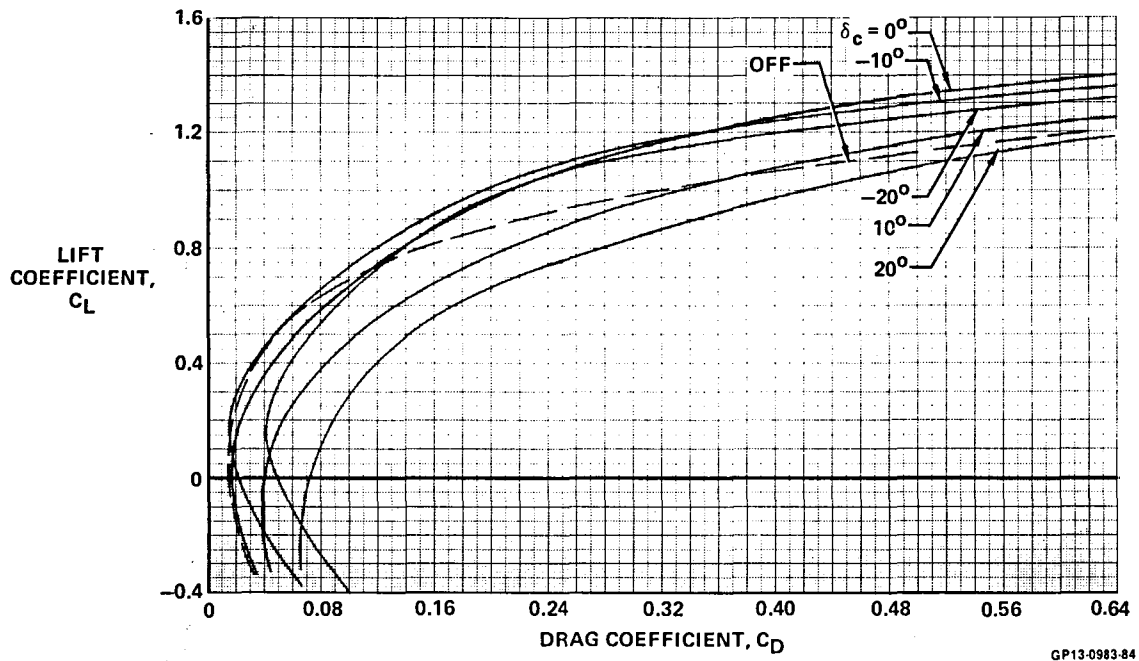
FIGURE 4-23
DRAG CHARACTERISTICS AT MACH 0.9
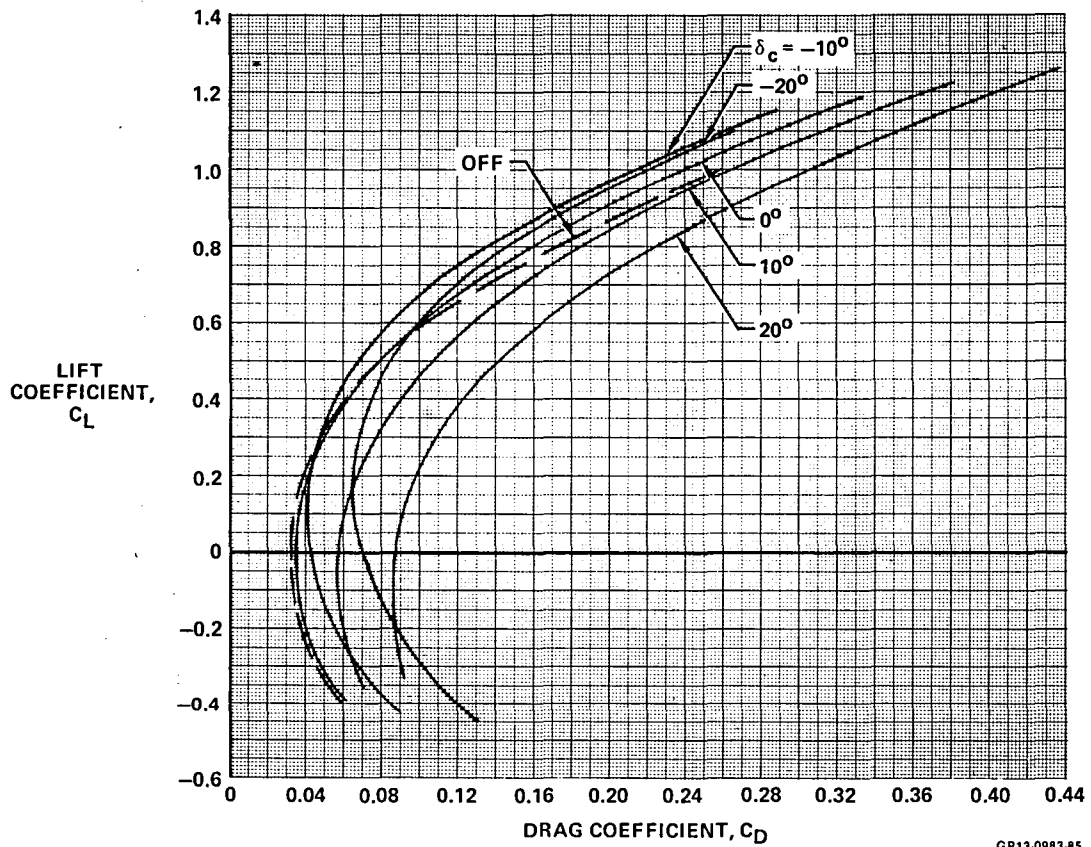
FIGURE 4-24
DRAG CHARACTERISTICS AT MACH 1.2
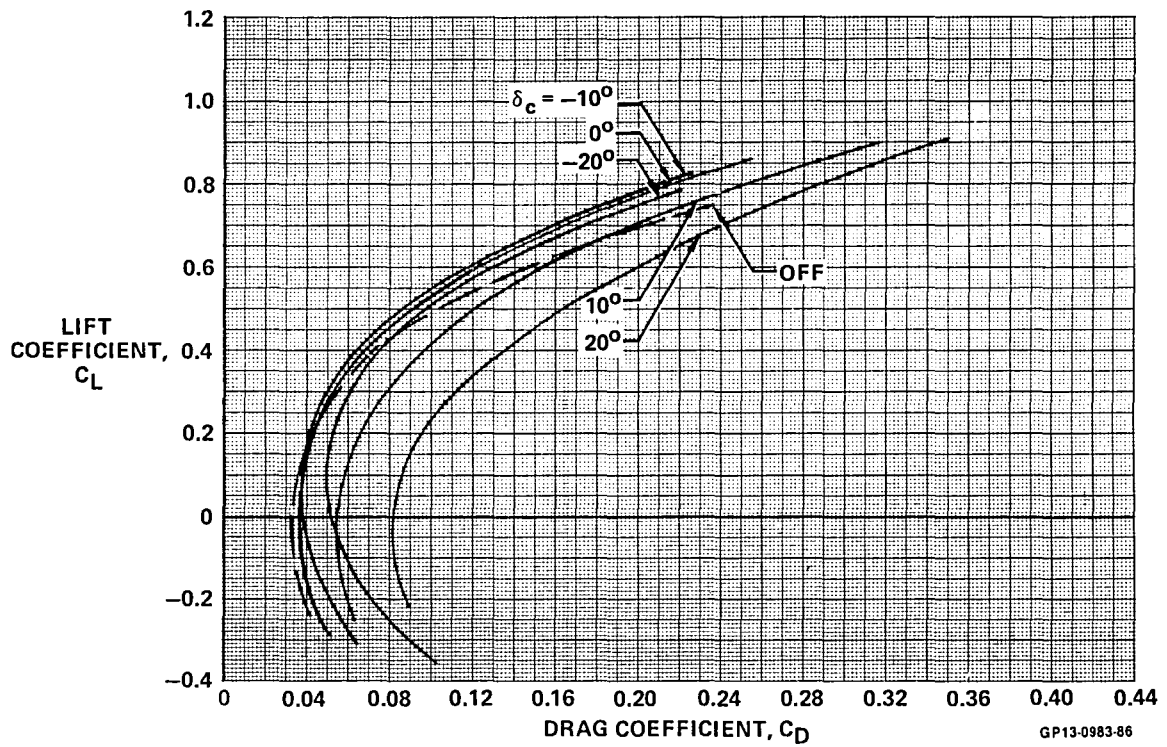
FIGURE 4-25
DRAG CHARACTERISTICS AT MACH 1.6
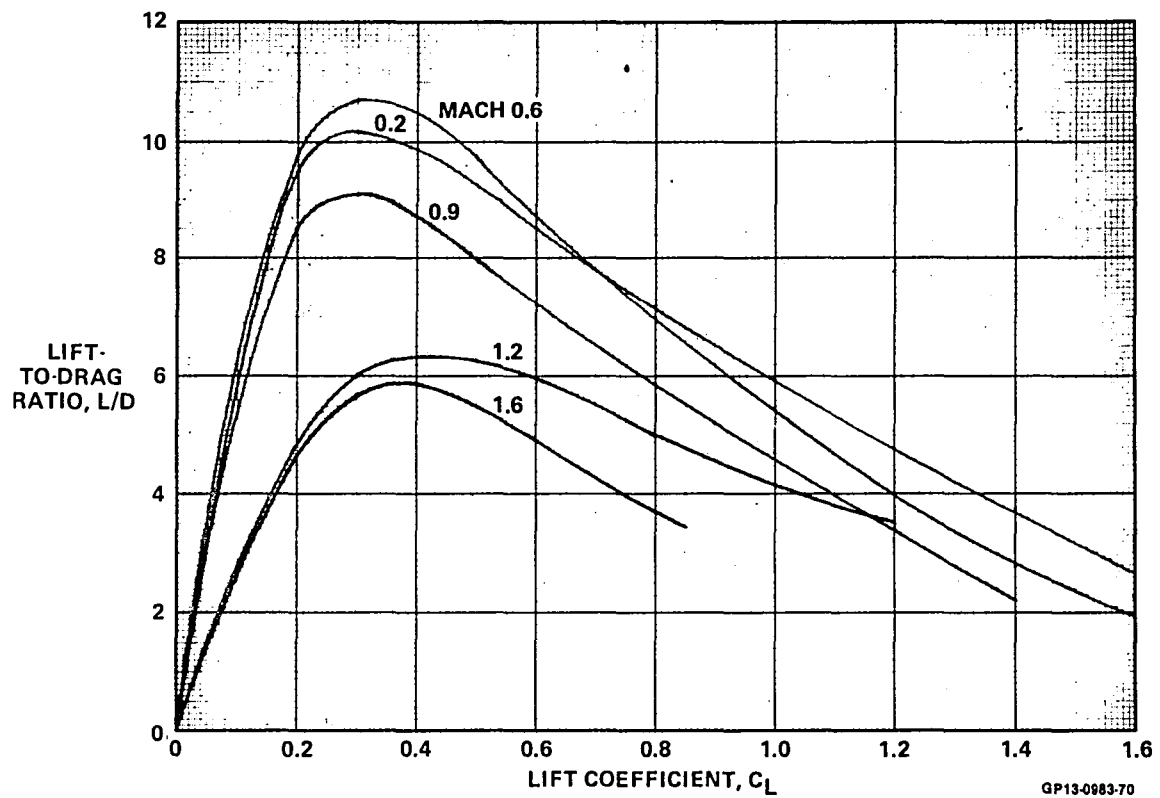
FIGURE 4-26
LIFT-TO-DRAG RATIO, $\delta_c = 0°$
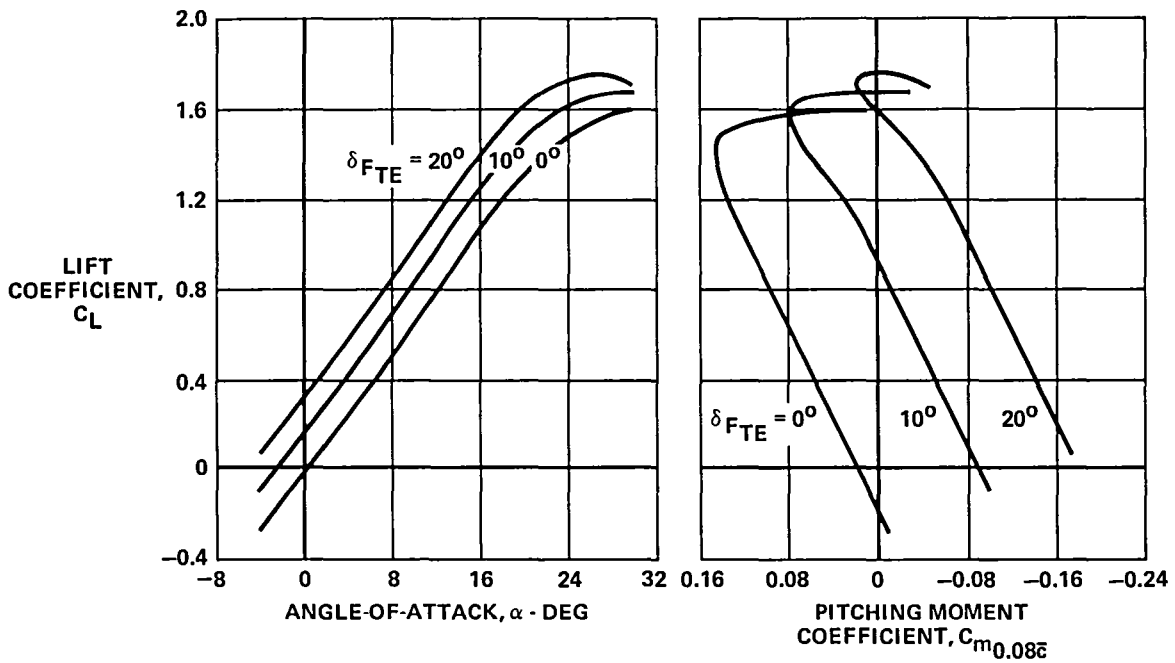
FIGURE 4-27
EFFECT OF TE FLAP DEFLECTION ON LIFT AND PITCHING
MOMENT AT MACH 0.2
$\delta_c = 0°$
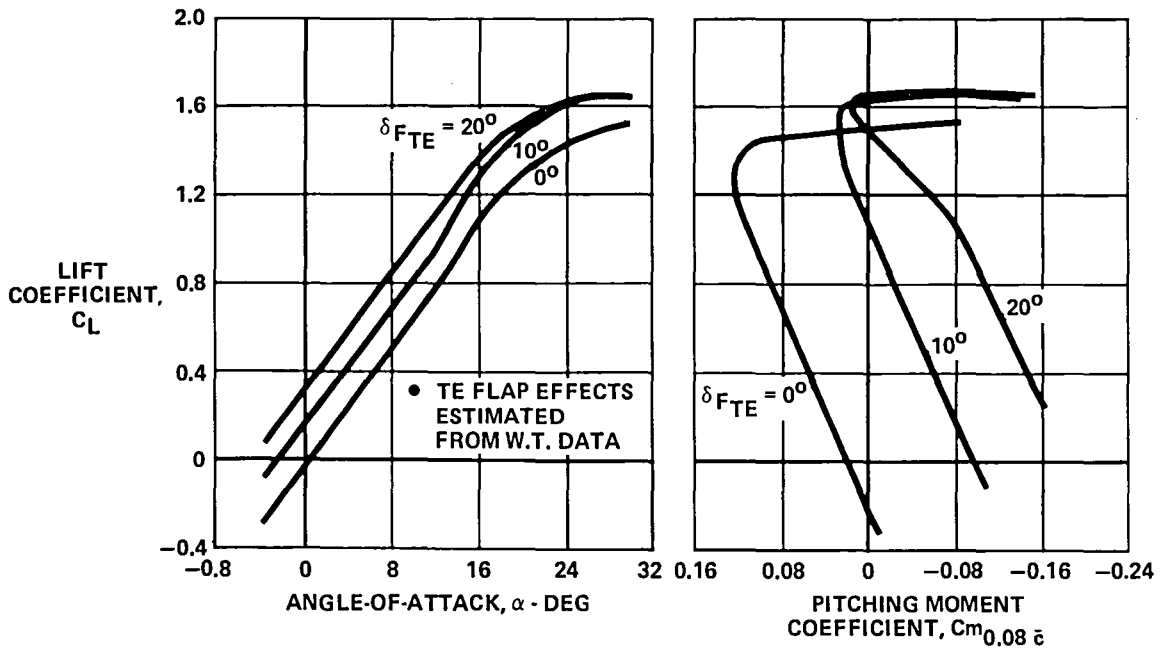
GP13-0983-249

FIGURE 4-28
EFFECT OF TRAILING EDGE FLAPS ON LIFT AND
PITCHING MOMENT AT MACH 0.6
$\delta_c = 0°$
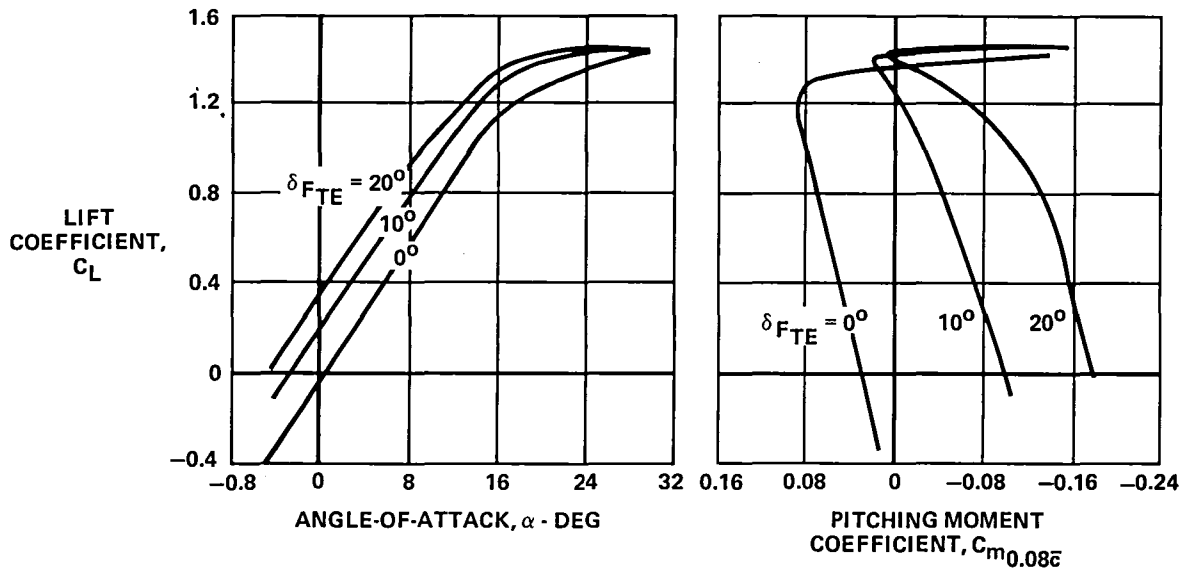
GP13-0983-99

GP13-0983-248

FIGURE 4-29
EFFECT OF TE FLAP DEFLECTION ON LIFT AND PITCHING
MOMENT AT MACH 0.90
$$\delta_c = 0°$$
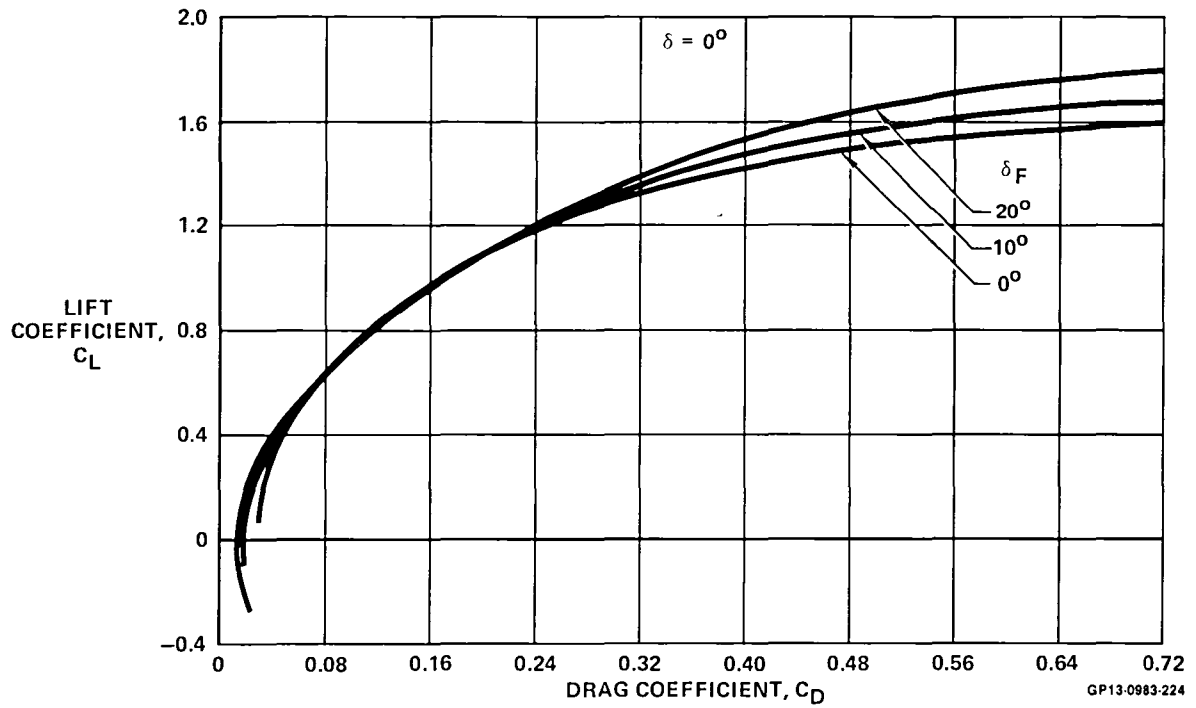
GP13-0983-224

FIGURE 4-30
EFFECT OF TRAILING EDGE FLAP DEFLECTION
ON DRAG CHARACTERISTICS AT MACH 0.2
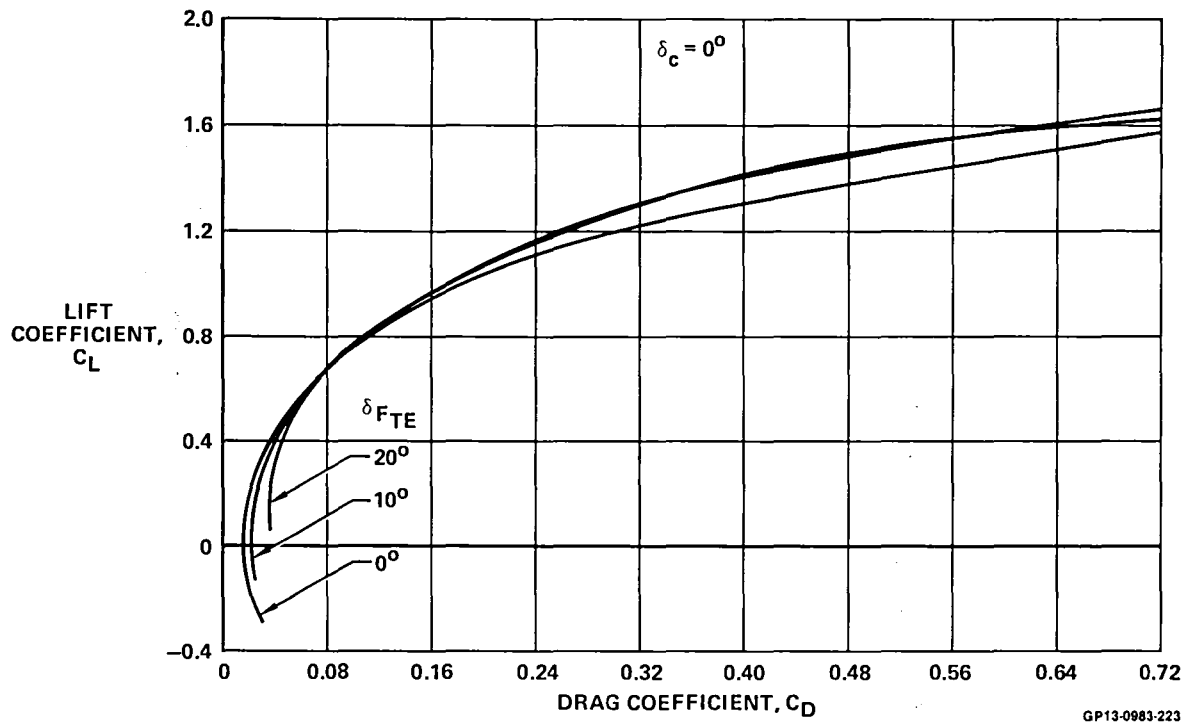
FIGURE 4-31
EFFECT OF TRAILING EDGE FLAP DEFLECTION
ON DRAG CHARACTERISTICS AT MACH 0.6
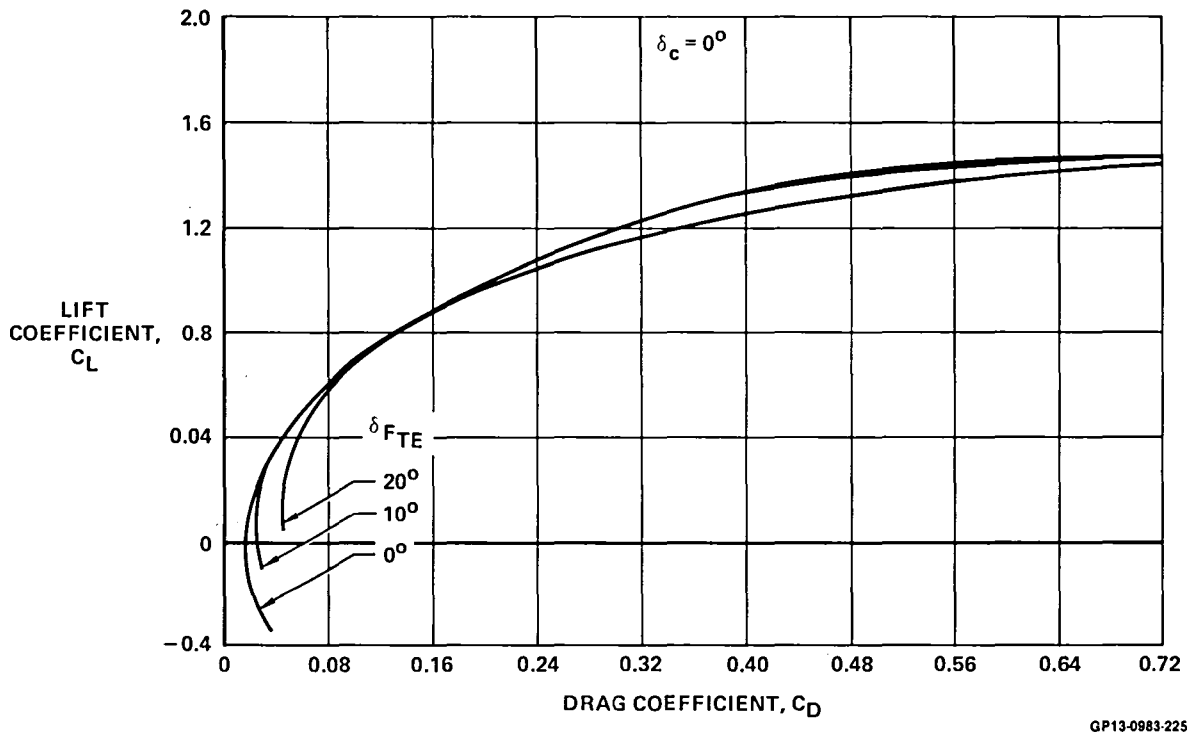
FIGURE 4-32
EFFECT OF TRAILING EDGE FLAP DEFLECTION
ON DRAG CHARACTERISTICS AT MACH 0.9

4-29
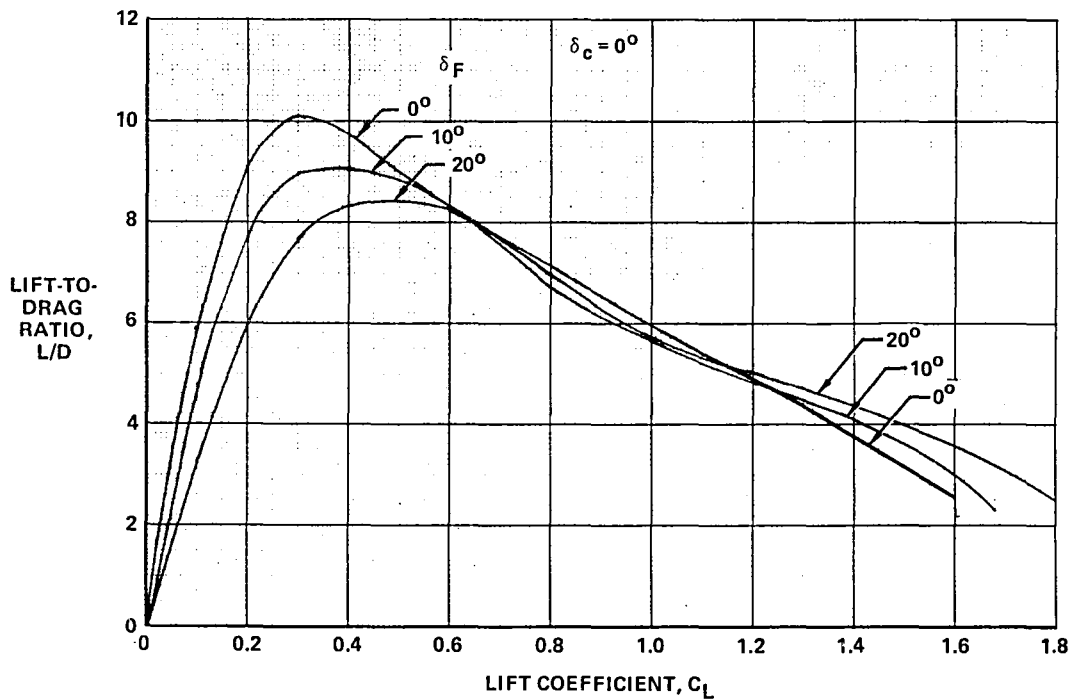
GP13-0983-235

FIGURE 4-33
LIFT-TO-DRAG RATIO WITH TRAILING EDGE FLAP DEFLECTION
Mach 0.2
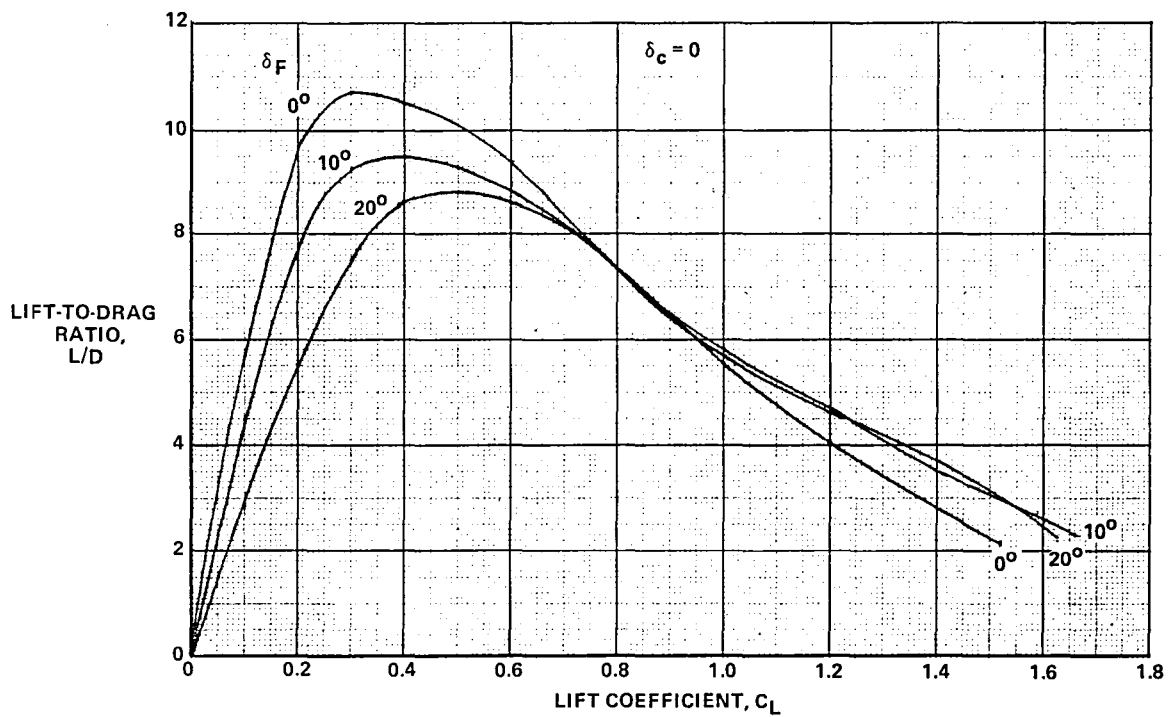
GP13-0983-193

FIGURE 4-34
LIFT-TO-DRAG RATIOS FOR TRAILING EDGE FLAP DEFLECTION
Mach 0.6
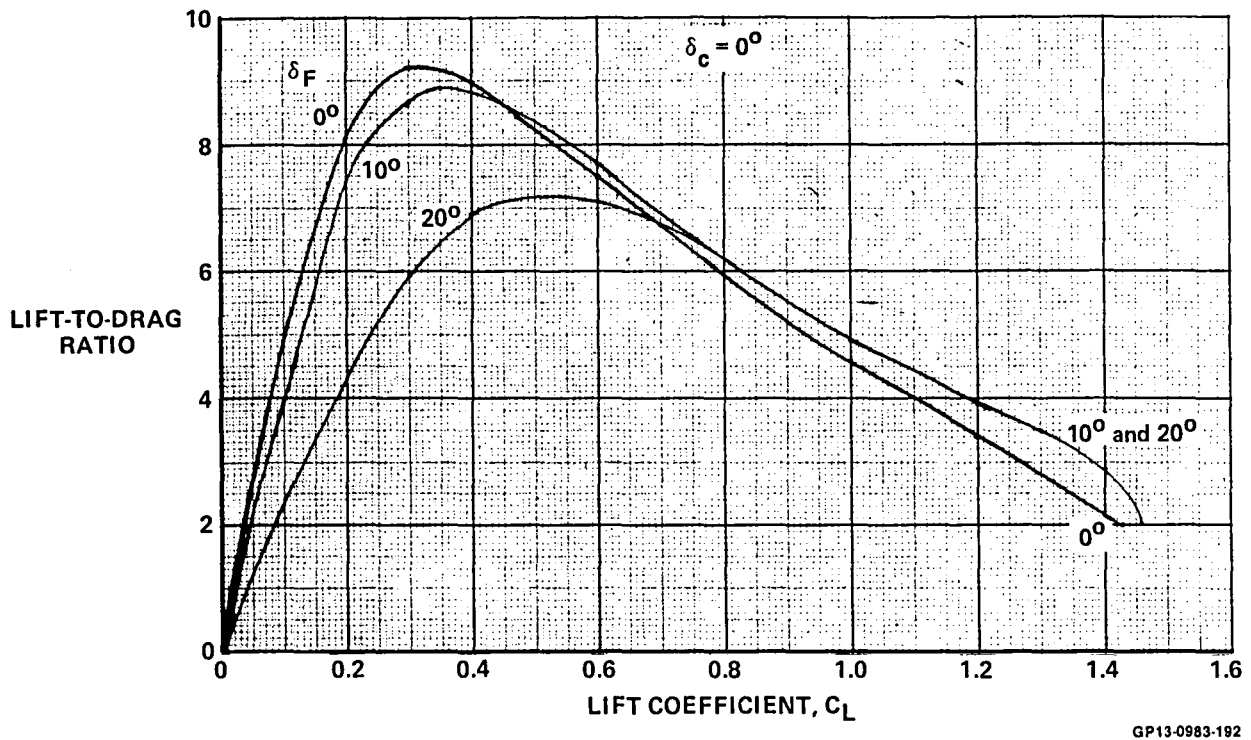
FIGURE 4-35
LIFT-TO-DRAG RATIOS FOR TRAILING EDGE FLAP DEFLECTION
Mach 0.9

GP13-0983-192

4.1.6 <u>TRIM CHARACTERISTICS</u> - Trim characteristics were computed at a center of gravity location of 8.0%c̄ and for two trim conditions: (1) trim with canard alone and (2) trim with a combination of canard and trailing edge flap for minimum drag. The former was computed for all Mach numbers while the latter was computed only in the subsonic region.

For trimming with the canard only ($\delta_F = 0°$), the untrimmed lift, pitching moment, and drag data were used. The resulting trimmed lift curves are presented in Figure 4-36 for all Mach numbers and the trimmed drag polars are presented in Figure 4-37. The trimmed L/D ratios are presented in Figure 4-38.

Figures 4-39 and 4-40 present the trimmed lift and drag at M = 0.2, 0.6 and 0.9 for the combination of canard and trailing edge flap deflections giving minimum trim drag. Figure 4-41 presents the optimum canard and flap deflection schedule for the trimmed characteristics shown in Figures 4-39 and 4-40. Figure 4-42 presents trimmed L/D ratio.

4-31
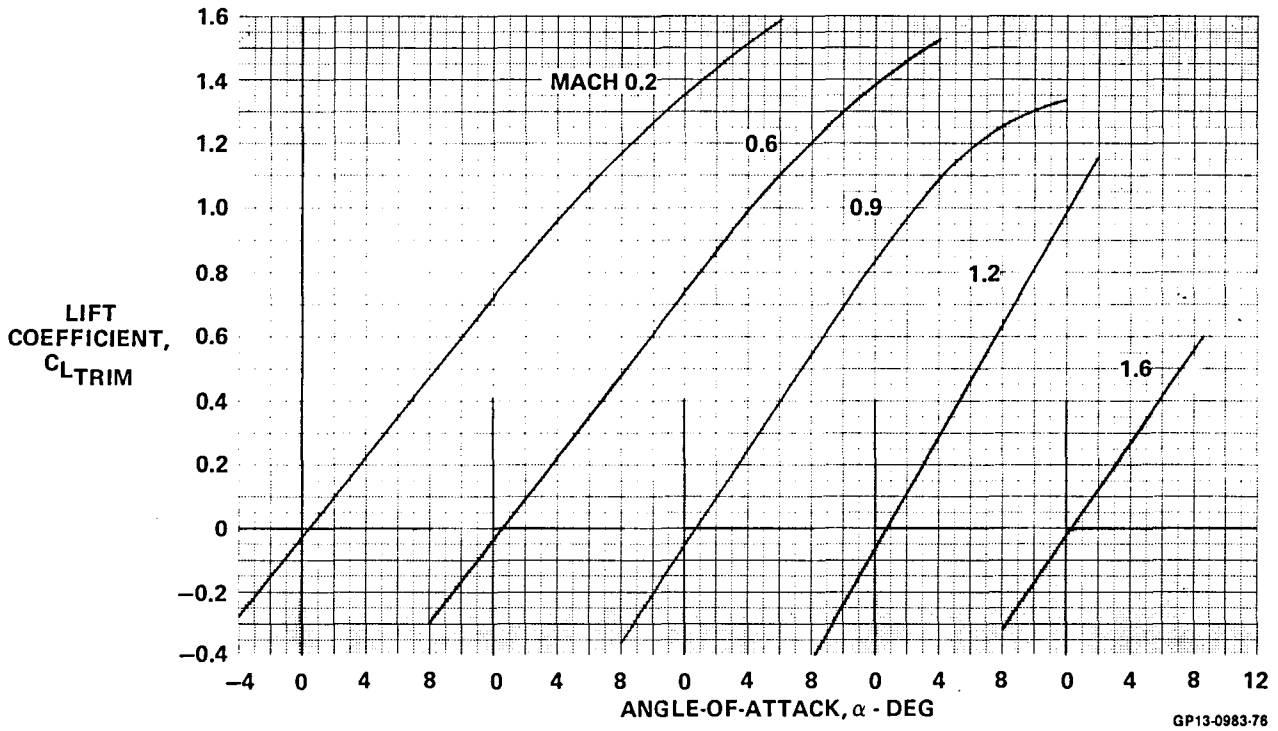
FIGURE 4-36
TRIMMED LIFT CHARACTERISTICS, $\delta_F = 0°$
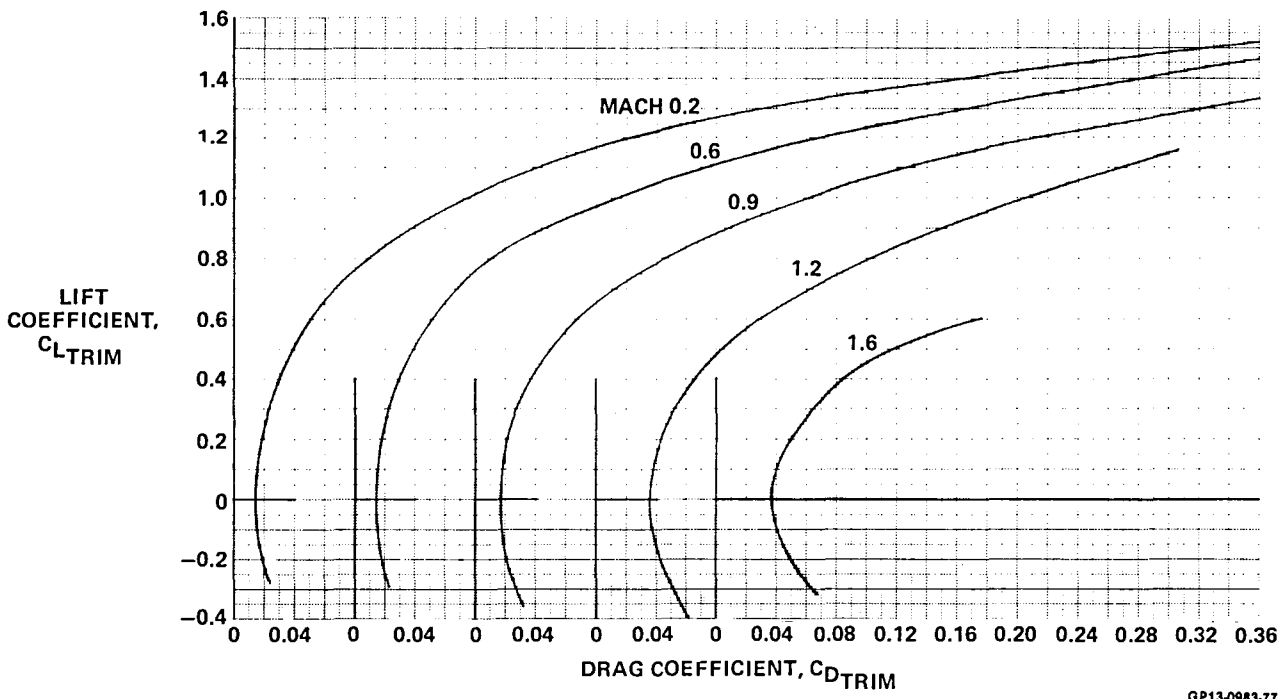
FIGURE 4-37
TRIMMED DRAG CHARACTERISTICS, $\delta_F = 0°$
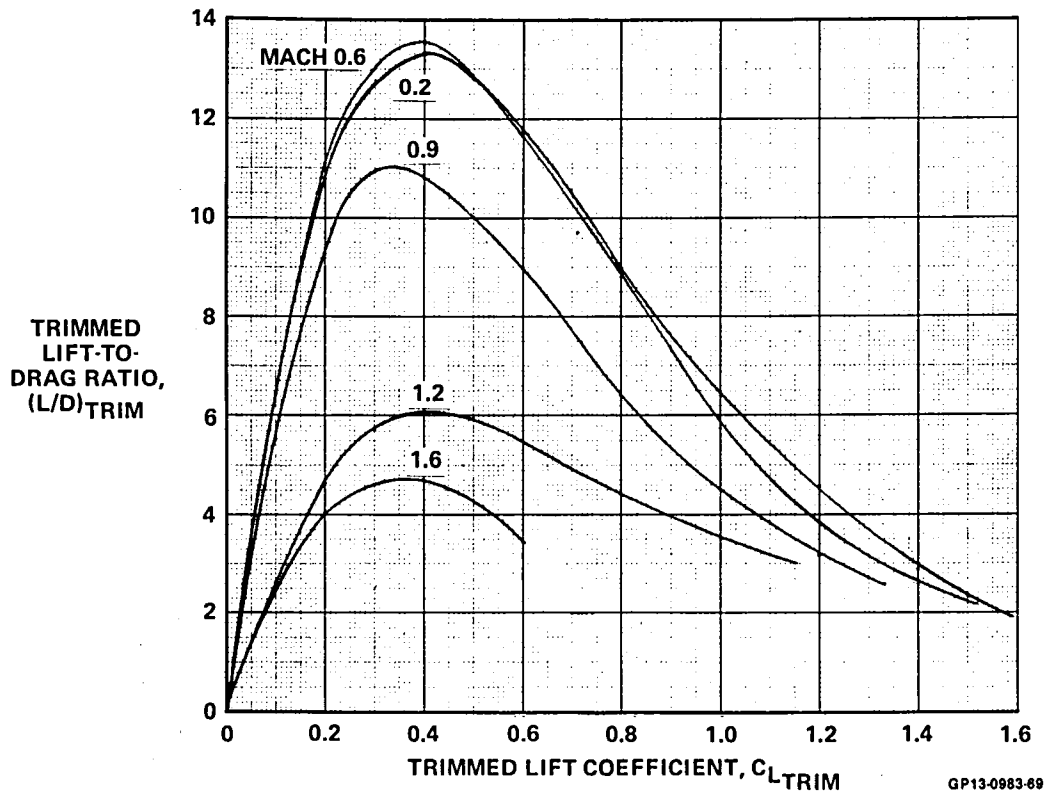
FIGURE 4-38
TRIMMED LIFT-TO-DRAG RATIO
$\delta_F = 0°$
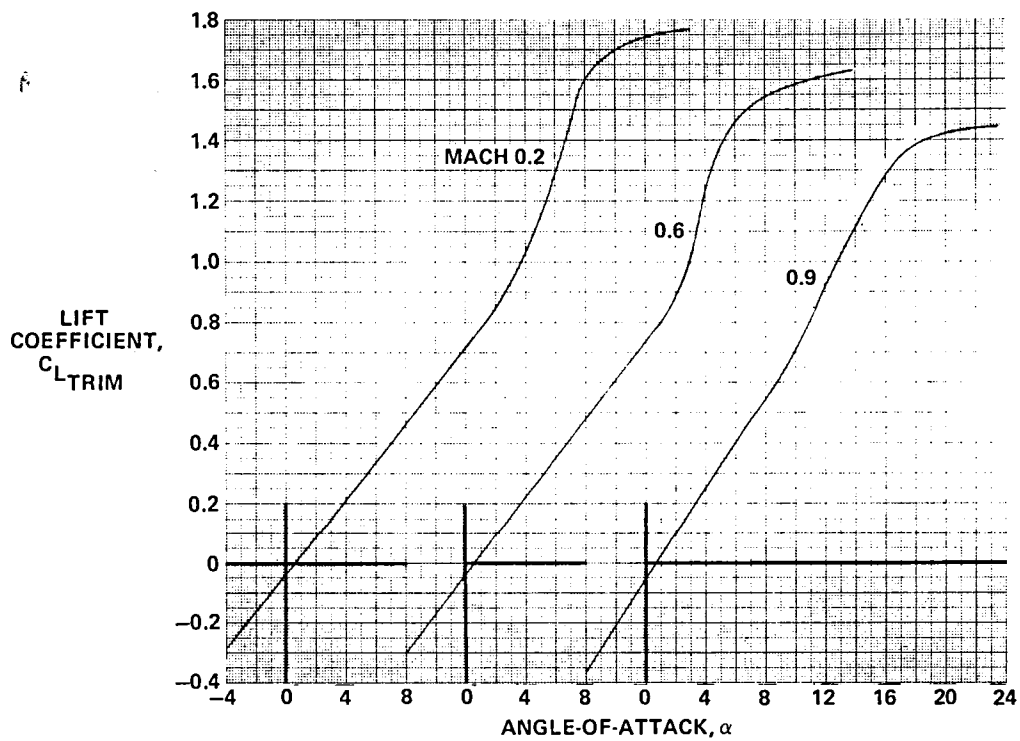
FIGURE 4-39
TRIMMED LIFT CHARACTERISTICS FOR COMBINED FLAP-CANARD TRIMMING
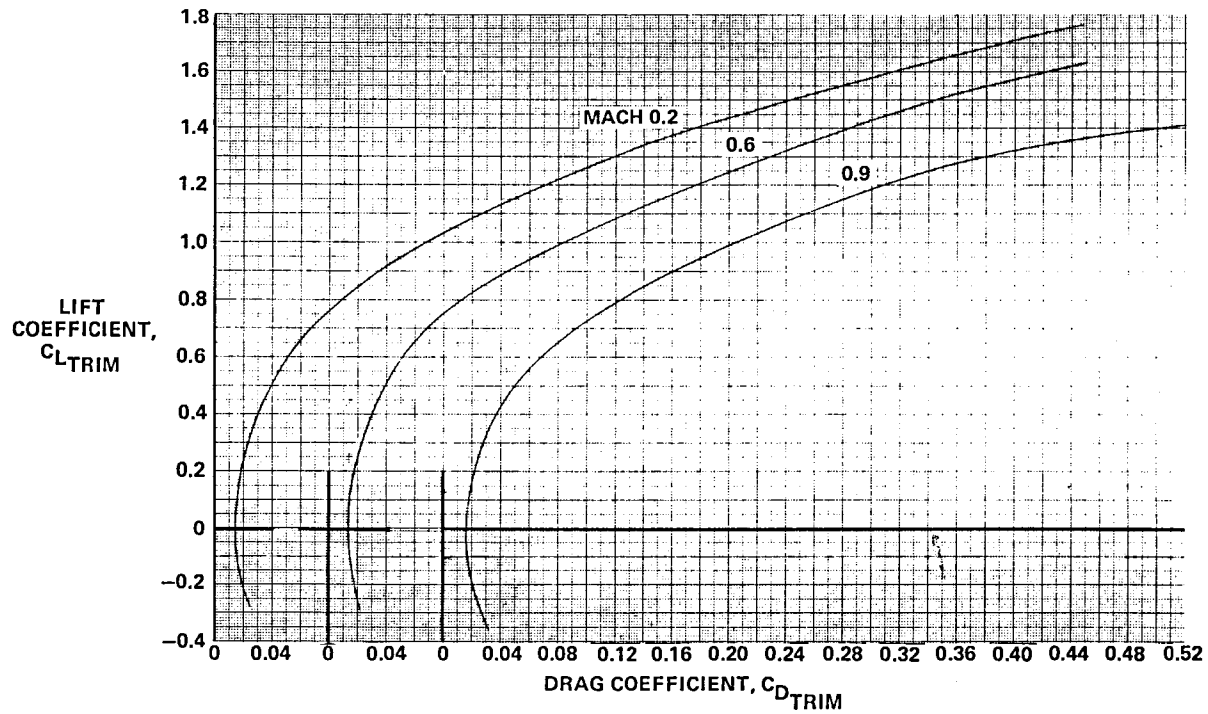
FIGURE 4-40
TRIMMED DRAG CHARACTERISTICS FOR COMBINED FLAP-CANARD TRIMMING
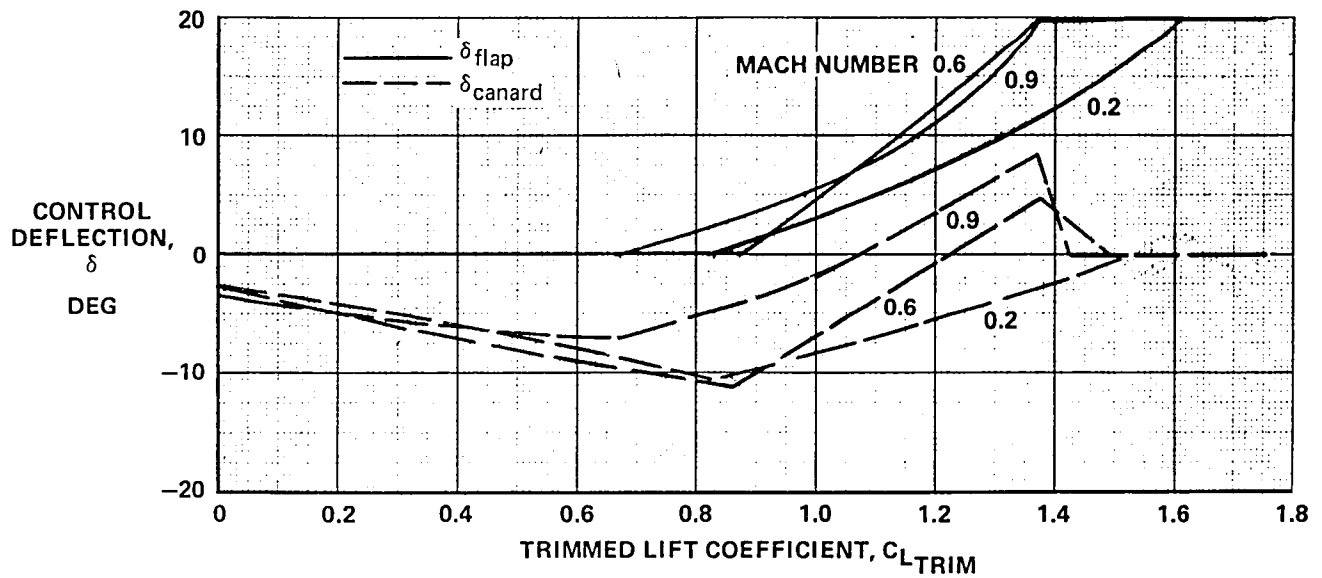
FIGURE 4-41
CANARD-FLAP SCHEDULE FOR MINIMUM DRAG
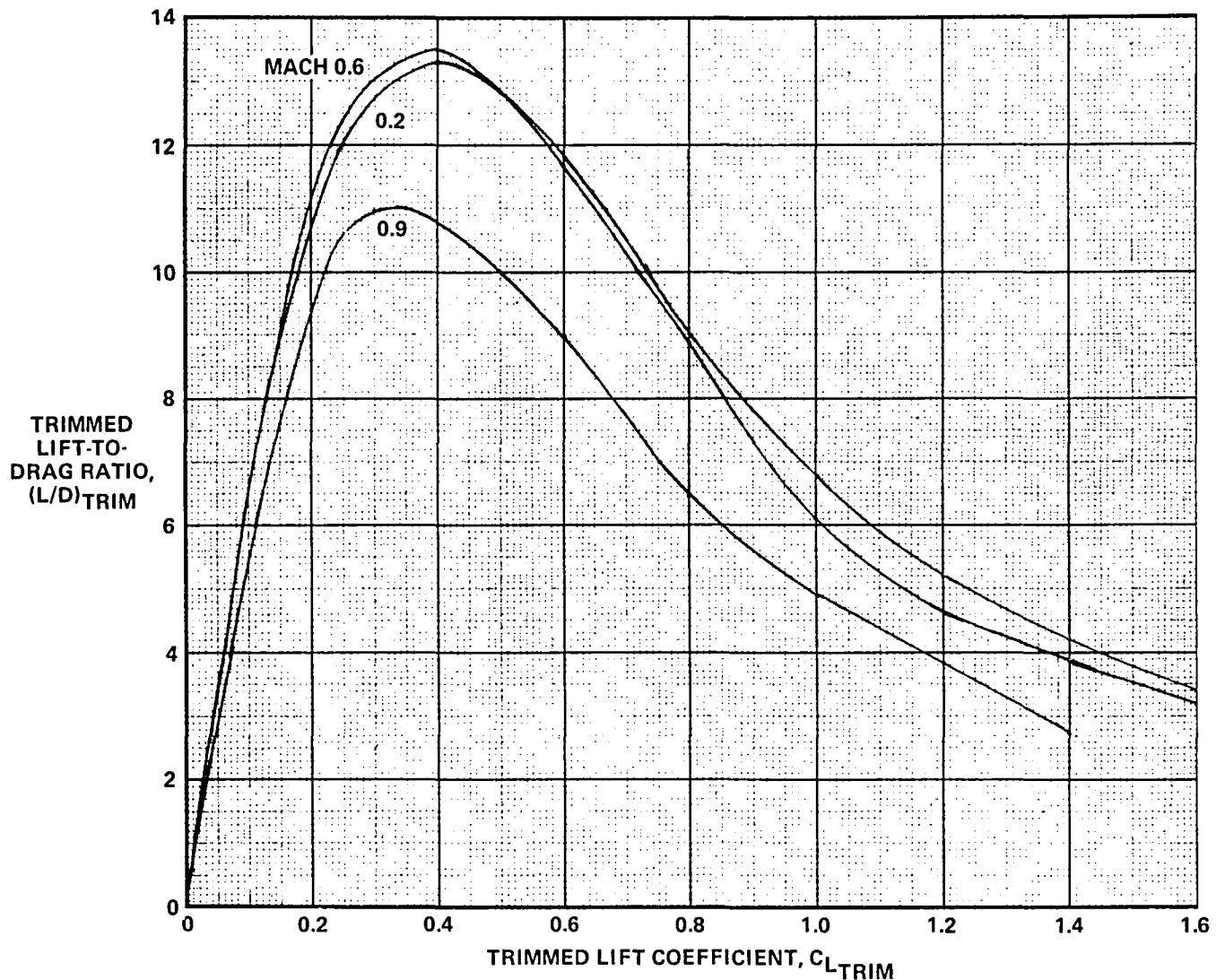
FIGURE 4-42
TRIMMED LIFT-TO-DRAG RATIO FOR FLAP-CANARD TRIMMING

GP13-0983-48

4.1.7 BUFFET ONSET - The lift coefficient for buffet onset is that at which major flow separation occurs on the upper surface of the wing. The MCAIR Semi-Empirical Method presents correlations relating this lift coefficient with wing geometric parameters for wing-body configurations. Wind tunnel data for a canard configuration (MCAIR PSWT Test No. 413) showed the angle of attack for leading edge or trailing edge separation of the wing is not affected significantly by the canard. The angle of attack for major flow separation obtained for the wing-body using the MCAIR Semi-Empirical Method was, therefore, assumed to be the same for the wing-body-canard. The lift coefficients for buffet onset was then taken from Figures 4-11 through 4-13 and are presented in Figure 4-43.
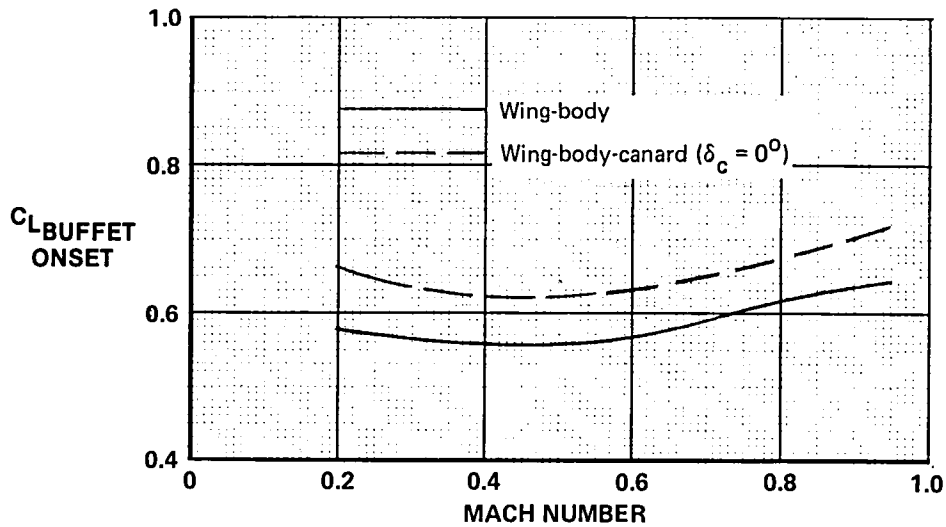
FIGURE 4-43
LIFT COEFFICIENT FOR BUFFET ONSET

4.1.8 <u>MAXIMUM LIFT COEFFICIENT</u> – Figure 4-44 presents the maximum trimmable lift coefficient for trimming with the canard alone ($\delta_F = 0°$) and for trimming with the canard and the trailing edge flap. This figure shows that a substantial increase in maximum trimmable lift coefficient can be achieved in the subsonic region if the trailing edge flap is used.
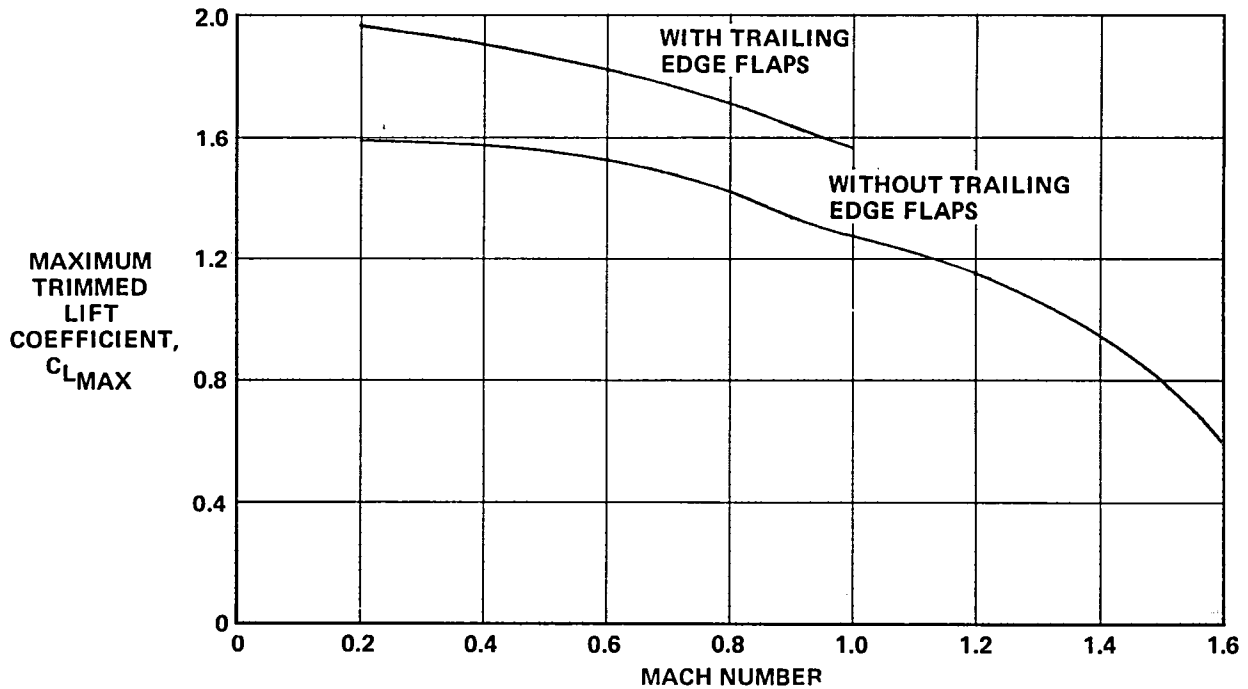
FIGURE 4-44
MAXIMUM TRIMMED LIFT COEFFICIENT WITH AND
WITHOUT TRAILING EDGE FLAPS

4.2 LATERAL-DIRECTIONAL CHARACTERISTICS

The estimated lateral-directional stability and control effectiveness characteristics of the Model 279-3 are presented in this section. Data are presented in body axes at 0.2, 0.6, 0.9, 1.2 and 1.6 Mach number for zero canard deflection. Lateral-directional stability characteristics are presented in terms of the stability derivatives $C_{Y\beta}$, $C_{n\beta}$ and $C_{l\beta}$ as a function of angle of attack. Canard wind tunnel data reviewed showed that side force, yawing moment and rolling moment vary linearly with sideslip angle ($-10° \leq \beta \leq 10°$) up to 30 degrees angle of attack at subsonic and transonic Mach numbers. Current techniques, also, are not capable of predicting nonlinearities with sideslip angle.

4.2.1 LATERAL-DIRECTIONAL STABILITY

The lateral-directional stability derivatives, $C_{Y\beta}$, $C_{n\beta}$, and $C_{l\beta}$, were obtained using DATCOM supplemented by available wind tunnel data for similar configurations. Several other methods for predicting these derivatives, including Vortex-Lattice and PANAIR were investigated. DATCOM correlations, however, gave better agreement with wind tunnel data. The DATCOM correlations are restricted to the linear angle of attack range and do not include canard effects. Available wind tunnel data for similar canard configurations were used to supplement the DATCOM correlations at high angles of attack and to estimate canard effects.

Side Force Derivative - Side force derivative, $C_{Y\beta}$, was obtained from DATCOM by component buildup beginning with the wing-body. To these values were added the contributions of the canard and the vertical tail. The resulting side force derivatives for the configuration were then adjusted for inlet momentum effects. A representative mass flow ratio of 0.75 was assumed.

Wind tunnel data indicate that $C_{Y\beta}$ is essentially independent of angle of attack. Figure 4-45 presents $C_{Y\beta}$ for the Model 279-3 configuration as a function of Mach number and is assumed to be constant with angle of attack. Shown also in Figure 4-45 is $C_{Y\beta}$ with the vertical tail off. This vertical tail increment compares very favorably with wind tunnel data for similar configurations.

Directional Stability - The directional stability derivative, $C_{n\beta}$, for the wing-body at zero angle of attack was obtained directly from DATCOM. The contribution of the vertical tail was obtained by multiplying the vertical tail $C_{Y\beta}$ increment and the vertical tail moment arm. This moment arm is the longitudinal distance from the aircraft moment reference center to the quarter chord of the vertical tail mean aerodynamic chord. The canard effect on $C_{n\beta}$ was estimated from available wind tunnel data. Also the inlet momentum effect on $C_{n\beta}$ was estimated by multiplying the side force component to a moment arm defined as the longitudinal distance from the moment reference center to the face of the inlet. Variation of $C_{n\beta}$ with angle of attack was based on available wind tunnel data.

Figure 4-46 presents the DATCOM computed $C_{n\beta}$ at zero angle of attack as a function of Mach number for both vertical tail on and vertical tail off. The variation with Mach number compares favorably with wind tunnel data for similar configurations. Figure 4-47 presents the estimated Model 279-3
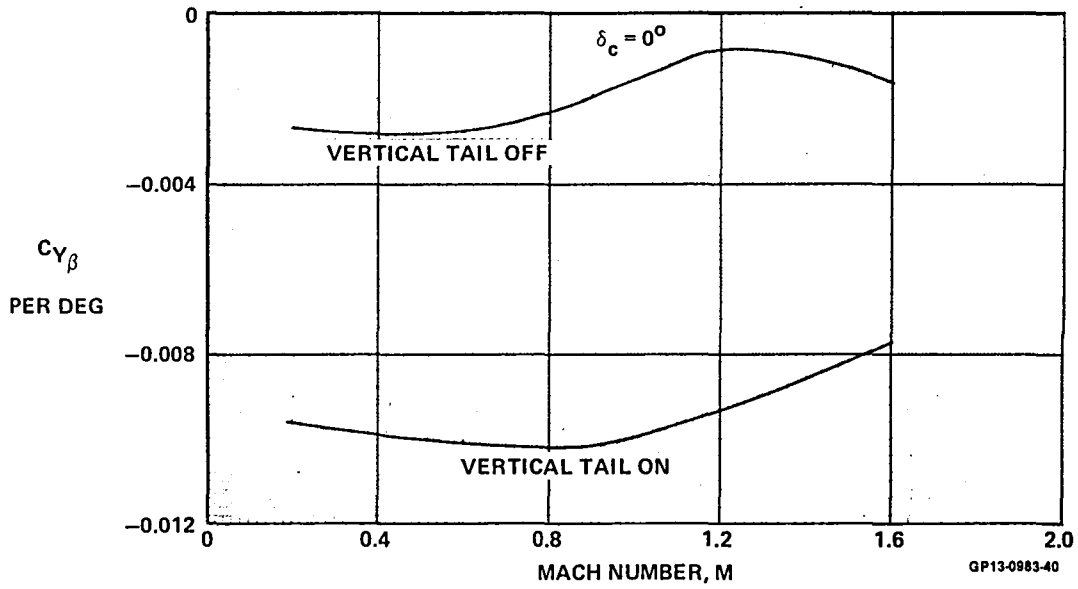
FIGURE 4-45
SIDE FORCE AT ALL α 's
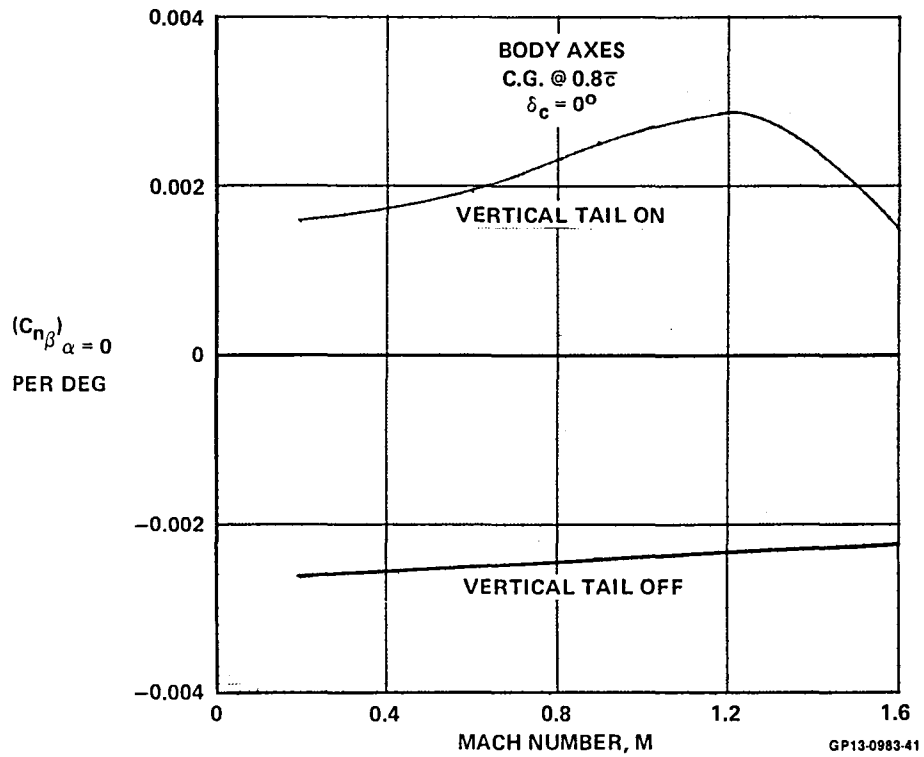
FIGURE 4-46
DIRECTIONAL STABILITY AT $\alpha = 0°$
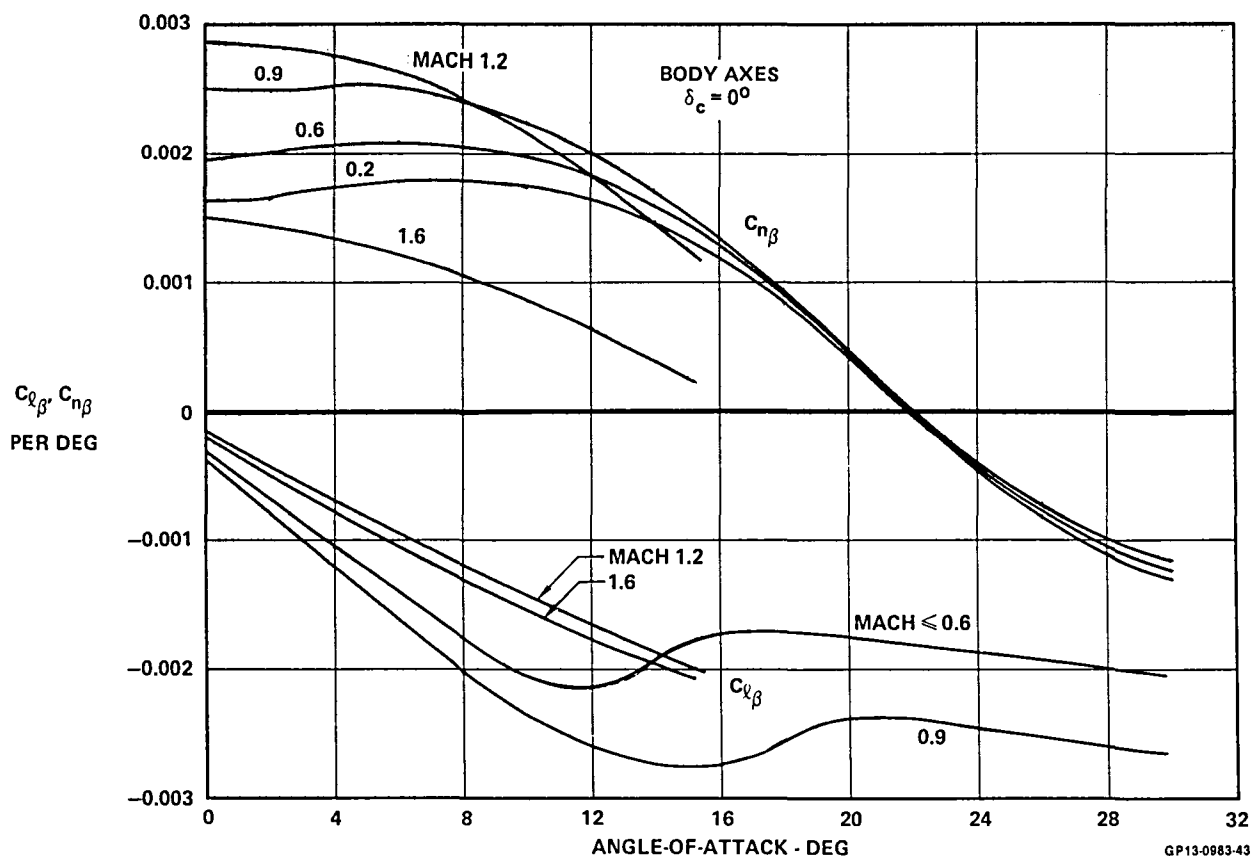
FIGURE 4-47
LATERAL-DIRECTIONAL STABILITY

directional stability as a function of angle of attack at 0.2, 0.6, 0.9, 1.2 and 1.6 Mach number. Positive directional stability at subsonic-transonic Mach numbers is available up to 22 degrees angle of attack.

Lateral Stability – The lateral stability derivative, C_{l_β}, for the wing-body was obtained using DATCOM correlations. These correlations include variations in C_{l_β} as a function of angle of attack. The vertical tail contribution to C_{l_β} was obtained by multiplying the vertical tail C_{Y_β} and the vertical moment arm from the moment reference center to the vertical tail mean aerodynamic chord.

The canard contribution to C_{l_β} was obtained from wind tunnel data. Differences in canard size and moment arm were accounted for in defining the canard contribution. The total Model 279-3 C_{l_β} was obtained by adding the estimated canard increment to the DATCOM defined C_{l_β} for the wing-body-vertical tail. Variation of C_{l_β} with angle of attack was based on characteristics of available canard wind tunnel data.

Figure 4-47 presents the Model 279-3 lateral stability as a function angle of attack and Mach number. Figure 4-48 presents the Model 279-3 lateral stability at zero angle of attack as a function of Mach number for the vertical tail on and off.
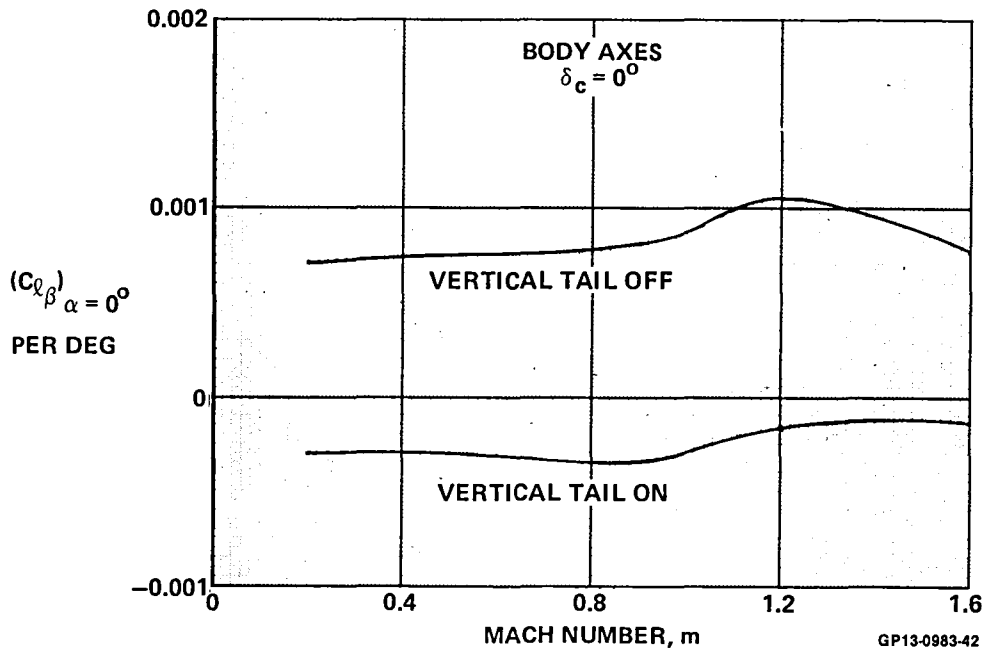
FIGURE 4-48
LATERAL STABILITY AT $\alpha, = 0°$

4.2.2 **LATERAL-DIRECTIONAL CONTROL EFFECTIVENESS** - The available methods for predicting the lateral-directional control effectiveness, including DATCOM, did not compare well with wind tunnel data. Therefore, the Model 279-3 control effectiveness characteristics presented in this section were derived from wind tunnel data.

Lateral Control Effectiveness - Three Surface F-15 wind tunnel data were used to estimate $C_{Y_{\delta_A}}$, $C_{n_{\delta_A}}$ and $C_{l_{\delta_A}}$. Corrections were made to the wind tunnel data to account for differences in the aileron geometry and the lateral moment arm between the wind tunnel configuration and the Model 279-3. Figures 4-49 through 4-51 present the estimated side force, yawing moment and rolling moment aileron control effectiveness derivatives for the Model 279-3. Positive roll control power is available to high angles of attack.

Directional Control - The Model 263 and 279-1 wind tunnel data were used to estimate $C_{Y_{\delta_R}}$, $C_{n_{\delta_R}}$ and $C_{l_{\delta_R}}$. These data were corrected for differences in rudder and vertical tail geometry and the moment arms between the wind tunnel configurations and the Model 279-3. Figure 4-52 presents the Model 279-3 side force, yawing moment and rolling moment control derivatives for rudder deflection. As can be seen from this plot, rudder effectiveness is maintained at high angle of attack at all Mach numbers.

4-40
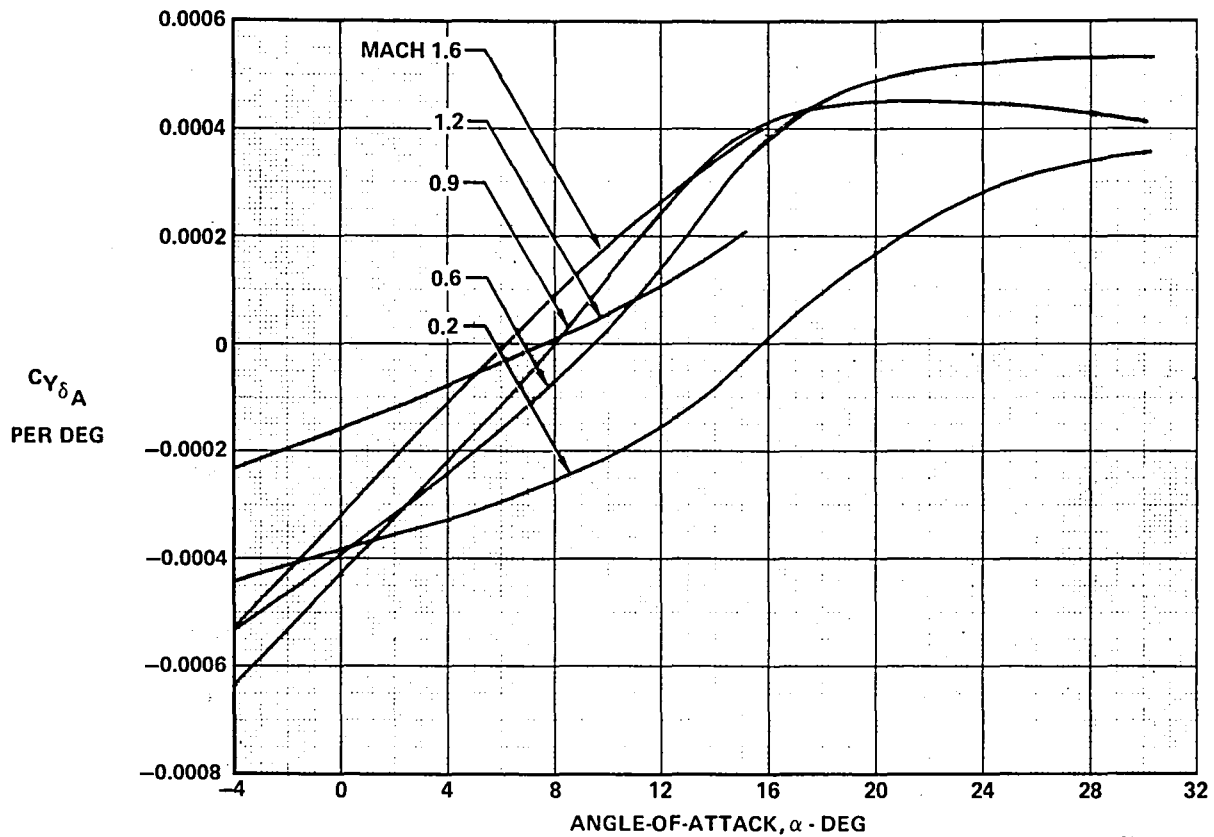
FIGURE 4-49
SIDE FORCE DUE TO AILERON DEFLECTION
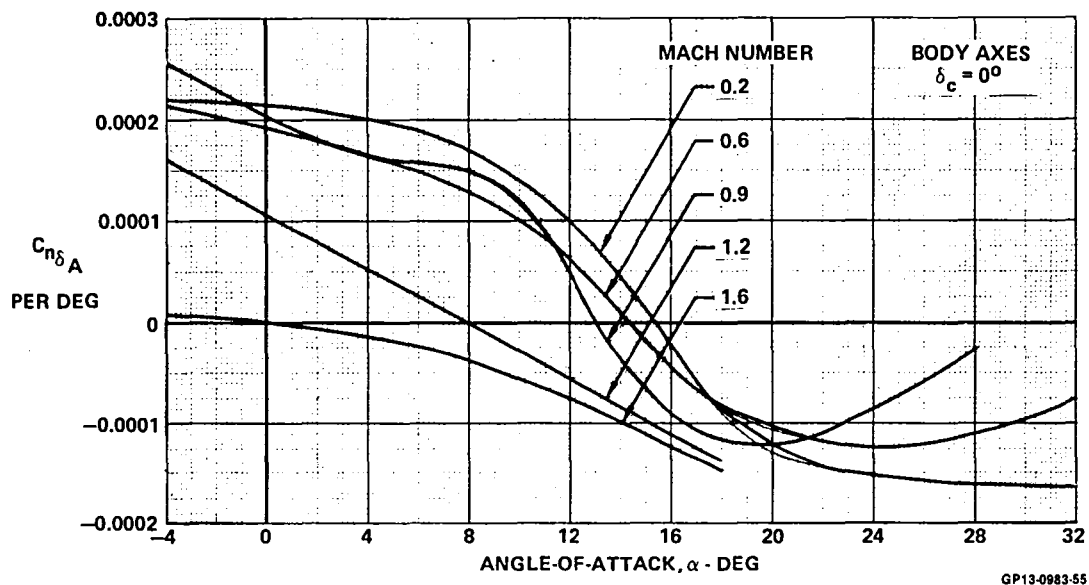
FIGURE 4-50
YAWING MOMENT DUE TO AILERON DEFLECTION
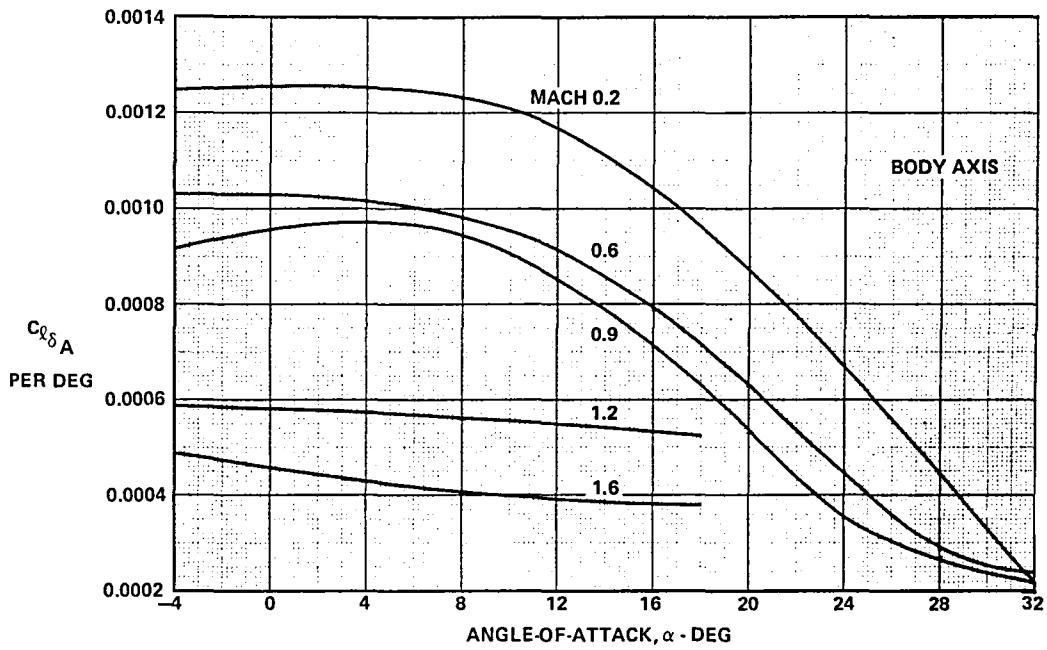
FIGURE 4-51
ROLLING MOMENT DUE TO AILERON DEFLECTION
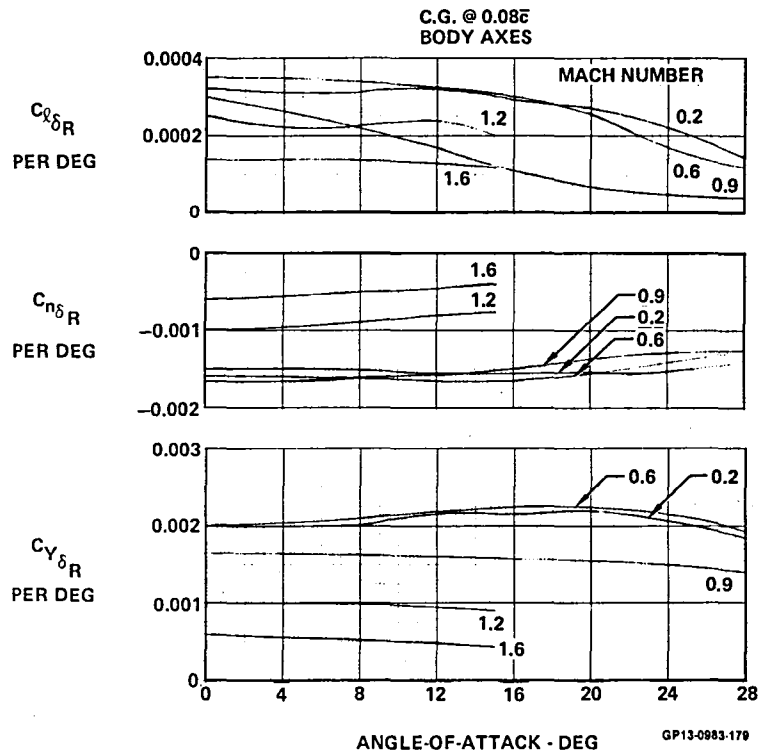
FIGURE 4-52
RUDDER EFFECTIVENESS

4.3 PROPULSION INDUCED EFFECTS

Aerodynamic forces and moments are introduced by the propulsion system through the four nozzle exhaust jets and the inlet momentum. During VTOL operations the exhaust jets interact to produce an upwash flow or fountain. This fountain results in significant forces and moments beneficial to VTOL lift. The lift due to the fountain is enhanced by airframe mounted fences called Lift Improvement Devices (LIDs) that contain and direct the fountain to maximize lift and minimize hot gas ingestion. The exhaust jets also entrain flow from the top of the aircraft and between the aircraft under surface and launching surface, creating a negative lift or suckdown. The fountain and suckdown effects are dependent on proximity to the launching surface. They also vary with aft deflection of the nozzles for STOL operation and transition. Complete definition of these jet effects requires extensive test data for the specific configuration, not available for the Model 279-3. The jet effects presented for the 279-3 are based on MCAIR advanced design techniques using test data correlations of similar aircraft. Test data for the four nozzle Y/AV-8B were used along with data from other models with different nozzle arrangements and aircraft planforms. The inlet momentum effects are based on predicted inlet ram drag values during forward flight, and account for the moments due to turning the inlet flow.

The combined fountain and suckdown effect on lift is shown in Figure 4-53. With the LIDs installed, there is a lift gain, +L/T, at zero main gear height equivalent to 3% of the engine installed gross thrust. The fountain capturing contribution of the LIDs is 8% at zero main gear height.
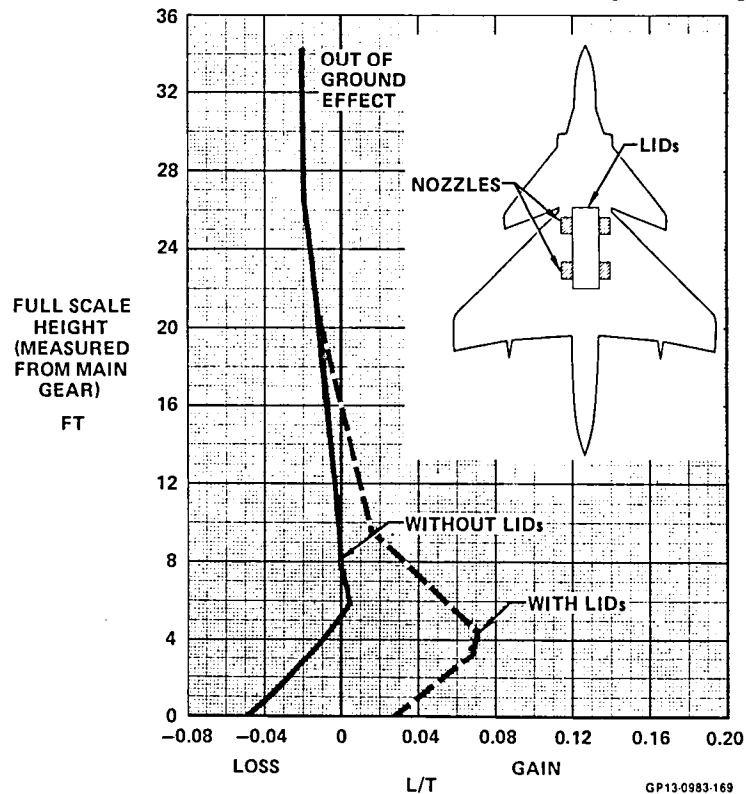
FIGURE 4-53
MODEL 279-3 PREDICTED VTOL JET INDUCED LIFT

The VTOL jet effects were predicted for the Model 279-3 (with and without LIDs) by making separate estimates of fountain and suckdown effects and combining these effects to obtain the net jet-induced lift. Data from a parametric fountain strength test program were used to estimate the fountain effects. The suckdown effects were estimated using available test data from aircraft planforms similar to the Model 279-3. This same technique was used to predict the jet-induced lift of the configuration shown in Figure 4-54. Measured and predicted jet-induced lift for this configuration were in good agreement.
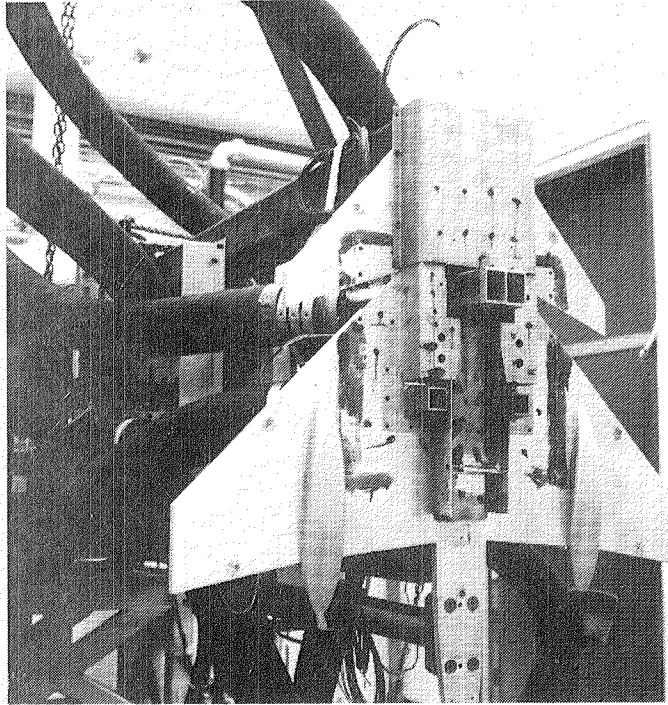
GP13-0983-174

FIGURE 4-54
MODEL 279-4 TEST INSTALLATION IN MCAIR PSTF

The effects of cross winds and transition nozzle deflections are similar to the Reference (28), Section 4, wind tunnel data for the YAV-8B. The powered model mounted in the MCAIR Minispeed Wind Tunnel is shown as Figure 4-55. High pressure air is ducted through the overhead strut. Aerodynamic forces and moments on the model, except for the nozzles, are measured by an internal six component balance.

Partial nozzle deflection is used at relatively low speeds for STOL operation. The influence of nozzle deflection and speed on jet effects can only be determined at the present time from wind tunnel testing. The YAV-8B jet effects trends, Section 4 of Reference (28), should be representative for the Model 279-3, especially in lift. The YAV-8B horizontal tail versus the 279-3 canard may introduce differences in pitching moment trends.
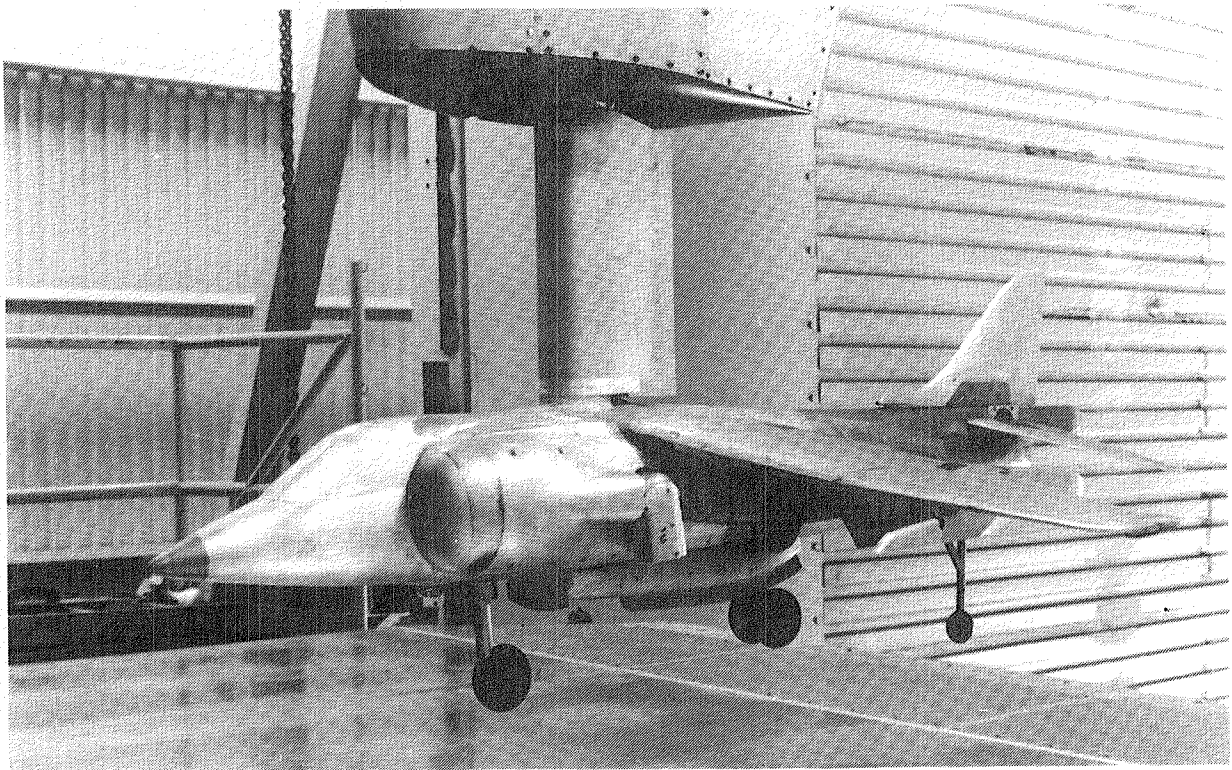
GP13-0983-175

FIGURE 4-55
15% SCALE YAV-8B POWERED MODEL IN MCAIR MINISPEED WIND TUNNEL

    Due to turning the inlet flow, moments are generated on the inlet. These
are a function of the inlet ram drag which is offset from the center of
gravity. The moments vary with angle of attack and sideslip. The inlet
momentum is destabilizing in pitch, Figure 4-56. The effect decreases with
increasing equivalent velocity ratio or aircraft forward speed. Inlet
momentum reduces directional stability, Figure 4-57, but increases the lateral
stability at higher angles of attack. These inlet momentum effects must be
considered in the control system design but can be controlled as evidenced by
flights of the YAV-8B aircraft.
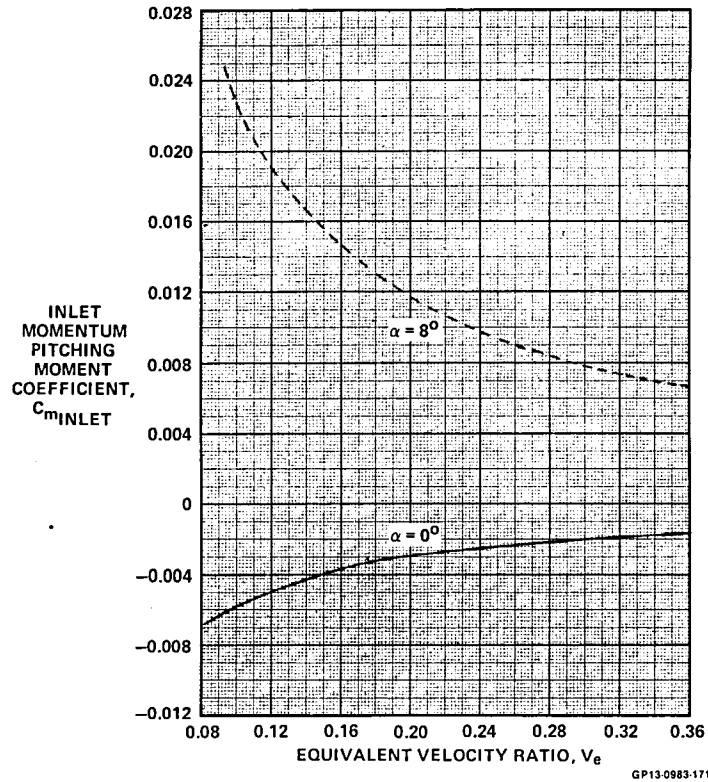
FIGURE 4-56
MODEL 279-3 INLET MOMENTUM PITCHING MOMENT COEFFICIENT
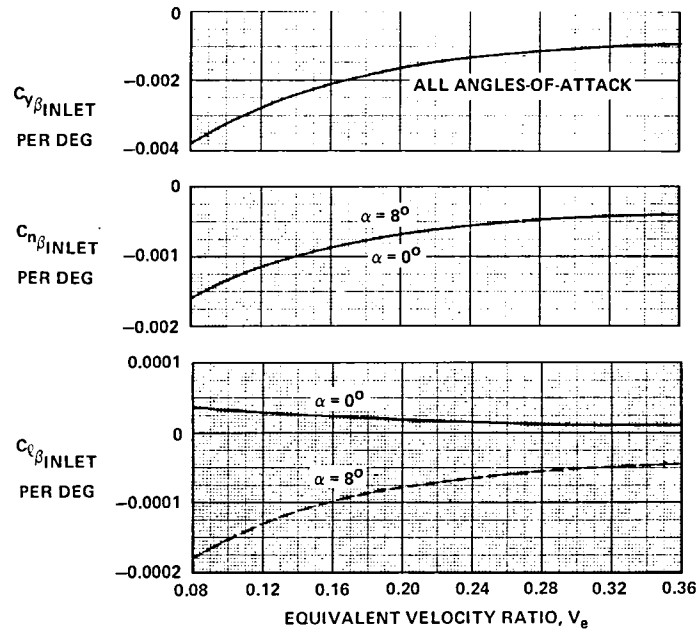
FIGURE 4-57
MODEL 279-3 INLET MOMENTUM LATERAL-DIRECTIONAL EFFECTS

4-46

5. PROPULSION

The design of the propulsion system on a V/STOL aircraft is challenging since it must provide V/STOL lift and control requirements in addition to thrust for acceleration, combat and efficient cruise. The Model 279-3 thrust vectoring engine with fan stream burning matches all these requirements efficiently. This section describes the propulsion system and its performance, the losses assumed due to aircraft installation, the reaction control system (RCS) capability, and the environment created during VTOL.

5.1 PROPULSION SYSTEM DESCRIPTION

A single, advanced technology (post 1990), vectored thrust engine provides the propulsive forces and moments for V/STOL flight. The air induction system has half-axisymmetric inlets and a bifurcated subsonic diffuser. Auxiliary inlets improve total pressure recovery at static conditions and at high angle of attack during flight. Two-dimensional variable area nozzles are used because of their superior airframe integration characteristics. Up to 25% of the high pressure compressor airflow is available to the reaction control system for aircraft control at low speeds where aerodynamic control surfaces are ineffective. Modulation of the fan stream burning and the fan speed are used to control the thrust split between the forward and aft nozzles. This balances the aircraft as the center of gravity shifts due to fuel use or expenditure of stores.

5.1.1 ENGINE – The advanced technology lift/cruise vectored thrust engine is a separated flow turbofan with two forward (fan flow) and two aft (core flow) variable area, two dimensional (2-D) vectoring nozzles. Fan flow thrust may be augmented by a Fan Stream Burner (FSB) in each forward nozzle for V/STOL operation and supersonic flight. The engine is a Pratt & Whitney Aircraft (P&WA) conceptual design designated STF561-C2. Maximum use is made of composite materials in the fan stream burner and nozzles to minimize weight. A more detailed description is precluded by its proprietary nature.

The cycle selected for this engine, together with the characteristics of FSB, provide attractive and matched V/STOL and supersonic performance without sacrificing subsonic cruise SFC. The fan stream burner operates much like a conventional afterburner, providing a wide range of thrust variation. In VTO, FSB temperature limit is 3390°F. During wingborne flight, maximum augmentation temperature is 3500°F. Engine cycle characteristics and physical characteristics are shown in Figure 5-1.

The four nozzles on the STF561-C2 engine are two-dimensional (2-D), convergent-divergent (C-D), fixed shroud ejector types with variable throat area. Approximately 3% secondary ambient airflow is pumped through the ejector shroud. Although the primary purpose of the secondary flow is to augment the engine thrust, it also cools the ejector shroud.

$F_{N_{TOTAL}}$: 34,316 LB* (T/W = 1.15)

THRUST SPLIT: FWD 61%, AFT 39%*

BPR = 1.16
FPR = 3.50
OPR = 25.0
CET_{MAX} = 3,200°F

$T_{FSB_{VTO}}$ = 3,390°F

$T_{FSB_{MAX}}$ = 3,540°F (MACH 2.0/25,000 FT)
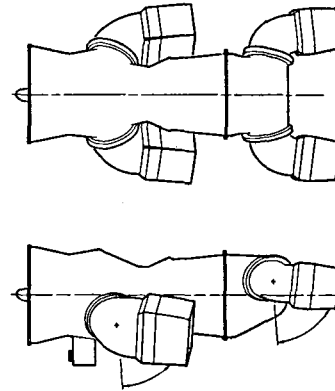
*Installed VTO performance (90°F day)

GP13-0983-124

FIGURE 5-1
P&WA STF561-C2
ADVANCED TECHNOLOGY TURBOFAN ENGINE

5.1.2 INLET – The inlet is a fixed, half-axisymmetric, single compression surface configuration. This inlet is configured with an auxiliary inlet to improve performance at static and high angle-of-attack conditions. The main inlet, shown in Figure 5-2, was selected because of its good airframe integration, with good pressure recovery performance, low drag and light weight. The design Mach number was set at 2.0, the approximate maximum Mach number capability of the aircraft. The 16.5° cone semivertex angle was selected as the best tradeoff between transonic acceleration and high speed (M = 2.0) performance. Although the subsonic diffuser has an offset of 22%, good performance is expected because of the low expansion ratio (1.17), low divergence angle (6°), short length and small cross sectional area change.
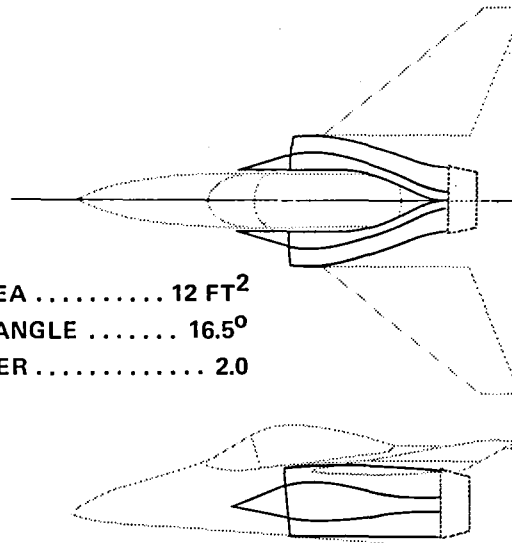
TOTAL CAPTURE AREA . . . . 12 FT^2
CONE SEMI-VERTEX ANGLE . . . . 16.5°
DESIGN MACH NUMBER 2.0

GP13-0983-184

FIGURE 5-2
BIFURCATED HALF-AXISYMMETRIC INLET

The auxiliary inlet is a translating cowl design shown in Figure 5-3. Only the upper half of the cowl translates forward. With the lower half of the inlet fixed, ingestion of the hot exhaust flow during VTOL is minimized. The auxiliary inlet is sized to allow approximately 50% of the engine airflow to enter through the translated cowl at static conditions. An auxiliary inlet contraction ratio of 1.25 and low inlet Mach number maximizes total pressure recovery and minimizes engine face pressure distortion. Alternative designs, such as the actuated longitudinal door shown in Figure 5-3, have also been studied.

a. TRANSLATING COWL

b. "LONGITUDINAL" OVERHEAD DOOR

TRANSLATING QUADRANT
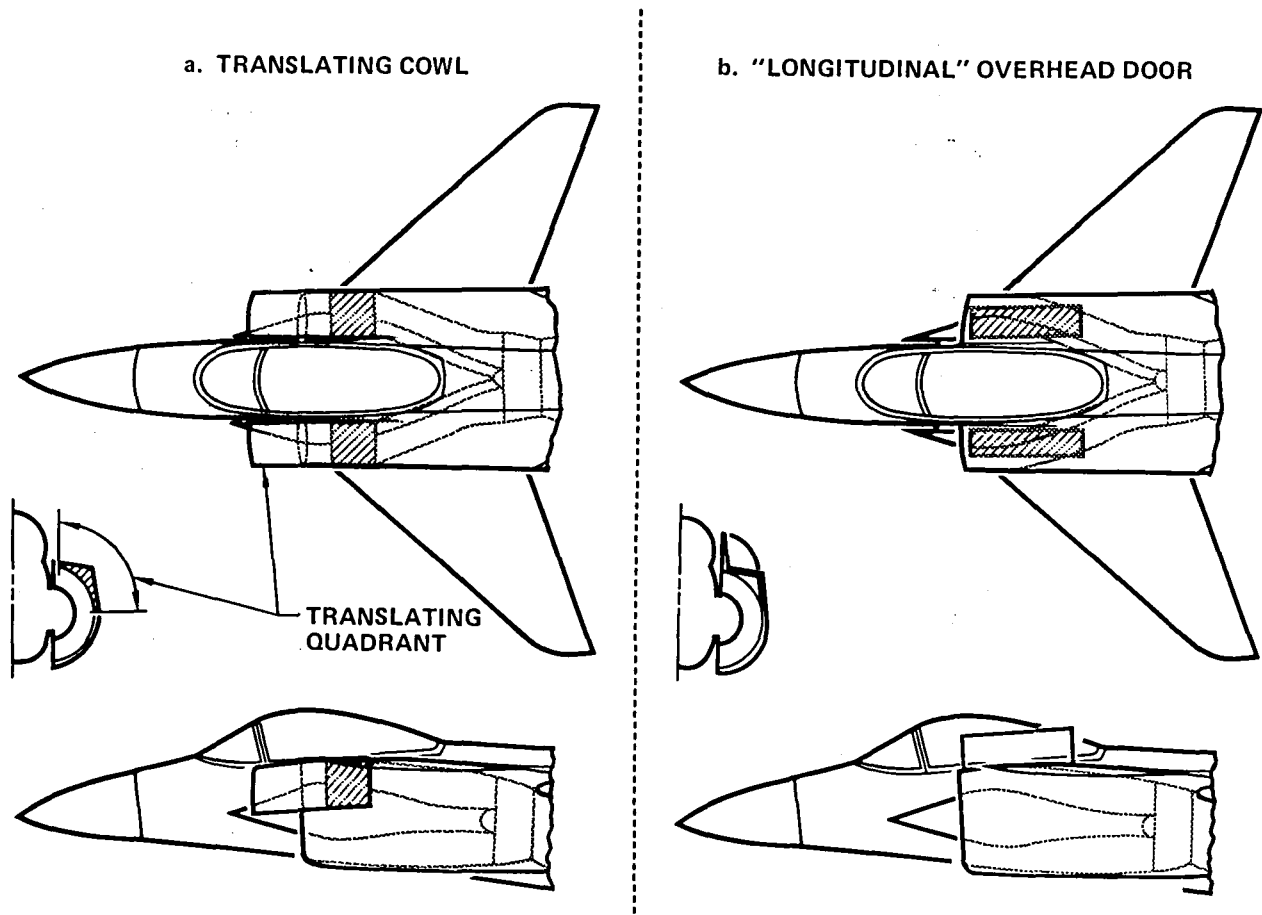
GP13-0983-236

FIGURE 5-3
AUXILIARY INLET DESIGNS

5.2 PROPULSION SYSTEM PERFORMANCE

The propulsion system performance was predicted analytically using the Pratt & Whitney Aircraft (P&WA) advanced V/STOL turbofan computer deck, CCD 1179-1.1, and standard MCAIR installation techniques. This section describes the assumptions and procedures used in generating the installed propulsion system performance and the results.

5.2.1 THRUST DRAG ACCOUNTING SYSTEM – The thrust drag accounting system used in this study provides a convenient transition from wind tunnel measurements to aircraft performance prediction. Included in the aerodynamic drag are all drag forces on the aircraft when 1) the inlet is operating at capture ratio (A_o/A_c) of 1.0, and 2) the nozzles are operating full open and at an exit pressure ratio (P_{exit}/P_o) of 1.0. Included in the net propulsive force, NPF, are any changes in aircraft drag due to inlet and nozzle variations from the reference conditions defined above.

The inlet drag is the incremental change from a capture ratio of 1.0 to the actual inlet operating point, and includes any change in aircraft forebody and inlet cowl drag. In addition, not all of the air which enters the inlet enters the engine. Air used for inlet ramp and throat bleed, ECS extractions, inlet leakage and engine compartment cooling must be accounted for. The drag associated with bringing the air on board without gaining appreciable thrust is charged against the inlet. Due to this airflow drag and cowl lip drag, inlet drag will not be zero even at A_o/A_c of 1.0.

The nozzle drag accounting system is similar to the inlet system. However, instead of one independent variable (A_o/A_c), there are two $(A_{exit}$ and $P_{exit}/P_o)$. Of these two variables, the exit area, A_{exit}, has the largest effect since projected area and boattail angle vary with exit area.

5.2.2 BLEED AND POWER EXTRACTIONS – Engine bleed and horsepower extractions are presented in Table 5-1. Engine bleed air is extracted at the compressor exit to power the ECS and, at low speed, to provide ejector flow for inducing ambient air through ECS heat exchangers. The RCS bleed air is handled separately. Horsepower is extracted from the high pressure spool to drive the aircraft electrical generator and hydraulic pumps.

TABLE 5-1
INSTALLATION LOSSES AND FACTORS

INSTALLATION FACTOR	VTO	CRUISE
INLET TOTAL PRESSURE RECOVERY	0.965	SEE FIGURE 5-4
COMPRESSOR BLEED (LBM/SEC)	1.2	$1.2^{(1)}$ $0.6^{(2)}$
HORSEPOWER EXTRACTION	200	200
SPLAY ANGLES	6° FRONT 0° REAR	6° FRONT 6° REAR
VECTOR ANGLES	90° FRONT 90° REAR	6° FRONT 6° REAR
PERCENTAGE OF INLET FLOW ALLOWED FOR ECS, LEAKAGE AND ENGINE COMPARTMENT COOLING	3%	3%

GP13-0983-36

(1) $M_o < 0.25$

(2) $M_o \geqslant 0.25$

5.2.3 <u>NOZZLE VECTOR AND SPLAY</u> - Nozzle vector angle is the angle between aircraft centerline and nozzle exhaust flow vector in side view. Splay angle is the angle between the nozzle exhaust flow vector and a vertical line in front view. In VTO, front and rear nozzles are vectored 90° down, the rear nozzles are vertical (no splay) and the front nozzles are splayed 6° toward the aircraft centerline. This splay converges the front jets at an aircraft height of 10 feet above the ground to minimize hot exhaust gas ingestion. In conventional flight, both front and rear nozzles are vectored 6° down and splayed 6° out to keep the hot exhaust jets away from the aircraft. Of course, gross thrust calculations reflect the trigonometric losses associated with vector and splay angles.

5.2.4 <u>INLET EFFECTS</u> - Inlet effects analyzed include recovery and drag. Inlet total pressure recovery at zero angle-of-attack is presented in Figure 5-4. Included in this recovery is the effect of the auxiliary inlets, which are required to provide the .965 static recovery.

- MAXIMUM ALLOWABLE AIRFLOW
- AUXILIARY INLET EFFECT INCLUDED
- ZERO ANGLE-OF-ATTACK AND SIDESLIP
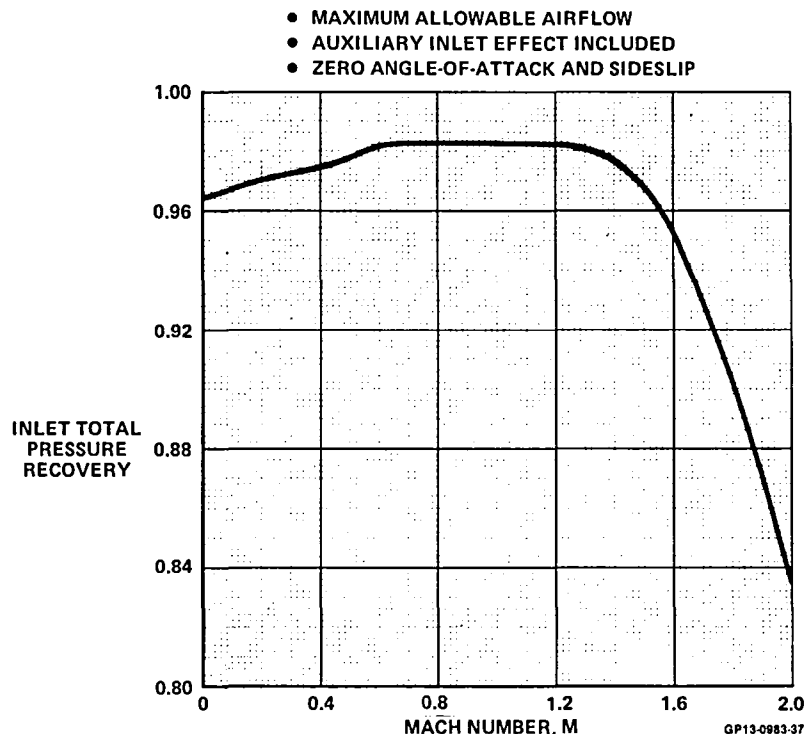
FIGURE 5-4
INLET TOTAL PRESSURE RECOVERY

A representative plot of the inlet drag is presented in Figure 5-5. Two inlet drag curves are plotted; one for the engine operating at maximum power, and one for flight idle. The flight idle curve is typically presented only for subsonic Mach numbers because inlet "buzz" precludes reduced airflow operation supersonically. As shown, idle power inlet drag is generally higher than maximum power drag due to increased inlet spillage.

- 36,089 FT ALTITUDE
- ZERO ANGLE-OF-ATTACK AND SIDESLIP
- INCREMENTAL DRAG FROM $A_0/A_c = 1.0$
- REFERENCED TO A_c

PROPULSION INCREMENTAL INLET DRAG COEFFICIENT, ΔC_{D_I}

MACH NUMBER, M
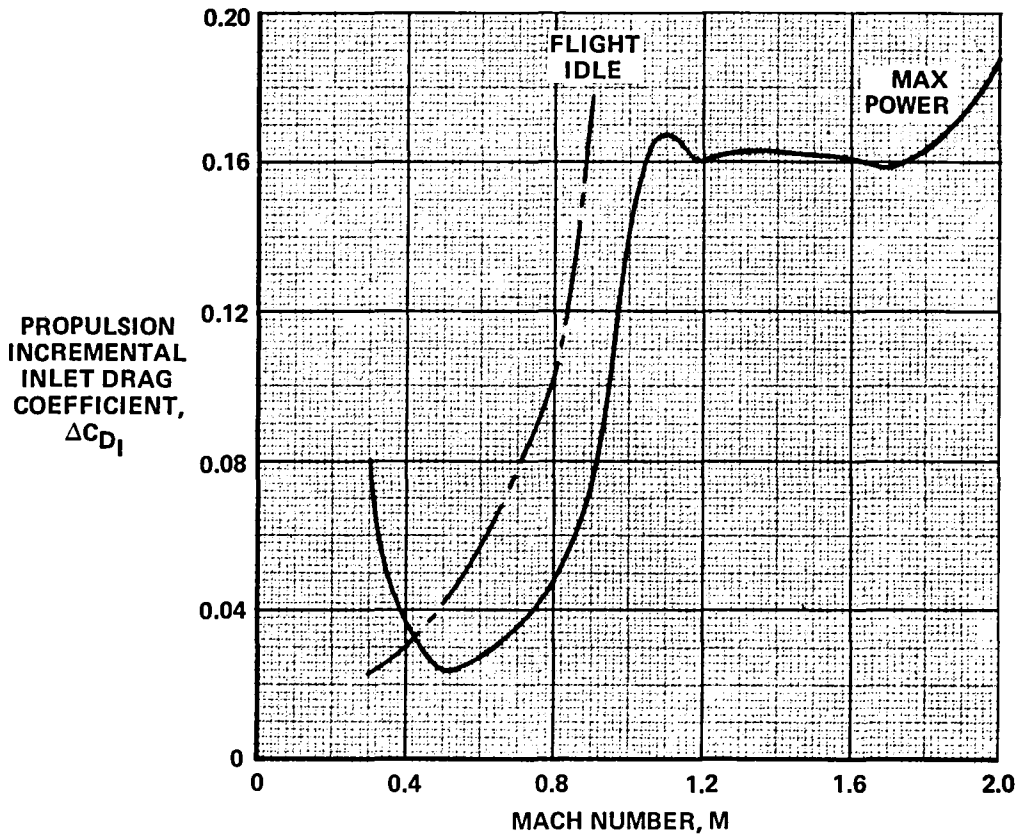
GP13-0983-31

FIGURE 5-5
INLET DRAG COEFFICIENT

5.2.5 NOZZLE DRAG - A representative plot of the nozzle drag included in the engine net propulsive force performance is presented in Figure 5-6. The drag levels shown are quite small as a result of the design of the nozzles and the thrust/drag accounting system. The nozzles, as described in Section 5.1 above, are of the fixed shroud, ejector type, which results in a fixed exit area and a small rear projected area. Since exit area is fixed in the P&WA C-D nozzle, the only propulsion charged nozzle drag is due to exit static pressure ratio (P_{exit}/P_0) variation from 1.0. The drag due to pressure ratio change is small, as reflected in Figure 5-6. The penalty paid for the fixed shroud, ejector nozzle is in internal performance (C_V) at small throat area, low nozzle total pressure ratio (NPR). At these conditions, the nozzle flow is unable to fill the entire exit area due to overexpansion of the jet and the flow separates from the expansion walls. This separation results in an internal nozzle performance penalty which is reflected in engine thrust, but has minimal effect on nozzle drag.

5-6

- MAXIMUM POWER
- 36,089 FT ALTITUDE
- INCREMENTAL DRAG FROM $P_{EXIT}/P_0 = 1.0$

NOZZLE DRAG, $\Delta D/q$ FT^2

MACH NUMBER, M

GP13-0983-30
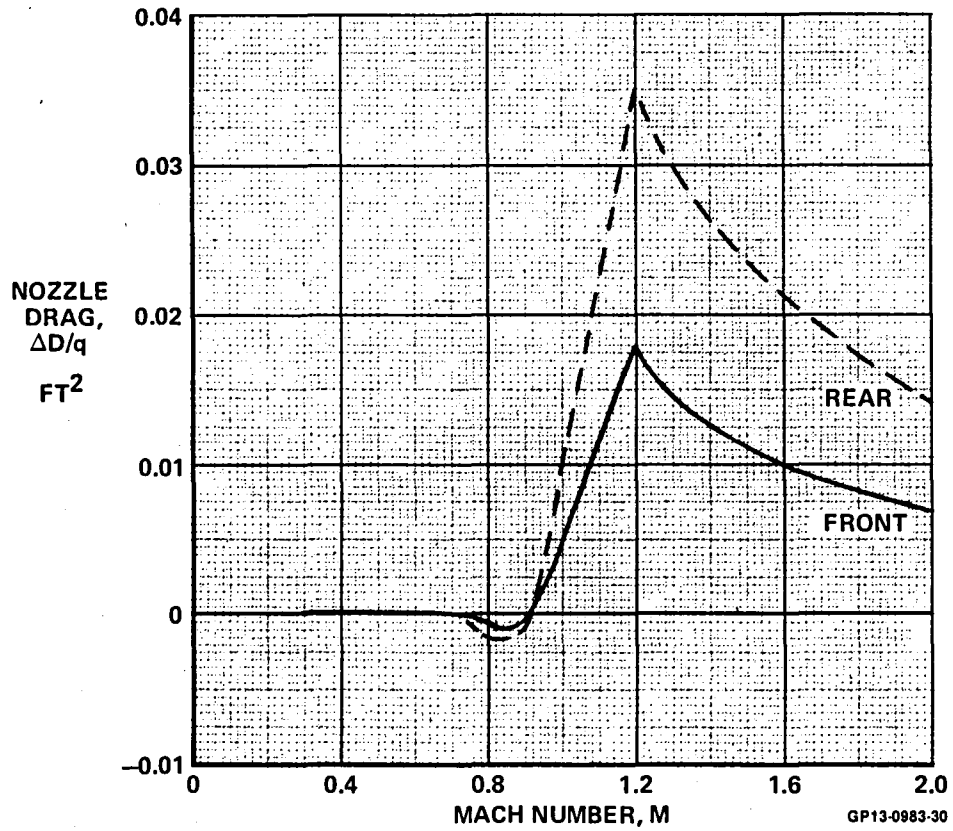
FIGURE 5-6
NOZZLE DRAG

5.2.6 INSTALLED ENGINE PERFORMANCE – These data are proprietary and not included in this report.

5.2.7 REACTION CONTROL SYSTEM (RCS) THRUST - The total thrust available for reaction control during VTOL operations is shown in Figure 5-7 for both standard (59°F) and tropic (90°F) day conditions. The RCS thrust is provided by bleeding a fraction of the high pressure compressor discharge air and ducting this air to the reaction control thrusters described in Section 3.3. In determining the RCS thrust, design duct pressure losses of 17 percent and nozzle thrust coefficients of 0.95 were assumed. As indicated in Section 6.3, the maximum total RCS thrust required for VTOL control is about 1800 lb. This maximum thrust requirement is met at corrected fan speeds equal to or greater than 90 percent of maximum for both standard and tropic day conditions.

CONTROL	MOMENT ARM (IN.)
ROLL	206
PITCH (FWD)	240
(AFT)	335
YAW	325

GP13-0983-121
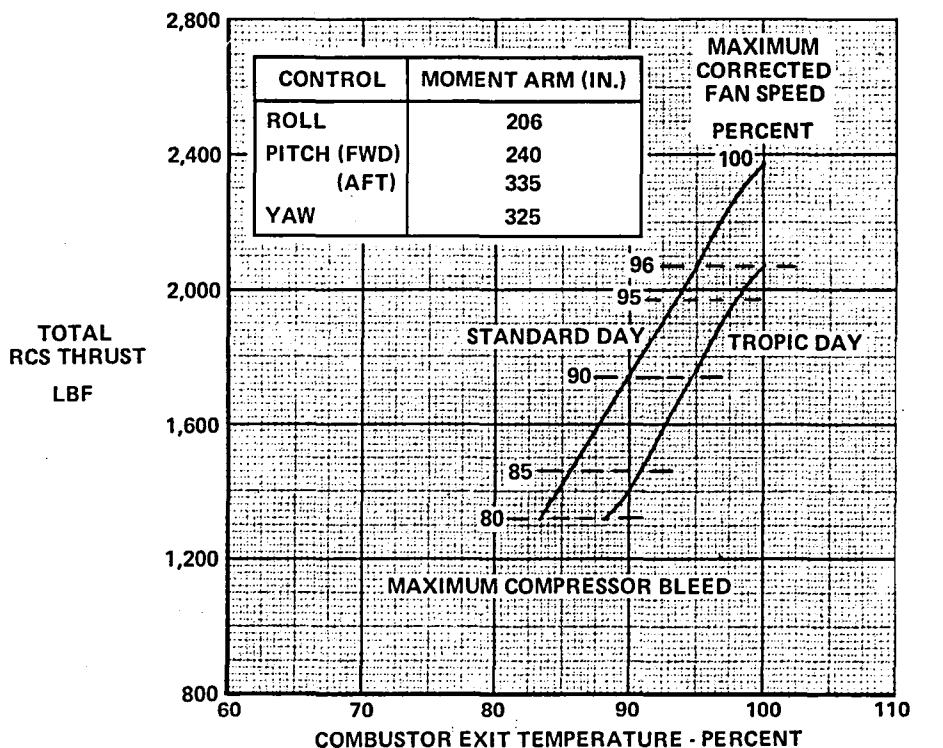
FIGURE 5-7
REACTION CONTROL SYSTEM (RCS) THRUST CAPABILITY

5.3 JET EFFECTS - IMPACT ON BASING OPERATIONS

Shipboard and shore operations for the Model 279-3 aircraft have been investigated. The aircraft, in its primary role as a STOVL fighter, takes-off STO at maximum FSB and lands vertically at a reduced FSB level. Study emphasis was placed on quantifying jet effects during the vertical landing phase. It was found that by maintaining a slight forward velocity (5 to 10 feet per second) while in proximity of the deck, exhaust heating and blast effects are significantly reduced. Such a rolling "V" retrieval operation is recommended as it permits continued use of existing shipboard and shore bases and minimizes the resultant impact on ground crew operations. AV-8 experience shows that such rolling vertical landings can be easily accomplished. Maximum gross weight VTO's will be performed from specially prepared launch areas.

5.3.1 <u>LANDING PAD TEMPERATURES</u> - Analyses to determine base temperatures during vertical landing operations were performed with MCAIR developed prediction techniques discussed in References (29) through (32). Comparisons to date indicate that predictions derived from scale model data correlations are in excellent agreement with full scale exhaust heating measurements.

Temperatures for representative shipboard and shore bases during vertical landing operations are presented in Figure 5-8. Heating of the deck is a maximum at flow impingement points (below nozzles), resulting in maximum temperatures of 700°F and 239°F for the AM-2 matting and 3/4 inch steel deck, respectively. As indicated in the figure, the maximum temperature region is very localized as the heating drops off quite rapidly with distance away from the impingement point. At a distance of 20 or 30 feet from the nozzles, the deck is essentially unheated.

FRONT (FSB) NOZZLES: T_T = 1,690°F
REAR NOZZLES: T_T = 1,500°F

AM-2 MATTING
(SHORE BASE OPERATION)

134°F   118°F

    154   131

        215   169

        700 □   □ 654
        239 □   □ 224

            120   108

    105   99

100°F   96°F

0.75 IN. STEEL DECK
(SHIPBOARD OPERATION)   GP13-0983-129
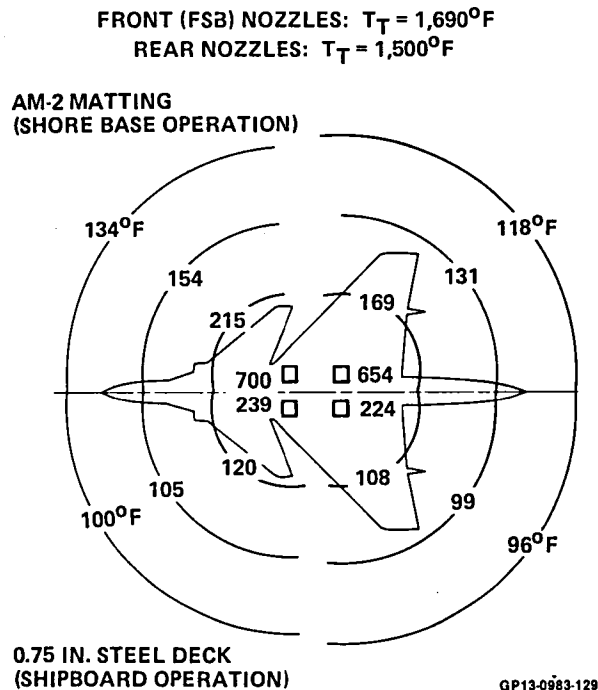
FIGURE 5-8
MODEL 279-3 MAXIMUM LANDING PAD TEMPERATURES DURING VERTICAL LANDING

Maximum temperatures and allowable temperature limits for various shipboard and shore base materials are presented in Table 5-3. It can be noted that for shipboard operations the maximum deck temperature is relatively insensitive to deck thickness. This is due to the fact that the heat build-up at the surface is primarily a function of how fast the heat can be transferred to the interior of the slab (thermal conductivity), rather than the material's total heat sink capacity. On the other hand, thermal stresses in the deck are highly thickness dependent. A carrier deck can be heated to nearly 1100°F without buckling, whereas the deck of an LPH must be limited to about 220°F for the heating conditions considered herein.

TABLE 5-2
MAXIMUM TEMPERATURES AND TEMPERATURE LIMITS FOR
VARIOUS LANDING PADS

OPERATION	LANDING PAD	MAXIMUM TEMPERATURE DURING VERTICAL LANDING (^{o}F)	LIMIT TEMPERATURE (^{o}F)	FAILURE MODE
SHIPBOARD				
CVA	1-9/16 IN. STEEL	230	1,090	BUCKLING[3]
LHA	3/4 IN. STEEL	239	321	BUCKLING[3]
LPH	9/16 IN. STEEL	250	220	BUCKLING[3]
SHORE BASE				
RUNWAYS	CONCRETE	809	200	SURFACE FLAKES[3]
			500	SURFACE SPALLS
AM-2 MATTING	0.15 IN. ALUMINUM[1]	700	>800°F	(2)

Notes:
(1) Thickness of AM-2 matting surface - matting is double wall waffle configuration
(2) During VAK-191B tests, matting temperatures between 700 - 800°F were experienced with no apparent degradation of matting, Reference (33)
(3) Reference (34)

GP13-0983-130

For shore basing, two potential landing pads were considered, AM-2 aluminum matting and concrete. During tests with the VAK-191B, Reference (37), AM-2 matting temperatures on the order of 800°F were recorded with no apparent degradation of the matting or its coating. With concrete, the low thermal conductivity restricts heat flow to the interior resulting in excessive heat build-up at the surface. This build-up would probably result in surface degradation and potential foreign object damage.

The above launch pad temperatures can be significantly reduced by maintaining a small forward velocity during vertical operations as illustrated in Figure 5-9. It was noted previously (Table 5-3) that, theoretically, a pure vertical landing would buckle the 9/16 inch steel deck of an LPH. However, with a forward velocity as low as 1 to 2 feet per second (see Figure 5-9) a rolling "V" landing can be safely performed. The rolling vertical landing can also significantly reduce maximum concrete temperatures, such that spalling of the material does not occur. For shore bases requiring pure vertical operations, AM-2 matting or its equivalent is recommended.
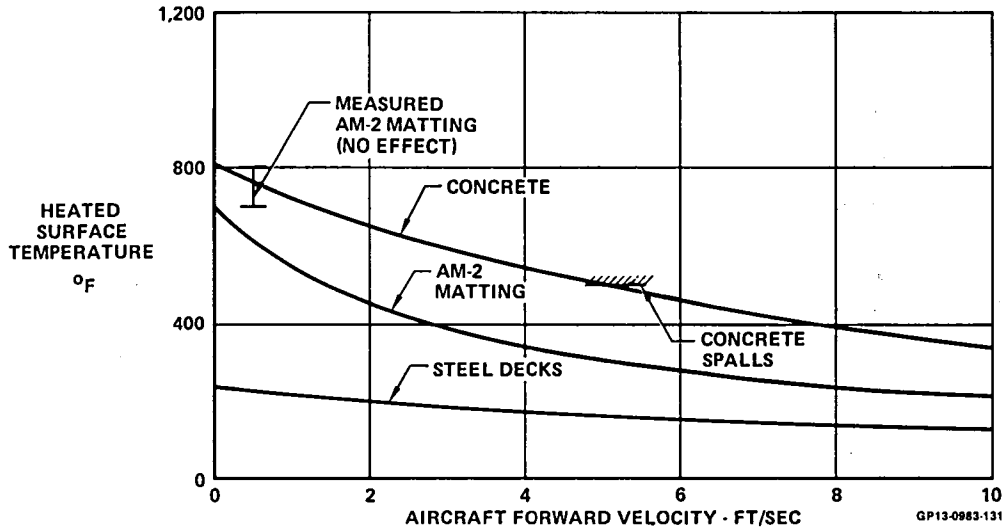
FIGURE 5-9
REDUCTION OF LAUNCH PAD TEMPERATURE
WITH AIRCRAFT FORWARD VELOCITY DURING VERTICAL TAKEOFF

5.3.2 <u>IMPACT ON GROUND CREW OPERATIONS</u> - When advanced V/STOL aircraft are in proximity of the ground, a high temperature, high velocity wall jet is formed, Figure 5-10, limiting ground crew operations in the immediate vicinity of the aircraft. The intensity of the jet decays quite rapidly, however, decreasing to an acceptable level (velocities less than 115 ft/sec and temperatures below 190°F - see Reference (35) for ground crew operations at a distance of approximately 10 feet abreast of the wing tips or aft of the tail.
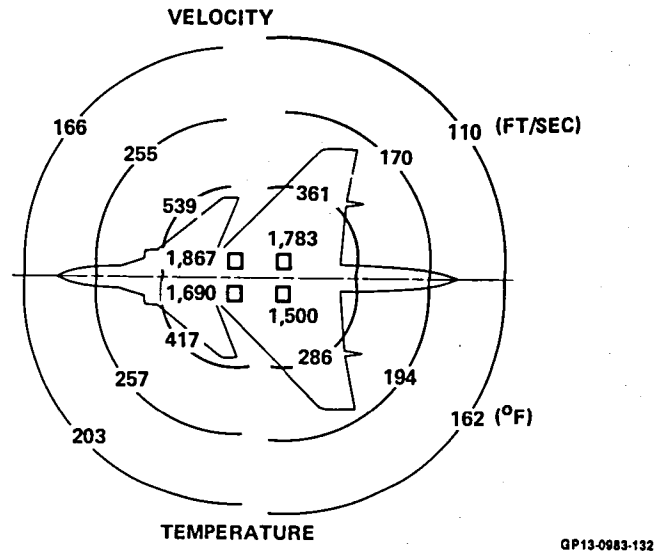
FIGURE 5-10
GROUND FLOW TEMPERATURES AND VELOCITIES
During Vertical Landing

6. AIRCRAFT PERFORMANCE

Once the configuration was sized to meet the study guidelines, a more extensive analysis of the maneuvering, mission, and V/STO performance was conducted. VTO control guidelines and phasing of reaction/aerodynamic controls were also assessed. The details of this effort are summarized below.

6.1 MANEUVERING PERFORMANCE

Maneuvering performance was computed at 88% VTOGW with two AMRAAM missiles, two AIM-9 missiles and one 25 mm gun with 400 rounds of ammunition. Maximum thrust with Fan Stream Burning (FSB) was used for all calculations with thrust support included in maneuvering performance.

The level flight envelope presented in Figure 6-1 is limited on the high speed side by the design dynamic pressure of 1800 PSF and the inlet design Mach number of 2.0. Absolute ceiling of 62,500 feet occurs at a Mach number of 1.5. The back side of the envelope is limited by maximum lift coefficient and can be extended to zero airspeed by vectoring the nozzles down as a function of altitude and Mach number.

Specific excess power is presented in Figures 6-2 through 6-5 as a function of load factor for sea level, 10,000, 20,000, and 30,000 feet, respectively. Data are presented for Mach numbers of 0.5, 0.6, and 0.9 for all altitudes, 1.2 Mach number at 10,000 feet and 1.2 and 1.6 Mach number at 20,000 and 30,000 feet which is consistent with the one g flight envelope. A load factor of 7.5, equal to the structural limit can be sustained at sea level for Mach numbers ranging from 0.6 to 0.9 and at 10,000 feet for Mach numbers between 0.9 and 1.2. The maximum specific excess power occurs at 0.9 Mach number at sea level and falls off with Mach number and altitude. The one g design requirement for P_S = 900 FPS at 0.9 Mach number at 10,000 feet is exceeded up to a load factor of 3.5.

Figures 6-6 through 6-9 present turn rate capability as a function of specific excess power contours overlaid on a Mach number – load factor carpet plot. Sustained turn rate and load factor are obtained from the P_S = 0 contour for a given Mach number. Instantaneous turn performance based on maximum lift coefficient is presented with and without thrust vectoring. To take advantage of thrust vectoring the Model 279-3 has been designed for an additional 1.5 g load factor due to vectoring the nozzles. Additional turn capability provided by thrust vectoring was achieved by deflecting the nozzles to provide maximum delta load factor.

Acceleration capability of the Model 279-3 is presented in Figure 6-10 for 25,000, 30,000, 35,000 and 45,000 feet. Acceleration time from 0.8 Mach number to 1.6 Mach number at 35,000 feet is 68 seconds.
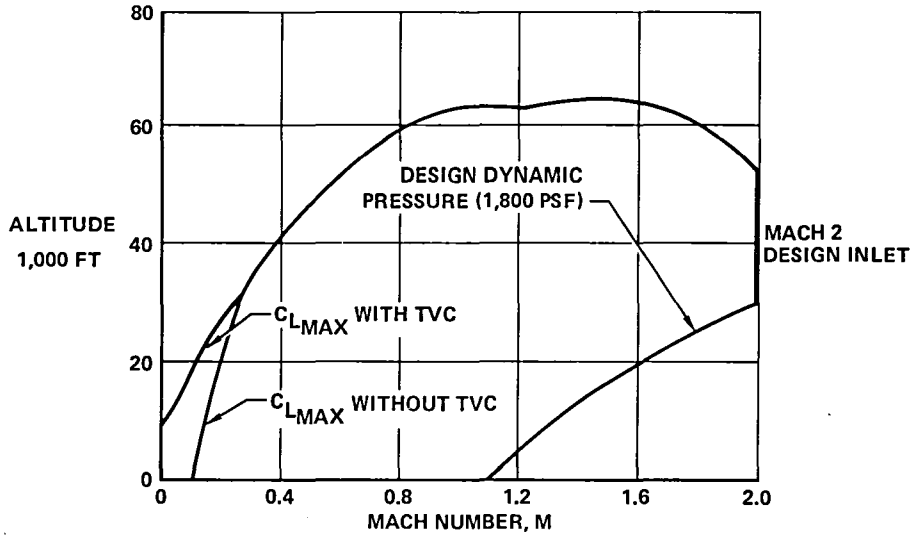
GP13-0983-94

FIGURE 6-1
MODEL 279-3 1 g FLIGHT ENVELOPE
(2) AMRAAM + (2) AIM-9 + 25 mm Gun with 400 Rounds Ammo
88% VTOGW = 26,260 Lb
Maximum Thrust (with Fan Stream Burning)
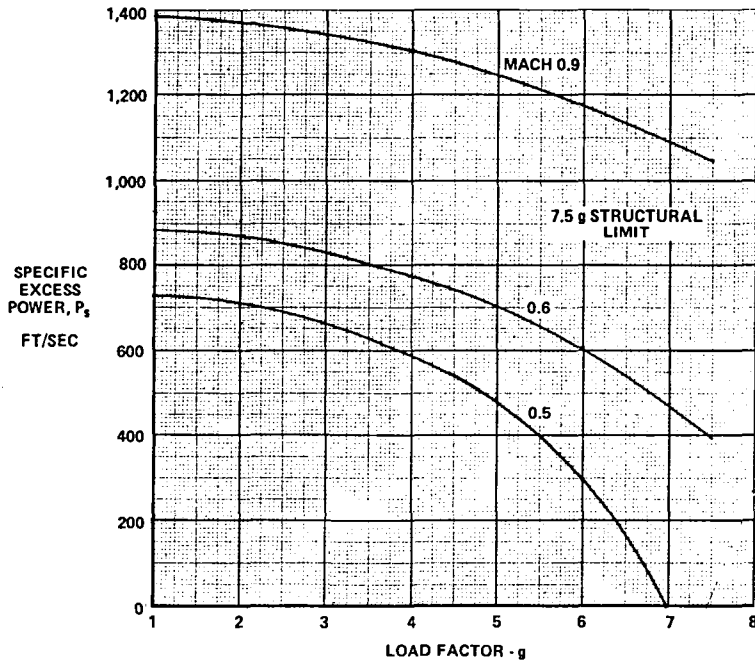
GP13-0983-118

FIGURE 6-2
SPECIFIC EXCESS POWER AT SEA LEVEL
(2) AMRAAM + (2) AIM-9 + 25 mm Gun with 400 Rounds Ammo
88% VTOGW = 26,260 Lb
Max Thrust (With Fan Stream Burning)
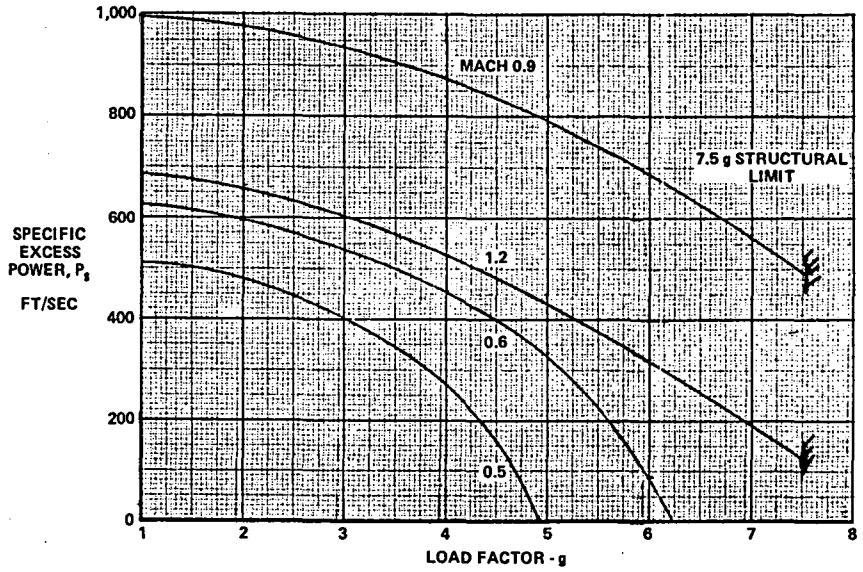
GP13-0083-119

FIGURE 6-3
SPECIFIC EXCESS POWER AT 10,000 FT
(2) AMRAAM + (2) AIM-9 + 25 mm Gun with 400 Rounds Ammo
88% VTOGW = 26,260 Lb
Max Thrust (With Fan Stream Burning)
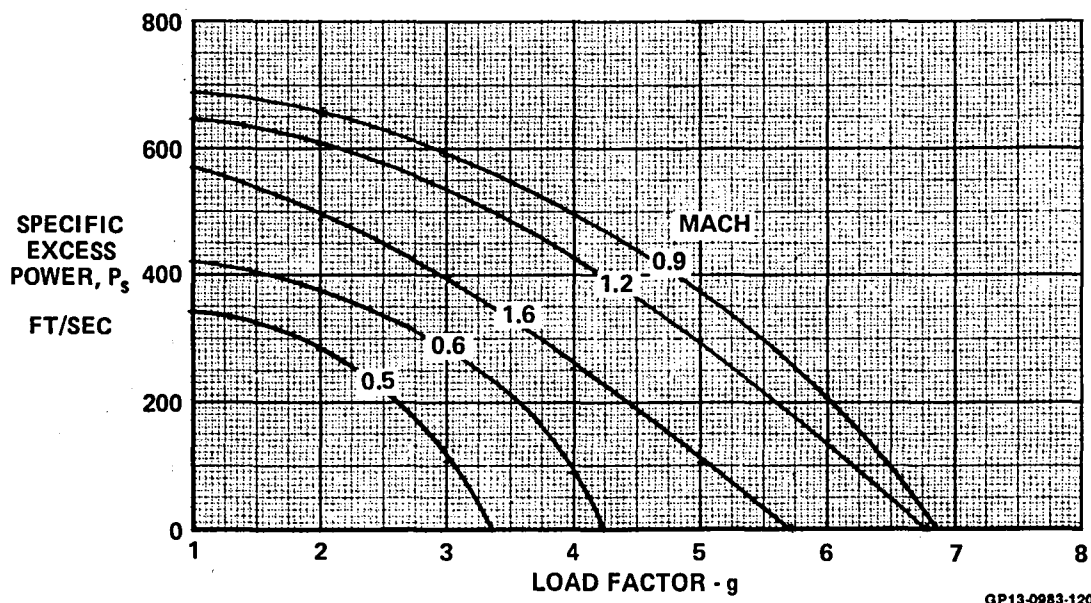
GP13-0983-120

FIGURE 6-4
SPECIFIC EXCESS POWER AT 20,000 FT
(2) AMRAAM + (2) AIM-9 + 25 mm Gun with 400 Rounds Ammo
88% VTOGW = 26,260 Lb
Max Thrust (With Fan Stream Burning)
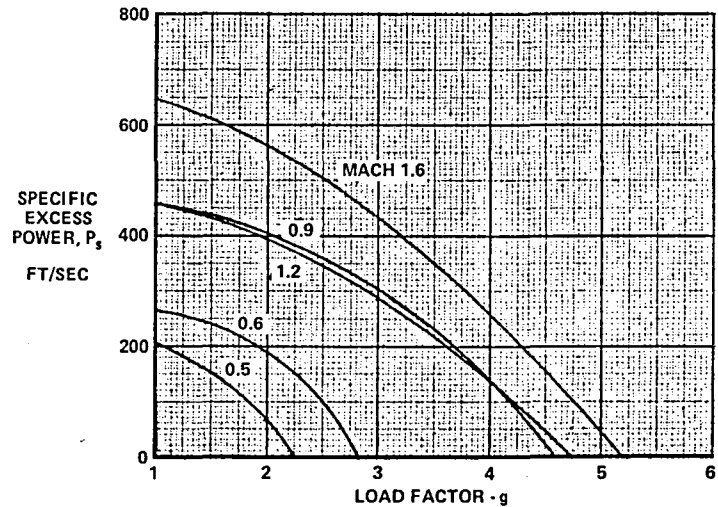
FIGURE 6-5
SPECIFIC EXCESS POWER AT 30,000 FT
(2) AMRAAM + (2) AIM-9 + 25 mm Gun with 400 Rounds Ammo
88% VTOGW = 26,260 Lb
Max Thrust (With Fan Stream Burning)
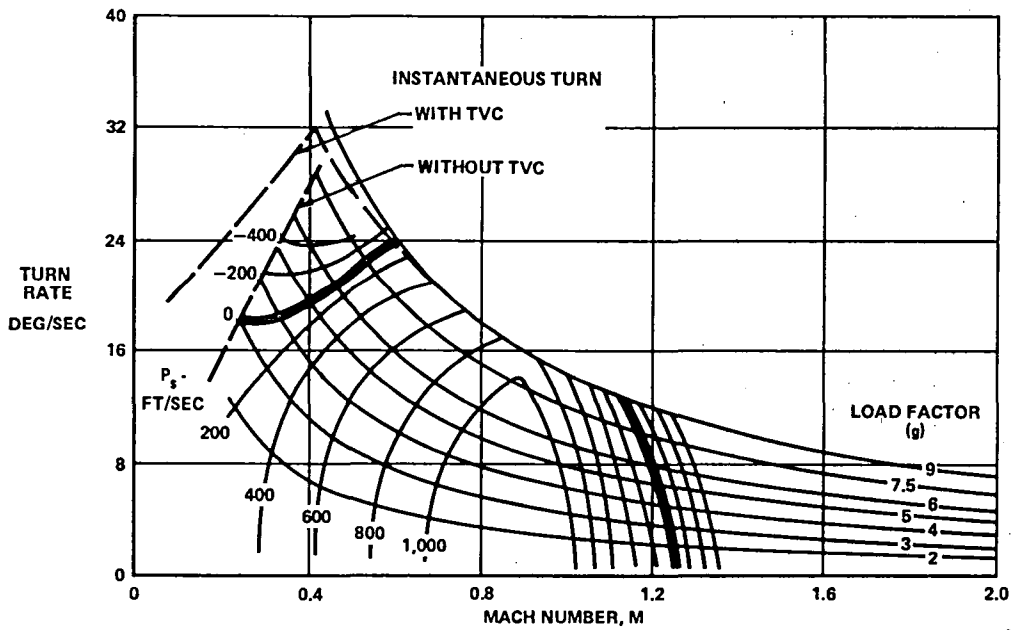
FIGURE 6-6
MODEL 279-3 TURN PERFORMANCE
Sea Level
(2) AMRAAM + (2) AIM-9 + 25 mm Gun with 400 Rounds Ammo
88% VTOGW = 26,260 Lb
Maximum Thrust (with Fan Stream Burning)
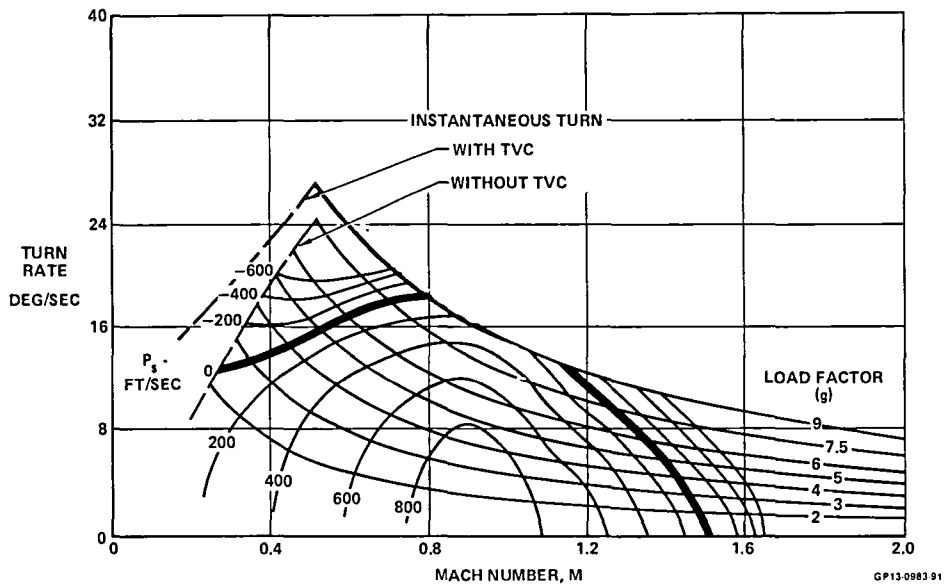
FIGURE 6-7
MODEL 279-3 TURN PERFORMANCE
Altitude = 10,000 Ft
(2) AMRAAM + (2) AIM-9 + 25 mm Gun with 400 Rounds Ammo
88% VTOGW = 26,260 Lb
Maximum Thrust (with/Fan Stream Burning)
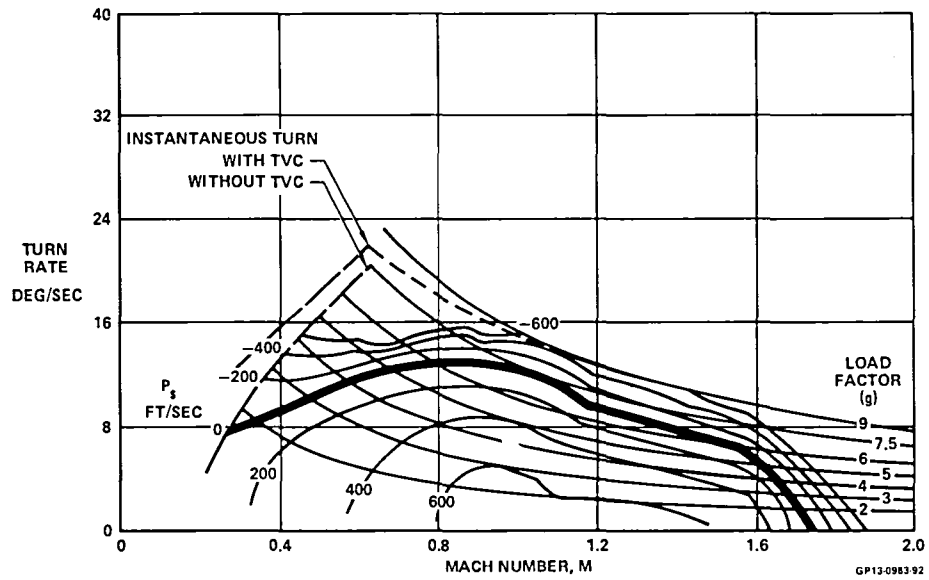
FIGURE 6-8
MODEL 279-3 TURN PERFORMANCE
Altitude = 20,000 Ft
(2) AMRAAM + (2) AIM-9 + 25 mm Gun with 400 Rounds Ammo
88% VTOGW = 26,260 Lb
Maximum Thrust (with/Fan Stream Burning)
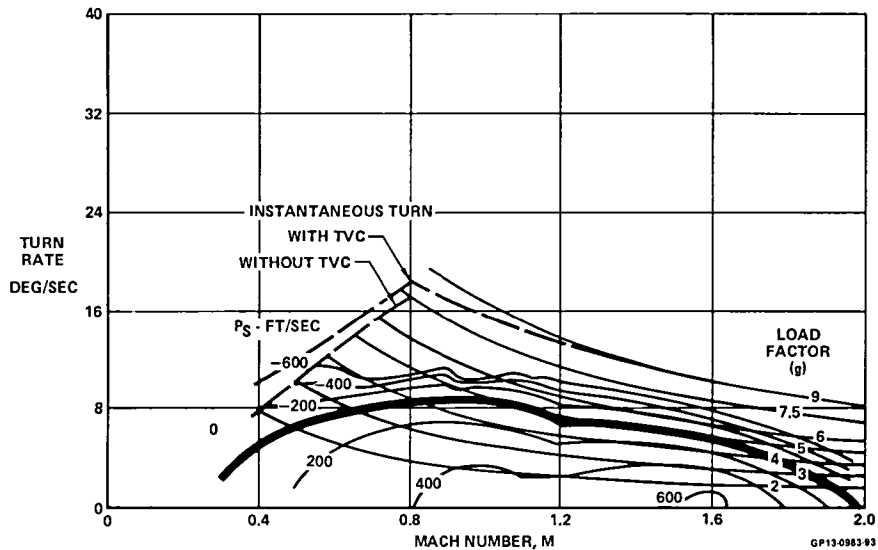
FIGURE 6-9
MODEL 279-3 TURN PERFORMANCE
Altitude = 30,000 Ft
(2) AMRAAM + (2) AIM-9 + 25 mm Gun with 400 Rounds Ammo
88% VTOGW = 26,260 Lb
Maximum Thrust (with Fan Stream Burning)
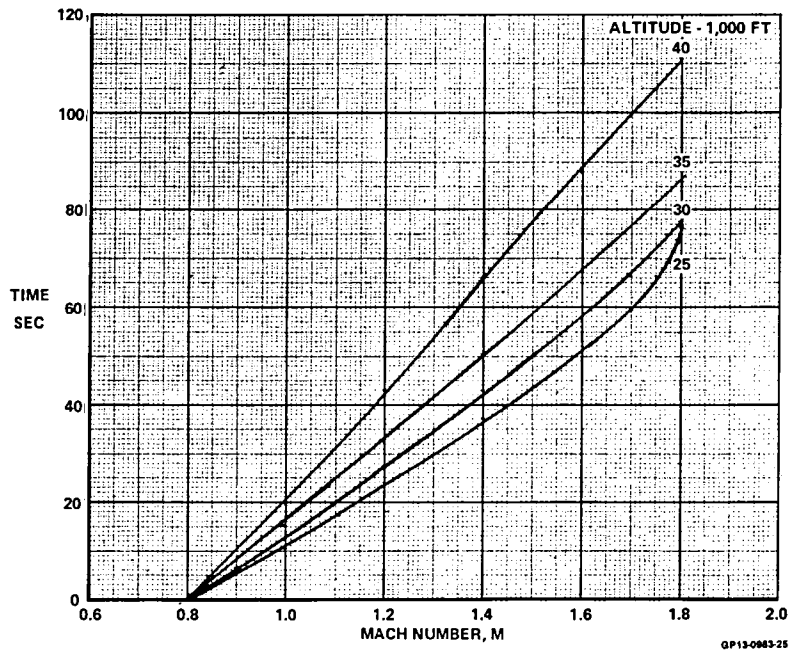
FIGURE 6-10
ACCELERATION PERFORMANCE
(2) AMRAAM + (2) AIM-9 + 25 mm GUN with 400 Rounds Ammo
88% VTOGW = 26,260 Lb
Max Thrust (With Fan Stream Burning)

6-6

6.2 MISSION PERFORMANCE

Model 279-3 mission performance was evaluated on three missions. Figures 6-11 through 6-13 present mission profiles and definitions for the Deck Launch Intercept (DLI), interdiction and ferry, respectively. DLI mission radius is presented in Figure 6-14 as a function of fuel. Model 279-3 has an internal
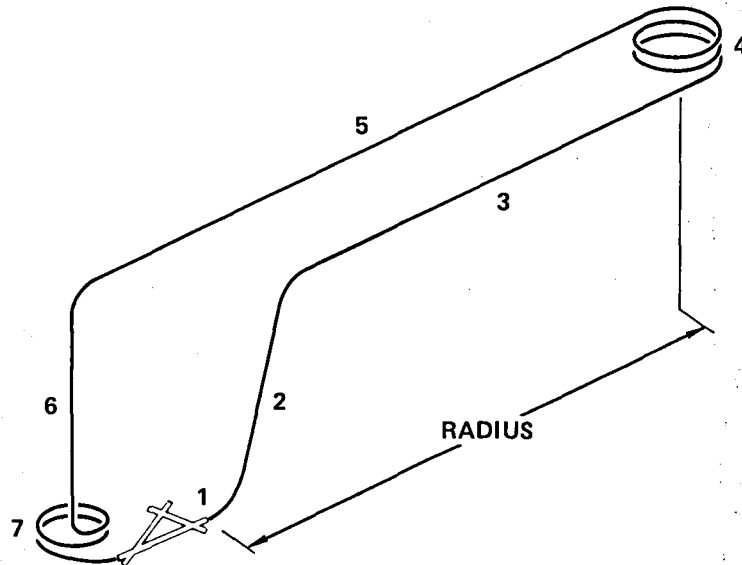
1. TAKEOFF ALLOWANCE
   - 2 MIN AT IRT RATING
   - 1/2 MIN AT MAXIMUM FSB
2. CLIMB/ACCELERATE
   - CLIMB FROM SEA LEVEL MACH 0.3 AT MAXIMUM FSB RATING TO MACH 1.6 AT 40,000 FT
3. DASH
   - DASH AT MACH 1.6 AT 40,000 FT TO TOTAL RADIUS (INCLUDING DISTANCE TRAVELED DURING CLIMB/ACCELERATE)
4. COMBAT ALLOWANCE
   - FUEL ALLOWANCE, 2 MIN MAXIMUM FSB RATING AT MACH 1.6 AT 40,000 FT
   - WEAPONS RETAINED
5. RETURN CRUISE
   - CRUISE CLIMB AT BEST CRUISE ALTITUDE AND VELOCITY
6. DESCEND TO SEA LEVEL
   - NO TIME, FUEL OR DISTANCE CREDITED
7. LANDING ALLOWANCE AND RESERVE
   - 10 MIN LOITER AT BEST ENDURANCE SPEED AT SEA LEVEL
   - 45 SEC AT LANDING POWER
   - 5% OF INITIAL FUEL

Note: 5% service tolerance on fuel flow

GP13-0983-61

FIGURE 6-11
DECK LAUNCH INTERCEPT MISSION PROFILE AND DEFINITION
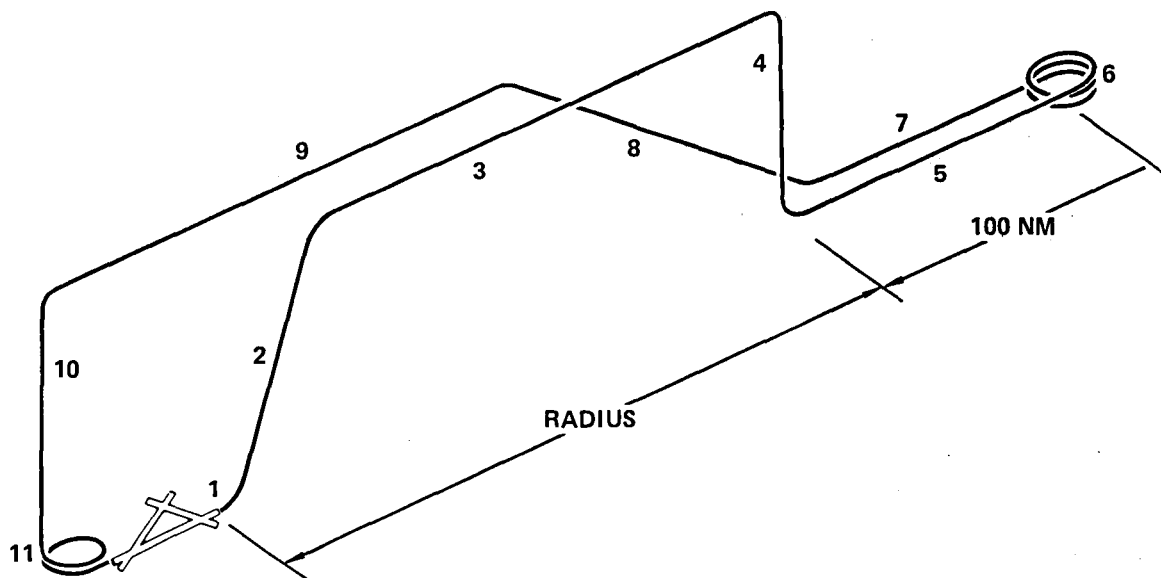
1. TAKEOFF ALLOWANCE
   - 2 MIN AT IRT RATING
   - 1/2 MIN AT MAXIMUM FSB
2. CLIMB ON COURSE
   - IRT RATING FROM SEA LEVEL TO BEST CRUISE ALTITUDE AND VELOCITY
3. CRUISE
   - AT BEST CRUISE ALTITUDE AND VELOCITY
4. DESCEND TO SEA LEVEL
   - NO TIME, FUEL OR DISTANCE CREDITED
5. RUN INTO TARGET
   - 100 NM, SEA LEVEL, MACH 0.85
6. COMBAT ALLOWANCE
   - 5 MIN, IRT RATING MACH 0.85, SEA LEVEL
   - DELIVER AIR-TO-GROUND WEAPONS
   - AIR-TO-AIR WEAPONS RETAINED
   - TANKS DROPPED WHEN EMPTY
7. RUN OUT FROM TARGET
   - 100 NM, SEA LEVEL, MACH 0.85
8. CLIMB ON COURSE
   - IRT RATING FROM SEA LEVEL TO BEST CRUISE ALTITUDE AND VELOCITY
9. RETURN CRUISE
   - AT BEST CRUISE ALTITUDE AND VELOCITY
10. DESCEND TO SEA LEVEL
    - NO TIME, FUEL OR DISTANCE CREDITED
11. LANDING ALLOWANCE
    - 10 MIN LOITER AT BEST ENDURANCE SPEED AT SEA LEVEL
    - 45 SEC AT LANDING POWER
    - 5% OF INITIAL FUEL

Note: 5% service tolerance on fuel flow

GP13-0983-62

FIGURE 6-12
INTERDICTION MISSION PROFILE AND DEFINITION
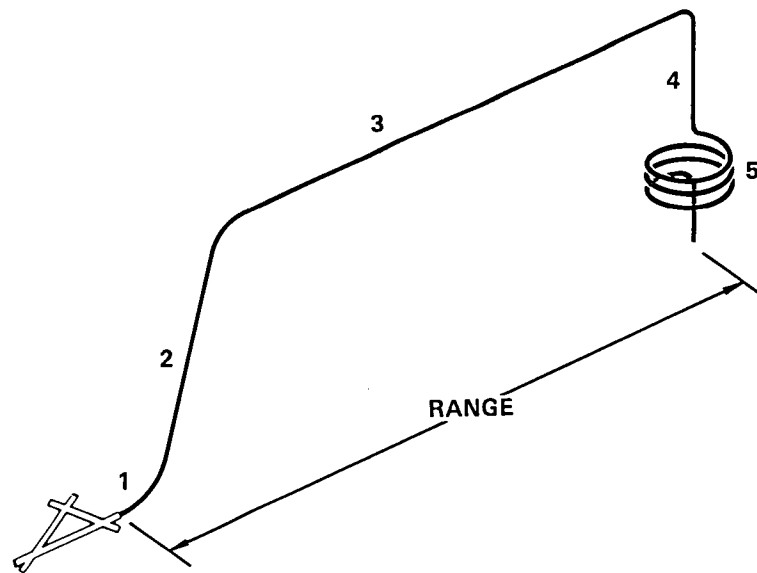
1. **TAKEOFF ALLOWANCE**
   - 2 MIN AT IRT RATING
   - 1/2 MIN AT MAXIMUM FSB
2. **CLIMB ON COURSE**
   - IRT RATING FROM SEA LEVEL TO BEST CRUISE ALTITUDE AND VELOCITY
3. **CRUISE**
   - AT BEST CRUISE ALTITUDE AND VELOCITY
4. **DESCEND TO SEA LEVEL**
   - NO TIME, FUEL OR DISTANCE CREDITED
5. **LANDING ALLOWANCE**
   - 10 MIN LOITER AT BEST ENDURANCE SPEED AT SEA LEVEL
   - 45 SEC AT LANDING POWER
   - 5% OF INITIAL FUEL

Note: 5% service tolerance on fuel flow

GP13-0983-63

FIGURE 6-13
FERRY MISSION PROFILE AND DEFINITION

fuel capacity of 9,950 lb. However, to meet the VTOGW capability 1,384 lb of fuel was off loaded and resulted in a DLI radius of 107 nm. If full internal fuel and a short takeoff are used, the radius increases to 150 nm. The effect of dash Mach number and altitude on DLI radius is presented in Figure 6-15. Mission radius can be increased from 107 nm to 154 nm by increasing the dash altitude from 40,000 feet to 50,000 feet. A DLI radius of 192 nm can be realized by lowering the Mach number from M = 1.6 to M = 1.4 at 50,000.

Payload-radius relationship for the interdiction mission with a 100 nm, .85 Mach number sea level dash is presented in Figure 6-16. MK-82 Snakeyes were carried as payload with two AIM-9 missiles and one 25 mm gun with 400 rounds of ammunition for self defense. The data are presented for a takeoff gross weight of 48,727 lb which requires a 520 ft deck takeoff with 20 knots wind-over-deck.

6-9
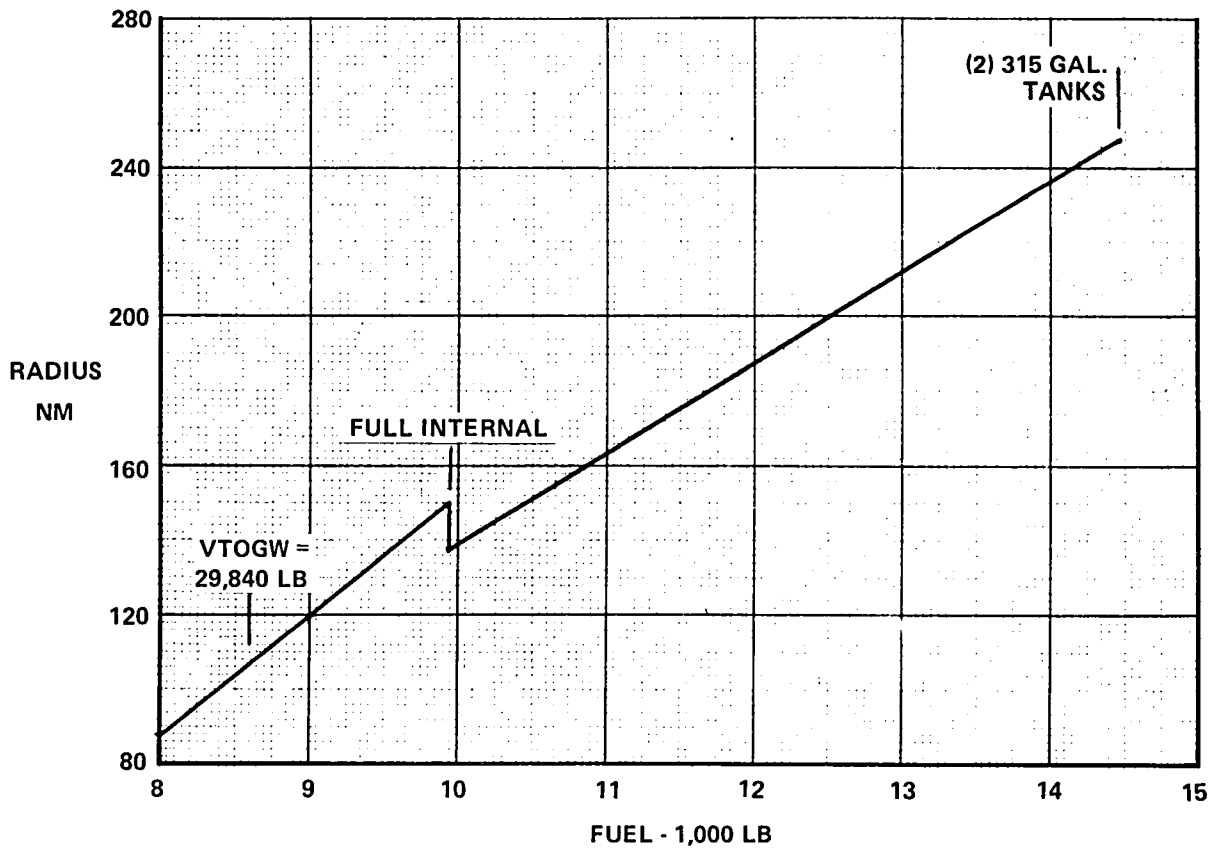
GP13-0983-64

FIGURE 6-14
MODEL 279-3 EFFECT OF FUEL QUANTITY ON DLI RADIUS
(2) AMRAAM + (2) AIM-9 + 25 mm Gun with 400 Rounds Ammo
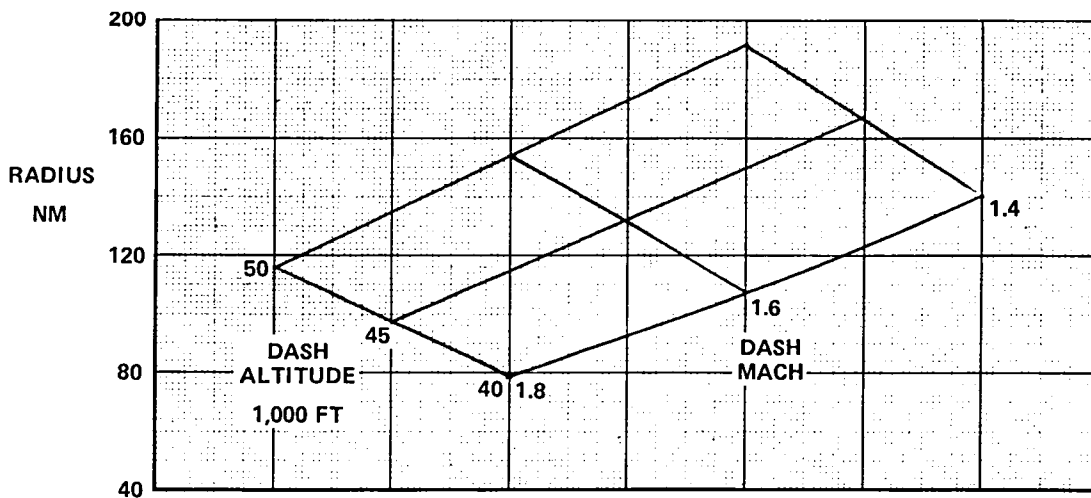
GP13-0983-65

FIGURE 6-15
EFFECT OF DASH MACH AND ALTITUDE ON DLI RADIUS
(2) AMRAAM + (2) AIM-9 + 25 mm Gun with 400 Rounds Ammo
VTOGW = 29,840 Lb
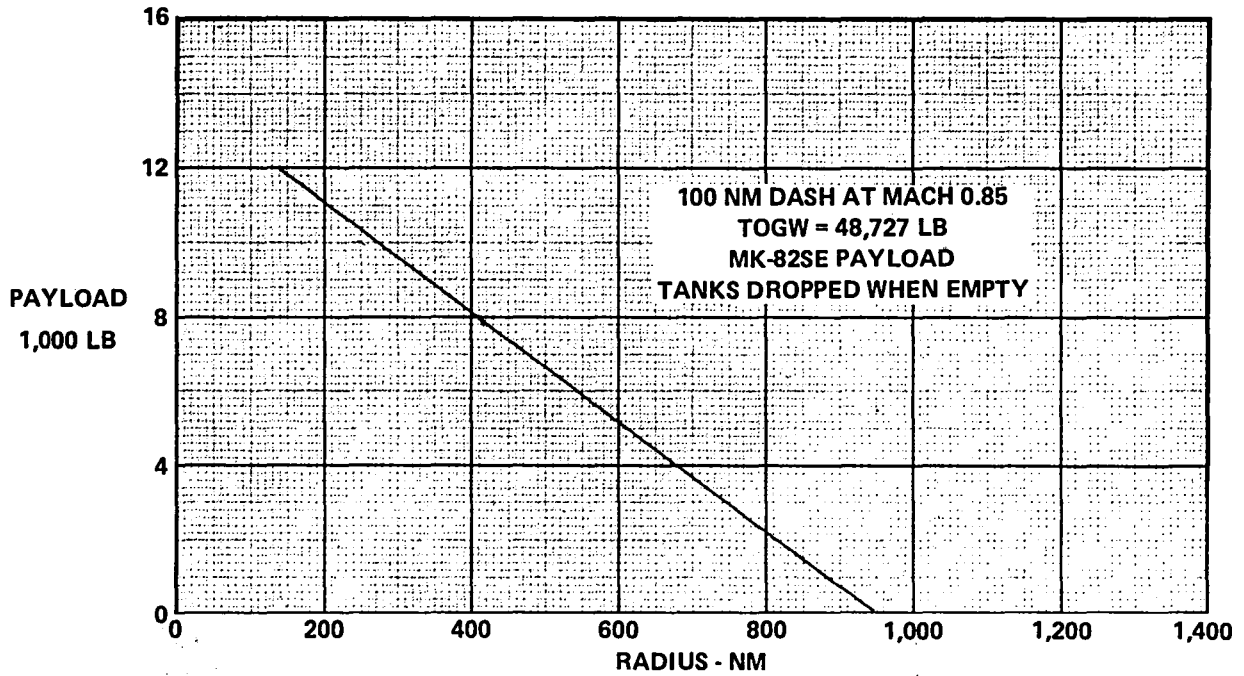
GP13-0983-87

FIGURE 6-16
MODEL 279-3 INTERDICTION MISSION PAYLOAD-RADIUS
(2) AIM-9 + 25 mm Gun with 400 Rounds Ammo

The effect of sea level dash distance and Mach number on interdiction radius is presented in Figure 6-17. A 100 nm dash at optimum Mach number will increase the radius from 417 nm to 540 nm.

Ferry range is presented in Figure 6-18 as a function of fuel carried. Ferry range of the Model 279-3 with four 600 gallon tanks retained and zero wind is 2,650 nm.

6.3 VTOL PERFORMANCE AND CONTROL GUIDELINES

The maximum VTO gross weight is 29,840 lb for a tropic day. The vertical landing, VL, maximum weight is 28,640 lb which is 1,200 lb lighter. The design thrust-to-weight ratios are presented in addition to guidelines for conducting a VTO and necessary control power.

6.3.1 VTO THRUST SIZING — Thrust sizing must include the effects of installation losses, ingestion thrust penalties, jet-induced lift characteristics and altitude control requirements. Excess thrust requirements for height control or VTO acceleration must also be considered, while accounting for engine scheduling and temperature limits. This approach requires an evaluation of each particular aircraft configuration in these areas and the calculation of the installed engine performance as a function of RCS bleed rates and engine inlet temperature levels.
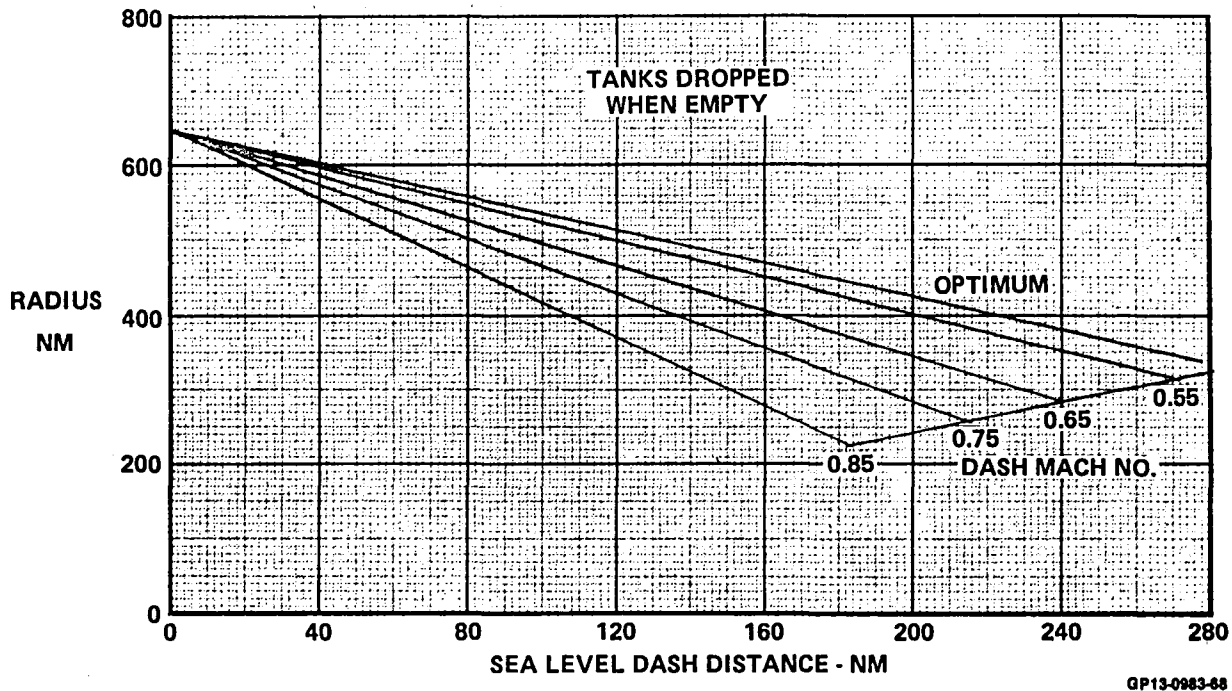
FIGURE 6-17
MODEL 279-3 EFFECT OF DASH DISTANCE AND MACH ON INTERDICTION RADIUS
(14) MK-82SE + (2) AIM-9 + (2) 600 Gal. Tanks + 25 mm Gun with 400 Rounds Ammo

Sizing of the Model 279-3 engine was accomplished using the procedure described below, before related ground effects data and prediction procedures became available. This simplified procedure led to a VTO T/W of 1.15, used in the study. The later predictions indicated that this number may be conservative by 3%, but detailed testing and manned VTO simulations are required to accurately assess the thrust requirements.

One approach for sizing the propulsion system for vertical takeoff is to add all of the maximum allowances for each of the various factors affecting vertical operation. However, operational experience with the AV-8A indicates this "static accounting" approach to be conservative. It results in a T/W of 1.24 (lift loss 2%, hot gas ingestion 6%, control 11%, acceleration 5%) for the AV-8A to operate vertically on a tropic day. Successful operation of the AV-8A has been demonstrated with a T/W of 1.11. Thus, for our sizing studies the static assessment has been reduced by the ratio 11/24 (0.46).

The static allowances for the Model 279-3 are; lift losses (3.5%), reingestion (8.0%), control (16.0%) and acceleration demands (5.0%). Scaling the allowance by 0.46 results in a tropic day VTO T/W of 1.15. An additional 4.8 percent thrust margin has been added for VL, based on AV-8 flight experience, to allow the pilot to slow a high rate of descent or to reverse a decision to land.

6.3.2 VTO PROFILE - A typical VTO profile including transition to wing-borne flight is presented as Figure 6-19. The vertical climb continues until the aircraft is out of ground effects to minimize control usage. Then the

6-12
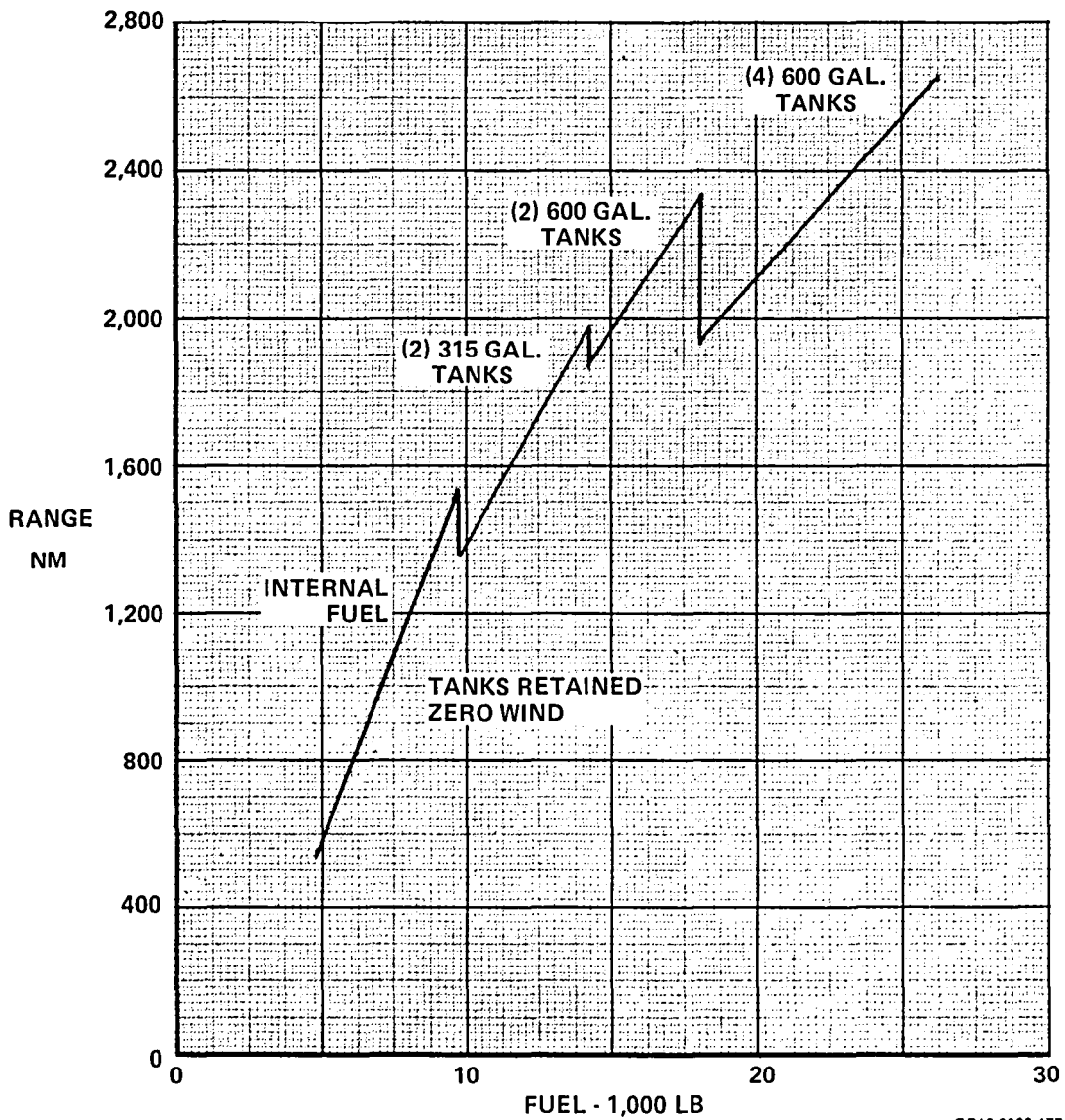
FIGURE 6-18
MODEL 279-3 FERRY RANGE

nozzles are deflected aft slowly to increase speed and provide wing lift at
the earliest possible time. The Reaction Control System, RCS, provides all of
the VTO control about all three axes and most of the control at low speeds.
At medium speeds the aircraft still has a high angle of attack, approximately
15°. This maximizes wing lift and allows the engine to accelerate, rather
than lift, the aircraft. At this medium speed, the engine thrust directed
through the partially deflected forward nozzles creates an aircraft nose up
moment which is approximately countered by the large deflection of the aft
nozzles. The remaining moment is countered by a combination of canard
deflection and tail up-thrust. As speed increases due to the large thrust-to-
weight ratio, the aircraft angle of attack decreases with flap retraction and
nozzle rotation aft. The aft nozzles rotate faster than the forward nozzles
to arrive simultaneously at the wingborne zero deflection where control is
provided by the canard.
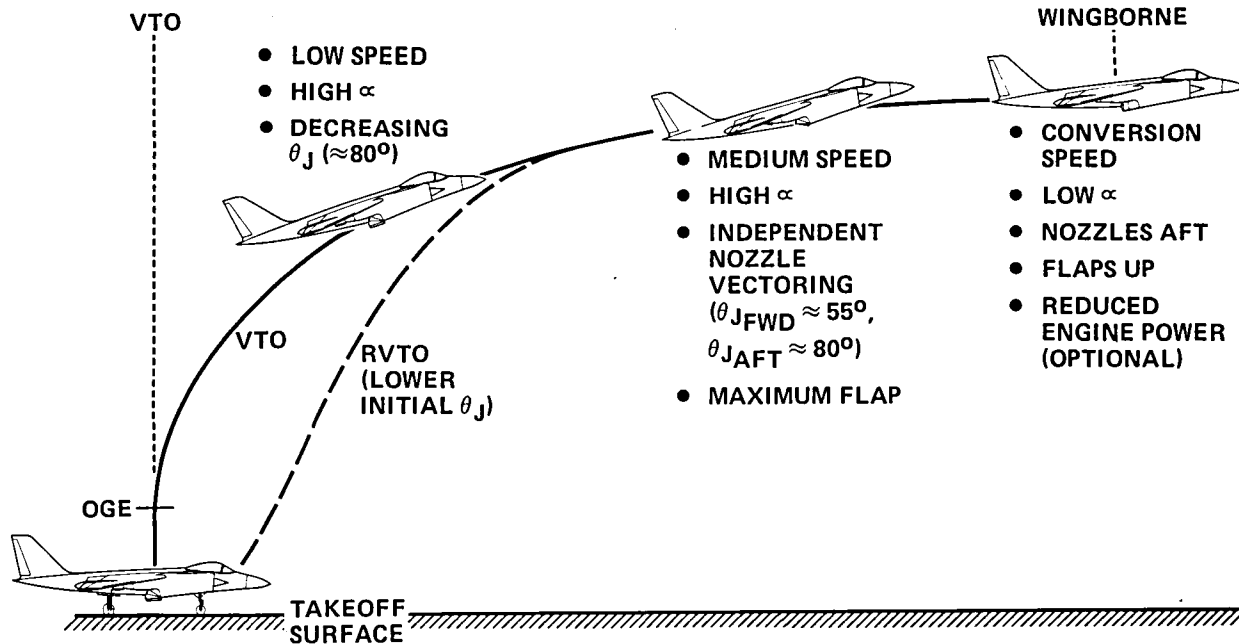
FIGURE 6-19
MODEL 279-3, VTO/RVTO AND TRANSITION PROFILES

A typical profile for Rolling Vertical Takeoff, RVTO, is also presented in Figure 6-19. The use of low nozzle deflections during the very short ground roll, followed by near vertical deflections at liftoff, increases the TOGW approximately ten percent and minimizes the thermal environment. A rolling vertical landing is also feasible with similar benefits. Both the VTO and RVTO techniques have been successfully flight demonstrated by the AV-8A and YAV-8B.

For the Model 279-3, the asymmetrical nozzle deflection will be scheduled using the fly-by-wire flight control system. The flap deflection will be scheduled to preclude adverse engine nozzle flow impingement. The control system will also schedule the RCS usage as a function of nozzle deflection, airspeed and control deflection requested by the pilot or stability augmentation system. After wingborne flight is attained the RCS will only be used for designated high angle of attack maneuvering.

6.3.3 CONTROL POWER REQUIREMENTS - MCAIR uses the guidelines shown in Table 6-1 in aircraft control requirements studies for Navy V/STOL aircraft concepts. The NAVAIR study guidelines were expressed in terms of attitude response as in MIL-F-83300 Paragraphs 3.2.3.1 and 3.2.3.2. These response criteria were interpreted by MCAIR into angular acceleration (radians/second^2) for ease of application in the conceptual definition phase of an aircraft configuration. The interpretation takes into consideration aircraft stability, wind conditions, and pilot controller travel ranges and schedules in consonance with the specifications of MIL-F-83300. Since wind effects on the aircraft are configuration dependent, some variation in the angular acceleration specification (in radians/second^2) will generally occur for different configurations. Aircraft weight and mass moments of inertia allow

6-14

TABLE 6-1
MODEL 279-3 REACTION CONTROL DESIGN CRITERIA

DESIGN CONDITION	PITCH	ROLL	YAW	UNITS
MINIMUM SIMULTANEOUS RESPONSE	4	6	3	ATTITUDE CHANGE (DEG IN 1 SEC)
	0.21	0.32	0.21	CONTROL POWER (RAD/SEC^2)
MINIMUM SINGLE AXIS RESPONSE (SENSITIVITY)	4	6	3	ATTITUDE CHANGE (DEG IN 1 SEC/IN.)
	0.53	1.31	0.28	CONTROL POWER (RAD/SEC^2)

GP13-0983-178

conversion of these angular acceleration criteria into RCS thrust and bleed flow requirements from the engine. The RCS thrust levels for this aircraft are shown in Figure 6-20. To increase longitudinal control power, it is desirable to incorporate an up-blowing (down-thrusting) aft RCS valve as shown in Figure 6-20. The basic advantages are: 1) increased control moment arm for most configurations and 2) reduced weight if the forward RCS valve can be eliminated and the aft RCS plumbing can be shared by both up- and down-thrusting valves. The main disadvantage occurs if there is a nose up trim requirement demanding constant down RCS thrusting. When this occurs, there is a reduction in hover capability equal to the propulsive lift loss due to bleed combined with the RCS downward thrust. Fortunately, use of compressor bleed causes the engine's thrust center to shift forward resulting in an effective increase of nose up pitching moment particularly for large values of bleed flow. Consequently, we have elected to retain the forward RCS valve with limited capability in our design and use the down-thrusting aft valve when we have reached limits of the control authority on the forward nozzle.

PITCH
1,700 LB DOWN-BLOWING
800 LB UP-BLOWING

NU PITCH
1,000 LB
DOWN-BLOWING ONLY

YAW
±1,320 LB

ROLL
EACH WING
1,000 LB DOWN-BLOWING
530 LB UP-BLOWING
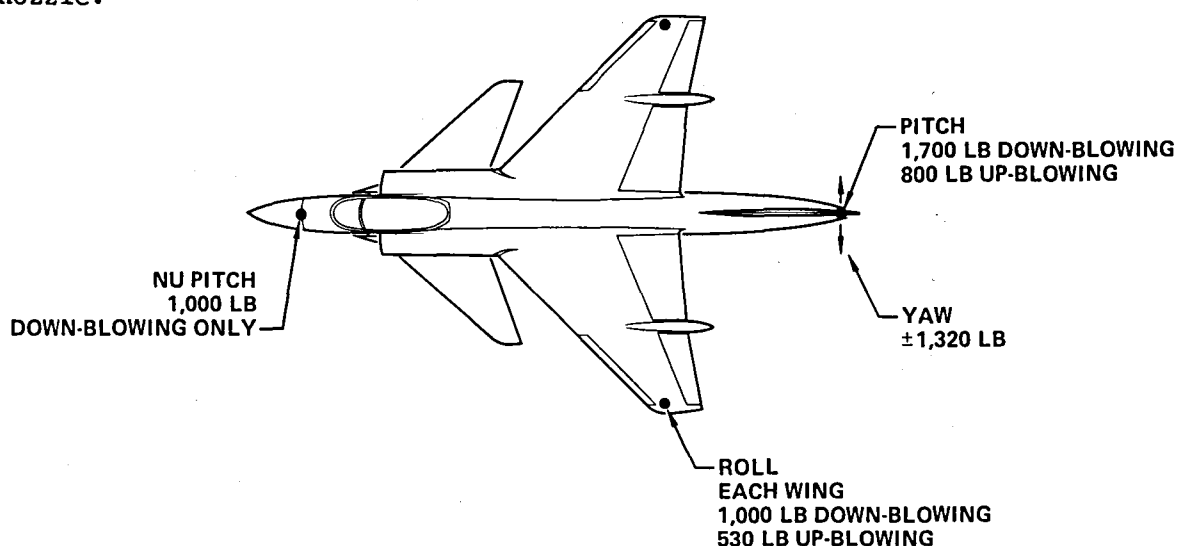
GP13-0983-180

FIGURE 6-20
MODEL 279-3 REACTION CONTROL FORCES
VTOGW = 29,840 Lb

The critical requirement which sizes the total bleed capability from the engine is the simultaneous control response criterion. Once this capability is established the individual capabilities are then determined and compared against control criteria for the individual axes. The capabilities of the control system as limited by the maximum available bleed and minimum thrust/weight of 1.0 at VTOGW, during control application while out of ground effect, are shown in Table 6-2. Note that the bottom line of the figure is the critical design condition which agrees exactly with its design criterion. All other conditions meet or exceed their respective criteria of Table 6-1.

TABLE 6-2
REACTION CONTROL POWER CAPABILITIES AT VTOGW
Rad/Sec^2

| CONDITION | PITCH | | ROLL | YAW |
	NU	ND		
SINGLE AXIS CONTROL	0.70	0.	0	0
	0	0.56	0	0
	0	0	1.35	0
	0	0	0	0.44
SIMULTANEOUS	0.33	0	0.32	0.21
	0	0.21	0.32	0.21

6.3.4 PHASING OF REACTION AND AERODYNAMIC CONTROLS – The amount of RCS control capability held in reserve has a direct bearing on how safely a V/STOL aircraft can be operated over a wide range of flight conditions. This is particularly true in the vertical take-off (VTO) and transition modes where virtually all aircraft control must be provided by the engine and RCS alone. If less bleed is needed to provide trim in normal VTO and transition, then more bleed will be available for aircraft control under emergency conditions such as severe atmospheric turbulence.

One method of achieving substantial RCS savings in VTO and transition is by the independent vectoring of the forward and aft engine nozzles. The proper selection of nozzle vectoring schedules will result in adequate aircraft control with minimum RCS bleed expenditure. The RCS savings achieved by independent over tandem vectoring is shown in Figure 6-21.

The VTO flight profile begins with a vertical take-off for 10 seconds before pilot begins vectoring. Average vectoring rate is about 5 degrees/second, and the aircraft exceeds 160 knots and 1,000 ft altitude in 30 seconds. This sample trajectory was used for comparison of the two vectoring schemes. Although in the independent vectoring case, the forward nozzles were vectored at twice the rate of the aft nozzles, the resultant thrust vector rate was about the same in both cases. Transition vectoring could further be enhanced by implementing a variable rate schedule with slow rates at the
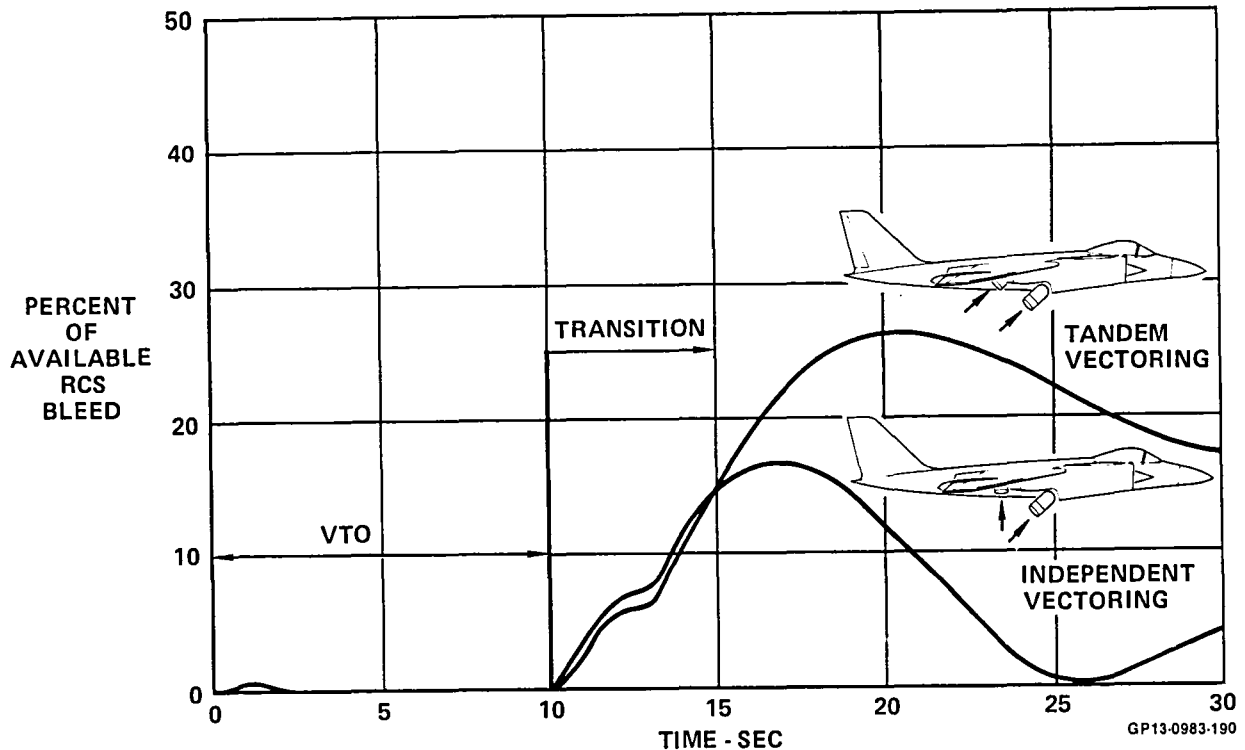
FIGURE 6-21
RCS PITCH TRIM REQUIREMENT

outset and building to higher rates as aerodynamic lift and control increases. Optimizing the vectoring schedules to enhance performance and aircraft controllability is a good candidate for future follow-on study.

Engine Thrust Characteristics for Trimming – Vectored thrust engines utilizing Fan Stream Burning (FSB) provide effective control system augmentation through automatic fan speed and FSB thrust modulation for pitch trim. When an external disturbance upsets aircraft trim balance, compensating pitch moments are generated by FSB thrust modulation while thrust-to-weight ratio is maintained by the simultaneous adjustment of engine power setting. The resulting change in the thrust split between forward and aft engine nozzles causes the thrust center to track the shift of the aircraft's center of gravity. The Reaction Control System (RCS) is thus reserved for use in aircraft attitude control.

The concept of integrated RCS and FSB thrust modulation for pitch trim is shown in Figure 6-22. Initial pitch control is provided by the RCS because of its faster response characteristics. However, compensating control moments are generated by changes in fan speed and FSB thrust which act to relieve the RCS. Ultimately, the FSB and engine generated moment completely controls the pitch disturbance, and the RCS is reserved for control requiring rapid response.

6-17
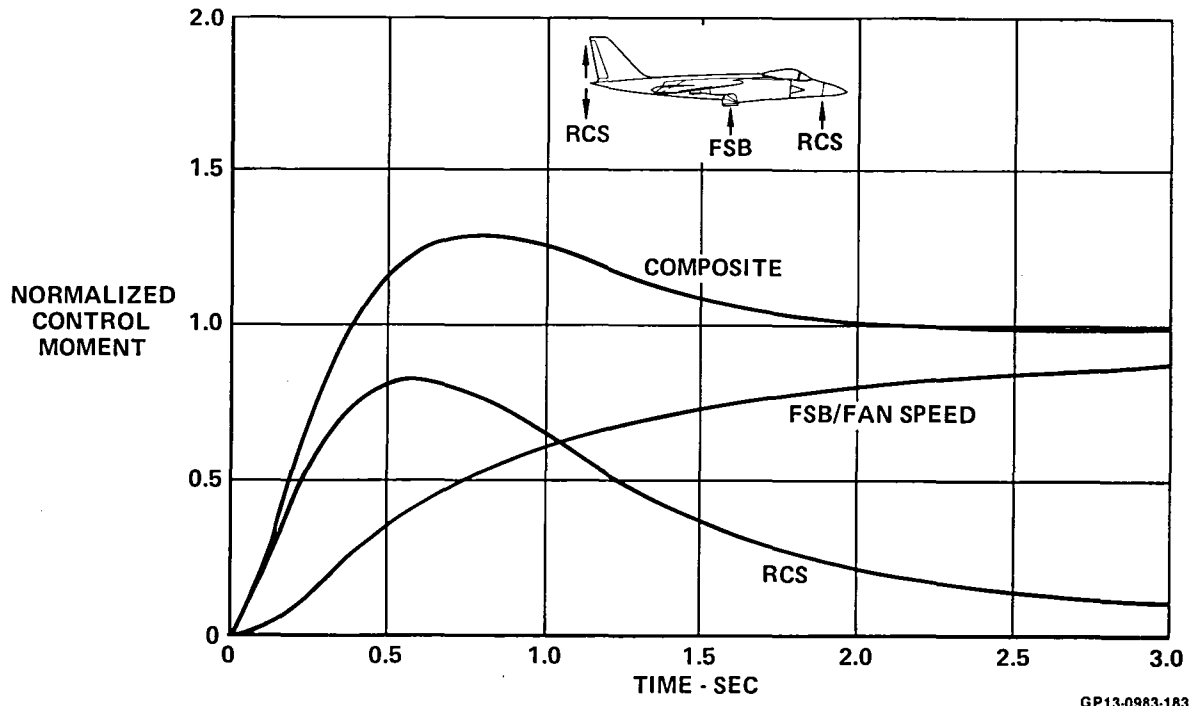
FIGURE 6-22
INTEGRATED CONTROL CHARACTERISTICS

In the integrated RCS and FSB thrust modulation control concept, the dynamic response of the thrust change must be matched to the engine response for uniformity in rates of change of total thrust for height control inputs. The characteristics of dynamic response to pitch control commands, as illustrated in Figure 6-22, indicate that the RCS will provide pitch control moments for all high frequency control activity. At low frequencies or inputs, however, FSB thrust changes will follow the initial RCS response and will relieve the RCS forces as the steady state commanded level is approached.

6.4 SHORT TAKEOFF AND LANDING

The STO performance presented in Figure 6-23 indicates 1,000 ft STO weights of 49,730 lb for sea level tropic and 52,150 lb for standard day. The technique used for STO is the same as the AV-8B. The aircraft is accelerated during the ground run with a nozzle setting of 10 degrees. As the aircraft reaches the rotation velocity the nozzles are rotated to a predetermined angle, based on the aircraft gross weight. A two degree of freedom computer program was used to define the takeoff distance-weight relationship.

Estimated carrier flat deck takeoff, Figure 6-24 indicates takeoff gross weights of 46,100 lb and 50,900 lb for deck lengths of 400 and 700 feet, respectively. These data are based on tropic day, 20 knot wind over deck and two feet of sink. The nozzles are rotated to an optimum setting 50 feet from the end of the deck to provide maximum performance for a given gross weight.
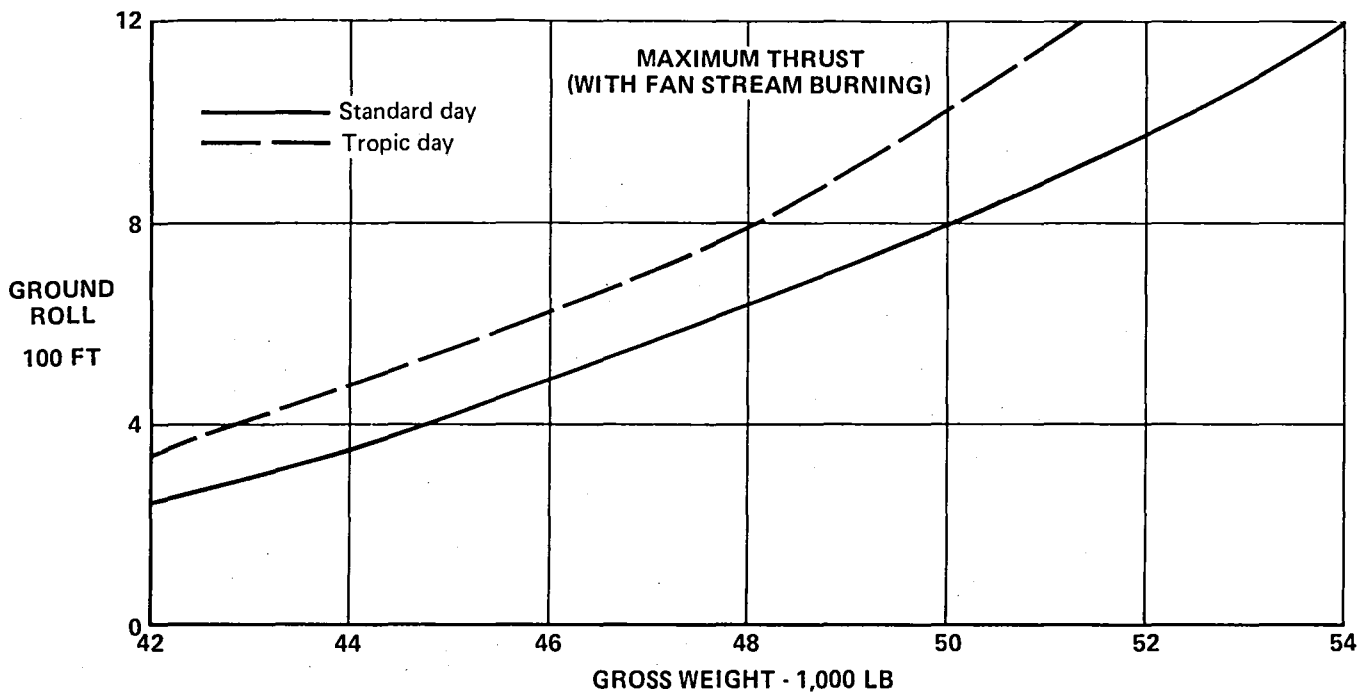
GP13-0983-203

FIGURE 6-23
SHORT TAKEOFF CAPABILITY
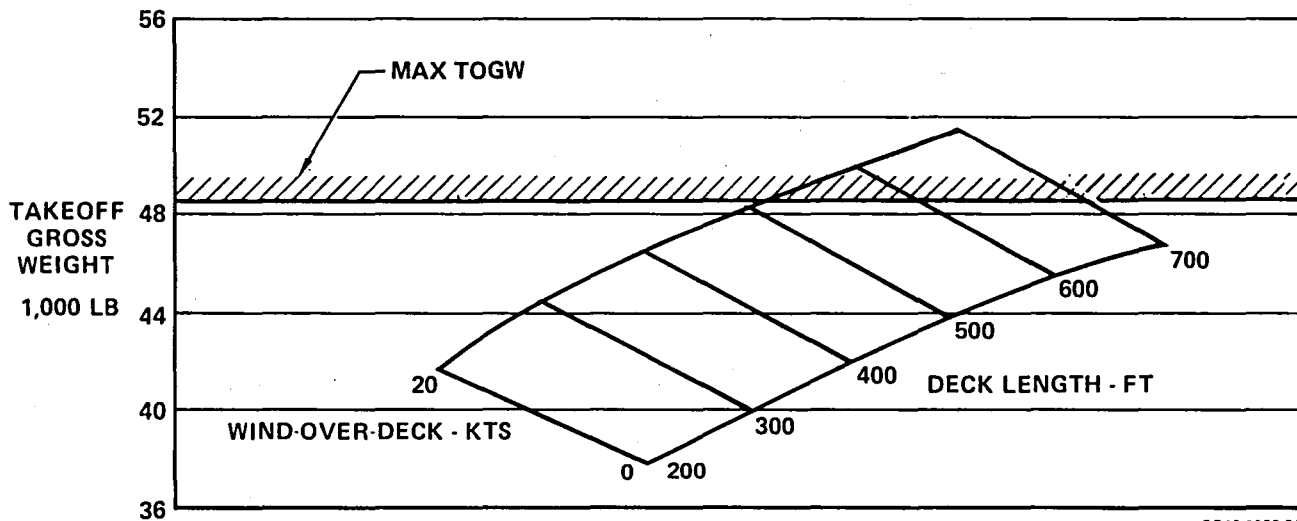
GP13-0983-241

FIGURE 6-24
FLAT DECK TAKEOFF PERFORMANCE
Maximum Thrust (With Fan Steam Burning)
Tropic Day   Two Feet Sink

6.5 SKI JUMP

The estimated ski jump capability, Figure 6-25, is based on a tropic day, deck takeoff from a 12 degree ramp. The ski jump technique is similar to the deck technique except that nozzle rotation doesn't occur until the aircraft leaves the ramp. Also, the angle of attack is different from a deck takeoff. Figure 6-26 presents the effect of ramp angle on ski-jump performance.
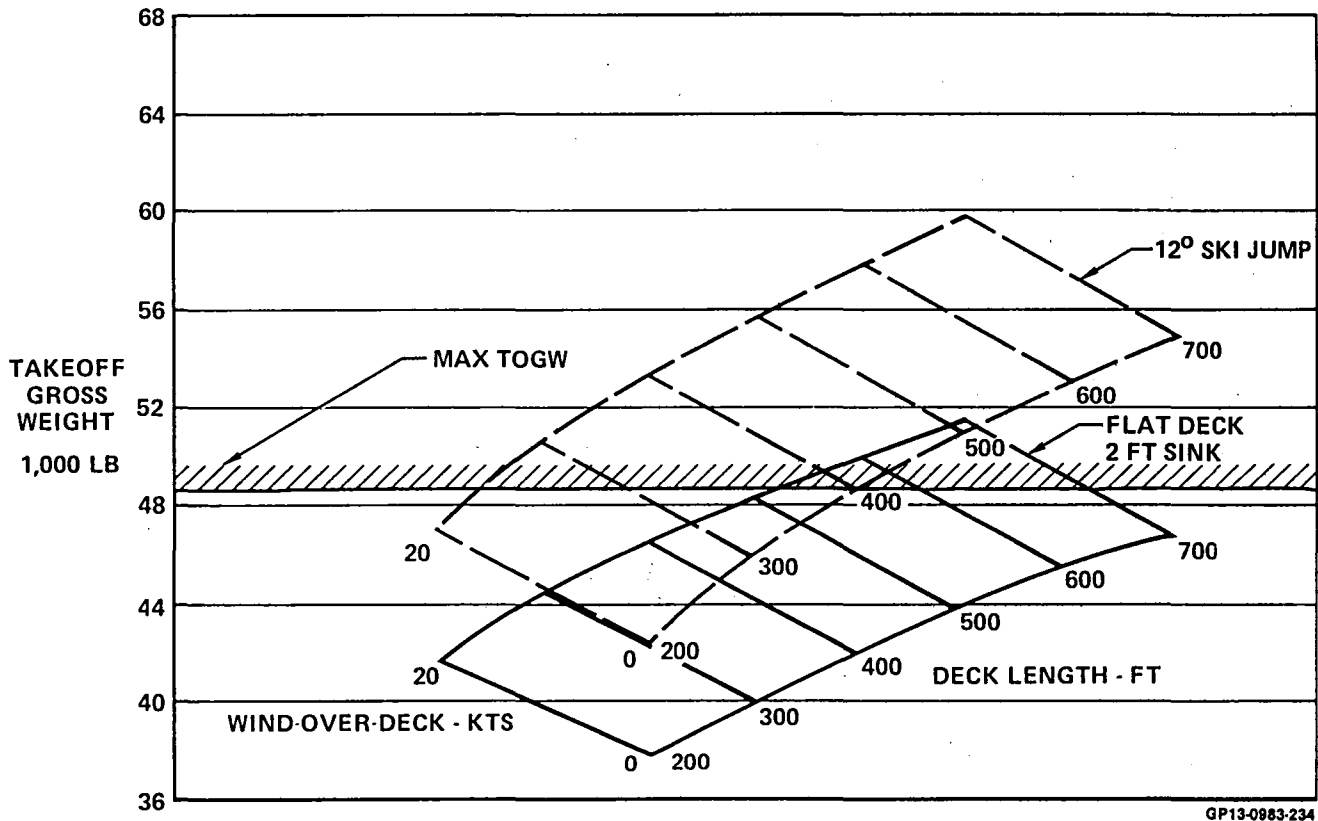
FIGURE 6-25
FLAT DECK/SKI JUMP TAKEOFF PERFORMANCE
Maximum Thrust (With Fan Stream Burning)   Tropical Day

The Model 279-3 is suited for a ski jump takeoff due to its high thrust to weight ratio, thrust vectoring capability, and reaction control system.

6.6 AIRCRAFT SENSITIVITES

To establish an understanding of the vehicle design drivers and their magnitudes, sensitivities of Vertical Takeoff Gross Weight (VTOGW), wing area and uninstalled thrust were computed. Parameters varied were, empty weight, zero lift drag, induced drag, engine thrust-to-weight ratio, specific fuel consumption, maneuvering requirements, design mission radius and VTO thrust-to-weight ratio. Variations in the above parameters were input into CADE and the Model 279-3 was sized to meet the NASA guidelines and a Vertical Takeoff DLI mission radius of 107 nm. Uninstalled thrust is for standard day, sea level static with the forward nozzles splayed 16 degree inward.
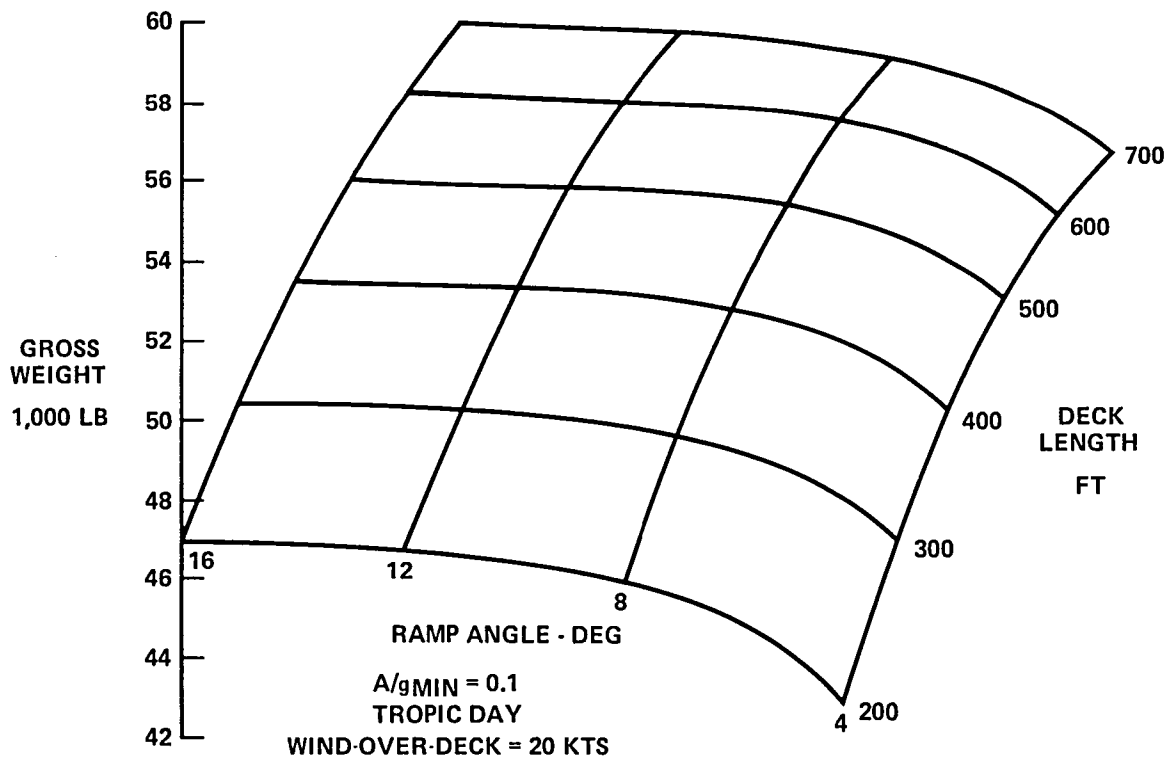
GP13-0983-115

FIGURE 6-26
EFFECT OF RAMP ANGLE ON SKI JUMP PERFORMANCE
Maximum Thrust (With Fan Stream Burning)

Figure 6-27 presents the effect of varying fixed empty weight. A 2,000 lb weight variation is approximately 10% of the empty weight and results in a VTOGW increase of 5,900 lb. For an aircraft sized to a VTO mission, empty weight has the greatest effect on aircraft size and weight. The effect of zero lift drag (C_{D_o}), Figure 6-28 and induced drag (C_{D_i}), Figure 6-29 are separated according to speed regime; subsonic, supersonic and subsonic and supersonic combined. Aircraft size is relatively insensitive to subsonic C_{D_o} but supersonic C_{D_o} has a much larger effect because of the 1.6 Mach number dash requirement of the DLI design mission. Just the opposite is true with induced drag, supersonically the dash occurs at a low lift coefficient and induced drag is small. However, subsonic induced drag drives the wing size required for maneuvering. The effect of uninstalled engine thrust-to-weight and Specific fuel consumption (SFC) are presented in Figure 6-30 and Figure 6-31 respectively. SFC is about twice as sensitive as the engine thrust-to-weight ratio. A 10% increase in SFC results in a 2,500 lb increase in VTOGW. Figure 6-32 presents the effect of maneuvering requirements. A 10% increase in sustained load factor results in a VTOGW increase of 2,600 lb. Figure 6-33 indicates a DLI mission radius of 125 nm would increase the VTOGW to 31,300 lb and the wing area to 455 ft^2. The effect of VTO thrust-to-weight ratio $(T/W)_{VTO}$ is presented in Figure 6-34. An increase in the $(T/W)_{VTO}$ of 10% increases the VTOGW by 1,000 lb.

The increase in $(T/W)_{VTO}$ oversizes the engine for cruise, loiter and dash resulting in higher SFC which drives the configuration to a larger size to complete the design mission.
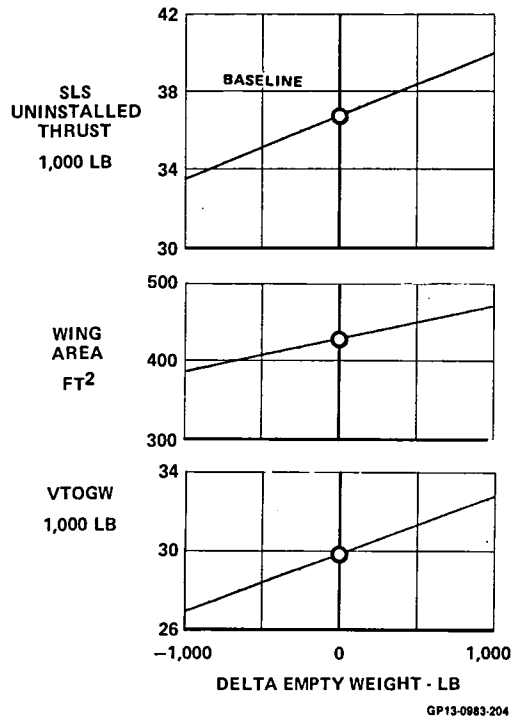
FIGURE 6-27
SENSITIVITY TO EMPTY WEIGHT
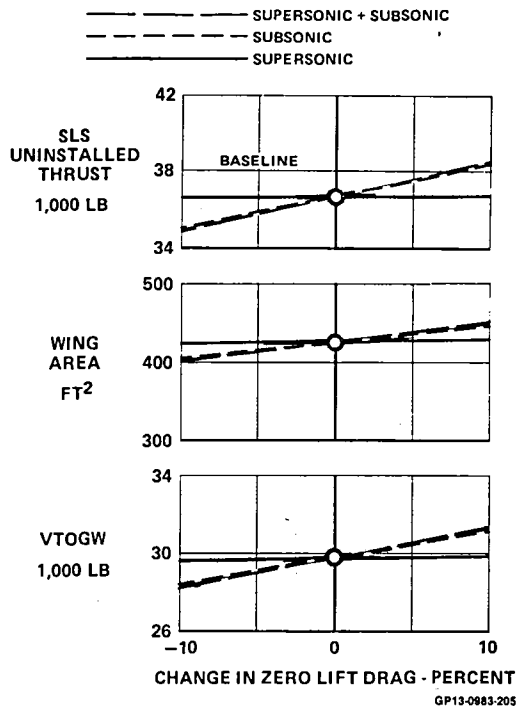
FIGURE 6-28
SENSITIVITY TO ZERO LIFT DRAG

SLS
UNINSTALLED
THRUST
1,000 LB

42

38

34

BASELINE

WING
AREA
FT^2

500

400

300

VTOGW
1,000 LB

34

30

26
-10   -5   0   5   10
DELTA INDUCED DRAG - PERCENT
GP13-0983-206
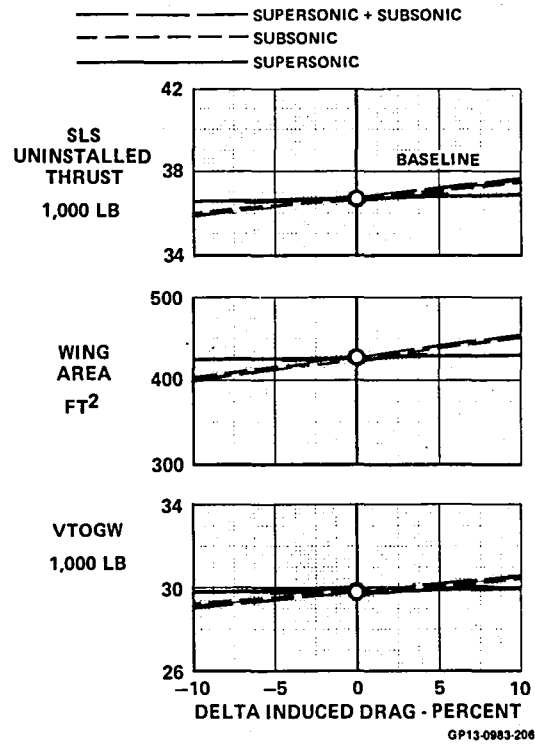
FIGURE 6-29
SENSITIVITY TO INDUCED DRAG

SLS
UNINSTALLED
THRUST
1,000 LB

42

38

34

BASELINE

WING
AREA
FT^2

500

400

300

VTOGW
1,000 LB

34

30

26
9   10   11   12
ENGINE THRUST-TO-WEIGHT RATIO
GP13-0983-207
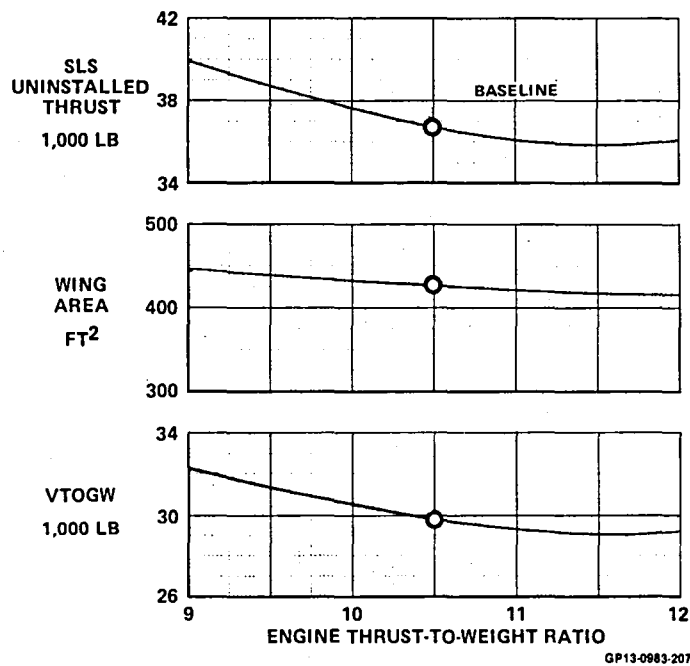
FIGURE 6-30
ENGINE THRUST-TO-WEIGHT RATIO SENSITIVITY

6-23
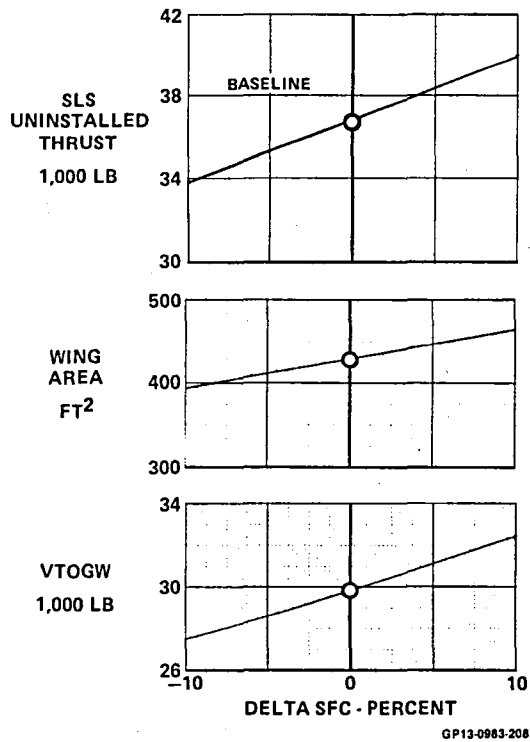
FIGURE 6-31
SENSITIVITY TO SPECIFIC FUEL CONSUMPTION
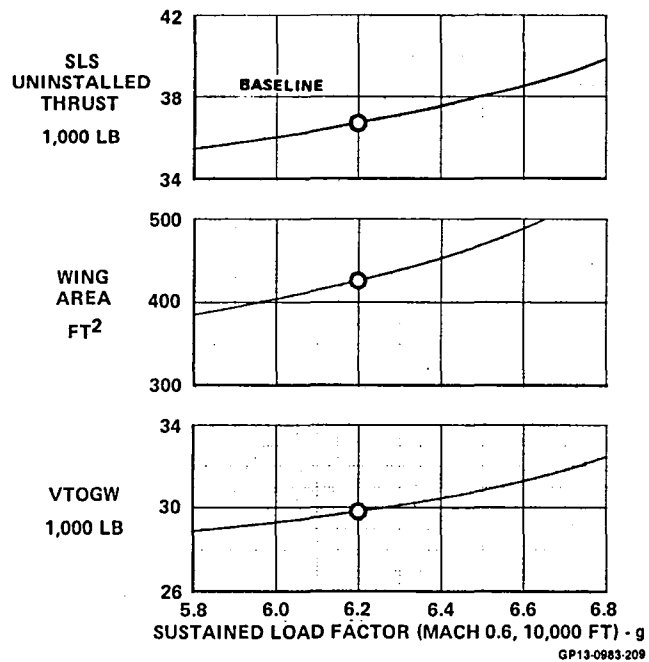
FIGURE 6-32
SENSITIVITY TO MANEUVERING REQUIREMENT
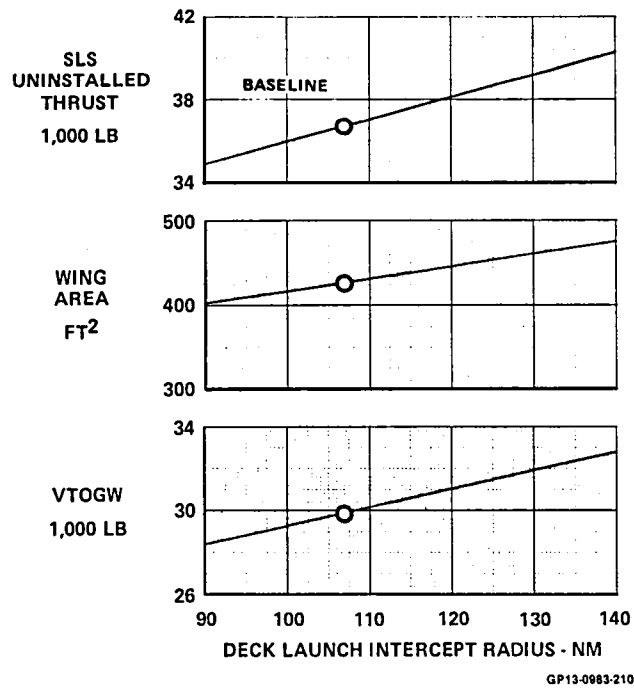
FIGURE 6-33
SENSITIVITY TO DESIGN MISSION (DLI) RADIUS
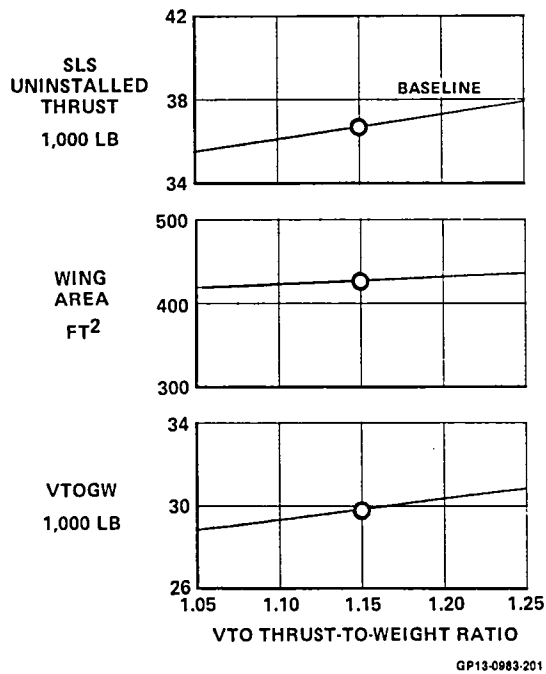
FIGURE 6-34
SENSITIVITY TO VTO THRUST-TO-WEIGHT RATIO

6-25

PAGE 6-26 IS BLANK

7. AERODYNAMIC UNCERTAINTIES

The aerodynamic characteristics of the Model 279-3, Section 4, have been estimated using a combination of analytical and empirical techniques. In the estimation of these characteristics, a number of aerodynamic parameters were identified that could not be quantified within an acceptable confidence level. When the design studies, Section 2, and performance sensitivity studies, Section 6, suggested that variations of the parameter within the confidence level would have a sufficient impact on the aircraft performance, maneuverability, stability or control to significantly affect its size and cost, the parameter was termed an uncertainty. The following sections describe and assess the selected uncertainties. In Section 8, a wind tunnel test program is proposed to resolve them.

7.1 SELECTION OF UNCERTAINTIES

Many of the aerodynamic uncertainties result from nonlinearities that occur as the angle of attack or control surface deflections cause regions of separated flow to occur on the aircraft. These must be resolved experimentally, but the reasons for their occurrence are known and expected. Other uncertainties arise from the interaction between closely coupled aerodynamic surfaces or between the aerodynamic surfaces and propulsion system. These uncertainties are highly configuration dependent.

Table 7-1 tabulates the aerodynamic uncertainties and identifies the source of the uncertainty. The impact of each uncertainty on aircraft performance was determined from the sensitivity studies described in Section 6 and its significance to a particular design parameter is shown in Table 7-2. It can be seen that each of these uncertainties has a major impact on the design of the aircraft. Therefore, it must be resolved and optimized before the source of the uncertainty can be fully exploited in the design process.

TABLE 7-1
AERODYNAMIC UNCERTAINTIES IDENTIFIED DURING STUDY

UNCERTAINTY	SOURCES			
	WING AND CLOSE-COUPLED CANARD	L E AND T E FLAPS	LARGE INLET	FORWARD LOCATION OF PROPULSION SYSTEM
$C_{D_{MIN}}$	√	√	√	√
DRAG DUE TO LIFT	√	√		√
TRIM DRAG	√	√		
C_L BUFFET ONSET	√	√		√
C_L MAXIMUM	√	√		
LONGITUDINAL STABILITY	√	√		√
LONGITUDINAL CONTROL	√	√		
LATERAL-DIRECTIONAL STABILITY	√		√	
LATERAL CONTROL	√	√		

GP13-0983-144

TABLE 7-2
SIGNIFICANCE OF UNCERTAINTIES

UNCERTAINTY	SIGNIFICANCE	
	FLIGHT	DESIGN
SUPERSONIC $C_{D_{MIN}}$ SUBSONIC $C_{D_{MIN}}$ DRAG DUE TO LIFT TRIM DRAG	PERFORMANCE ↓	ENGINE SIZE FUEL FRACTION WING/ENGINE SIZE AND FUEL FRACTION WING/ENGINE SIZE AND FUEL FRACTION
C_L BUFFET ONSET C_L MAX	MANEUVERABILITY ↓	WING SIZE WING SIZE
LONGITUDINAL STABILITY LONGITUDINAL CONTROL STATIC LATERAL-DIRECTIONAL STABILITY LATERAL CONTROL	STABILITY AND CONTROL ↓	STATIC MARGIN CONTROL SURFACE SIZE TAIL SIZE AND WING DIHEDRAL CONTROL SURFACE SIZE

Significant aerodynamic uncertainties are associated with the close proximity of the horizontal canard to the wing. In general, the advantages of such a configuration are known, and are illustrated in Figure 7-1. Above the angle of attack at which the wing alone would stall, the vortex field of the canard augments the vortex field of the wing and causes the wing to continue to develop lift to higher angles of attack. This is true even when the canard itself is stalled. However, this increased wing lift cannot be accurately predicted nor can the stall angle of attack of the canard-wing combination be defined. The resulting interference flow field is very complex and current prediction techniques are inadequate. The paths of the shed vorticity cannot be predicted; especially when they combine with the vortex shed from the nose of the aircraft. The close coupled canard also leads to nonlinearities in the incremental effects of leading and trailing edge flaps and control surfaces, whether lateral or directional. Prediction methods for these uncertainties need to be developed but, in the meantime, these effects have to be resolved experimentally.

Another source of uncertainty lies in the interactive flow field between the aircraft and the propulsion system when it is located forward in the fuselage and in close proximity to the wing. One unknown arises from the power dependent effects of variable mass flow into or spillage from the inlets. This is not unique to the Model 279-3 configuration, but the large size of the inlets accentuates its impact. Another aerodynamic uncertainty is due to the change of cross-sectional area distribution resulting from the forward location of the propulsion system, including the nozzles. Since it is different from the other aircraft making up the empirical data base, these effects are hard to estimate. The cross sectional area distribution affects the aircraft integration, Figure 7-2, and the validity of the aerodynamic predictions, especially at supersonic speeds. The necessity of resolving this uncertainty is shown by the zero-lift drag sensitivity studies of Section 6.6. Both uncertainties can be investigated with a flow-through wind tunnel model, and are addressed in the proposed research plan.
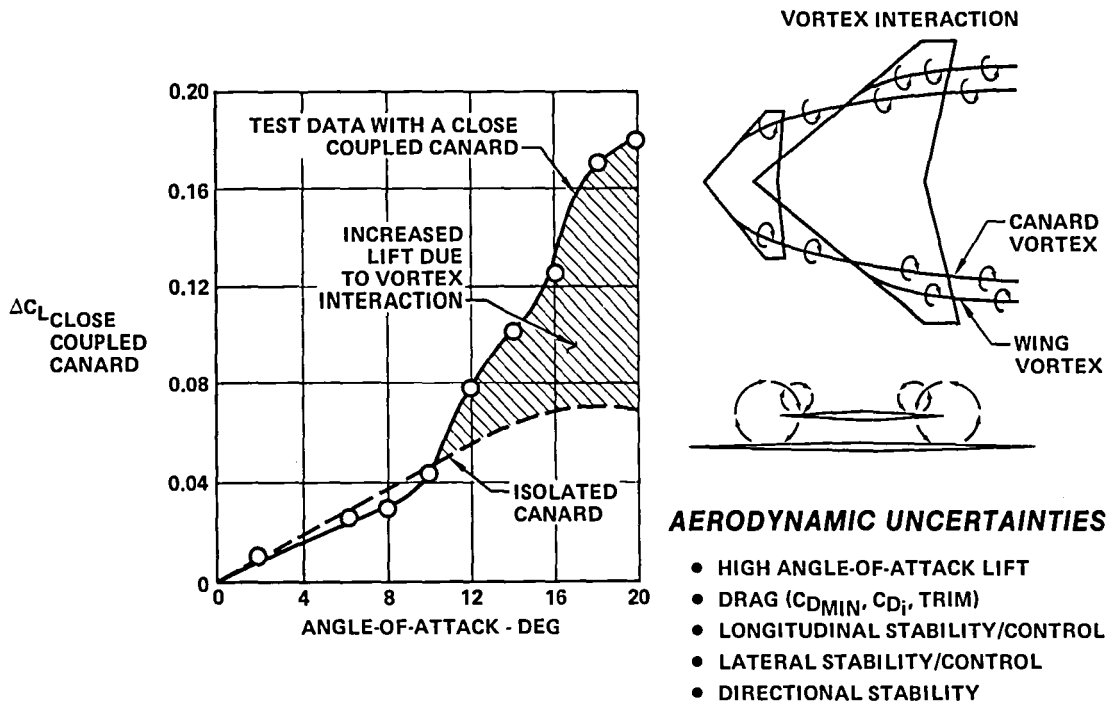
FIGURE 7-1
AERODYNAMIC UNCERTAINTIES DUE TO CLOSE-COUPLED CANARD

AIRCRAFT INTEGRATION

- MID TO HIGH WING
- HIGH CANARD LOCATION
- LARGER VERTICAL TAIL
- INLET/DIFFUSER INTEGRATION
- INCREASED $S_{C/S}$ RATE OF CHANGE
- NOZZLE FLOW IMPINGEMENT
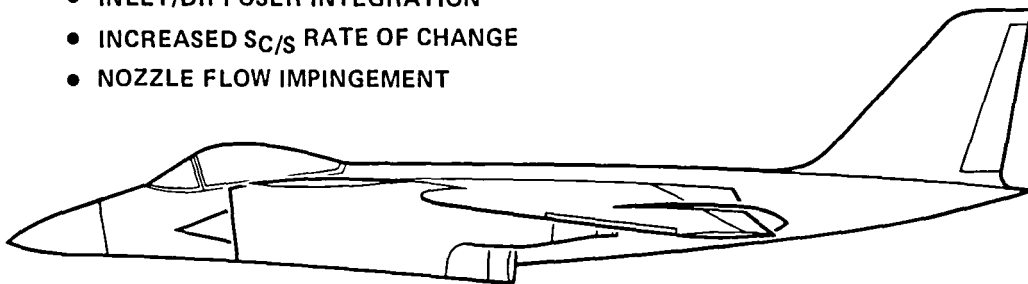
AERODYNAMIC UNCERTAINTIES

- MINIMUM DRAG (SUBSONIC AND SUPERSONIC)
- DRAG DUE TO LIFT
- BUFFET ONSET LIFT COEFFICIENT
- LONGITUDINAL STABILITY
- INDUCED LIFT

GP13-0983-165

FIGURE 7-2
AERODYNAMIC UNCERTAINTIES DUE TO FORWARD LOCATION OF PROPULSION SYSTEM

7-3

Other uncertainties develop from interactions between the high energy exhaust jets of the propulsion system and the aircraft flow field. These include plume and scrubbing drag effects, induced flow field effects on the wing, and interference between the jets and the maneuvering flap system. The effects of these uncertainties are large and must be investigated. However, provision of the high velocity jets requires a specialized jet effects model. Such a model is outside the scope of the proposed Phase II research plan but, due to the importance of the power induced uncertainties, conversion of the proposed flow-through model into a jet-effects model is discussed in Section 8.2.

7.2 DESCRIPTION OF THE UNCERTAINTIES

While the aerodynamic uncertainties can be described in terms of lift, drag, side force and their respective moments, it is more informative from the point of view of the design of an experimental program to determine which configurational components contribute to the uncertainties. In this way the matrix of test variables can be reduced to include only those shown to have the most pronounced effect. Consequently, this section addresses not only the uncertainty and the configurational component, but does so from the point of view of comparative examples to show the source and magnitude of the uncertainty.

7.2.1 DRAG - Minimum drag can be estimated from analytical methods based on the theory of boundary layer flow on flat plates and coupled with empirical factors to account for three-dimensional and thickness effects. Such empirical factors are very configuration oriented. They are usually restricted to simple configurations where spanwise and chordwise pressure variations are small. However, closely coupled canard-wing configurations establish an interactive flow field between the two. Local supervelocities set up pressure fields that have large three-dimensional gradients. Calculation of the boundary layer flow in such pressure fields is currently beyond the state-of-the-art and, therefore, drag must be determined experimentally. This is especially true when the wing or canard is cambered and/or twisted.

When a trailing edge flap is included, the problem is compounded. The canard generates a downwash field that should help the flow remain attached to the flap surface. However, this is only true for that portion of the flap inboard of the canard tip vortex or the combined vortex of the interacting wing and canard. Outboard of this vortex there is an upwash on the flap that should promote premature separation. Again, the complexity of this flow field requires experimental resolution of the uncertainty in predicting the effects of the canard and canard deflection.

The uncertainties resulting from prediction of the induced drag of a wing-canard configuration are associated with:

   o Wing-body interference,

   o Effect of horizontal canard, and

   o Effect of trailing edge flaps.

Those associated with analytically predicting the induced drag of a simple wing-body configuration are addressed in Figure 7-3. Even though the Vortex-Lattice method includes 100% leading edge suction, the camber and twist distribution of the test wing causes its induced drag to be smaller than the analytical predictions at low lift coefficients. At the larger lift coefficients, local flow separations cause the drag to increase rapidly. The linearized vortex-lattice method cannot predict the effects of these separations. However, the MCAIR statistical method shows good agreement with test data over the entire range of lift coefficients. This method was developed specifically for wing-body and wing-body-horizontal tail configurations. As long as the given configuration fits within the matrix used in its development, it yields good results up to high angle of attack and over the Mach number range.
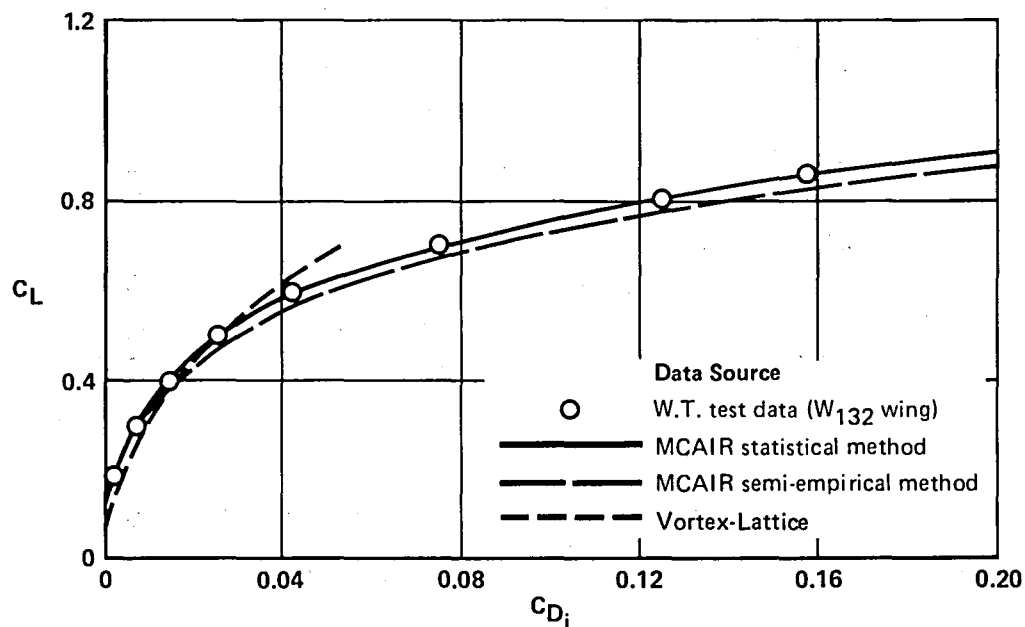
GP13-0983-155

FIGURE 7-3
MODEL 279-3 WING-BODY INDUCED DRAG AT MACH 0.6

Addition of a canard to the wing-body configuration invalidates the use of the MCAIR Statistical or Semi-Empirical Methods, which have no provision for a horizontal canard, to predict the wing-body-canard induced drag. Figure 7-4 presents a comparison of analytically and empirically predicted induced drag increments due to the Model 279-3 canard. The empirical estimate for the Model 279-3 was determined from 3-Surface F-15 test data. The analytical Vortex-Lattice predictions shown in Figure 7-4 underestimated the canard induced drag at low lift coefficients. Analytical methods like Vortex-Lattice also cannot predict the influence of the horizontal canard on the drag break due to leading edge boundary layer separation.

A combination of analytical methods also was tried. Since the induced drag prediction of the MCAIR statistical method is valid for the canard-off configuration, it was subtracted from the wing-body-canard induced drag as predicted by the Vortex-Lattice method. This increment also shows poor agreement with the empirically derived curve in Figure 7-4.
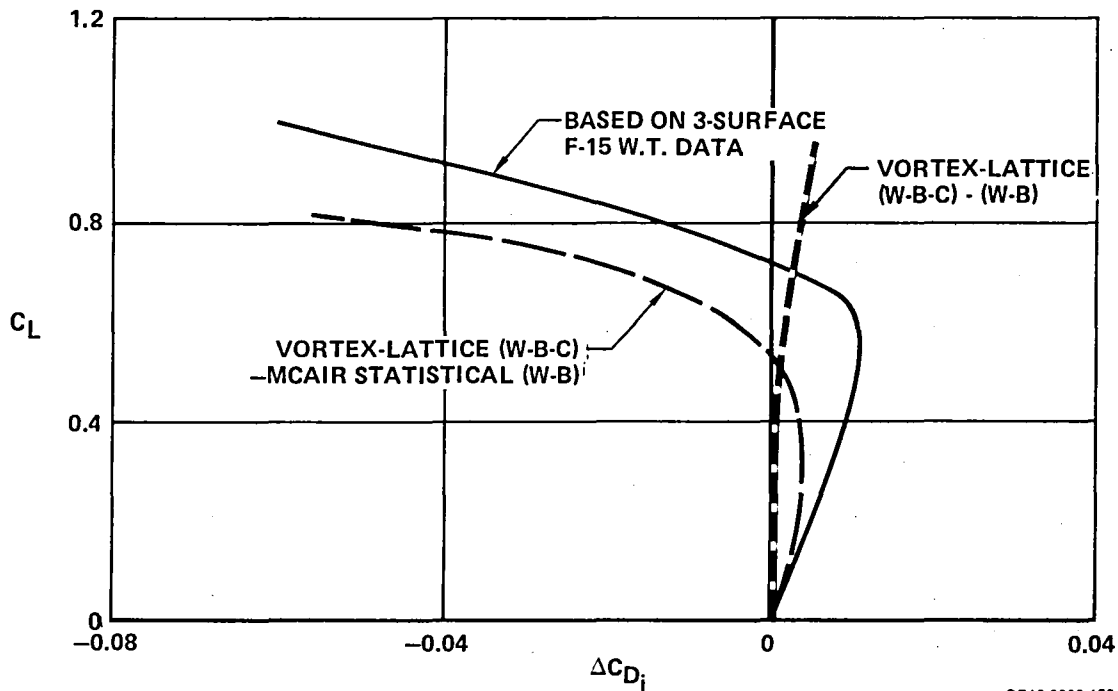
FIGURE 7-4

MODEL 279-3 EFFECT OF HORIZONTAL CANARD ON INDUCED DRAG AT MACH 0.6

Section 6-6 shows that the aircraft design parameters are sensitive to variations of induced drag subsonically. In addition, good estimates of the trimmed drag are necessary for accurate performance calculations at all Mach numbers. Since existing analytical methods do not appear to provide accurate estimation of wing-body-canard induced drag, especially at high angle of attack, the induced drag is a major uncertainty to be found experimentally.

7.2.2 <u>LIFT</u> – As mentioned earlier, the interaction between the canard and the wing sets up a pressure field on the wing that has strong spanwise and chordwise gradients. This makes separation dependent phonomena, such as the maximum lift coefficient or the lift coefficient for buffet onset, very hard to predict, either analytically or empirically. In addition, interaction of the leading edge vortices from the canard and wing has a pronounced effect on the lifting combination. Lift continues to increase linearly with increasing angle of attack, even though wing surface flow visualization data indicate that the flow in this region is predominately spanwise. When this occurs, the maximum lift coefficient and buffet onset lift coefficient become functions of vortex bursting. Unfortunately, vortex bursting cannot yet be predicted analytically, nor are its scaling laws understood.

At transonic and supersonic speeds, the presence of the canard modifies the shock wave patterns on the wing. The canard either modifies the onset flow of the wing or, for some variations of Mach number and configuration, shock waves from the canard impinge on the wing. The results are deviations of lift and drag from values predicted by linearized methods. Specifically, the transonic or supersonic lift curve slope cannot be accurately established for the canard-wing combination.

7.2.3 LONGITUDINAL STABILITY - The flow phenomena discussed above, that change the lift and drag of canard-wing aircraft configurations in an unpredictable fashion, affect the stability and control characteristics in a like manner. Attempts to analytically predict the longitudinal stability characteristics of several canard-wing configurations have identified a number of uncertainties. They are:

o The level of supersonic stability,

o Linearity with angle of attack,

o The effect of a canard at high angle of attack, and

o The difficulty of scaling canard wind tunnel data.

Current prediction methods are known to predict the neutral point of wing-horizontal tail configurations quite well in the subsonic flow regime. This holds true for canard-wing or 3-surface configurations as well, although these configurations are more sensitive to the paneling methods used to represent the aircraft components. Supersonically, the analytical methods are not as dependable. Figures 7-5 and 7-6 compare the results of neutral point
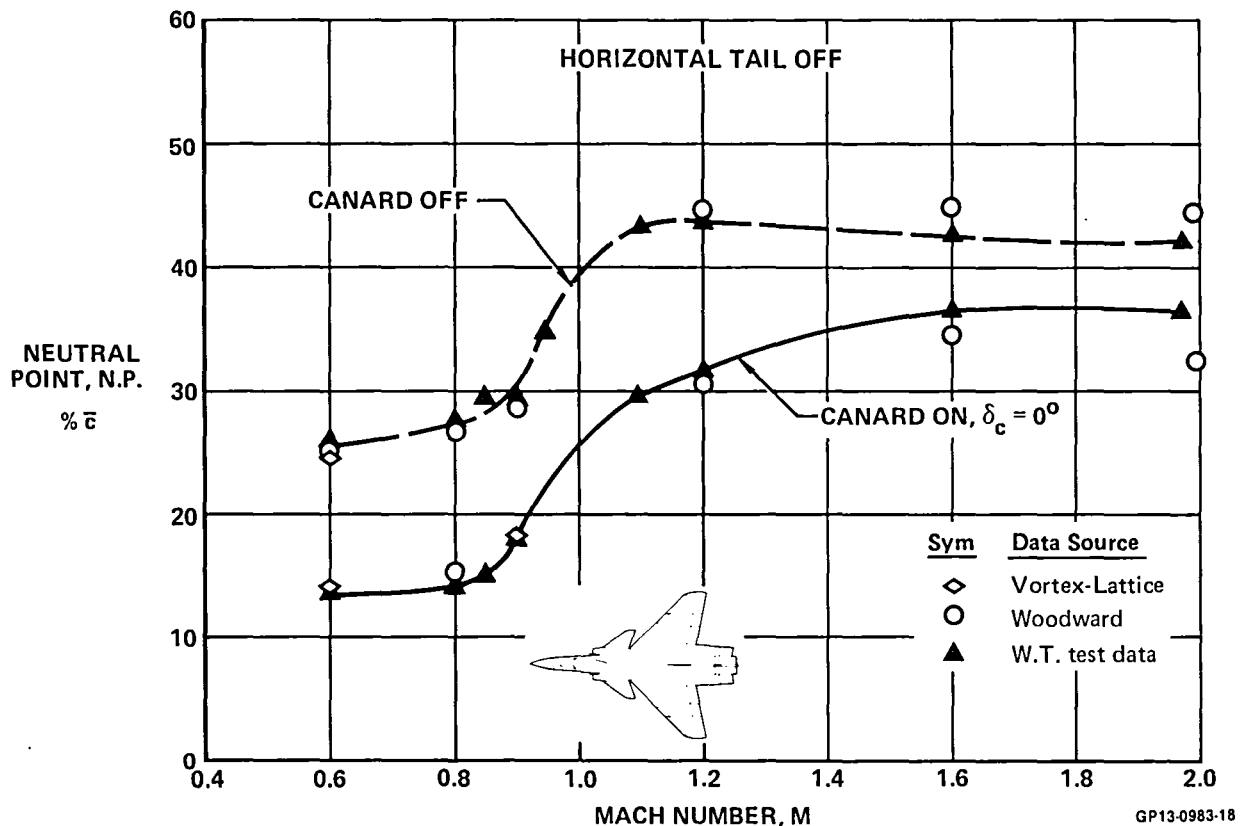
GP13-0983-18

FIGURE 7-5

MODEL 263 (ANF) · LONGITUDINAL STABILITY CHARACTERISTICS
Comparison of Analytical Results and Wind Tunnel Test Data
$S_C/S_W = 0.96$
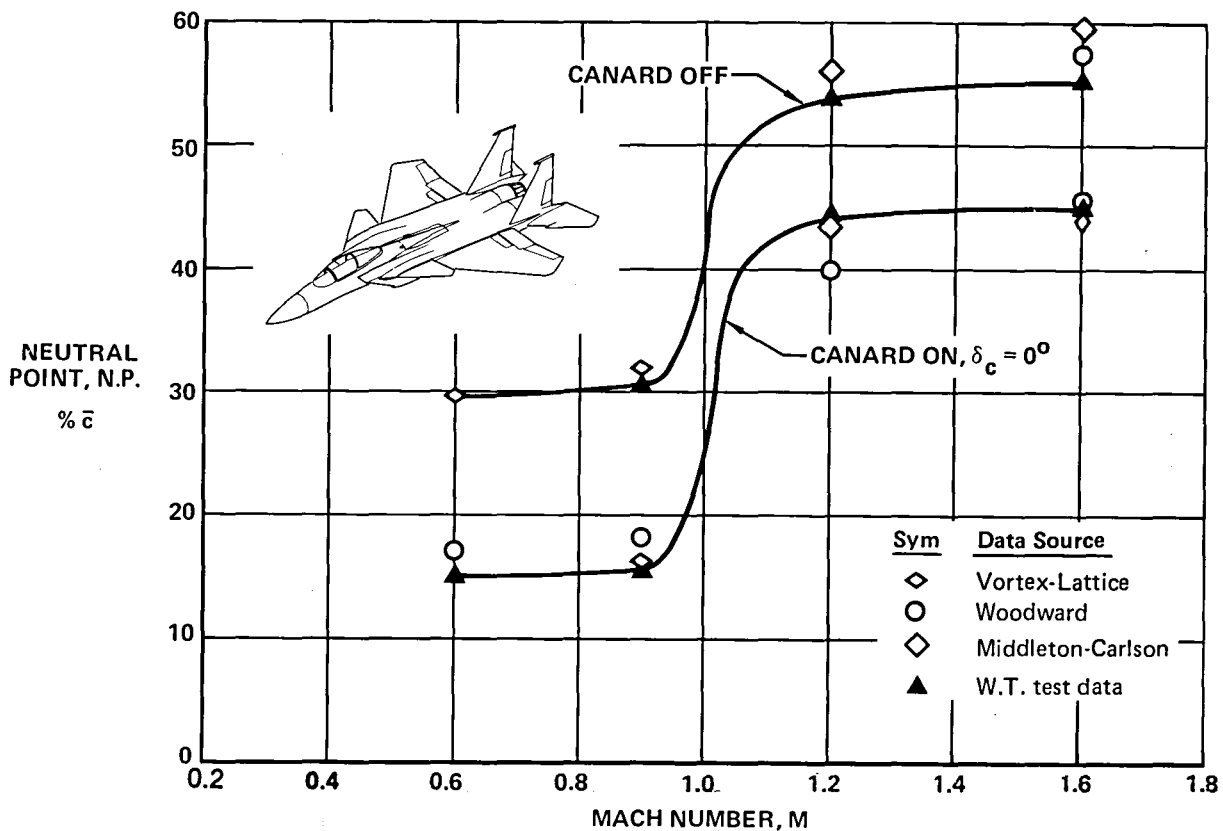
FIGURE 7-6

3-SURFACE F-15 LONGITUDINAL STABILITY CHARACTERISTICS
Comparison of Analytical Results and Wind Tunnel Test Data
$S_C/S_W = 0.099$

calculations for two configurations for which wind tunnel test data were available. In both cases the analytical methods overpredict the supersonic aft neutral point shift for the wing—body combination. When the canard is added the analytical methods significantly over-predict its destabilizing effect supersonically from 55 to 75%.

Figure 7-7 shows the longitudinal stability characteristics of the Model 279-3 as predicted by the various analytical methods. There is a good agreement between the methods in the subsonic speed range. Thus, the subsonic neutral point was estimated with confidence. Supersonically, the two methods show much poorer agreement. For the wing-body configuration there is approximately 2% c̄ difference between the predictions of the two methods. The Woodward method also predicts a greater effect of the presence of the canard, differing from the Middleton-Carlson method, by 4% at Mach 1.6. The supersonic Model 279-3 neutral point location shown in Figure 7-7 was arrived at by adjusting the analytically estimated neutral point reflecting the differences shown in Figures 7-5 and 7-6. These values vary from the analytical predictions by 3% to 5% c̄. This level of uncertainty of the neutral point is carried over to the static margin once the aircraft is balanced. Uncertainties in static margin lead to uncertainties of maneuverability, trim drag or other performance parameters.
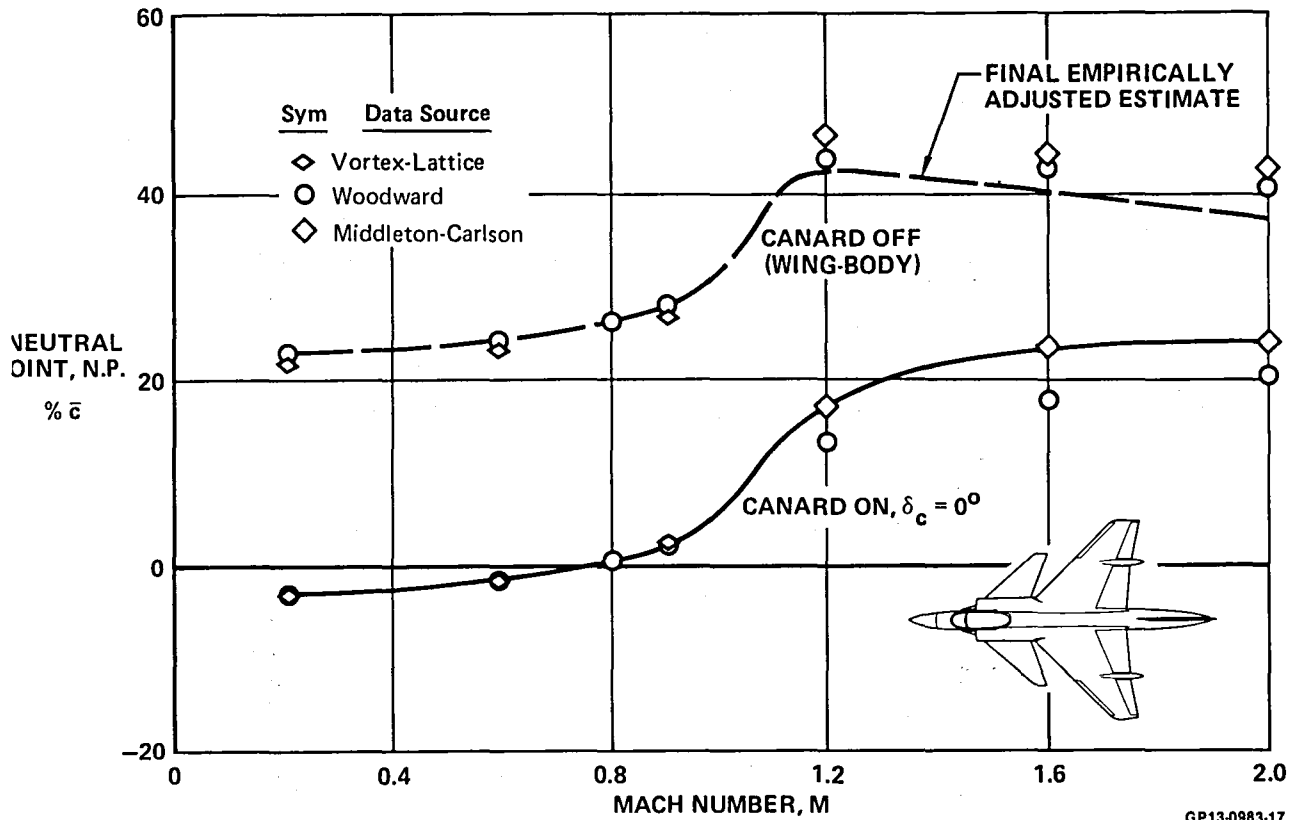
FIGURE 7-7
MODEL 279-3 LONGITUDINAL STABILITY CHARACTERISTICS
$S_C/S_W = 0.2$

The method used to empirically scale data from one configuration to another can also add to the uncertainties unless the configurations are very similar. This is illustrated in Figure 7-8 where the canard effect on lift and pitching moment of the Model 279-1 configuration was empirically predicted using 3-Surface F-15 canard data. First the 3-Surface F-15 canard effects were scaled on the basis of the exposed canard area. These predicted increments were twice as much as those determined by Model 279-1 wind tunnel test. They were then scaled on the basis of the theoretical canard area. This resulted in predicted increments smaller than the test results. The inability to accurately scale 3-Surface F-15 canard effects to those of the Model 279-1 was attributed to the difference in the canard configurations. The 3 Surface F-15 horizontal canard is mounted on the side of the inlets where as the Model 279-1 canard is mounted on the fuselage since it has a chin inlet. The F-15 canard therefore has a larger carryover (effective area) than that of the 279-1. Canard effects therefore have to be scaled based on this effective area rather than exposed or theoretical area.

The same 3-Surface F-15 data were used to predict the canard effects of a parametric model which has side mounted inlets and thus a wide fuselage in the region of the canards like the F-15. For this configuration the empirically predicted increments, scaled using exposed canard area, agree very well with those determined by test, Figure 7-9.

CONFIGURATION	S_c/S_w (EXPOSED)	$\overline{V}_c$ (EXPOSED)	S_c/S_w (THEO)	$\overline{V}_c$ (THEO)
MODEL 279-1	0.2	0.154	0.279	0.24
3 SURFACE F-15	0.099	0.057	0.323	0.274

————————— Model 279-1 (chin inlet)
— — — — — Scaled 3-Surface F-15 data
(based on exposed canard area)
— — — Scaled 3-Surface F-15 data
(based on theoretical canard area)
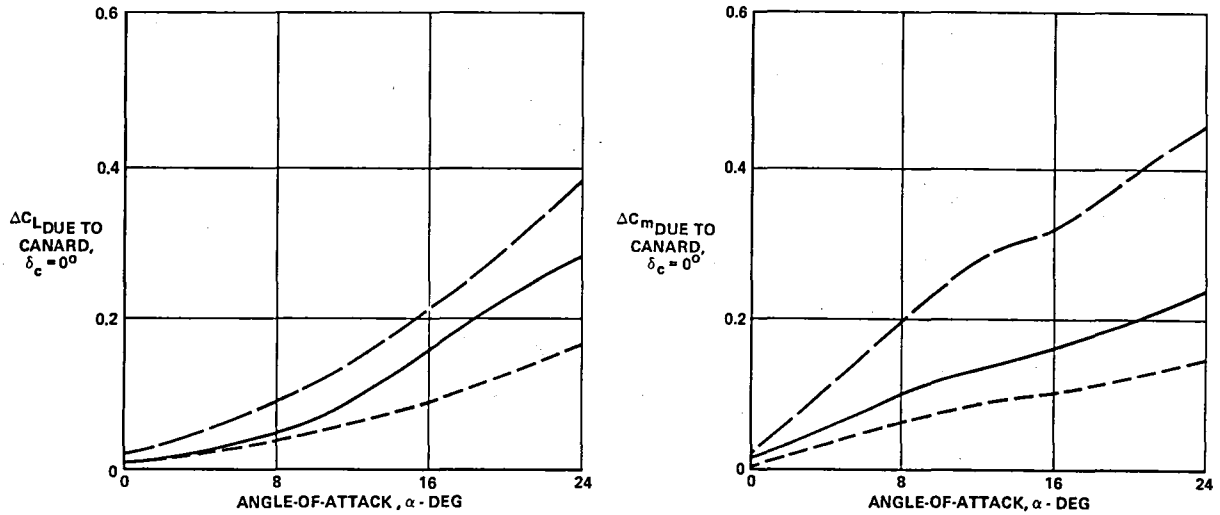
GP13-0983-97

FIGURE 7-8
COMPARISON OF MODEL 279-1 CANARD INCREMENTS TO SCALED 3-SURFACE F-15 DATA
Mach 0.2

CONFIGURATION	S_c/S_w (EXPOSED)	$\overline{V}_c$ (EXPOSED)
MODEL 279-4	0.200	0.103
3-SURFACE F-15	0.099	0.057

————— Parametric model (side inlets)
— — — Scaled 3-surface F-15 data
(Based on exposed canard area)
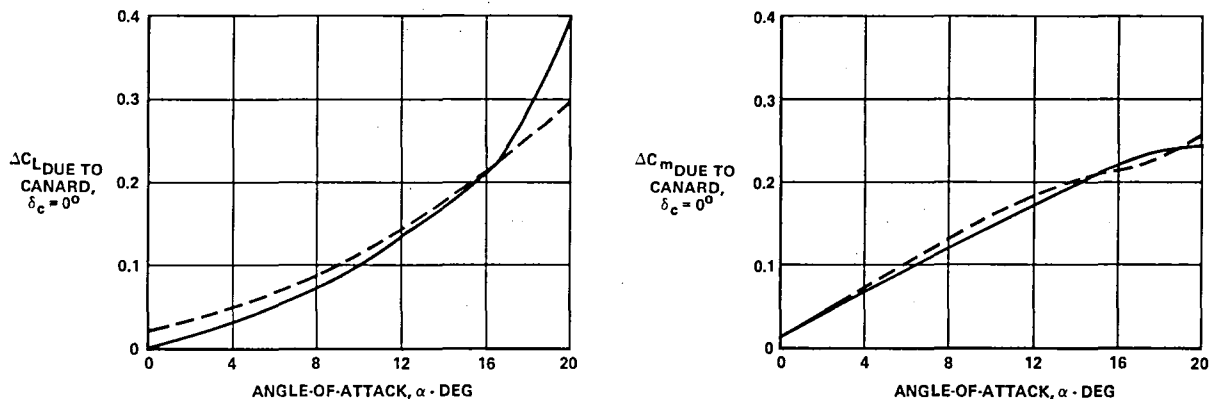
GP13-0983-88

FIGURE 7-9
COMPARISON OF MODEL 279-4 CANARD INCREMENTS TO SCALED 3-SURFACE F-15 DATA
Mach 0.2

Additional uncertainties also can arise in trying to scale canard effects at high angle of attack. An example is shown in Figure 7-10 for the 3-Surface F-15. As the size of the canard is increased, the increment of lift due to the canard increases. For small canards, or at transonic speeds, the region of influence of the canard is restricted to the wing root region. In this case, the incremental lift due to canard size increases approximately linearly.
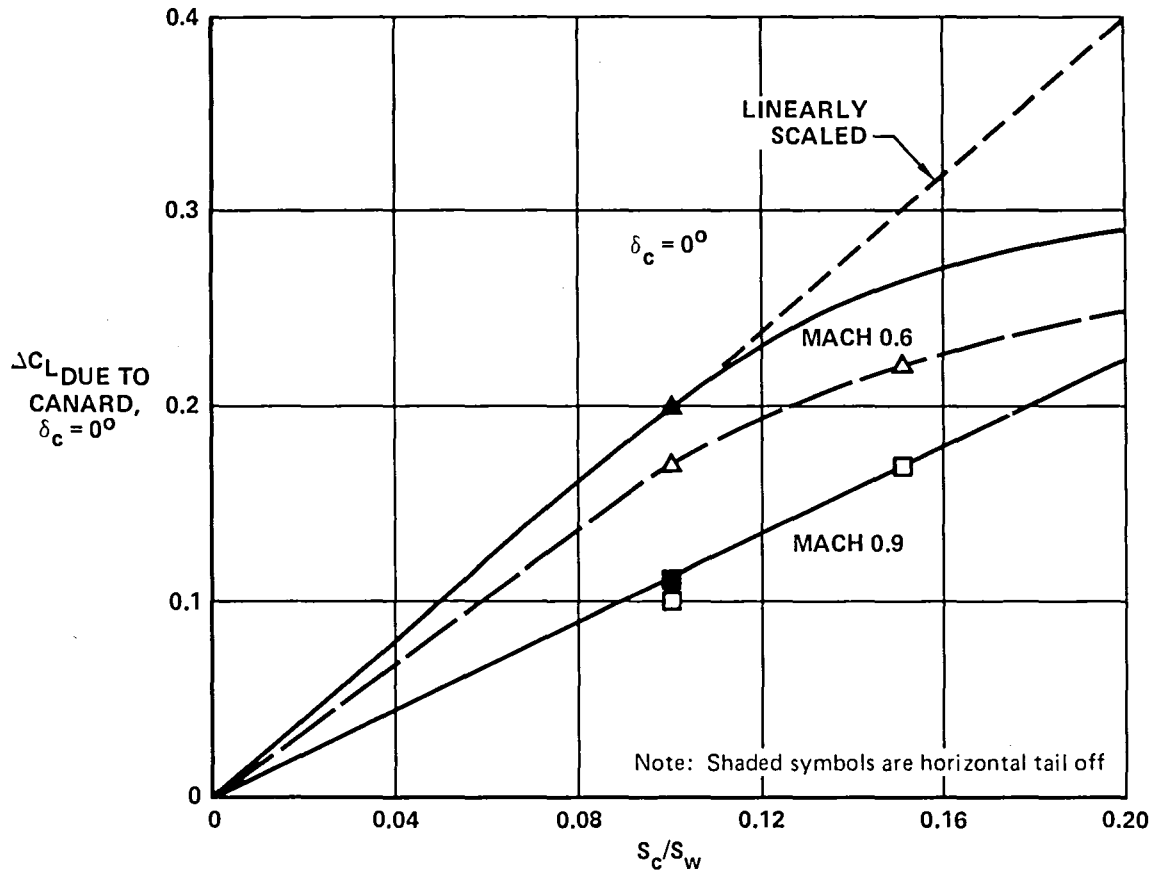
GP13-0983-23

FIGURE 7-10
3-SURFACE F-15 EFFECT OF HORIZONTAL CANARD ON LIFT AT $\alpha = 24°$
$h_c/c \simeq 0.1$

However, as canard size is increased, the region of influence extends toward the wing tip. The reduced lift potential at the tip reduces the rate at which the presence of the canard can increase lift. In Figure 7-10, the lift increment for a canard with an exposed area of 20% of the wing area would have been overpredicted by 40% if a linear scaling had been used. These effects are very configuration dependent and can only be accurately determined by wind tunnel testing.

7.2.4 <u>LONGITUDINAL CONTROL</u> – The uncertainties identified in estimating the longitudinal control characteristics of the Model 279-3 configuration are:

    o Supersonic canard effectiveness,

    o Variation of longitudinal control with canard deflection,

o Variation with angle of attack,

o Effect of the canard on trailing edge flap effectiveness, and

o Difficulty of scaling canard wind tunnel data.

The uncertainties stem from limitations of the analytical methods at supersonic speeds, the occurrence of large regions of separation on the wing or control surfaces, and the distortion of the trailing vorticity by the flow field around the total aircraft configuration. Comparisons with wind tunnel data are used to illustrate the magnitude of the uncertainties.

The available aerodynamic analysis methods were used to predict the canard powers of the 3-Surface Model 263 (ANF) configuration, Figure 7-11 and the 3-Surface F-15 configuration, Figure 7-12. The results corroborated the conclusions of the previous section. Subsonically, the prediction methods determined the canard powers of both configurations within 10%. Supersonically, the prediction methods were high from 30% to 60%. The canard pitch control effectiveness of the Model 279-3 aircraft was estimated as shown in Figure 7-13. The Vortex-Lattice method results were considered accurate subsonically. The results of the supersonic prediction methods had the proper trends, but were empirically reduced by 33% to estimate the proper level. This determined level of supersonic pitch control effectiveness also agreed well with that from scaled 3-Surface F-15 data. Wind tunnel testing, however, is the only way to accurately determine the right values.
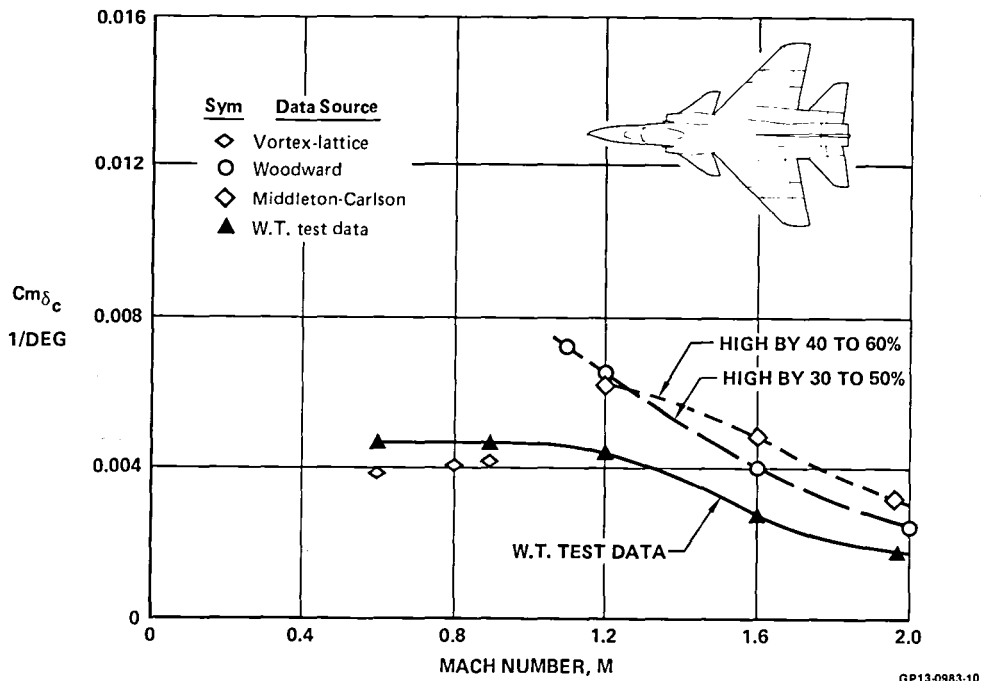
FIGURE 7-11

MODEL 263 (ANF) HORIZONTAL CANARD PITCH CONTROL EFFECTIVENESS

C.G. @ 0.15c̄

$S_C/S_W = 0.096$
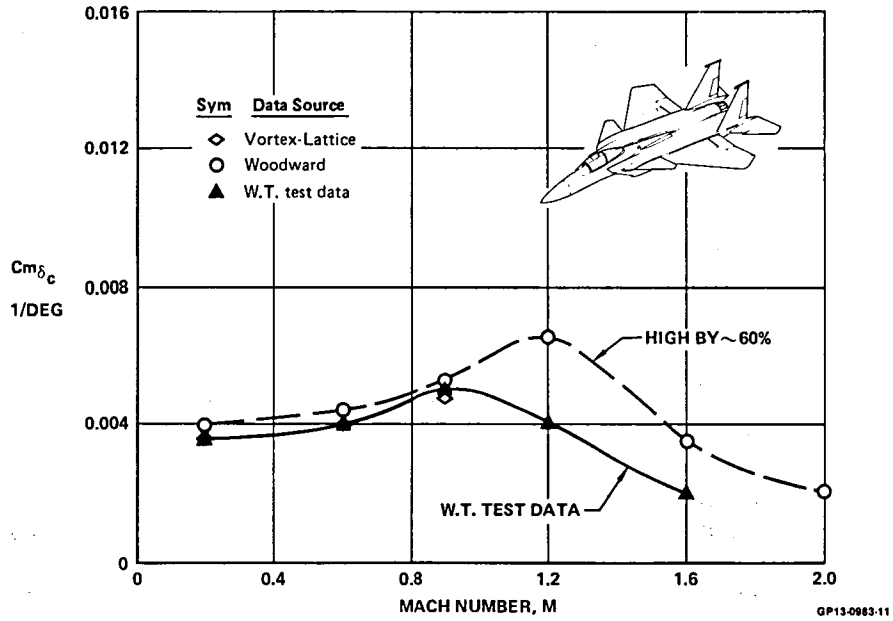
FIGURE 7-12
3-SURFACE HORIZONTAL CANARD PITCH CONTROL EFFECTIVENESS
C.G. @ $0.2565\bar{c}$ $S_c/S_w = 0.099$
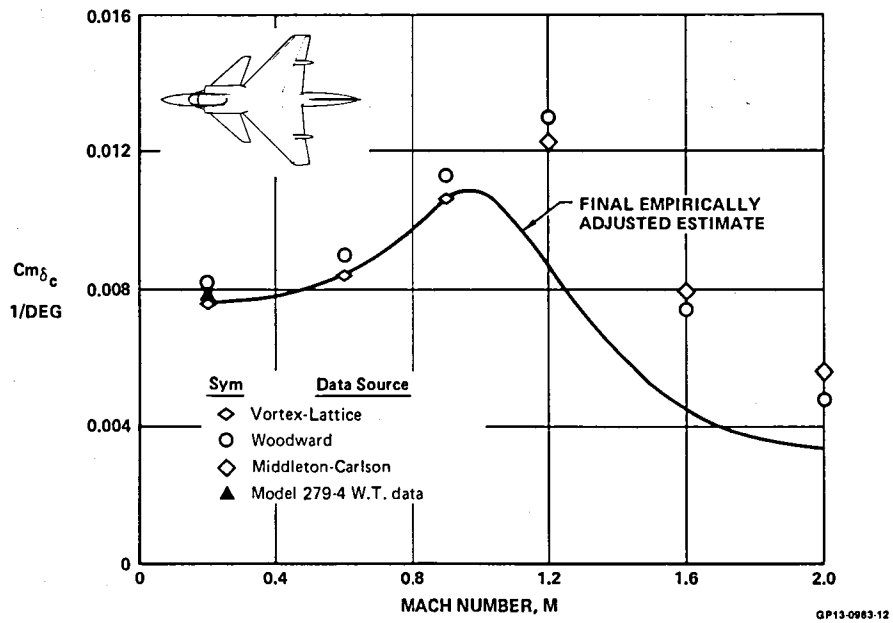
FIGURE 7-13

MODEL 279-3 HORIZONTAL CANARD PITCH CONTROL EFFECTIVENESS

When the canard is deflected to large angles or the angle of attack of
the aircraft is increased, separation can occur on the canard, the wing or
both. Separation causes the forces and moments to deviate from the linearized
predictions. The effects of separation can be predicted analytically only for
the case of leading edge separation that rolls up into a leading edge vortex.
Otherwise, the effects of separation can only be estimated as incremental
deviations from the linearized values as determined from very similar configur-
ations. The estimated canard pitching moment effectiveness at Mach 0.9
for the Model 279-3 aircraft is shown as Figure 7-14. It can be seen that
there is not only a loss of the canard effectiveness due to separation, but
that the favorable interference between the canard and wing is retained only
over a small range of canard deflections. Since this favorable interference
is a configuration dependent effect, the uncertainty arising from this effect
is appreciable.
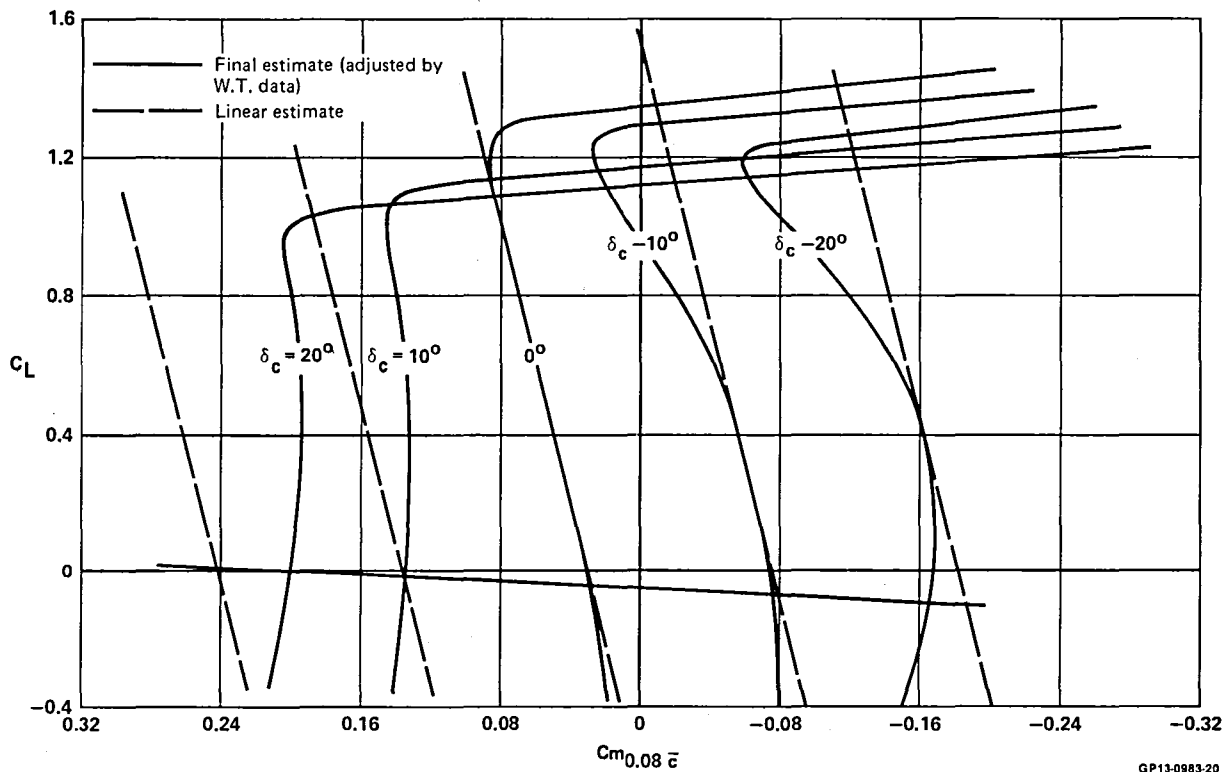
FIGURE 7-14
COMPARISON OF LINEAR AND FINAL ESTIMATED CANARD PITCHING
MOMENT EFFECTIVENESS AT MACH 0.9

The estimated canard pitching moment effectiveness at Mach 1.2 is shown
in Figure 7-15. The difference between the original linear estimate and
the empirically determined estimate corresponds to the correction for the
theoretical deficiencies shown in Figure 7-13. In addition to this correction,
pitching moment effectiveness for the large positive canard deflection decreases
significantly with angle of attack. Since this change degrades the
supersonic maneuvering capability of the aircraft, there is an
uncertainty associated with this estimate that can only be assessed with wind
tunnel testing.
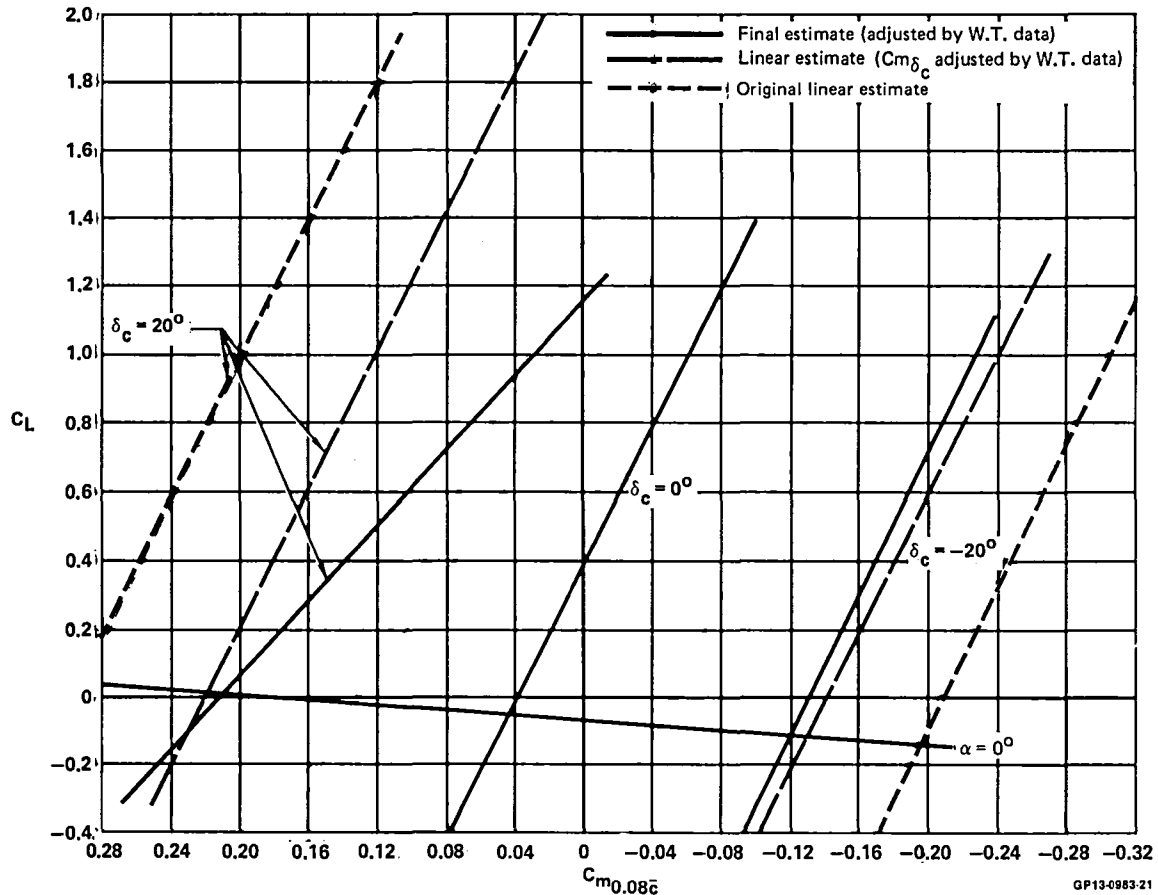
FIGURE 7-15
COMPARISON OF LINEAR AND FINAL ESTIMATED CANARD PITCHING
MOMENT EFFECTIVENESS AT MACH 1.2

Since maneuvering flaps are used as a means of enhancing the maneuvering performance of this canard-wing configuration, it is necessary to accurately determine flap lift and pitching moment effects over the entire subsonic-transonic Mach number and angle of attack range. However, separation usually occurs on flaps, even at small deflections. Figure 7-16 compares lift and pitching moment predictions by the Vortex-Lattice method with wind tunnel test data for the Model 279-1 aircraft. It can be seen that separation has reduced the effectiveness of the flaps. Also, the lift decrement due to separation occurs over the entire wing even though the separation is limited to a portion of the flap. For this reason the pitching moment change due to separation is very difficult to predict. This uncertainty is illustrated by the pitching moment increment due to flap deflection which shows no canard effect even though the inviscid theory predicts one.

The wind tunnel measured flap effectiveness of the 3-Surface F-15 at subsonic and transonic speeds is shown in Figure 7-17. These data show an effect due to the presence of a canard at low angles of attack, in contrast to the data of Figure 7-16. At high angle of attack, data at both Mach numbers show a significant canard effect. The canard effect also varies with Mach number. These effects cannot be predicted by linearized theory and also are very configuration dependent.
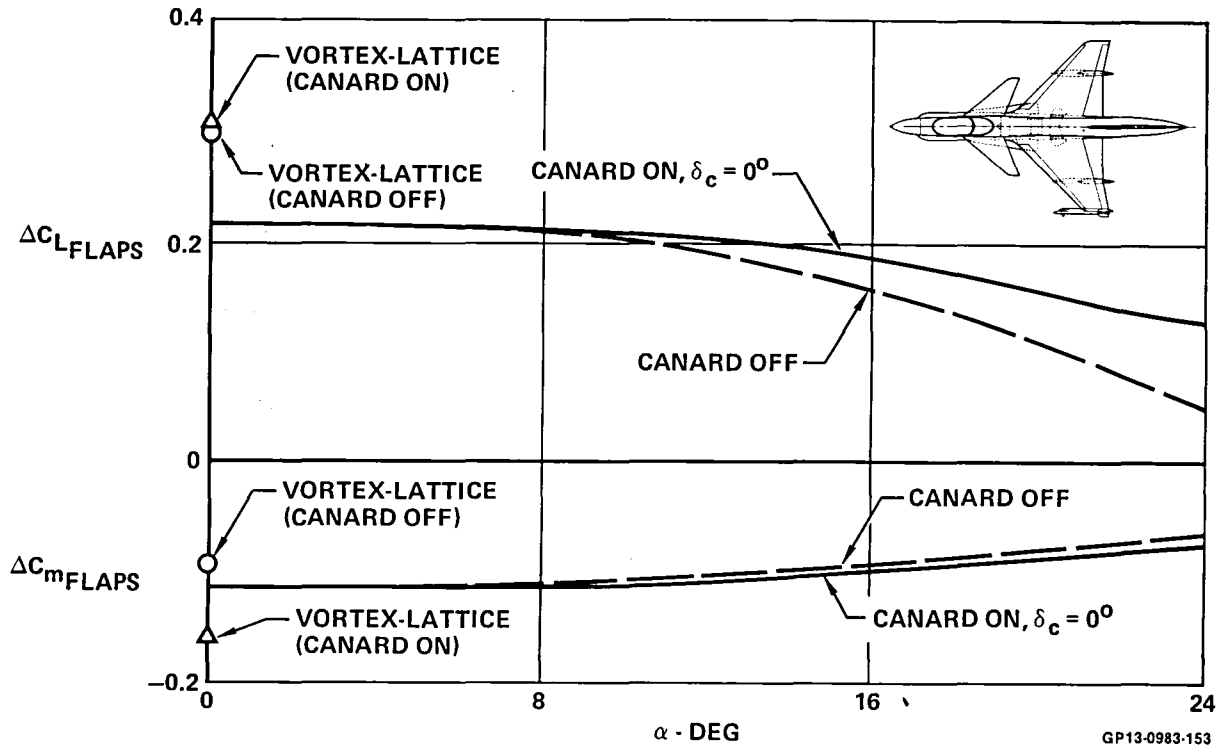
FIGURE 7-16
MODEL 279-1 CANARD EFFECT ON TE FLAP EFFECTIVENESS
Mach 0.2 $\delta_F = 15°$

GP13-0983-153
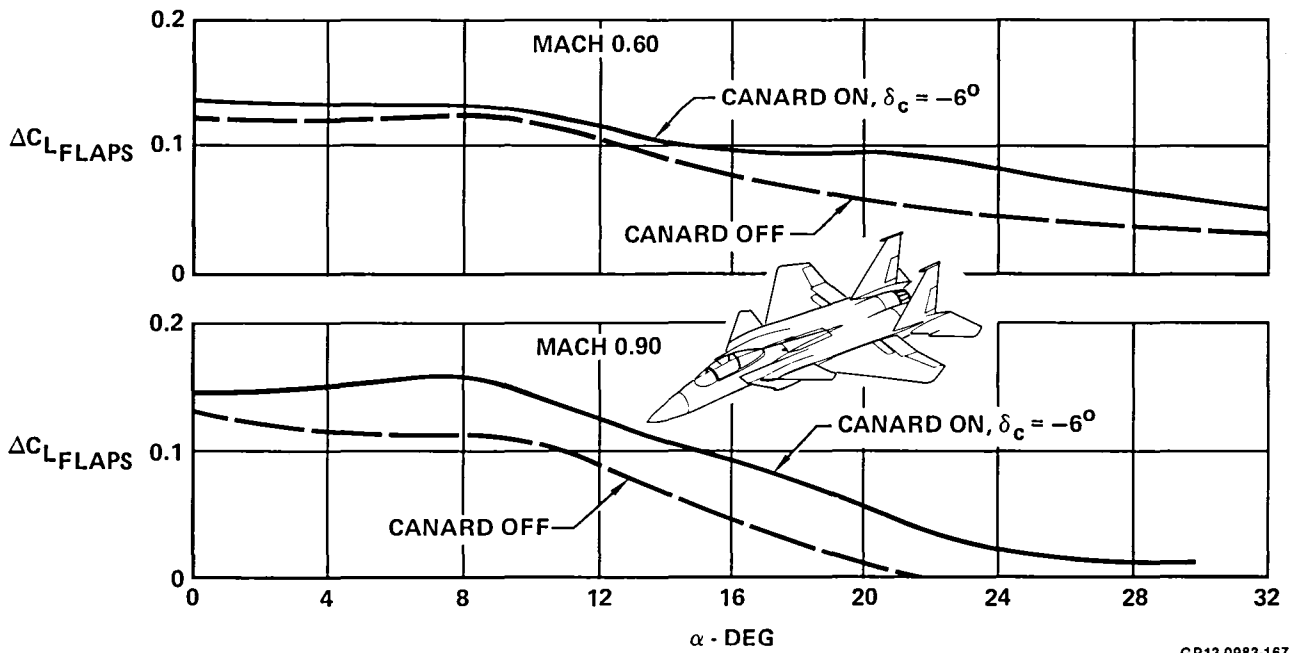
FIGURE 7-17
3-SURFACE F-15 CANARD EFFECT ON TE FLAP EFFECTIVENESS
$\delta_F = 20°$

GP13-0983-167

7.2.5 <u>LATERAL-DIRECTIONAL STABILITY</u> – The uncertainties identified in this study that affect the determination of lateral-directional stability characteristics are:

o High angle of attack characteristics,

o Vertical tail effectiveness at high angle of attack,

o Canard effects,

o Scaling of canard wind tunnel data, and

o Inlet momentum effects

The side force, yawing moment and rolling moment developed at combined angles are non-linear with respect to both sideslip and angle of attack. This is due to the viscous cross flow effects and cross coupling of the downwash and sidewash velocities. These viscous effects make it extremely difficult to determine the forces and moments due to sideslip, particularly at the high angles of attack. Discrepancies that exist between the actual and the predicted values of these forces and moments affect the determination of the vertical tail effectiveness and thus the sizing of the vertical tail.

The addition of the canard further complicates the flow patterns. Vortices shed from the canard, combining with the canard-wing interference, affect the lateral-directional stability. This can be seen in Figure 7-18 which shows the incremental effect of canards on the lateral-directional stability derivatives C_{l_β} and C_{n_β}, for three different canard configurations. These data show a directionally destabilizing effect due to canards in all cases and for two of the configurations a large directionally destabilizing effect on the vertical tail. Figure 7-19 shows this effect also by illustrating the effect of the canards on vertical tail effectiveness. Changing canard size, shape, dihedral and horizontal and vertical location will influence these effects greatly.

The effect of the canard on the lateral-directional stability of a given configuration can be obtained by scaling wind tunnel data from a similar configuration. However, the scaling involves only changes in canard area and moment arm and does not include changes in canard effect due to differences in canard shape, dihedral angle, and second order location effects. These can be substantial, particularly for large canard deflection angles.

Another source of uncertainty in predicting the lateral-directional stability for a configuration such as the Model 279-3 with its large side inlets is the inlet momentum effects. With the configuration at an angle of sideslip it is necessary for the inlet stream tube to be turned through the sideslip angle. This creates a momentum change in the direction normal to the configuration surface, resulting in a side force on that surface and a yawing moment on the configuration. The magnitude of this force and its action point cannot be computed accurately by analytic or empirical techniques. Its uncertainty influences the sizing of the vertical tail.
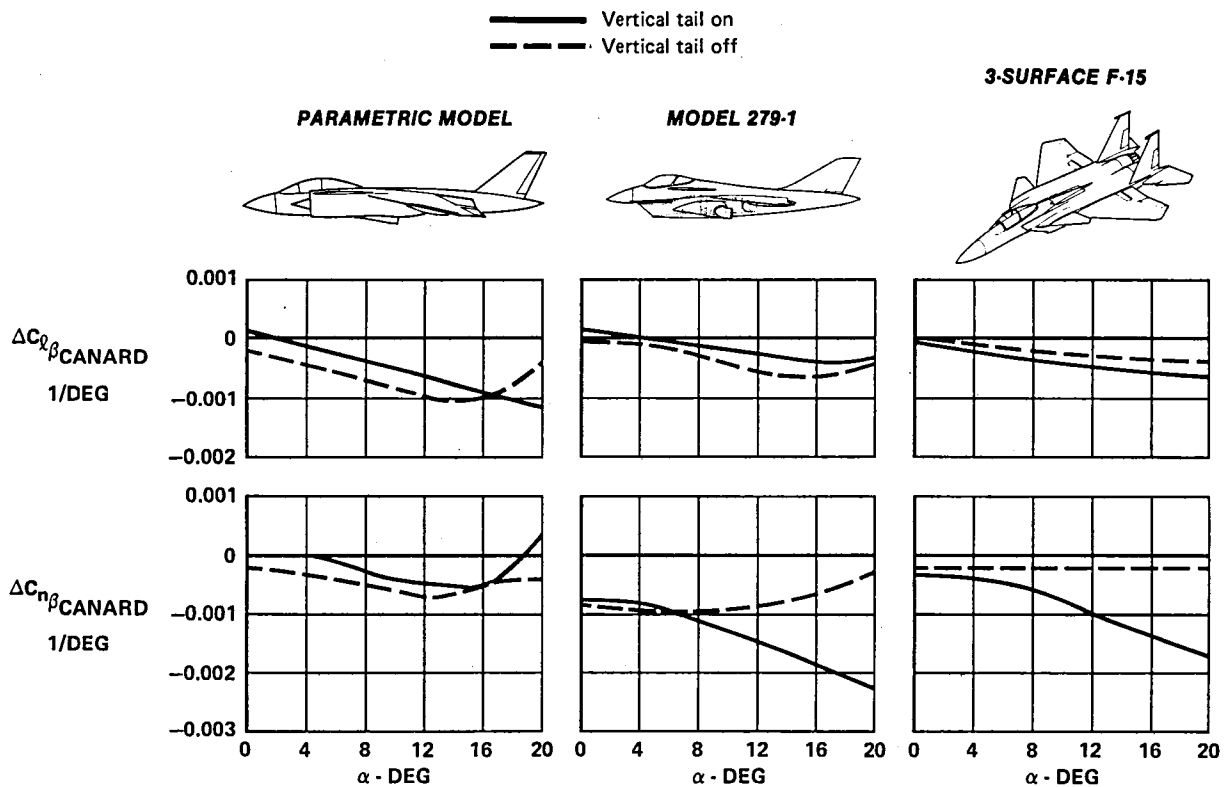
FIGURE 7-18

EFFECT OF HORIZONTAL CANARDS ON LATERAL-DIRECTIONAL STABILITY

Mach 0.2
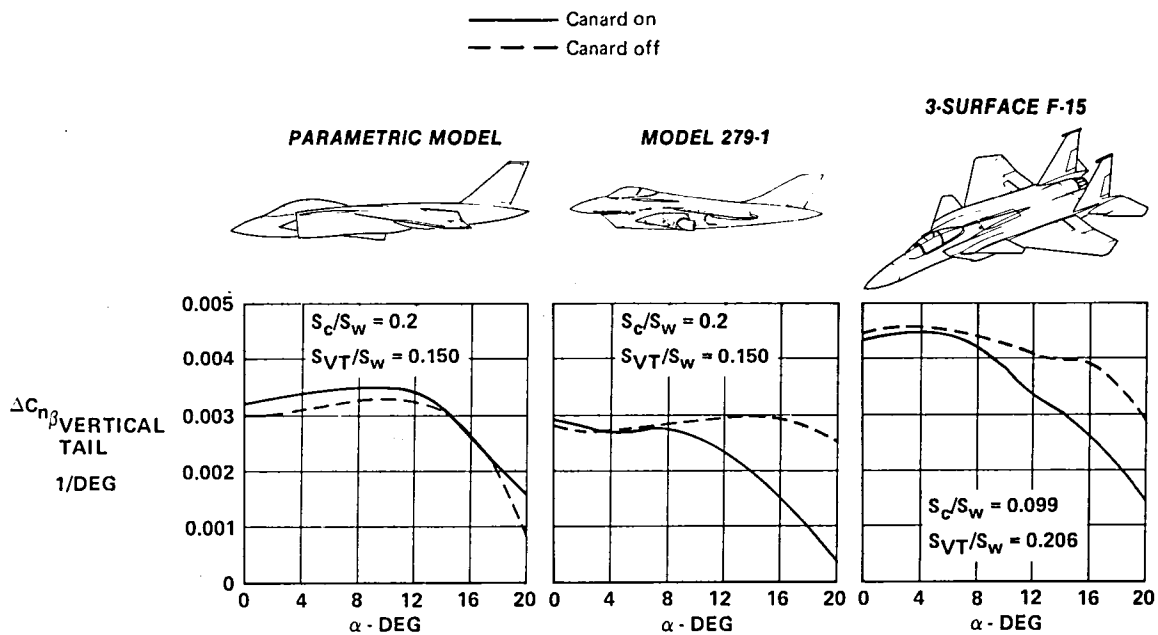
FIGURE 7-19

EFFECT OF HORIZONTAL CANARDS ON VERTICAL TAIL EFFECTIVENESS

Mach 0.2   Body Axes

7.2.6 LATERAL-DIRECTIONAL CONTROL - Figure 7-20 presents the rolling moment effectiveness due to aileron deflection for the 3-Surface F-15 aircraft. It can be seen that the canard enables the aileron to retain its effectiveness up to higher angles of attack. This increased effectiveness affects the aileron size and roll performance of the configuration. However, the extent of the increased aileron effectiveness due to the presence of the canard is a function of the relative sizes and placement of the surfaces. Since this canard effect cannot be predicted analytically, it is an uncertainty that has to be resolved experimentally.
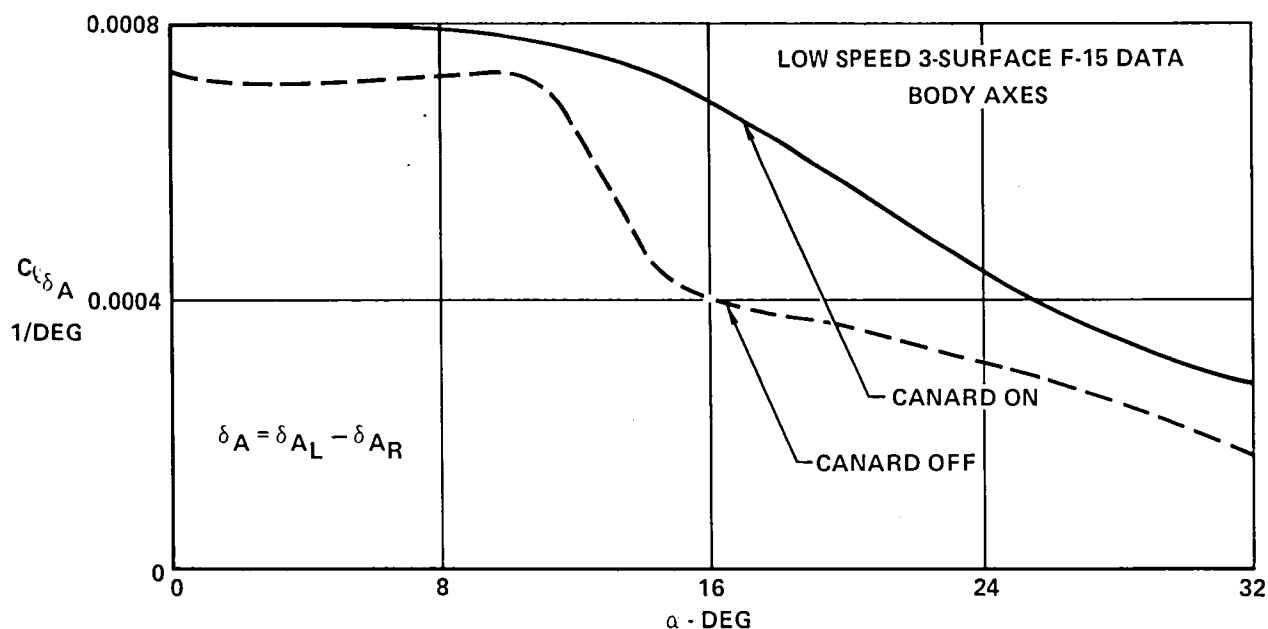
GP13-0983-158

FIGURE 7-20
EFFECT OF CANARD ON 3-SURFACE F-15 AILERON EFFECTIVENESS

7.2.7 PROPULSION INDUCED EFFECTS - The forward location of the propulsion system of a vectored thrust aircraft places the nozzles and their attendant jet exhaust plumes in close proximity to the maximum cross-sectional area of the aircraft. This causes the jet plume to affect the local flow field over a larger part of the aircraft than do conventional configurations. Tests have been conducted by the Rolls Royce engine manufacturers to determine what wave drag interference effects can result. The results at a supersonic Mach number are shown in Figure 7-21 and compared with analytical predictions. The test results were only corrected for the jet-off base drag, so that the body-plus-plume drag includes the jet effects due to interference, scrubbing, and separation.
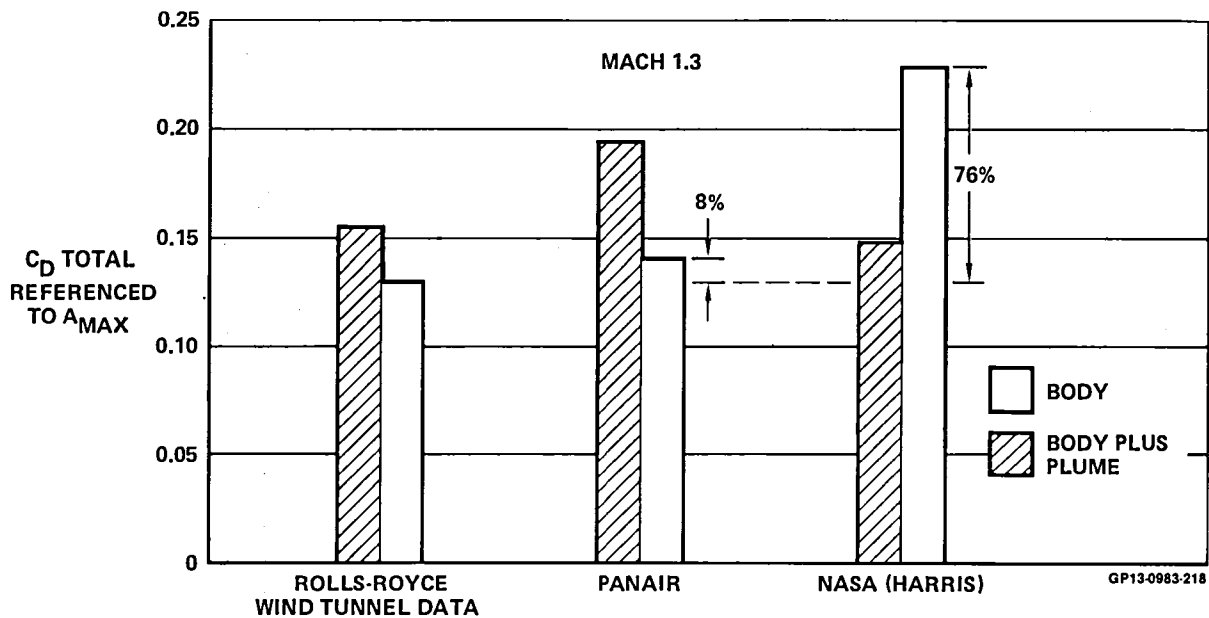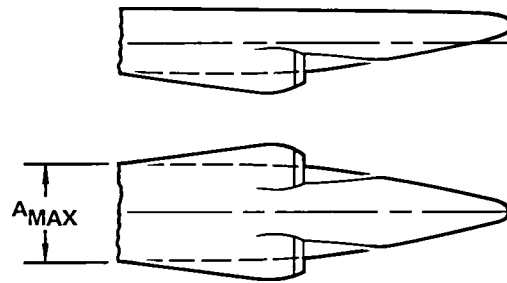
FIGURE 7-21
COMPARISON OF BODY AND PLUME DRAG DATA
WITH THEORETICAL ESTIMATES

The analytical predictions were made with the PANAIR, Reference (25) and NASA (Harris) Wave Drag, Reference (20) computer programs. These programs represent the state-of-the-art of analytical methods. The area distribution of the plume was modeled as two solid circular bodies. Its shape was determined analytically and sealed to the exit area of the Rolls Royce model. Friction and scrub drag of the model were estimated and added to the theoretically estimated wave drag to obtain total drag.

Figure 7-21 shows large differences between the theoretical estimates of the computer programs. The NASA wave drag method overpredicts the body drag by 76% but predicts a negative drag increment due to the presence of the plume. On the other hand, the PANAIR method agrees much better with the test data. Body drag is still overpredicted by 8% and the plume effect is greater than twice that shown by test. Since the sensitivity studies of Section 6.6 show that overestimates of supersonic zero-lift drag have an appreciable effect on the aircraft design parameters, this uncertainty should be resolved experimentally. A jet effects model will be necessary and is discussed in Section 8.2.6.

8. PROPOSED RESEARCH PLAN

A proposed research model, Figure 8-1, is presented to experimentally investigate the aerodynamic uncertainties identified in this study, Table 8-1. By so doing, it will be possible to (1) verify the estimates, (2) identify the strengths and weaknesses of the estimation methods, (3) identify means of improving the estimates and the estimation procedures, and (4) extend the existing data base into more extensive angle of attack, sideslip angle and Mach number ranges. The definition of powered model testing and the variables to be tested are briefly discussed, along with the modifications that will be necessary to adapt the flow-through model to jet effects testing.

VERTICAL TAIL
- RUDDER DEFLECTION
- ON/OFF

WING
- LOCATION
- DECAMBER FLAP
- AILERON
- FLAP
- ON/OFF

CANARD
- ON/OFF
- DEFLECTION

INLET
- HALF AXISYMMETRIC

NOZZLES
- MASS FLOW CHOKES

HORIZONTAL TAIL
- ON/OFF
- DEFLECTION

GP13-0983-13
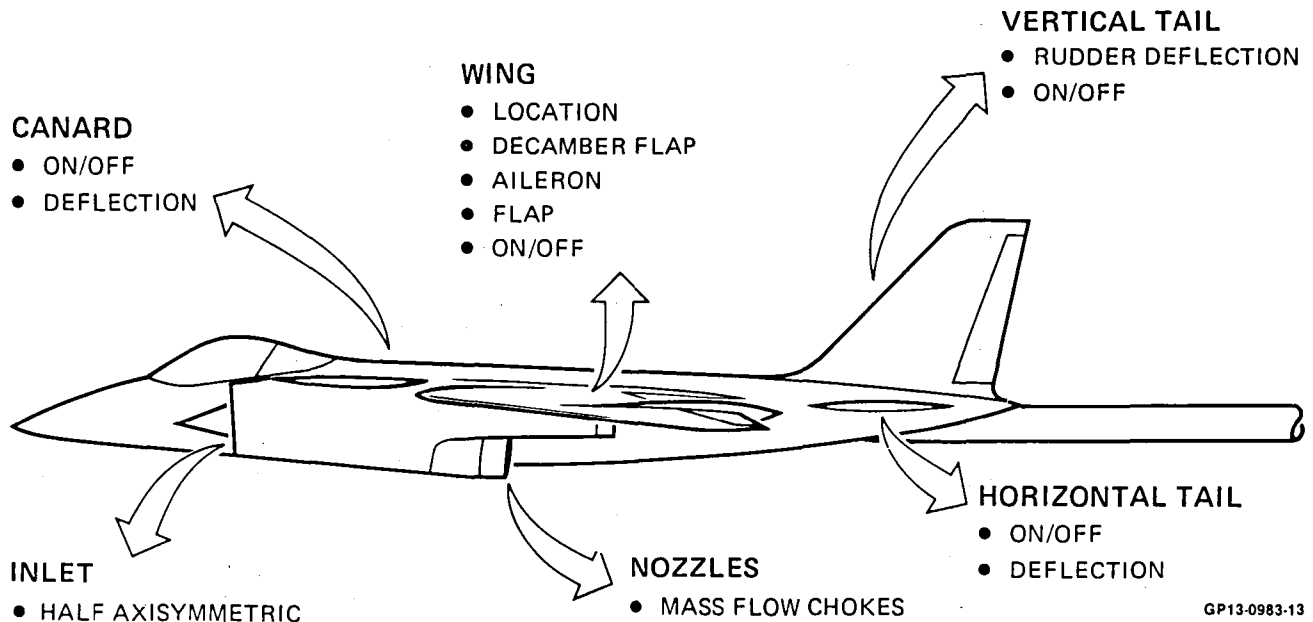
FIGURE 8-1
MODEL REQUIRED TO RESOLVE UNCERTAINTIES

8.1 WIND TUNNEL MODEL DESCRIPTION

The conceptual design of the model was developed for both performance testing and stability and control testing. Therefore, lateral-directional as well as longitudinal measurements will be necessary. For this reason a rear entry sting support was chosen. This system provides excellent high angle of attack testing capability and low support system interference. The sting will be fabricated of ultra high strength maraging steel (VASCOMAX) to minimize sting size and hence aft fuselage distortion.

Preliminary analysis of the balance-sting deflection and stability (divergence), using a MCAIR developed procedure shows that the sting is stable for the expected maximum loads. A detailed analysis of the model/balance/sting arrangement will be included in the Phase II stress analysis.

TABLE 8-1
SUMMARY OF UNCERTAINTY RESOLUTION

UNCERTAINTIES	DATA TO BE ACQUIRED
SUPERSONIC $C_{D_{MIN}}$	EFFECT OF CANARD AND DEFLECTION EFFECT OF DECAMBER FLAP EFFECT OF MASS FLOW RATIO EFFECT OF CANARD-WING LOCATION VARIATION WITH MACH NUMBER
SUBSONIC $C_{D_{MIN}}$	SAME AS SUPERSONIC $C_{D_{MIN}}$ PLUS EFFECTS OF RN
DRAG DUE TO LIFT TRIM DRAG C_L BUFFET ONSET C_L MAXIMUM LONGITUDINAL STABILITY	CANARD-WING vs WING-TAIL vs 3-SURFACE EFFECT OF DECAMBER FLAP EFFECT OF TRAILING EDGE FLAP EFFECT OF RN VARIATION WITH MACH NUMBER
LONGITUDINAL CONTROL	CANARD-WING vs WING-TAIL vs 3-SURFACE EFFECT OF CANARD AND DEFLECTION EFFECT OF TRAILING EDGE FLAP VARIATION WITH MACH NUMBER
LATERAL-DIRECTIONAL STABILITY	CANARD-WING vs WING-TAIL vs 3-SURFACE EFFECT OF CANARD VERTICAL TAIL EFFECTIVENESS EFFECT OF DECAMBER FLAPS AND TE FLAPS EFFECT OF MASS FLOW RATIO
LATERAL CONTROL	CANARD-WING vs WING-TAIL vs 3-SURFACE EFFECT OF DECAMBER FLAPS

GP13-0983-247

8.1.1 <u>FLOW-THROUGH MODEL DESCRIPTION</u> – Once the geometrical variables to be tested were identified, a preliminary layout of the model was made. This is shown as Figure 8-2. The model is designed around a stainless steel balance beam sized to accept a MCAIR furnished 2.5 inch diameter, six-component, internal strain gage balance. The wing attaches to the balance beam in either of two positions, forward or aft. This requirement causes the wing attachment cross-sectional area to be relatively small. In addition, the wing lifting surface is relatively large. Combined with the high dynamic pressure and angle of attack requirements of the test, this leads to high bending stresses in the area of the wing root. Preliminary stress analysis of the wing to balance beam attachment indicates that the wings should be of stainless steel. The sting shield aft of the balance housing is also stainless steel for rigidity.

Other considerations dictated the material selection for the remainder of the model. The bulk of the large parts are made of aluminum in order to keep the model as light as possible. Brass parts are used where material erosion is likely to be a problem or instrumentation is soldered to the part. Where parts are of an unusual shape or internal dimensions and finishes are important, electroformed nickel is specified. The parts breakdown for the model, including the number of parts required and the recommended materials, is shown as Table 8-2.
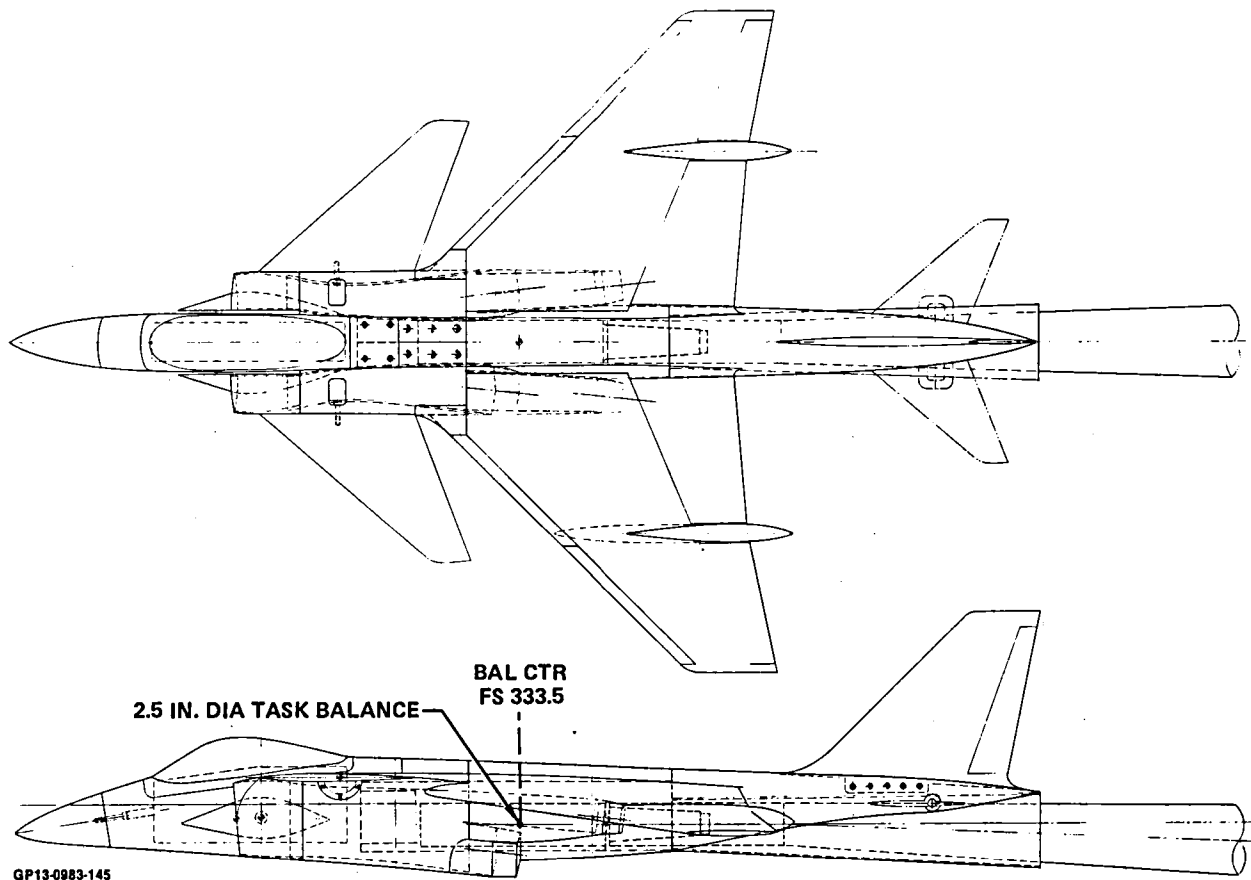
FIGURE 8-2
FLOW-THROUGH FORCE AND MOMENT MODEL

After the model parts have been specified, the conceptual geometrical variables identified in Figure 8-1 are related to the set of model parts in Table 8-3. Also shown is the range of full scale sizes or deflections that is covered within the parts list. In those cases where a number of deflected positions is anticipated (the canard and horizontal tail), gears allowing movement in pre-set increments are provided.

8.1.2 MODEL SCALING CRITERIA - In order to provide the best possible wind tunnel simulation of full scale flight conditions, it is necessary to test a large scale model. This increases the Reynolds number and improves model moldline accuracy. Therefore, the important scaling considerations, such as leading edge radii, camber, twist and the thickness distributions of the wing, canard and tails better represent full scale physical dimensions. The large scale model also provides better integration of pressure recording devices, balances, internal ducting and movable surface attachments. However, while it is desirable to design the model for the maximum size possible, consideration must be given to tunnel size compatibility and propulsion simulator airflow capacity.

8-3

TABLE 8-2
FLOW-THROUGH MODEL PARTS DESCRIPTION

DESCRIPTION	QUANTITY		MATERIAL
	LH	RH	
BALANCE HOUSING OR BEAM	1		STAINLESS STEEL
STING	1		VASCOMAX
STING SHROUD	1		STAINLESS STEEL (SHT)
FLOW-THROUGH DUCTS	1	1	ELECTROFORMED NICKEL
INLETS	1	1	BRASS
INLET CENTER BODY	1	1	BRASS
FORWARD FUSELAGE	1		ALUMINUM
CANOPY	1		ALUMINUM
NACELLES	1	1	ALUMINUM
CANARDS AND ATTACH FITTINGS	1	1	ALUMINUM/STEEL
CENTER FUSELAGE	1		ALUMINUM
CENTER FUSELAGE CAP	1		ALUMINUM
AFT FUSELAGE	1		ALUMINUM
VERTICAL TAIL	1		ALUMINUM
RUDDER	2		STAINLESS STEEL
WING ASSEMBLY	1	1	STAINLESS STEEL
LEADING EDGE FLAP	3	3	ALUMINUM
TRAILING EDGE FLAP	3	3	ALUMINUM
AILERONS	2	2	ALUMINUM
FORWARD NOZZLE	1	1	BRASS
FORWARD NOZZLE CHOKE PLATES	1	1	ALUMINUM
AFT NOZZLE	1	1	BRASS
AFT NOZZLE CHOKE PLATES	1	1	ALUMINUM
HORIZONTAL TAIL AND ATTACH FITTINGS	1	1	ALUMINUM/STEEL
OUTRIGGER FAIRINGS	1	1	BRASS

GP13-0983-246

TABLE 8-3

WIND TUNNEL MODEL CONFIGURATION VARIABLES

CONFIGURATION ITEM	SYMBOL	FULL SCALE SIZE OR DEFLECTION
FUSELAGE	B	672 IN.
WING	W_{40}	428 FT^2
WING	W_5	428 FT^2
CANARD	C	85.6 FT^2/$\pm 30^0$
LEADING EDGE FLAPS	L	0^0, -10^0, $+20^0$
TRAILING EDGE FLAPS	F	0^0, 10^0, 20^0
AILERONS	A	$\pm 20^0$
VERTICAL TAIL	V_1	65 FT^2
RUDDER FOR V_1	R_1	0^0, 15^0
HORIZONTAL TAIL	H	85.6 FT^2/$\pm 21^0$
CHOKE SETS	d_1	
$BCW_5LF\ AV_1 d_1$	Δ	

GP13-0983-161

Two wind tunnel factors which limit the maximum size of the model are the model wing area to tunnel cross section area ratio and the model frontal area to tunnel cross section area ratio, both of which are blockage ratios. These area ratios are expressed in terms of the full scale aircraft dimensions and a scale factor. Then, using the "rule-of-thumb" guidelines set forth by NASA Ames for sizing models for their tunnels (shown in Table 8-4), it was determined that the model wing area to tunnel cross section area ratio was the driving factor. When this ratio was limited to 3.0 percent for the 11 ft x 11 ft Unitary Transonic Wind Tunnel (TWT), the model scale of 9.2 percent was established. This model scale gives a blockage ratio higher than the recommended value for the smaller 12 ft Pressure Wind Tunnel (PWT) and 9 ft x 7 ft Supersonic Wind Tunnel (SSWT). However, MCAIR experience has shown that higher blockage ratios can be tolerated under some circumstances. In the case of the 9 ft x 7 ft SSWT, the maximum angle of attack will be limited and the conservative blockage ratio can be exceeded.

Based on the sizing data in Table 8-4, the 9.2% scale model could be tested in the 11 ft and 12 ft wind tunnels with no limitations to model angle of attack and at reasonably high wind tunnel dynamic pressures. This scale model can also be tested in the 9 ft x 7 ft SSWT up to an angle of attack of approximately 15 degrees, sufficient to provide all of the necessary data. Model to test section blockage ratios are low for the three tunnels shown, and therefore, tunnel start up loads, flow disturbances and wall effects should be minimized.

If the Model 279-3 is scaled to the airflow of the Compact Multi-Mission Aircraft Propulsion Simulator (CMAPS) of Reference (36), it results in a 6.2% scale. However, the CMAPS will not fit inside a model of this size. On the other hand, the 9.2% size is geometrically compatible with the CMAPS, but the application of the engine simulator to the proposed concept is more difficult than for a conventional turbofan engine installation for which the CMAPS was designed to simulate. However, there are potential methods of utilizing the

TABLE 8-4
MODEL SCALING CRITERIA

NASA AMES WIND TUNNEL TEST SECTION DIMENSIONAL DATA

WIND TUNNEL	WIDTH (FT)	HEIGHT (FT)	LENGTH (FT)	EFFECTIVE CROSS SECTION (FT^2)
11 FT	11	11	22	121
12 FT	11.3	11.3	18	100
9 FT x 7 FT	7	9	18	63

RECOMMENDED CRITERIA

	FRONTAL AREA T.S. AREA	WING AREA T.S. AREA	WING SPAN T.S. WIDTH
NASA AMES	0.005	0.03	0.50
MCAIR	0.005 - 0.010	0.05	0.50 - 0.60

WIND TUNNEL SIZING DATA FOR 9.2% SCALE MODEL

WIND TUNNEL	FRONTAL AREA T.S. AREA	WING AREA T.S. AREA	WING SPAN T.S. WIDTH	MODEL LENGTH T.S. LENGTH
11 FT	0.002	0.030*	0.300	0.234
12 FT	0.002	0.036	0.292	0.286
9 FT x 7 FT	0.003	0.058	0.471	0.286

*Sizing conditions

CMAPS in the proposed thrust vectoring concept, which could provide both proper inlet and nozzle flow simulation. One approach would be to utilize the CMAPS compressor flow to simulate the core flow (or aft nozzle flow) of the thrust vectoring engine. In this method, a solid mixer would be utilized and the turbine drive air would be bled off entirely. At the maximum CMAPS airflow (1.65 lb/sec) the core nozzle pressure ratio and flow rates are reasonably matched. A portion of the turbine bleed air could then be used to power ejectors in the front nozzles to simulate the PCB nozzle conditions and to induce additional airflow through the inlet system. This could provide reasonable simulation of inlet operating conditions. An alternate approach would be to drive the ejectors through a separate high pressure air supply line entering through a strut or wing tip support.

8.1.3 BALANCE SELECTION CRITERIA - In order to determine the expected maximum loads likely to be imposed on the model balance, it was determined that the critical operating condition would occur in the 11 ft x 11 ft TWT at 0.90 Mach number, 1450 lb/ft^2 dynamic pressure and a unit Reynolds number of 8.0 x 10^6 per ft. At this worst operating condition, an anticipated angle of attack range of -4 to +15 degrees was used in combination with 8 degrees of sideslip, ±24 degrees of canard deflection, ±20 degrees of stabilator deflection and

maneuvering flap deflections. Assuming the moment reference center at 5% of the wing mean aerodynamic chord and the critical combination of model variables, the maximum expected loads were calculated as:

Component	Maximum Expected Load
Normal Force	6000 lb
Side Force	+650 lb
Axial Force	800 lb
Pitching Moment	-19,500 to +24,500 in-lb
Yawing Moment	+8300 in-lb
Rolling Moment	+5000 in-lb

Because of the need for an early balance selection, these values were based on low speed tests of a similar configuration with compressibility effects included. For the Phase II testing, the critical operating conditions of the wind tunnel will be redefined on the basis of the improved aerodynamic analysis of the previous sections.

Once the anticipated loads were established, candidate balances were reviewed in order to ensure that the loads fell within their capabilities. A representative comparison of loads and balance capabilities for normal forces and pitching moments is shown in Figure 8-3. The balances shown are Task Corporation six component internal strain gage balances owned by MCAIR and NASA Ames. It can be seen that if the NASA Ames MK XX or MK XXXII balances were used, the wind tunnel operating conditions would have to be limited or the range of test variables reduced. In addition to these normal force and pitching moment limitations, the maximum axial forces and rolling moments anticipated for this model are also beyond the capabilities of the NASA Ames balances.

The 2.5 inch diameter MK XXV balance is preferred over the 2.75 inch diameter MK III balance due to the reduced volume required for installation in the model. This leaves additional clearance between the balance housing and the model for bridging of the balance by instrumentation and/or air lines.

The model balance and sting arrangement will be common for the three wind tunnel installations. The support sting will be attached to the main support systems of the 11 ft x 11 ft TWT and the 9 ft x 7 ft SSWT using existing NASA Ames unitary sting adapters. It can also be used for the 12 ft PWT installation by providing an adapter to mate it to the existing high angle of attack support system.

8.1.4 INSTRUMENTATION AND CALIBRATION - The six component internal strain gage balance discussed in the previous section will be the principal force and moment measurement device. In addition, instrumentation will be provided for specialized measurements. Model angle of attack will be measured by means of an inclinometer placed on a leveling plate to be included as part of the model. A strain gage to measure the wing root bending moment and a wing tip accelerometer will detect buffet onset and measure its intensity respectively. Internal balance cavity pressures will be measured, and the mass flow and internal duct drag of each nozzle will be determined from total and static pressure measurements.
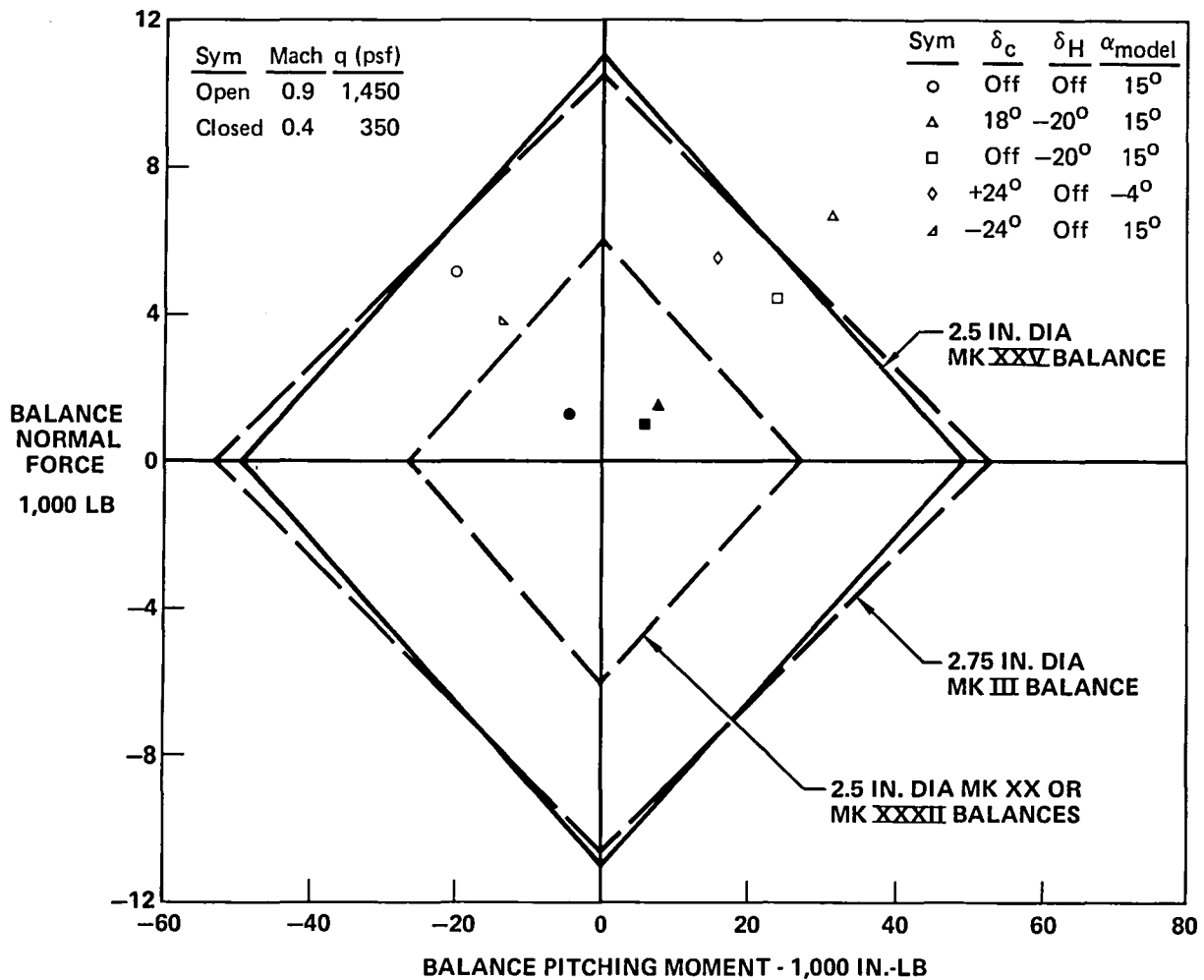
FIGURE 8-3
MAXIMUM WIND TUNNEL MODEL LOADS AND NORMAL FORCE-PITCHING
MOMENT ENVELOPES FOR CANDIDATE BALANCES
9.2% Scale Model

Chart axes:
- Vertical axis: BALANCE NORMAL FORCE 1,000 LB, from -12 to 12
- Horizontal axis: BALANCE PITCHING MOMENT - 1,000 IN.-LB, from -60 to 80

Sym	Mach	q (psf)
Open	0.9	1,450
Closed	0.4	350

Sym	δ_C	δ_H	α_{model}
o	Off	Off	15°
△	18°	−20°	15°
□	Off	−20°	15°
◊	+24°	Off	−4°
◢	−24°	Off	15°

2.5 IN. DIA MK XXV BALANCE

2.75 IN. DIA MK III BALANCE

2.5 IN. DIA MK XX OR MK XXXII BALANCES

GP13-0983-244

The wing tip accelerometer and the wing root bending moment strain gage will be integral parts of the wind tunnel model. The test technique requires continuous recording at discrete angles of attack with sufficient time provided at each angle to define the frequency characteristics. Signals are conditioned online in order to identify the changes of the frequency response characteristics that identify buffet onset. It is anticipated that NASA Ames will calibrate the instrumentation for buffet evaluation.

The inlet mass flow of the flow-through model will be controlled by chokes at the nozzle duct exits. The flow area of the chokes to be used is derived from an assessment of the required mass flow range to be covered within the test matrix. For application to a thrust vectoring engine, the flow split between the forward and aft nozzles is also considered for sizing. The proper flow split is a function of the specific engine and the engine condition being simulated. External rakes will be provided so the mass flow ratio and internal duct drag of each nozzle can be determined.

Each nozzle choke will be statically calibrated in the MCAIR Mass Flow Calibration Facility (MFCF) over the anticipated pressure ratio range. The major components of the MFCF are the precalibrated venturi meter section and a 74 inch ID test chamber, Figure 8-4. Complete wind tunnel models can be mounted in the pressurized chamber allowing air to pass through the model air induction system and exit to ambient conditions through the nozzle. With the nozzle pressure instrumentation described above, the calibration will provide the normalized mass flow $(W\sqrt{T_T}/P_T)$ as a function of the nozzle exit pressure ration (P_e/P_{T_o}). This parameter is then used for the calculation of inlet mass flow ratio and internal duct drag during the wind tunnel tests.
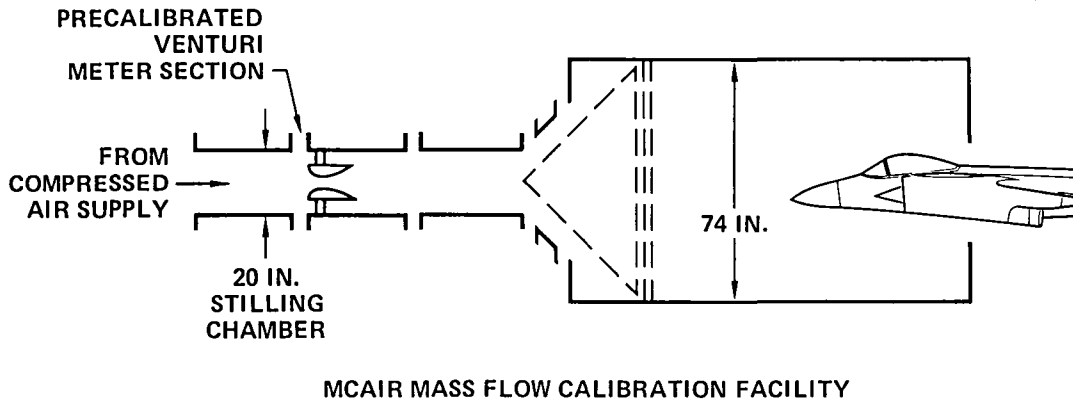
MCAIR MASS FLOW CALIBRATION FACILITY

FIGURE 8-4

GP13-0983-242

INLET DUCT MASS FLOW AND DRAG CALIBRATION

The external exit rakes will be provided for test definition of the nozzle exit momentum. Each rake consists of 9 total pressure and 4 static pressure tubes per nozzle. There is a separate rake for the forward and aft nozzles. The rake will be used for the static calibration and, in addition, a calibration of the internal duct drag as part of the wind tunnel test.

8.1.5 MODEL INSTALLATION – After a review of the capabilities of the NASA Ames Research Center wind tunnels, it has been determined that the 11 ft x 11 ft Unitary Transonic Wind Tunnel lends itself to the investigation of the major areas of uncertainty. Thus, it is anticipated that the major portion of the testing would be conducted in this facility. A sketch of the model installed in this wind tunnel is shown as Figure 8-5. This installation provides a large angle of attack range, which has been shown to be important in the previous sections.

The previous sections also show that the. basic aerodynamic uncertainties span the entire speed range from subsonic through supersonic conditions. The 11 ft x 11 ft wind tunnel has a Mach number range from 0.5 to 1.4. Since the 9 ft x 7 ft supersonic wind tunnel has a capability of Mach 1.5 to 2.5, a combination of tests in the two wind tunnels would provide data applicable over the full speed range of the Model 279-3 aircraft. The 9 ft x 7 ft wind tunnel installation would utilize the same support hardware that is used in the 11 ft x 11 ft wind tunnel.
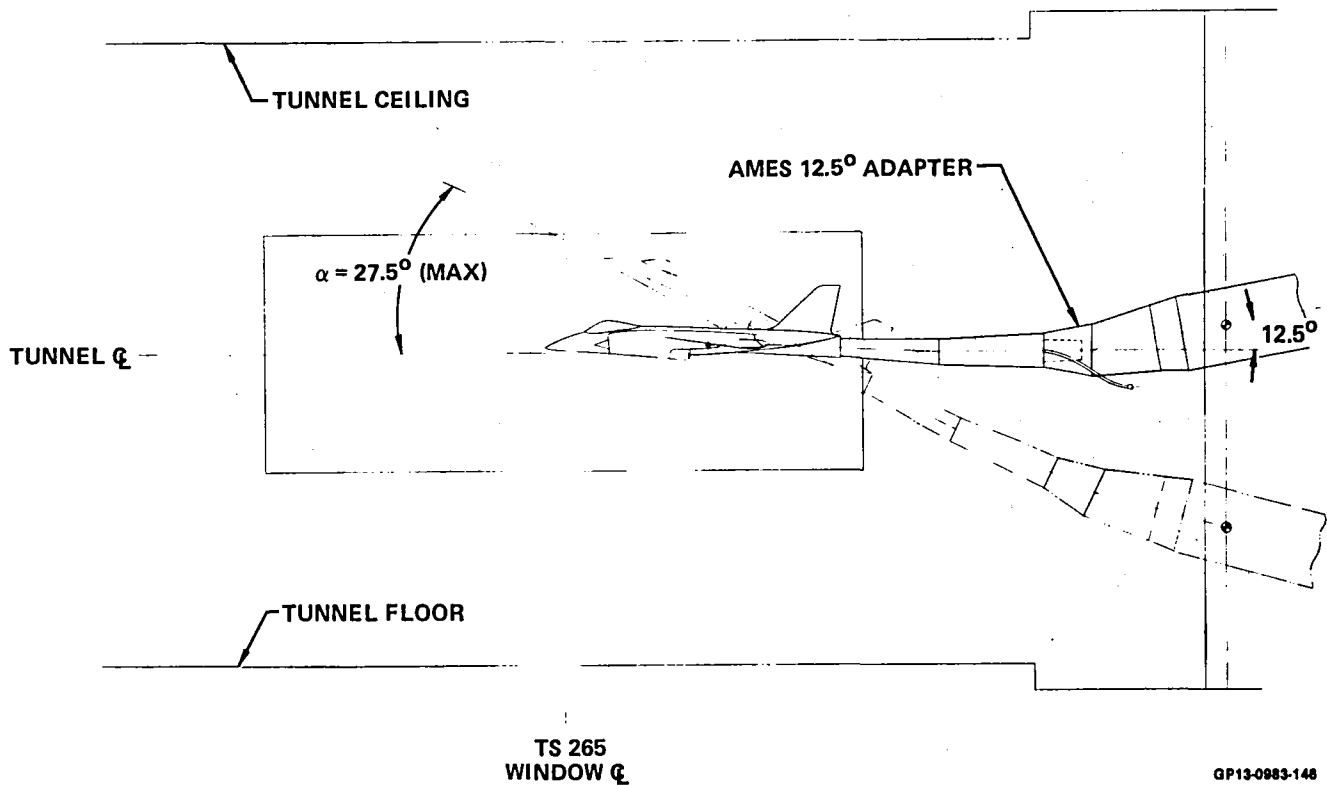
FIGURE 8-5

MODEL INSTALLATION IN NASA AMES 11 FT x 11 FT TRANSONIC UNITARY WIND TUNNEL

For testing at angles of attack above 27 degrees, it is necessary to utilize the 12 ft Pressure Wind Tunnel. This tunnel is particularly suited by its support system to conduct tests to very high angles of attack at lower speeds. Its variable density capability also permits exploration of the effects of Reynolds number at less than 0.5 Mach number. An illustration of the Model 279-3 aircraft model installed in the 12 ft PWT is shown in Figure 8-6.

8.1.6 MODEL CONVERSION FOR JET EFFECTS TESTING - The flow-through model was designed with consideration for low cost conversion to the jet effects mode. The objective was to maintain as much hardware commonality as possible. In particular, those items requiring close adherence to dimensional tolerances and surface finish, such as the wing and control surfaces, were retained.

The aerodynamic uncertainties to be addressed by the jet-effects model are listed in Table 8-5. Since these uncertainties involve the power-induced effects on the aircraft aerodynamics, the propulsive thrust is not measured. Instead, the inlets are faired over and the the jet exit nozzles are maintained non-metric. This has the further advantage of not requiring bridging of the balance by the nozzle flow high pressure lines.

8-10
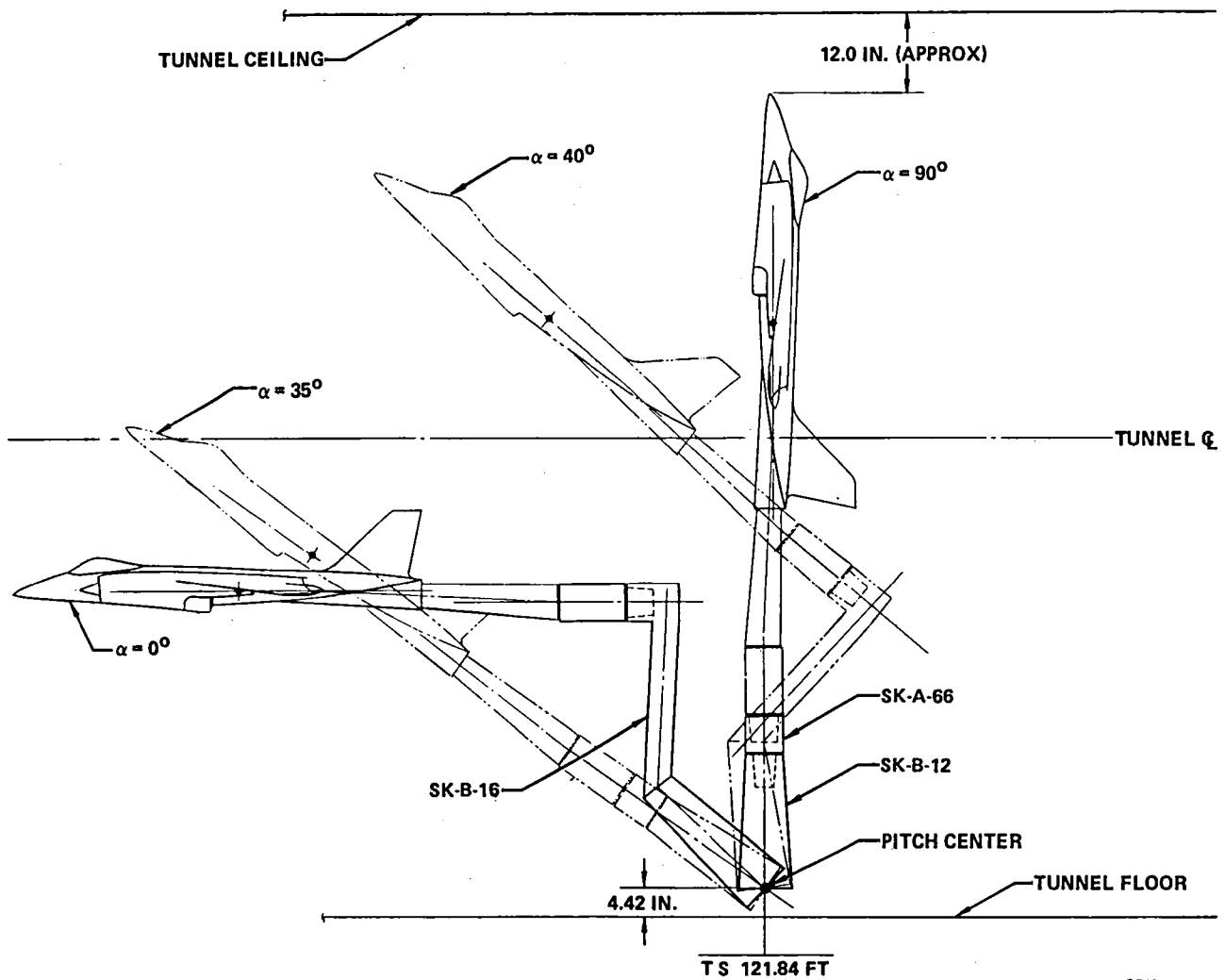
FIGURE 8-6
MODEL INSTALLATION IN NASA AMES 12 FT PRESSURE WIND TUNNEL

The proposed jet effects model is shown in Figure 8-7, and the parts that will be used by the jet effects model alone are listed in Table 8-6. The power block will be attached to the same rear entry sting support that will be used for the flow-through model. It will contain the plenum chambers for the non-metric exit nozzles and the attachments for the nozzles themselves. Nozzles and nozzle chokes in addition to those of the flow-through model will be required due to the high pressure, high flow rate supply air and the elimination of the instrumentation requirement. The power block will be fed by a high pressure secondary source of air via high pressure stainless steel air lines that will be attached to the sides of the suppport sting.

TABLE 8-5
JET-EFFECTS MODEL CONFIGURATION VARIABLES

AERODYNAMIC UNCERTAINTIES
POWER INDUCED EFFECTS ON PERFORMANCE
POWER INDUCED EFFECTS ON STABILITY AND CONTROL
EXHAUST PLUME INTERACTION EFFECTS

TEST OBJECTIVES
FORCE AND MOMENT MEASUREMENTS
QUANTIFY POWER DEPENDENT DRAG INCREMENTS
IDENTIFY PLUME IMPINGEMENT AREAS

DETERMINE JET INDUCED AERODYNAMIC INTERACTIONS
   • WING PRESENCE
   • TAIL EFFECTS
   • JET TO FLAP COUPLING

EVALUATE AND IMPROVE PREDICTION TECHNIQUES

TEST VARIABLES
MACH NUMBER
ANGLE-OF-ATTACK
ANGLE-OF-YAW
NOZZLE EXIT AREA
NOZZLE PRESSURE RATIO

GP13-0983-243

TABLE 8-6
DESCRIPTION OF PARTS PECULIAR TO POWERED MODEL

DESCRIPTION	QUANTITY		MATERIAL
	LH	RH	
BALANCE HOUSING OR BEAM	1		STAINLESS STEEL
POWER BLOCK	1		STAINLESS STEEL
FORWARD NOZZLES	2	2	ELECTROFORMED NICKEL
FORWARD NOZZLE CHOKES	2	2	STAINLESS STEEL
FORWARD NOZZLE SHROUDS	1	1	ELECTROFORMED NICKEL
AFT NOZZLES	1	1	ELECTROFORMED NICKEL
AFT NOZZLE CHOKES	2	2	STAINLESS STEEL
AFT NOZZLE SHROUDS	1	1	ELECTROFORMED NICKEL
AIR LINES	3		STAINLESS STEEL
CENTER FUSELAGE	1		ALUMINUM
CENTER FUSELAGE CAP	1		ALUMINUM
INLET FAIRINGS	1	1	ALUMINUM

GP13-0983-250

SCANIVALVE

BAL CTR
FS 377

2.5 IN. DIA TASK BALANCE
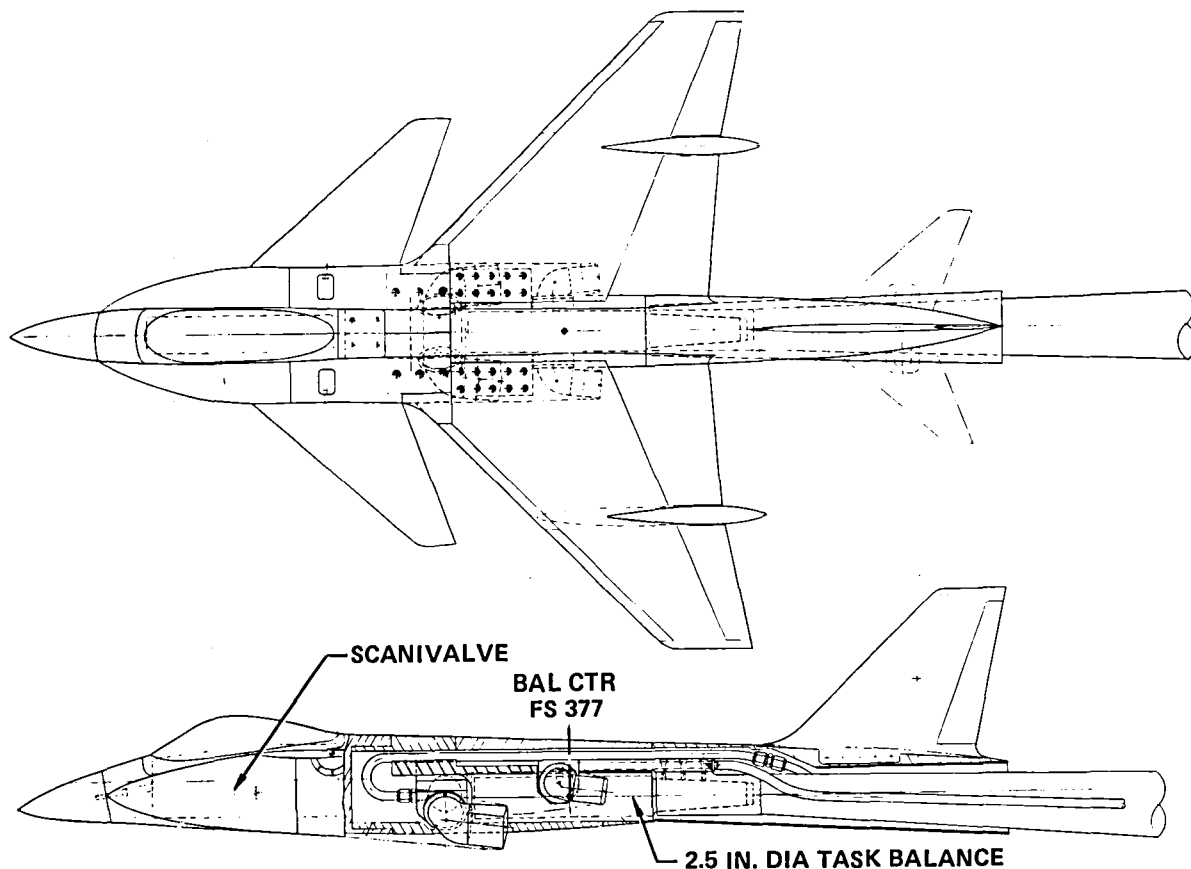
GP13-0983-140

FIGURE 8-7
JET-EFFECTS FORCE AND MOMENT MODEL

The model will be carried by the same 2.5 inch diameter internal strain gage balance to be used for the flow-through model. However, the balance beam will be changed due to the need to clear the power block. For the same reason a new center fuselage and center fuselage cap will be required. Inlet fairings will replace the flow-through model inlets and nozzle shrouds will replace the flow-through nozzles. The shrouds also maintain the fuselage mold lines close to, but not touching, the jet nozzles.

8.2 PHASE II WIND TUNNEL TEST PLAN

As part of the development of the test plan, the Mach number, Reynolds number and angle of attack ranges were determined over which each aerodynamic uncertainty is to be resolved. While not all of the uncertainties have to be resolved over the entire range of the variables, the variety of the uncertainties is sufficiently great that the test plan had to include the full range. The majority of the testing can be conducted in the transonic speed range and within an angle of attack range large enough to define the aircraft stall and/or buffet boundary. However, it is also necessary to test at high Mach numbers and, independently, at high angles of attack and sideslip. The latter requirements involve less extensive testing programs to be conducted within other, more specialized, wind tunnels.

With the wide range of potential test variables, the test schedule was tailored to provide the most efficient use of occupancy time, with consideration given to model changes, data acquisition rates, and usable run time. The final test program is summarized in Table 8-7. The range of aerodynamic variables to be addressed in each wind tunnel is shown along with the estimated number of occupancy hours. This summary was, in turn, developed from more extensive summaries for each of the wind tunnels considered. The summary test matrix for the 11 ft x 11 ft Unitary Transonic Wind Tunnel is shown in Table 8-8, that for the 9 ft x 7 ft Supersonic Wind Tunnel is shown in Table 8-9, and that for the 12 ft Pressure Wind Tunnel in Table 8-10. The detailed run schedule is shown in Table 8-11. It is felt that this run schedule fully addresses the data requirements necessary to resolve the aerodynamic uncertainties summarized in Figure 8-2.

TABLE 8-7
WIND TUNNEL TEST PLAN SUMMARY

NASA-AMES WIND TUNNEL	TEST OBJECTIVE	MACH NUMBER	ANGLE-OF-ATTACK (DEG)	ANGLE-OF-SIDESLIP (DEG)	ESTIMATED OCCUPANCY (HR)
11 FT x 11 FT TRANSONIC	SUBSONIC/TRANSONIC FORCE AND MOMENT DATA	$0.5 \rightarrow 1.4$	$-3 \rightarrow 27$	$-10 \rightarrow 10$	240
9 FT x 7 FT SUPERSONIC	SUPERSONIC FORCE AND MOMENT DATA	$1.6 \rightarrow 2.0$	$-3 \rightarrow 15$	$-10 \rightarrow 10$	80
12 FT PRESSURE	LOW SPEED, HIGH ANGLE-OF-ATTACK, HIGH SIDESLIP ANGLE FORCE AND MOMENT DATA. REYNOLDS NUMBER EFFECTS	$0.2 \rightarrow 0.4$	$0 \rightarrow 90$	$-10 \rightarrow 30$	60

GP13-0983-149

TABLE 8-8
WIND TUNNEL TEST PLAN SUMMARY
NASA Ames 11 Ft x 11 Ft Wind Tunnel

CONFIGURATION BALANCE	MACH NUMBER	RN x 10^6 PER FT	α RANGE (DEG)	β RANGE (DEG)	CANARD (C) δ RANGE (DEG)	H TAIL (H) δ RANGE (DEG)	LE FLAP (L) δ RANGE (DEG)	TE FLAP (F) δ RANGE (DEG)	AILERON (A) δ RANGE (DEG)	V TAIL (V_1)	RUDDER (R_1) δ RANGE (DEG)	CHOKE (d) SIZE	OCCUPANCY (HR)
SUBSONIC WING AFT (BASIC) $BCW_5 LFAV_1 R_1 d_1 = \Delta$	$0.5 \rightarrow 0.95$	$3.0 \rightarrow 8.0$	$-3 \rightarrow 27$	$+10 \rightarrow -10$	± 30 AND OFF	OFF	0, 20	0, 10, 20	± 20	ON AND OFF	+15	VAR	80
WING FORWARD $BW_{40} LFAV_1 Hd_1$	$0.5 \rightarrow 0.95$	$3.0 \rightarrow 8.0$	$-3 \rightarrow 27$	$+10 \rightarrow -10$	OFF	± 21	0, 20	0, 10, 20	± 20	OFF	+15	1	60
THREE SURFACE $BCW_5 LFAV_1 R_1 Hd_1 = \Delta + H$	$0.5 \rightarrow 0.95$	3.0	$-3 \rightarrow 27$	$+10 \rightarrow -10$	± 30 AND OFF	± 21	0, 20	0, 10, 20	0	ON	+15	1	40
SUPERSONIC WING AFT $= \Delta$	$1.05 \rightarrow 1.4$	$3.0 \rightarrow 8.0$	$-3 \rightarrow 15$	$+10 \rightarrow -10$	± 30 AND OFF	OFF	0, -10	0, 10, 20	± 20	ON AND OFF	+15	VAR	25
WING FORWARD $BW_{40} LFAV_1 Hd_1$	$1.05 \rightarrow 1.4$	$3.0 \rightarrow 8.0$	$-3 \rightarrow 15$	$+10 \rightarrow -10$	OFF	± 21	0, -10	0	± 20	OFF	+15	1	20
THREE SURFACE $= \Delta + H$	$1.05 \rightarrow 1.4$	3.0	$-3 \rightarrow 15$	$+10 \rightarrow -10$	± 30 AND OFF	± 21	0, -10	0, 10, 20	0	ON	+15	1	15
												TOTAL	240

GP13-0983-162

8-14

TABLE 8-9
WIND TUNNEL TEST PLAN SUMMARY
NASA Ames 9 Ft x 7 Ft Wind Tunnel

CONFIGURATION BALANCE	MACH NUMBER	$RN \times 10^6$ PER FT	α RANGE (DEG)	β RANGE (DEG)	MODEL PART AND MAXIMUM RANGE OF VARIABLES									
					CANARD (C) δ RANGE (DEG)	H. TAIL (H) δ RANGE (DEG)	LE FLAP (L) δ RANGE (DEG)	TE FLAP (F) δ RANGE (DEG)	AILERON (A) δ RANCE (DEG)	V TAIL (V_1)	RUDDER (R_1) δ RANGE (DEG)	CHOKE (d) SIZE	OCCUPANCY (HR)
WING AFT (BASIC) $BCW_5LFAV_1R_1d_1$	1.6 → 2.0	3.0	-3 → 15	+10 → -10	·30 AND OFF	OFF	0, -10	0	±20	ON AND OFF	+15	VAR	40
WING FORWARD $BW_{40}LFAV_1Hd_1$	1.6 → 2.0	3.0	-3 → 15	+10 → -10	OFF	±21	0, -10	0	±20	OFF	0	1	20
3-SURFACE $BCW_5LFAV_1R_1Hd_1$	1.6 → 2.0	3.0	-3 → 15	+10 → -10	±30	±21	0, -10	0	0	ON	+15	1	20
												TOTAL	80

GP13-0983-163

TABLE 8-10
WIND TUNNEL TEST PLAN SUMMARY
NASA Ames 12 Ft Pressure Wind Tunnel

CONFIGURATION BALANCE	MACH NUMBER	$RN \times 10^6$ PER FT	α RANGE (DEG)	β RANGE (DEG)	MODEL PART AND MAXIMUM RANGE OF VARIABLES									
					CANARD (C) δ RANGE (DEG)	H. TAIL (H) δ RANGE (DEG)	LE FLAP (L) δ RANGE (DEG)	TE FLAP (F) δ RANGE (DEG)	AILERON (A) δ RANGE (DEG)	V TAIL (V_1)	RUDDER (R_1) δ RANGE (DEG)	CHOKE (d) SIZE	OCCUPANCY (HR)
WING AFT (BASIC) $BCW_5LFAV_1R_1d_1X$ ∗ ∆	0.2 → 0.4	0.6 → 6.0	0 → 90	-10 → 30	·30 AND OFF	OFF	0, 20	0, 10, 20	±20	ON AND OFF	+15	1	30
WING FORWARD $BW_{40}LFAV_1Hd_1$	0.2 → 0.4	0.6 → 6.0	0 → 90	-10 → 30	OFF	±21	0, 20	0	·20	OFF	+15	1	15
3-SURFACE $BCW_5LFAV_1R_1Hd_1$ ∗ ∆ ∗ H	0.2	0.6 → 6.0	0 → 90	-10 → 30	±30 AND OFF	·21	0, 20	0, 10, 20	0	ON	+15	1	15
												TOTAL	60

GP13-0983-164

The wind tunnel test plan was developed under the assumption that the stated wind tunnels would be available for the required number of occupancy hours within the required time frame. It is recognized that this assumption may not hold. In this case substitutions may have to be made, although any substitutions will compromise the quality of the data, or limit the range of the variables to be addressed. For example, if the 12 ft Pressure Wind Tunnel is not available, the high angle of attack data could be acquired in the 14 ft x 14 ft Transonic Wind Tunnel by sacrificing the Reynolds number range of the data and the confidence in the data acquired at the highest angles of attack. Alternatively, if the 11 ft x 11 ft Unitary Transonic Wind Tunnel is not available for the full number of occupancy hours required, a compromise plan could be to limit testing in this tunnel to that necessary to establish the performance characteristics of the model (Subsonic and Supersonic $C_{D_{min}}$ in Figure 8-2). Incremental data to resolve the other uncertainties could then be found in another tunnel (such as the 14 ft TWT) after a number of the performance data runs had been repeated. This would, of course, increase the number of occupancy hours required.

TABLE 8-11(a)
PROPOSED WIND TUNNEL TEST PROGRAM
BASIC WING-CANARD CONFIGURATION

CONFIGURATION	δ_C	δ_L	δ_F	δ_A	δ_H	δ_R	α	β	R.N. M/FT	.2 (12 FT PWT)	.4	.6 (11 FT TWT)	.8	.9	.95	1.05	1.1	1.2	1.4	1.6 (9x7 FT SWT)	2.0	REMARKS
Bd	OFF	OFF	OFF	OFF	OFF	OFF	A1	0	3.0	X		X		X				X		X	X	Model Buildup
BdC	0						A1	0				X		X				X		X	X	
	-10						A1	0				X		X				X		X		
BdCW5	0	0	0	0			A1	B1		X		X		X	X	X		X		X	X	
BdW5	OFF						A1	B1		X		X		X	X	X		X		X	X	
BdW5V1						0	A1	B1		X	X	X	X	X	X	X	X	X	X	X	X	
BdCW5V1	0						A1	B1	Var.	X	X	X	X	X	X	X	X	X	X	X	X	Basic Model
	-30						A1	0	3.0	X		X		X								Canard Effect.
	-20						A1	B1		X		X		X				X		X		
	-10						A1	0		X		X		X				X		X	X	
	-5						A1	0		X		X	X	X	X			X		X	X	
	10						A1	0		X		X		X				X		X	X	
	20						A1	B1		X		X		X				X		X	X	
	30						A1	0										X		X	X	
	20/-20						A1	B1		X		X		X								Differential Canard
	0		10				A1	0		X		X	X	X								Flap Effect.
			20				A1	0		X		X	X	X								
		20/20					A1	0		X		X		X								Full Span L.E. Flap
		0/20					A1	B1		X		X	X	X								Outb'd L.E. Flap
			10				A1	0		X		X	X	X								
			0				A1	0		X		X		X								
		0/-10					A1	0									X	X	X	X	X	Decamber Flap
		-10/-10					A1	0									X	X	X	X	X	
		0/-10	10				A1	0									X	X	X			Supersonic Flap Effect
		0	20				A1	0									X	X	X			
			0	20/-20			A1	0		X		X		X				X		X	X	Aileron Effect
	-10	0/20	20	0			A1	0				X		X								Canard Power
	10						A1	0				X		X								with flaps
	0	0	0			15	A1	B1		X		X		X				X		X	X	Rudder Effect.
BCW5V1						0	A1	B1				X	X	X	X			X				Mass Flow Effects

TABLE 8-11(b)
PROPOSED WIND TUNNEL TEST PROGRAM
WING-HORIZONTAL TAIL CONFIGURATION

CONFIGURATION	δ_C	δ_L	δ_F	δ_A	δ_H	δ_R	α	β	R.N. M/FT	12 FT PWT .2	.4	11 FT TWT .6	.8	.9	.95	1.05	1.1	1.2	1.4	9x7 FT SWT 1.6	2.0	REMARKS
BdW_{40}	OFF	0	0	0	OFF	OFF	A1	B1	3.0	X		X		X				X		X	X	Model Buildup
$BdW_{40}V_1$					↓	0	A1	B1	↓	X		X		X				X		X	X	Forward Wing
$BdW_{40}H_1$					0	OFF	A1	B1	↓	X		X		X				X		X	X	
$BdW_{40}H_1V_1$					↓	0	A1	B1	Var.	X	X	X	X	X	X	X	X	X	X	X	X	
					21		A1	B1	3.0	X		X		X								Horizontal Tail
					12		A1	0		X		X		X				X		X	X	Effect.
					6		A1	0		X		X		X				X		X	X	
					-6		A1	0		X		X		X				X		X	X	
					-12		A1	0		X		X		X				X		X	X	
					-21		A1	B1		X		X		X				X		X	X	
					9/-9		A1	B1		X		X		X				X		X	X	Differential H. Tail
					-3/-21		A1	B1		X		X		X				X		X	X	
		0/20			0		A1	0		X		X		X								Flap Effect
		0/-10					A1	0									X	X	X	X	X	
		-10/-10					A1	0									X	X	X			
		0		20/-20		↓	A1	0		X		X		X				X		X	X	Aileron Effect.
		↓	↓	0	↓	15	A1	B1	↓	X		X		X				X		X	X	Rudder Effect.

8-17

TABLE 8-11(c)
PROPOSED WIND TUNNEL TEST PROGRAM
THREE SURFACE CONFIGURATION

CONFIGURATION	δ_C	δ_L	δ_F	δ_A	δ_H	δ_R	α	β	R.N. M/FT	12 FT PWT .2	.4	11 FT TWT .6	.8	.9	.95	1.05	1.1	1.2	1.4	9x7 FT SWT 1.6	2.0	REMARKS
BdW5H1V1	OFF	0	0	0	0	0	A1	0	3.0	X		X		X				X		X		
BdC1W5H1V1	0						A1	B1	Var.	X	X	X	X	X	X	X	X	X	X	X	X	
	-20						A1	B1	3.0	X		X		X				X		X		Canard Effect.
	-10						A1	0		X		X		X				X		X	X	
	-5						A1	0		X		X		X				X		X	X	
	10						A1	0		X		X		X				X		X	X	
	20						A1	B1		X		X		X				X		X	X	
	20/-20						A1	0		X		X		X								Differential Canard
	0				21		A1	B1		X		X		X				X		X	X	Horizontal Tail Effect.
					12		A1	0		X		X		X				X		X	X	
					6		A1	0		X		X		X				X		X	X	
					-6		A1	0		X		X		X				X		X	X	
					-12		A1	0		X		X		X				X		X	X	
					-21		A1	B1		X		X		X				X		X	X	
					-3/-21		A1	B1		X		X		X				X		X	X	Differential H. Tail
					9/-9		A1	B1		X		X		X				X		X	X	
			10		0		A1	0		X		X		X								Flap Effect. (Canard On)
			20				A1	0		X		X		X								
	0	0	20		12		A1	0				X		X								Horizontal Tail Effect. with Flaps
					-12		A1	0				X		X								
		0/20			0		A1	0		X		X		X								
			10				A1	0		X		X		X								
			0				A1	0		X		X		X								
BdW5H1V1	OFF	0	10				A1	0		X		X		X								Flap Effect (Canard Off)
			20				A1	0		X		X		X								
BdC1W5H1V1	0	0/-10	0				A1	0									X	X	X	X	X	Decamber Flap Supersonic Flap Effect.
			10				A1	0									X	X	X			
			20				A1	0									X	X	X			
BdW5H1V1	OFF		10				A1	0									X	X	X			
			20				A1	0									X	X	X			
BdC1W5H1V1	0	0	0			15	A1	B1		X		X		X				X		X	X	Rudder Effect.

9. CONCLUSIONS

Phase I of this NASA and Navy sponsored single-cruise-engine V/STOL fighter/attack aircraft technology study program has been completed. A viable supersonic V/STOL fighter/attack aircraft concept has been defined which satisfies all the study guidelines. This canard-wing configuration, in the 30,000 pound VTOGW class, features a propulsion system with side mounted half axisymmetric inlets, an advanced technology separated flow engine with fan stream burning and four vectored thrust nozzles.

Aerodynamic and aerodynamic-propulsion interaction uncertainties associated with this concept were identified and their significance assessed. Many of these uncertainties are configuration dependent and are associated with:

o The close-coupled horizontal canard,
o The leading and trailing edge flaps,
o The large inlet for the high bypass ratio engine, and
o The forward location of the vectored thrust propulsion system.

Improved methods are required to more accurately predict the effect of horizontal canards on aerodynamic characteristics. Supersonically, existing linear theory methods tend to over estimate by 55 to 75% the destabilizing effect of horizontal canards and their control effectiveness capability by as much as 60%. Subsonic high angle of attack canard effects as well as flap effects and canard-flap interactions also cannot be adequately predicted. Canard effects on lateral-directional stability are very configuration dependent, with wind tunnel testing being the only way to accurately predict them. Power dependent effects of varying inlet mass flow on canard-wing characteristics and lateral-directional stability are also difficult to estimate.

Wind tunnel testing is required to accurately assess the uncertainties identified in the study. The aft sting mounted aerodynamic flow through model defined for Phase II will permit assessment of most of the aerodynamic uncertainties and some of the aerodynamic-propulsion interaction uncertainties. A Phase II wind tunnel test program to acquire the necessary subsonic and supersonic aerodynamic data has been defined. This program, which also will provide an extensive aerodynamic data base for future use, includes testing in the following NASA Ames Research Center test facilities:

o 11 Ft x 11 Ft Transonic Wind Tunnel (240 hours)
o 9 Ft x 7 Ft Supersonic Wind Tunnel (80 hours)
o 12 Ft Pressure Wind Tunnel (60 hours)

A powered model is required to evaluate the uncertainties that cannot be investigated with a flow through model. A jet effects model with faired-over inlets can be used to investigate nozzle exhaust interactions with the airframe. The flow through wind tunnel model defined for the Phase II wind tunnel test program can be converted, at low cost, to a jet effects model. A Compact Multi-Mission Aircraft Propulsion Simulator (CMAPS) model is needed to quantify inlet-exhaust flow interaction effects.

10. REFERENCES

1. NASA RFP 2-28182(CA), "Study of Aerodynamic Technology for Single-Cruise-Engine V/STOL Fighter/Attack Aircraft", 12 August 1980.

2. Burns, C. S., "Wind Tunnel Test Results of Two Minimum Drag Wing Designs in the McDonnell Polysonic Wind Tunnel, Series III, PWT 325," McDonnell Douglas Report MDC A2173, April, 1973.

3. Lacey, D. W., "Aerodynamic Characteristics of the Close-Coupled Canard as Applied to Low-to-Moderate Swept Wings - Vol. 1, General Trends", DTNSRDC-79/001, Final Report, January, 1979.

4. Gloss, B. B., "The Effect of Canard Leading Edge Sweep and Dihedral Angle on the Longitudinal and Lateral Aerodynamic Characteristics of a Close-Coupled Canard-Wing Configuration", NASA TN D-7814, 1974.

5. Tryon, P. F. and Hess, J. R., "Wind Tunnel Test of a 5% Scale Model 263 With High Lift Devices on the Wing and Canard, Cambered Canard, and Increased Aspect Ratio Vertical Tail," McDonnell Douglas Report MDC A3607, 11 August 1975.

6. Hess, J. R. and Lyerla, G. W., "AFTI-15 Series X High Speed Wind Tunnel Test Data Analysis," McDonnell Douglas Report MDC A5951, 25 May 1979.

7. Beavers, N. D. "High Speed Aerodynamic Characteristics of a 4.7% Scale Three Surface TF-15 Model Tested in the MCAIR Polysonic Wind Tunnel, PSWT Test No. 415" McDonnell Douglas Report MDC A6228, 8 December 1980.

8. Beavers, N. D., "Low Speed Aerodynamic Characteristics of a 13% Scale Three Surface F-15 Model Tested in the MCAIR Low Speed Wind Tunnel, Series II, LSWT Test No. 381," McDonnell Douglas Report MDC A6848, 19 December 1980.

9. Simon, W. E., "V/STOL Lift/Cruise Vectoring Supersonic Fighter/Attack Concept," McDonnell Douglas Report MDC A6534, 30 June 1980.

10. Gross, L. W. and Althuis, G. A., "ADWT Test of a Twin Engine Vectored Thrust V/STOL Fighter/Attack Concept," McDonnell Douglas Report MDC A7444, 29 January 1982.

11. Thomas, R. W., "AFTI-15 Series VI High Speed Wind Tunnel Test Analysis," McDonnell Douglas Report MDC IR0112, 15 May 1978.

12. Thomas, R. W., "AFTI-15 Series VII High Speed Wind Tunnel Test Analysis," McDonnell Douglas Report MDC IR0111, 15 May 1978.

13. Agnew, J. W. and Mello, J. F., "MCAIR Design Philosophy for Fighter Aircraft Departure and Spin Resistance", SAE Paper 791081, December, 1979.

14. Margason, R. J. and Lamar, J. E., "Vortex-Lattice Fortran Program for
    Estimating Subsonic Aerodynamic Characteristics of Complex Planforms,"
    NASA TN D-6142, February 1971.

15. Hoak, D. E., et.al., "USAF Stability and Control DATCOM", USAF WADD
    TR-60-261, Revised April 1978.

16. Schlichting, H., "Boundary Layer Theory", McGraw Hill, 1960.

17. Sommer, S. C., and Short, B. J., "Free-Flight Measurements of Turbulent
    Boundary Layer Skin Friction in the Presence of Severe Aerodynamic
    Heating at Mach Numbers from 2.8 to 7.0", NACA TN3391, March, 1955.

18. Hoerner, S. F., "Fluid Dynamic Drag", self published, 1965.

19. Walck, K. J., "Parametric Evaluation of Nacelle Integration Drag at
    Subsonic Speeds", McDonnell Douglas Report MDC IR0144, December, 1978.

20. Harris R. V., "An Analysis and Correlation of Aircraft Wave Drag", NASA
    TMX-947, March, 1964.

21. Stoddard, C. H., "Correlation of Wing Pressure Drag", McDonnell Aircraft
    Company Report EN-30, 30 July 1953.

22. Simon, W. E., et.al., "Prediction of Aircraft Drag Due to Lift",
    AFDL-TR-71-84, July, 1971.

23. Shrout, Barrett L., "Extension of a Numerical Solution for the
    Aerodynamic Characteristics of a Wing to Include a Canard or Horizontal
    Tail", NASA TMX-66,886, January, 1971.

24. Woodward, F. A. and Hague, D. S. "A Computer Program for the Analysis and
    Design of Wing-Tail-Body Combinations at Subsonic and Supersonic Speeds",
    ARC-TN-19, March, 1969.

25. Moran, J. et.al., "User's Manual - Subsonic/Supersonic Advanced Panel
    Pilot Code", NASA CR-152047, February, 1978.

26. Beavers, N. D. and Lyerla, G. W., "Low Speed Aerodynamic Characteristics
    of a 13% Scale Three Surface F-15 Model Tested in the MCAIR Low Speed
    Wind Tunnel, LSWT No. 370," McDonnell Douglas Report MDC A6215,
    15 November 1979.

27. McDonnell Douglas Report MDC A4987, "Wind Tunnel Data System,"
    July, 1978.

28. McDonnell Douglas Corporation Report MDC A4637, "YAV-8B Aerodynamic
    Stability and Control and Flying Qualities Report," Revision C,
    January, 1980.

29. McDonnell Douglas Corporation Report MDC A0853-7-2," 1979 Independent Research and Development. Aircraft Exhaust Heating," Project No. 97770, January, 1979.

30. McDonnell Douglas Corporation Report MDC Q0857-7-4, "1980 Independent Research and Development. Aircraft Jet Exhaust Heating," Project No. 107770, January, 1980.

31. McDonnell Douglas Corporation Report MDC Q0860-7-4, "1981 Independent Research and Development. Aircraft Jet Exhaust Thermal Environment and Heating, Project No. 117770, March, 1981.

32. Scuderi, L. F., "Comparisons of Jet Exhaust Heating Predictions with Full Scale Test Data," McDonnell Douglas Corporation Report MDC IR0224, August, 1980.

33. Brown, M. W., "USN/FMOD FRG, VAK-191B Joint Flight Test Program, Volume II, AM-2 Aluminum Airfield Landing Mat Tests," Report NAVAIR-11R-76, August, 1976.

34. Fluk, H., "Runway and Deck Temperatures in Vertical Takeoff/Landing Operations," AIAA Paper P-81-1623, AIAA Aircraft Systems and Technology Conference, 11-13 August 1981.

35. Cyrus, J. D., "Study of the Effect of the Hot Gas Efflux from VTOL Aircraft upon the Crew, Ship, and Aircraft," NADC-77249-60, February 20, 1978.

36. AFAPL-TR-79-3, "Turbine Engine Multi-Mission Propulsion Simulator Wind Tunnel Demonstration," November, 1976.

APPENDIX A

CONVERSION FACTORS FROM ENGLISH
SYSTEM TO METRIC SYSTEM

Velocity

ft/sec	multiply by .3048	to get meters/sec
knots/hour	multiply by 1.854	to get kilometers/hour

Distance

inches	multiply by 25.4	to get millimeters
inches	multiply by 2.54	to get centimeters
feet	multiply by .3048	to get meters
Nautical miles	multiply by 1.854	to get kilometers

Wing Loading

lb/ft^2	multiply by 4.882	to get $kilogram/meters^2$

Area

ft^2	multiply by .09290	to get $meters^2$

Weight (Mass)

lb_m	multiply by .4536	to get kilograms

Force

lb_f	multiply by 4.448	to get Newtons

Capacity

gallons	multiply by 3.785	to get liters

Temperature

°F −32	multiply by 5/9	to get °C

Mass Flow

lb_m/sec	multiply by .4536	to get kilogram/second

Moment of Inertia

$slug\ ft^2$	multiply by 1.355	to get $kilogram\ meter^2$

1. Report No. NASA CR-166269	2. Government Accession No.	3. Recipient's Catalog No.
4. Title and Subtitle Study of Aerodynamic Technology for Single-Cruise-Engine V/STOL Fighter/Attack Aircraft		5. Report Date March 1982
		6. Performing Organization Code
7. Author(s) J. R. Hess R. L. Bear		8. Performing Organization Report No. MDC IR0285
		10. Work Unit No.
9. Performing Organization Name and Address McDonnell Aircraft Company P. O. Box 516 St.Louis, Missouri 63166		11. Contract or Grant No. NAS2-11001
12. Sponsoring Agency Name and Address National Aeronautics and Space Administration,Washington,D.C.20546 David Taylor Naval Ship R&D Center, Carderock, Md. 20034 Naval Air Systems Command, Washington, D. C. 20361		13. Type of Report and Period Covered Contractor Final Report June 1981 to February 1982
		14. Sponsoring Agency Code RTOP 505-43-01

15. Supplementary Notes

Technical Monitors: D. A. Durston/W. P. Nelms, NASA-Ames Research Center, Mail Stop 227-2,
Moffett Field, Ca. 94035, FTS 448-5855/5879
Point of Contact: J. H. Nichols, Jr., DTNSRDC
Point of Contact: M. W. Brown, NAVAIR

16. Abstract

A viable single engine, supersonic V/STOL fighter/attack aircraft concept has been
defined which satisfies all the study guidelines. This vectored thrust, canard-wing
configuration utilizes an advanced technology separated flow engine with fan stream burning.
The aerodynamic characteristics of this configuration were estimated and performance evaluated.
Significant aerodynamic and aerodynamic-propulsion interaction uncertainties requiring
additional investigation were identified. A wind tunnel model concept and test program to
resolve these uncertainties and validate the aerodynamic prediction methods were defined.

17. Key Words (Suggested by Author(s)) V/STOL, Vectored Thrust, Fan Stream Burning, Horizontal Canard	18. Distribution Statement FEDD Distribution Subject Category 02
19. Security Classif. (of this report) Unclassified	20. Security Classif. (of this page) Unclassified	21. No. of Pages 180	22. Price*

Available: NASA's Industrial Applications Centers

End of Document